Mechanics of Instability-driven Geodynamic Processes: A Theoretical and Experimental Study

A thesis submitted for the degree of

Doctor of Philosophy (Science) of

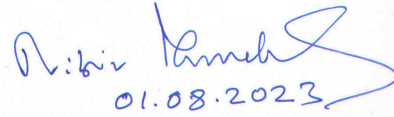*Jadavpur University*

By

Arnab Roy

Department of Geological Sciences
Jadavpur University
Kolkata-700032, India

August
2023

CERTIFICATE FROM THE SUPERVISOR

This is to certify that the thesis entitled "**Mechanics of instability-driven geodynamic processes: a theoretical and experimental study**" submitted by **Sri. Arnab Roy** who got his name registered on **30.08.2019** for the award of **Ph. D. (Science)** degree of Jadavpur University, is absolutely based upon his own work under the supervision of **Professor Nibir Mandal** and that neither this thesis nor any part of it has been submitted for either any degree / diploma or any other academic award anywhere before.

....

01.08.2023

....

(Signature of the Supervisor(s) date with official seal)

NIBIR MANDAL
Professor
Dept. of Geological Sciences
Jadavpur University
Kolkata - 700 032

ACKNOWLEDGEMENTS

TABLE OF CONTENTS:

CHAPTER 3: THE DYNAMICS OF PLUMES IN A GLOBALLY FLOWING EARTH'S MANTLE..59-92

CHAPTER 4: EFFECTS OF GLOBAL FLOWS ON GRAVITATIONAL INSTABILITIES: A THEORETICAL PERSPECTIVE 93-122

Journal Publications

Conference Abstracts

ABSTRACT

A variety of geodynamical phenomena originate from mechanical, thermo-mechanical, and thermo-chemical instabilities in Earth's interior. These dynamic instabilities are triggered by inherently or induced unstable mechanical states of a system, tending to achieve a stable mechanical state under a given set of physical conditions. These destabilizing actions set in motion, which in turn operates tectonic activities on different scales, ranging from local to planetary scale. The present thesis focuses on four major types of instability-driven geodynamic processes, with an objective to explain the evolutionary dynamics of lithospheric scale tectonic systems.

A direction of this thesis concerns the problem of primary plumes originating from deep-mantle sources (buoyant layers) located at the core-mantle boundary. Their formation is subject to Rayleigh-Taylor (RT) instabilities, which critically determine the initiation of a plume and its subsequent growth. Previous studies investigated the mechanics of RT instabilities, taking into account various physical parameters, such as density, viscosity, and the relative proportions of layer thickness between the denser overlying layer and the buoyant source layer. None of these studies, however, addressed a crucial question- how the presence of horizontal unidirectional global flows in Earth's mantle can influence the plume mechanics. A part of this thesis combines the results from 2D computational fluid dynamics (CFD) model simulations with a linear stability analysis to resolve the issue, showing that the global flow acts as a counter factor to dampen the growth rate of instabilities. At a threshold global flow velocity, the dampening effects completely suppress instabilities, allowing the entire system to advect in the horizontal direction. Furthermore, the stability analysis predicts a non-linear increase in the instability wavelength with increasing global flow velocity, implying lowering of the spatial plume frequency in kinematically active regions of Earth's mantle. This study leads to a new hypothesis for unusually large spacing between major hotspots scattered around the globe. The present thesis investigates another important gravitational instability to explain the development of "same-dip" double subduction systems. Understanding the dynamics and evolutionary pathways of such complex tectonic systems is pivotal to unravel the enigmatic and anomalous geological observations from both paleo and presently active convergent plate boundaries. This study aims to explore the coupled evolution of two subduction zones that are spatially separated, but mutually influencing each other. Using CFD models it is demonstrated that they can initiate spontaneously and evolve self-consistently, but in a competing mode depending on the tectonic settings. The initiation and stabilization of a second subduction zone switches transformation of a single subduction into a self-sustaining double subduction system, or vice versa. Three plate tectonic settings considered for this double-subduction modelling yield the following results. 1) Oceanic setting: the second subduction initiates within a large oceanic plate, 2) oceanic-continental setting: the second subduction initiates at the margin between an oceanic plate and a continental block, and 3) multiple continental setting: double subduction initiates in the presence of multiple continental blocks but reverts back to a single subduction setting due to slab detachment. The effects of dynamic variations of the double subduction system on the Moho boundary of the descending slab and the temperature distribution along the slab's top surface are also investigated. The modelling establishes a set of distinctive imprints of double subduction systems that can be used to reconstruct the evolution of tectonic plate configurations. For validation, the thesis

compares the model findings with real-world examples of same-dip double subduction systems.

The geological history of the Himalaya-Tibet Mountain Range reveals two significant extensional tectonic events driven by gravitational collapse, which is a consequence of topographic instability. It has been shown from geological evidences that a north-south extension occurred in the Himalaya-Tibet transition zone, active from 22 Ma to 11 Ma, coupled with another extensional tectonic event, but in the east-west direction that occurred in southern and central Tibet, starting at around 18 Ma and persisting until approximately 4 Ma. The E-W extension had a time overlap with the north-south extension for about 7 Ma. This thesis investigates the driving factors of these two extensional tectonic events. It is demonstrated from laboratory experiments that a decrease in the India-Asia convergence velocity resulted in a gravitational collapse of the Tibetan plateau, which in turn initiated both extensional events, but in different mechanisms. In the southern Tibet region, pressure relaxation in the underlying Himalayan wedge caused gravitational collapse, leading to north-south extension between 22 and 11 Ma. In contrast, the rigid Tarim block in north-western Tibet induced differential topographic uplift from west to east during the initial rapid stage of the India-Asia collision (dating back to over 22 Ma), which subsequently underwent gravitational collapse, setting in eastward crustal flows and E-W extensional tectonics between 18 and 4 Ma.

The final part of the thesis is dedicated to examine mechanisms of strain localization in the perspective of an instability-driven geodynamic process, with an aim to address the problem of secondary shear band formation and their spatial patterns in ductile shear zones under simple shear kinematics. Field studies in Eastern India, reveal the presence of extensive deformation bands (C-bands) parallel to the shear direction on both micro- and macro scales. Interestingly, laboratory-scale simple shear experiments with wet sand (Coulomb) and putty (visco-plastic) showed different band structures: low-angle and high-angle shear bands in sand, and a single set of low-angle shear bands (LSB) in putty. To explore the cause of this discrepancy, 2D CFD models are employed based on viscoplastic rheology. The models revealed that the C-band and LSB formation compete with each other and their competing growth depends on the shear zone parameters: geometric (shear zone thickness), kinematic (shear rate), and rheological (bulk viscosity). Two non-dimensional factors are identified, a dynamic factor (Ω) and a geometric factor (δ), to constrain the conditions of LSB and C-band formation. A theoretical analysis is presented to predict the shear band orientations as a function of these factors.

Chapter 1.

INTRODUCTION

1.1. DYNAMICS OF THE EARTH

The study of Earth's dynamics, a branch called *geodynamics*, encompasses the mechanisms and energies that shape the planet and propel its diverse geological and geophysical processes (Turcotte & Schubert, 2014). These processes play the underlying role in operating planetary scale tectonics, manifested in the formation of mountain belts, continents, and ocean basins, and a wide range of geological events, such as earthquakes and volcanic eruptions. Understanding their dynamics is critically important to explain the geological phenomena on short as well as long time scales.
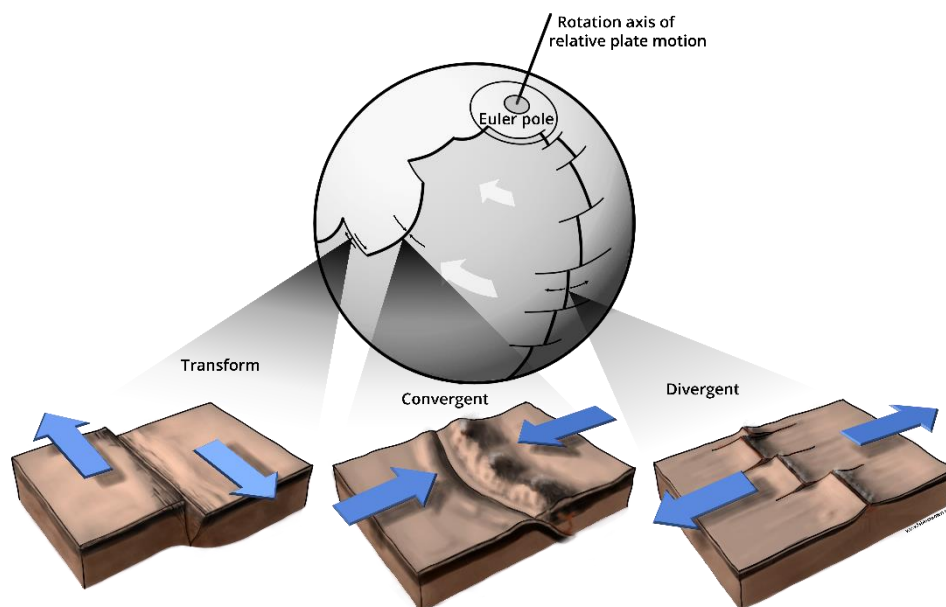
Figure 1.1: The movement of relatively rigid portions on the surface of a sphere can be explained as a rotation around an axis called the Euler pole. This rotation axis intersects the surface at a specific point. The motion of these plates is primarily accommodated by localized deformation occurring at plate boundaries. Three main types of plate boundaries: transform plate boundaries enable plates to move parallel to each other, convergent plate boundaries involve the collision and destruction of plates, and divergent plate boundaries involve the separation and creation of new plates.

The principal dynamic processes in the Earth can be broadly itemized along the following lines:

➢ *Plate Tectonics*: This study concerns mainly fundamental processes involved in the movement of lithospheric plates and their mutual interactions. The relative plate movements result in the formation of divergent, convergent, and transform tectonic settings (Fig. 1.1) at their boundaries (Dewey, 1975; McKenzie, 1970; Stern, 2018).

➢ *Mantle Convection*: Heat generated within the Earth's interior undergo radially outward transport, setting in convection currents in the mantle on geological time scales (Bercovici, 2003; Davies & Christensen, 2001; W. Jason Morgan,
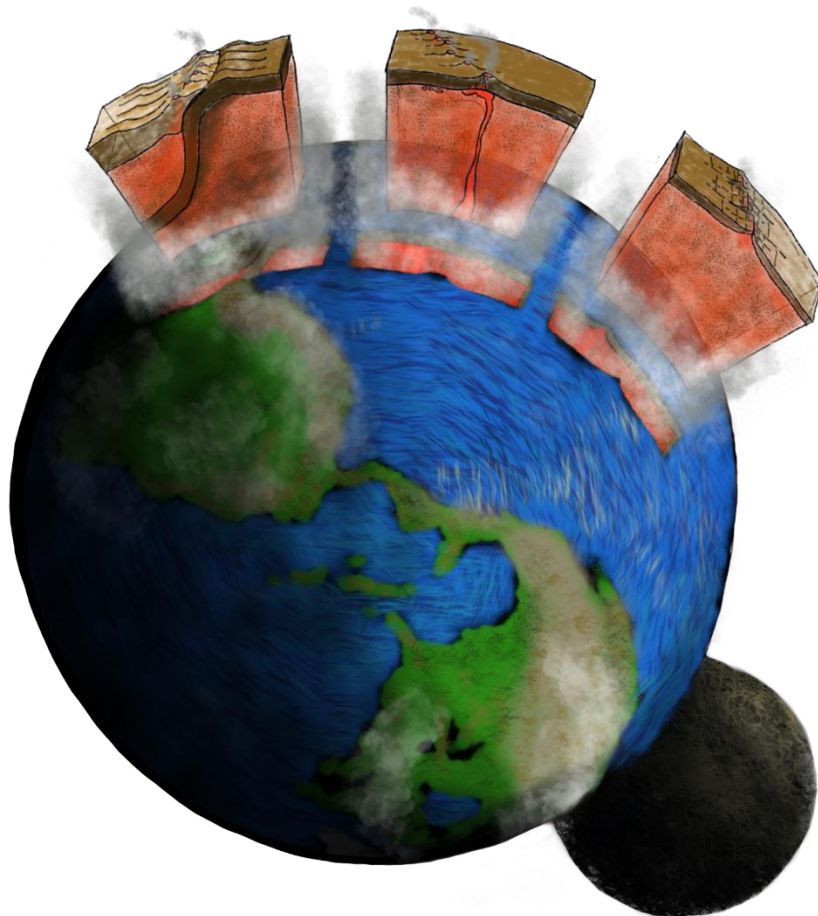
Figure 1.2: Visual representation of the Earth, with sections of its mantle removed to depict the subduction, formation, and cooling of tectonic plates.

1972; Parsons & McKenzie, 1978; Schubert et al., 2001). The currents involve the ascent of hotter material and the descent of cooler material, ultimately driving most of the global tectonic processes encountered on the Earth's surface.

➤ *Subduction*: At the convergent plate boundaries a tectonic plate approaches to eventually underthrust beneath another plate by a process, called *subduction* (Fig. 1.2). However, an open-ended question still remains- what drives a plate to subduct? The generally accepted hypothesis in the present literature (Mulyukova & Bercovici, 2019; Stern, 2004; Stern & Gerya, 2018) considers negative buoyancy of the plates as the driving forces to the plate subduction (Guillaume et al., 2021; Lithgow-Bertelloni, 2016; Schellart, 2004; Van Summeren et al., 2012). Denser oceanic lithosphere sinks beneath less dense continental or oceanic plates. Oceanic subduction usually triggers several tectonic events to operate on large scales, such as deep-ocean trench formation, island arcs, and volcanic activity.

➤ *Orogeny*: The collision between converging tectonic plates forces the crustal masses to uplift preferentially along their boundaries, forming mountain ranges (John F. Dewey & Burke, 1973; Forsyth & Uyeda, 1975; Malinverno & Ryan, 1986; Uyeda & Kanamori, 1979; Whipple & Meade, 2006). The participating continental plates cannot subduct because they have similar densities. The crust in such a convergent setting undergo intense deformation and folding in the mountain building process e.g., the Himalayas (Bilham et al., 1997; Yin & Harrison, 2000) or the Alps (Lyon-Caen & Molnar, 1989; Schlunegger & Kissling, 2015).

> ➢ *Divergent tectonics*: The convergent tectonics discussed above is usually
> coupled with divergent tectonics (Fig. 1.2), characterized by pull-apart relative
> movement between two adjoining lithospheric plates (Davis & Lister, 1974;
> Pichon, 1968). The divergent plate kinematics create extensional tectonic
> regimes at their boundaries, as observed in various geological settings, e.g.,
> mid-ocean ridges, continental rift systems and back-arc basins (Molnar et al.,
> 1975; Sears et al., 2005).

These dynamic processes, as noted above have been continuously operating with the evolving Earth to configure the Earth's lithospheric plates that again underwent modification and re-modification throughout d its entire geological history over billions of years. They contributed to the formation of diverse landscapes, including their climate patterns, and also played a critical role in the distribution of natural resources on Earth.

1.2. PLATE TECTONICS VERSUS GRAVITATIONAL TECTONICS

Plate tectonics and gravitational tectonics emerged as two parallel concepts, both aiming to explain the of Earth's lithospheric dynamics. The theory of plate tectonics is the most widely accepted scientific theory that elegantly describes the geometry and motion of lithospheric plates (Korenaga, 2013; McKenzie, 1970; Morgan, 1972; Stern, 2018). On the other hand, the theory of gravitational tectonics builds the concept in the premises of density-driven gravity forces that act mostly in the vertical direction (Bally, 1981; King et al., 2010; North, 1964). The plate tectonic theory, as conceived earlier, envisages the plate motion driven entirely by the convective currents in the underlying mantle. A plethora of geological evidence, such as earthquakes distribution, volcanic activities, and the ocean-floor magnetic patterns have
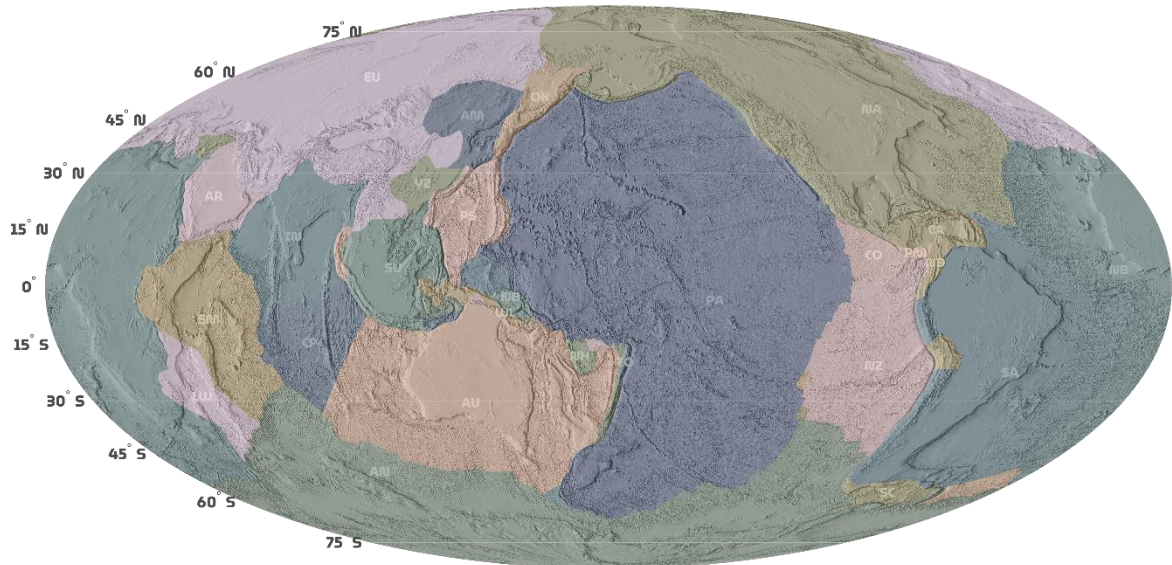
Figure 1.3: Cartographic representations displaying the Earth's tectonic plates, comprising a total of 56 distinct plates identified by abbreviations provided in Argus et al. (2011).

supported this theory (Anderson, 1995; Fischer et al., 2010; Green et al., 2010). The remarkable success of plate tectonics stands on its ability of unifying various geodynamical phenomena geoscientists recognized from isolated observations. On the other hand, gravitational tectonics suggests that the primary driver of tectonic activity on Earth is the gravitational forces, rather than the convective motions in Earth's interior. It is now widely acknowledged that gravitational forces do have a significant impact on plate tectonics, especially in subduction zones, where denser plates sink due to gravity, and mantle plume formation in different regions of Earth mantle. However, the primary driving force behind the motion and dynamics of tectonic plates is generally attributed to the convective currents within the Earth's mantle.

In summary, plate tectonics, a widely accepted scientific theory and supported by substantial evidence, explains the movement of tectonic plates (Fig. 1.3) in terms of convective mantle dynamics. Gravitational tectonics, on the other end, indirectly

affects the dynamics of the Earth's crust, as seen from geological evidences from fold-thrust belts and subduction systems.

1.3. GEODYNAMIC INSTABILITIES

A range of geodynamical phenomena is initiated as mechanical, thermo-mechanical, thermo-chemical instabilities in stratified structures of the Earth (McNamara & Zhong, 2004; Morgan, 1971; Ramberg, 1968a, 1968b; Zhou et al., 2021). Such dynamic instabilities result from an inherently or induced unstable mechanical state of a system with a motif to attain a stable mechanical state under a given set of conditions. These destabilizing effects set in motion in the Earth system, and which in turn triggers various tectonic activities. The instabilities can occur on various scales, from local to regional-scale geological processes. More importantly, they play crucial roles in initiating geodynamic settings, a few examples of which are given below:

> ➢ Subduction zones: Natural subduction zones form as a consequence of gravitational instabilities, where the denser lithosphere sinks into the lighter asthenosphere (Fig. 1.4). The processes of initiation of such subduction zones are still poorly understood and offers an important aspect of geoscientific research (Bercovici & Ricard, 2012; Stern, 2004; Stern & Gerya, 2018).
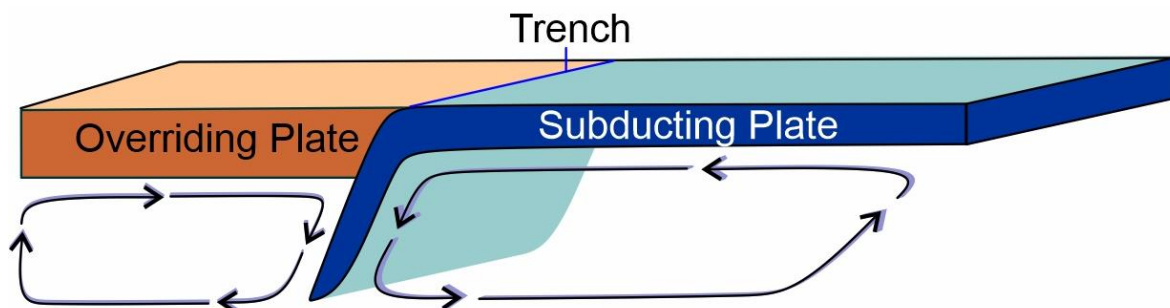
Figure 1.4: The basic units of terrestrial subduction process where the denser subducting plate is pushed below the lighter overriding plate.

➢ Mantle Plumes and Hotspots: Mantle plumes are upwellings of abnormally hot materials originating from deep regions in Earth's mantle (Courtillot & Olson, 2007; French & Romanowicz, 2015; Koppers et al., 2021; Lei et al., 2020; van der Meer et al., 2018). These plumes can lead to geodynamic instabilities when they interact with the lithosphere. They can cause localized uplift, volcanic activity, and the formation of volcanic hotspots, such as the Hawaiian Islands.

➢ Continental Collision zones: When two continental plates collide, the immense forces involved can lead to complex instabilities (Brown et al., 2011; Copley et al., 2010; John F. Dewey & Burke, 1973). The compression and deformation of the crust can cause folding, faulting, resulting in the development of mountain ranges. There are also several instances where mountains and plateaus raised due to convergence forces start to lose their elevation through the process of gravitational collapse, which is another type of instability.

➢ Lithospheric strain localization: Strain localization refers to the occurrence of an instability phenomenon in deformable materials that experience dissipative deformation mechanisms (Anand & Spitzig, 1980; Cobbold, 1977; Gueydan et al., 2014; Hutchinson & Tvergaard, 1980, 1981; Willis et al., 2019). Lithospheric scale strain localization is responsible for most of the catastrophic events in earth like earthquakes and landslides (England & Houseman, 1986; Houseman & England, 1986).

Understanding the geodynamic processes in the light of instability mechanics is crucial for predicting many dynamical phenomena, such as earthquakes, volcanic eruptions, and landslides. This approach provides a quantitative basis to comprehend the dynamic behavior of the Earth's crustal systems, which has implications in

assessing the risks and management of natural hazards, especially in tectonically active regions.

1.4. LITHOSPHERIC DEFORMATION AND FAILURE PROCESSES

A variety of geological phenomena, such as breaking and fracturing of Earth's lithosphere originate from intense deformation localization, often leading to failure in lithospheric plates (Watts et al., 2013; Watts & Schubert, 2007). Understanding the failure processes is a fundamental step to explain important tectonic activities that contribute to shaping the landscapes of Earth's surface. The study primarily aims to examine how the outer layers of the Earth respond to large-scale and long-lasting surface pressures. These layers are also subjected to various types of loads on different temporal and spatial scales, each scale determines how the Earth's outer layers respond. Loads of intermediate duration, for instance, are connected to a "transient" state in which the outer layers gradually deform in response to loading and unloading. The lithosphere, in particular, undergoes deformation as a result of loading forces on three distinct timescales: short-term (ranging from seconds to a few years), intermediate (around 10,000 years), and long-term (over a million years).
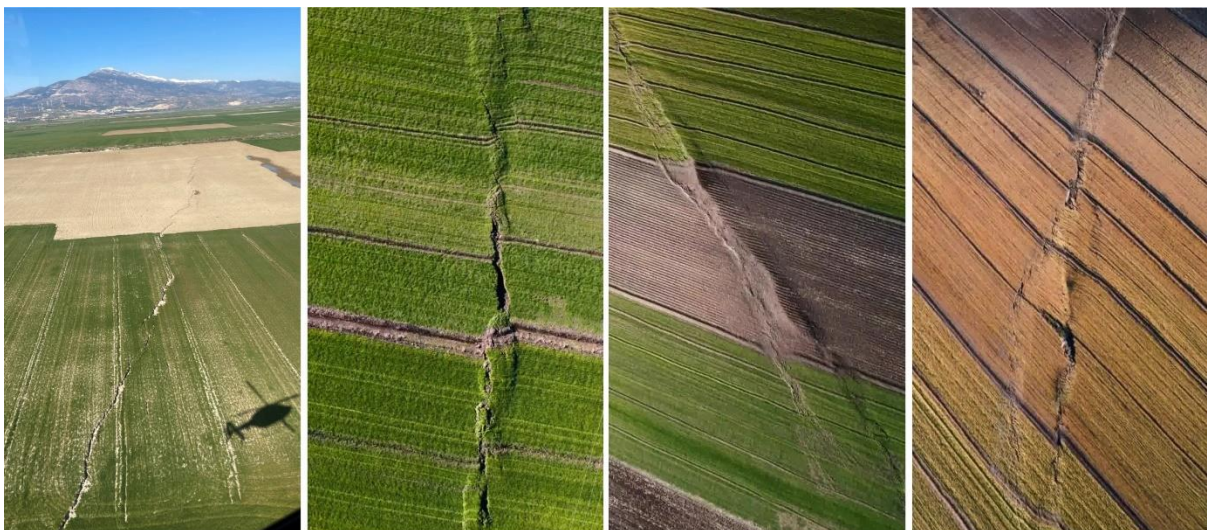
Figure 1.5: Surface manifestation of strain localization in the form of lithospheric ruptures formed during the Turkey-Syria earthquake 2023. Photos taken form UAV and belongs to @MohammedKosen.

The moment release in a seismic event can be categorized as a short-term load on the Earth's crust and lithosphere, causing them to deform almost instantaneously (Fig. 1.5). The deformation pattern allows geoscientists not only to reveal the fault surfaces responsible for generating the earthquakes, but also sheds light on the rheological characteristics of the crust and lithosphere. The expansion and contraction of ice sheets exert pressure on Earth's crust and lithosphere, often causing them to undergo flexural deformations, which can be viewed as a typical case of intermediate loading. The Last Glacial Maximum (LGM), which occurred around 21,000 years ago involved such an intermediate time scale of loading by a thick ice sheet over 1 kilometer in depth, covering a significant portion of the Northern Hemisphere. As the climate became progressively warm, the ice sheet retreated, leaving behind large meltwater lakes like former Lake Agassiz and Lake Algonquin (Watts & Schubert, 2007). Previous pioneering works (McConnell, 1968) suggest that the deformation following the ice retreat provides valuable information not only about the asthenospheric viscosity, but also enable one to constrain the elastic thickness of the lithosphere. Studying the way, the lithosphere respond to long-term loading is also a crucial mechanical aspect of great concern in tectonic studies. For example, the flexural response resulting from sediment loading provides valuable insights into the long-term mechanical characteristics of the lithosphere. Furthermore, examining strain localization in the form of shear zones within subduction settings is crucially important to interpret the rheological and mechanical behavior of rocks under extreme conditions.

1.5. GEODYNAMIC MODELLING: NEW DEVELOPMENTS

To overcome the limitations of human observations, especially in terms of geological time scales, and reaching deep Earth's interior, many geoscientists have adopted advanced mathematical modeling techniques, facilitated by the rapid advancements in computer technology. Nowadays, this approach revolutionized several disciplines of science, including geosciences. The new wave serves several purposes, hypothesis testing, hypothesis generation, which has reshaped geology as a branch of natural science, transforming from being observational and intuitive to deductive and predictive. Numerical geodynamic modeling involves the use of various
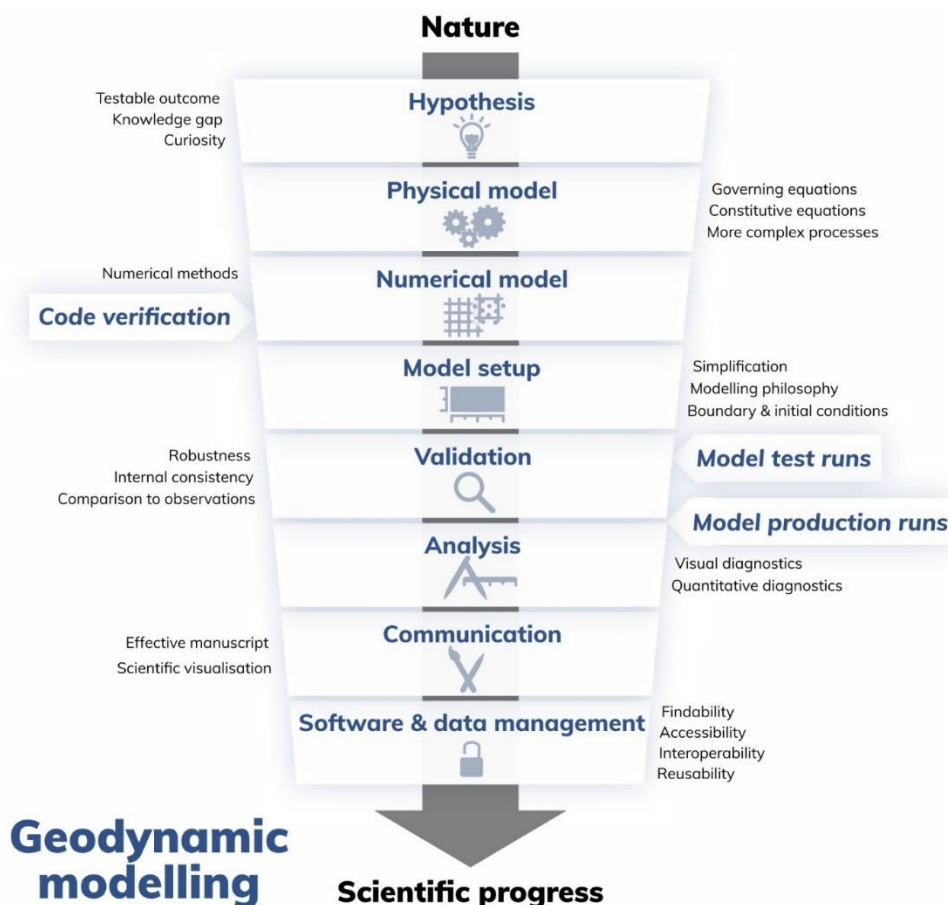
Figure 1.6: Summary of the process of conducting a geodynamic modeling study. It involves several steps, starting with the construction of both a physical and numerical model using a verified numerical code. This is followed by designing a simplified model setup based on a specific modeling approach, validating the model through rigorous testing, conducting impartial analysis of the model output, and communicating the modeling approach and findings through oral, written, and graphical means.

computational methods and algorithms to simulate and study the dynamic processes

operating in the Earth's interior (Gerya, 2009; Mckenzie et al., 1974). This computational approach aims to investigate the behavior and evolution of the Earth's lithosphere, mantle, and other geophysical processes with the help of numerical simulations based on a set of governing mathematical equations (Fig. 1.6). The theoretical formulation integrates various physical principles, such as conservation laws of mass, momentum, and energy, as well as rheological properties of rocks, considering a set of boundary conditions, initial system configuration. The recent developments point to a remarkable success of the computational geodynamics, paving excellent directions of simulation-based studies of various large-scale processes, like plate tectonics, mantle convection, crustal deformation, seismic activity, and magma dynamics. The model simulations are extensively used to investigate a wide range of geodynamic processes, explore the effects of different parameters, and gain insights into the Earth's past and future behavior. This approach allows the geoscientists to test hypotheses, make predictions, and refine our understanding of Earth's geological history.

Geo-modeling and geo-visualization techniques have emerged as powerful tools in bridging different branches of geosciences, in particular, for planning and conducting cutting-edge interdisciplinary research. Geodynamics has recently taken a new turn with the applications of numerical modeling techniques Plate tectonics has remained a central theme in geodynamic studies. Numerical modeling has become an indispensable tool for studying tectonic processes in the light of observational or acquired geophysical data.

To summarize, the past few decades have witnessed a significant and rapid progress in the field of numerical geodynamic modeling with the advent of various

numerical methods. Geodynamic modeling has eventually emerged as one of the most vibrant and cutting-edge research fronts in solid earth geosciences.

1.6. THE PRESENT THESIS: SCOPES AND OBJECTIVES

In the perspective of recent developments, as discussed in the preceding sections, the present thesis focuses on a set of important instability driven geodynamic processes. The work embodied in this thesis can be introduced with the following three main points.

➢ To explore the role of mechanical/thermomechanical instabilities in driving major geodynamic processes of the Earth on varied time scales.

➢ To understand the geological and geophysical factors governing such instability driven processes through a multidirectional approach: model simulation techniques, theoretical analyses and physical experiments.

➢ To develop comprehensive spatio-temporal evolutionary models for such geodynamic systems.

The next chapter (Chapter 2) presents a comprehensive description of the theoretical framework of computational fluid dynamics. This includes a thorough examination of rheological considerations, mathematical principles, and the numerical methods applied in this thesis work. Chapter 3 deals provides a detailed account of the existing literature on the mantle plume formation driven by gravitational instability in Earth's mantle. This chapter develops an original and novel study that addresses the problem of origin of deep-source mantle plumes emerging from the D'' layer at the core-mantle boundary (CMD) of Earth. A 2D finite element particle-in-cell numerical method is employed to conduct computational fluid dynamics (CFD) simulation experiments,

which show the growth of Rayleigh-Taylor (RT) instability at the core-mantle boundary (CMB) under the influence of a global horizontal flow within the mantle. The CFD simulations are utilized to find a critical velocity of the global horizontal flow in the mantle, beyond which the instability can be fully suppressed. This threshold would prevent the development of any plumes originating from the buoyant source layer at the CMB. In order to support the findings from the numerical results, a linear stability analysis is developed to derive a dispersion relation of RT instabilities as a function of layer-parallel flow in the overlying mantle, which is presented in Chapter 4. Finally, this Chapter finally discusses the problem considering the numerical and analytical results to propose a new conceptual framework for the origin of unusually large inter-hotspot spacing and sporadically distributed hotspots of deep-mantle source plumes.

In Chapter 5, a different type of instability-controlled geodynamic process is considered to describe the mechanics of complex subduction systems. This study focuses on double-subduction systems with an objective to show the interconnected evolution of two spatially apart subduction zones, resulting in a mechanically coupled subduction process. To analyze the factors controlling the initiation and stabilization of a second subduction zone, and the conversion of a single subduction system into a self-sustaining double subduction system (or vice versa), time-dependent and self-consistently evolving particle-in-cell finite element numerical models are utilized. Additionally, the chapter includes description highlighting the effects of dynamic variations in the double subduction evolution on the slab-Moho (the boundary between the crust and mantle) and the slab-top temperatures. These variations leave distinct footprints in the geological record, which can aid in identifying the presence

of extinct double subduction systems. Finally, the chapter presents a section to compare the findings of the numerical models with real-world examples of double subduction systems with similar morphologies.

In the next chapter (Chapter 6), a third type of instability-driven geodynamic process, gravitational collapse in elevated orogens is invoked to investigate the crustal flow patterns in the Tibetan Plateau. Using laboratory scale analogue models this study addresses the question- was the temporally varying collision dynamics a crucial factor in controlling the gravitational collapse of the Tibetan Plateau and in turn shaping the tectonic changes in the Himalaya-Tibet orogen system? And if it was, what were the additional impacts caused by the diverse characteristics of the crust in the lateral direction? These issues form the primary focus of this original chapter.

The penultimate chapter (Chapter 7) deals with an instability phenomenon resulting in strain localization in a continuum to form shear bands. The majority of the previous studies have focused on the origin of low- and high-angle shear bands, which are relative rare in natural ductile shear zones. In contrary, the shear zones commonly display shear-parallel C bands, imparting a shape fabric in the sheared rocks. These findings hardly agree with that produced in earlier experimental shear zones dominated by low-angle shear bands with little to no C-shear bands. Such contrasting observations prompt a straightforward question: what factors influence the development of C-shear bands in natural ductile shear zones? This question is addressed in this chapter. Finally, the last chapter (Chapter 8) concludes the major findings from this thesis work.

1.7. REFERENCES

Anand, L., & Spitzig, W. A. (1980). Initiation of localized shear bands in plane strain. *Journal of the Mechanics and Physics of Solids*. https://doi.org/10.1016/0022-5096(80)90017-4

Anderson, D. L. (1995). Lithosphere, asthenosphere, and perisphere. *Reviews of Geophysics*, *33*(1), 125–149. https://doi.org/10.1029/94RG02785

Bally, A. W. (1981). Thoughts on the tectonics of folded belts. *Geological Society Special Publication*, *9*, 13–32. https://doi.org/10.1144/GSL.SP.1981.009.01.03

Bercovici, D. (2003). The generation of plate tectonics from mantle convection. *Earth and Planetary Science Letters*, *205*(3–4), 107–121. https://doi.org/10.1016/S0012-821X(02)01009-9

Bercovici, D., & Ricard, Y. (2012). Mechanisms for the generation of plate tectonics by two-phase grain-damage and pinning. *Physics of the Earth and Planetary Interiors*, *202–203*, 27–55. https://doi.org/10.1016/J.PEPI.2012.05.003

Bilham, R., Larson, K., Freymueller, J., Jouanne, F., Le Fort, P., Leturmy, P., et al. (1997). GPS measurements of present-day convergence across the Nepal Himalaya. *Nature 1997 386:6620*, *386*(6620), 61–64. https://doi.org/10.1038/386061a0

Brown, D., Ryan, P. D., Afonso, J. C., Boutelier, D., Burg, J. P., Byrne, T., et al. (2011). Arc-continent collision: The making of an orogen. *Frontiers in Earth Sciences*, *4*, 477–493. https://doi.org/10.1007/978-3-540-88558-0_17/COVER

Cobbold, P. R. (1977). Description and origin of banded deformation structures - 1. Regional strain, local perturbations, and deformation bands. *Can J Earth Sci*, *14*(8), 1721–1731. https://doi.org/10.1139/e77-147

Copley, A., Avouac, J. P., & Royer, J. Y. (2010). India-Asia collision and the Cenozoic slowdown of the Indian plate: Implications for the forces driving plate motions. *Journal of Geophysical Research: Solid Earth*. https://doi.org/10.1029/2009JB006634

Courtillot, V., & Olson, P. (2007). Mantle plumes link magnetic superchrons to phanerozoic mass depletion events. *Earth and Planetary Science Letters*, *260*(3–4), 495–504. https://doi.org/10.1016/J.EPSL.2007.06.003

Davies, G. F., & Christensen, U. (2001). Dynamic Earth: Plates, Plumes and Mantle Convection. *American Journal of Physics*, *69*(5), 620–621. https://doi.org/10.1119/1.1356060

REFERENCES

Davis, E. E., & Lister, C. R. B. (1974). Fundamentals of ridge crest topography. *Earth and Planetary Science Letters*, *21*(4), 405–413. https://doi.org/10.1016/0012-821X(74)90180-0

Dewey, J. F. (1975). Plate tectonics. *Reviews of Geophysics*, *13*(3), 326–332. https://doi.org/10.1029/RG013I003P00326

Dewey, John F., & Burke, K. C. A. (1973). Tibetan, Variscan, and Precambrian Basement Reactivation: Products of Continental Collision. *Https://Doi.Org/10.1086/627920*, *81*(6), 683–692. https://doi.org/10.1086/627920

England, P., & Houseman, G. (1986). Finite strain calculations of continental deformation: 2. Comparison with the India-Asia Collision Zone. *Journal of Geophysical Research: Solid Earth*. https://doi.org/10.1029/jb091ib03p03664

Fischer, K. M., Ford, H. A., Abt, D. L., & Rychert, C. A. (2010). The Lithosphere-Asthenosphere Boundary. *Https://Doi.Org/10.1146/Annurev-Earth-040809-152438*, *38*, 551–575. https://doi.org/10.1146/ANNUREV-EARTH-040809-152438

Forsyth, D., & Uyeda, S. (1975). On the Relative Importance of the Driving Forces of Plate Motion*. *Geophysical Journal of the Royal Astronomical Society*, *43*(1), 163–200. https://doi.org/10.1111/J.1365-246X.1975.TB00631.X

French, S. W., & Romanowicz, B. (2015). Broad plumes rooted at the base of the Earth's mantle beneath major hotspots. *Nature 2015 525:7567*, *525*(7567), 95–99. https://doi.org/10.1038/nature14876

Gerya, T. (2009). *Introduction to numerical geodynamic modelling. Introduction to Numerical Geodynamic Modelling* (Vol. 9780521887540). https://doi.org/10.1017/CBO9780511809101

Green, D. H., Hibberson, W. O., Kovács, I., & Rosenthal, A. (2010). Water and its influence on the lithosphere–asthenosphere boundary. *Nature 2010 467:7314*, *467*(7314), 448–451. https://doi.org/10.1038/nature09369

Gueydan, F., Précigout, J., & Montési, L. G. J. (2014). Strain weakening enables continental plate tectonics. *Tectonophysics*. https://doi.org/10.1016/j.tecto.2014.02.005

Guillaume, B., Funiciello, F., & Faccenna, C. (2021). Interplays Between Mantle Flow and Slab Pull at Subduction Zones in 3D. *Journal of Geophysical Research: Solid Earth*, *126*(5), e2020JB021574. https://doi.org/10.1029/2020JB021574

Houseman, G., & England, P. (1986). Finite strain calculations of continental deformation: 1. Method and general results for convergent zones. *Journal of Geophysical Research: Solid Earth*. https://doi.org/10.1029/jb091ib03p03651

Hutchinson, J. W., & Tvergaard, V. (1980). Surface instabilities on statically strained plastic solids. *International Journal of Mechanical Sciences*, *22*(6), 339–354.

Hutchinson, J. W., & Tvergaard, V. (1981). Shear band formation in plane strain. *International Journal of Solids and Structures*. https://doi.org/10.1016/0020-7683(81)90053-6

King, R. C., Backé, G., Morley, C. K., Hillis, R. R., & Tingay, M. R. P. (2010). Balancing deformation in NW Borneo: Quantifying plate-scale vs. gravitational tectonics in a delta and deepwater fold-thrust belt system. *Marine and Petroleum Geology*, *27*(1), 238–246. https://doi.org/10.1016/J.MARPETGEO.2009.07.008

Koppers, A. A. P., Becker, T. W., Jackson, M. G., Konrad, K., Müller, R. D., Romanowicz, B., et al. (2021). Mantle plumes and their role in Earth processes. *Nature Reviews Earth & Environment 2021 2:6*, *2*(6), 382–401. https://doi.org/10.1038/s43017-021-00168-6

Korenaga, J. (2013). Initiation and Evolution of Plate Tectonics on Earth: Theories and Observations. *Https://Doi.Org/10.1146/Annurev-Earth-050212-124208*, *41*, 117–151. https://doi.org/10.1146/ANNUREV-EARTH-050212-124208

Lei, W., Ruan, Y., Bozdağ, E., Peter, D., Lefebvre, M., Komatitsch, D., et al. (2020). Global adjoint tomography—model GLAD-M25. *Geophysical Journal International*, *223*(1), 1–21. https://doi.org/10.1093/GJI/GGAA253

Lithgow-Bertelloni, C. (2016). Driving forces: Slab pull, ridge push. *Encyclopedia of Earth Sciences Series*, *Part 2*, 193–196. https://doi.org/10.1007/978-94-007-6644-0_105-1/COVER

Lyon-Caen, H., & Molnar, P. (1989). Constraints on the deep structure and dynamic processes beneath the Alps and adjacent regions from an analysis of gravity anomalies. *Geophysical Journal International*, *99*(1), 19–32. https://doi.org/10.1111/J.1365-246X.1989.TB02013.X

Malinverno, A., & Ryan, W. B. F. (1986). Extension in the Tyrrhenian Sea and shortening in the Apennines as result of arc migration driven by sinking of the lithosphere. *Tectonics*, *5*(2), 227–245. https://doi.org/10.1029/TC005I002P00227

REFERENCES

McConnell RK, & JR. (1968). Viscosity of the mantle from relaxation time spectra of isostatic adjustment. *Journal of Geophysical Research*, *73*(22), 7089–7105. https://doi.org/10.1029/JB073I022P07089

McKenzie, D. P. (1970). Plate Tectonics of the Mediterranean Region. *Nature 1970 226:5242*, *226*(5242), 239–243. https://doi.org/10.1038/226239a0

Mckenzie, D. P., Roberts, J. M., & Weiss, N. O. (1974). Convection in the earth's mantle: towards a numerical simulation. *Journal of Fluid Mechanics*, *62*(3), 465–538. https://doi.org/10.1017/S0022112074000784

McNamara, A. K., & Zhong, S. (2004). Thermochemical structures within a spherical mantle: Superplumes or piles? *Journal of Geophysical Research: Solid Earth*, *109*(B7), 7402. https://doi.org/10.1029/2003JB002847

van der Meer, D. G., van Hinsbergen, D. J. J., & Spakman, W. (2018). Atlas of the underworld: Slab remnants in the mantle, their sinking history, and a new outlook on lower mantle viscosity. *Tectonophysics*, *723*, 309–448. https://doi.org/10.1016/J.TECTO.2017.10.004

Molnar, P., Atwater, T., Mammerickx, J., & Smith, S. M. (1975). Magnetic Anomalies, Bathymetry and the Tectonic Evolution of the South Pacific since the Late Cretaceous. *Geophysical Journal International*, *40*(3), 383–420. https://doi.org/10.1111/J.1365-246X.1975.TB04139.X

Morgan, W. J. (1971). Convection Plumes in the Lower Mantle. *Nature 1971 230:5288*, *230*(5288), 42–43. https://doi.org/10.1038/230042a0

Morgan, W. Jason. (1972). Plate Motions and Deep Mantle Convection. *Memoir of the Geological Society of America*, *132*, 7–22. https://doi.org/10.1130/MEM132-P7

Mulyukova, E., & Bercovici, D. (2019). The Generation of Plate Tectonics From Grains to Global Scales: A Brief Review. *Tectonics*, *38*(12), 4058–4076. https://doi.org/10.1029/2018TC005447

North, F. K. (1964). Gravitational Tectonics. *Bulletin of Canadian Petroleum Geology*, *12*(2), 185–225.

Parsons, B., & McKenzie, D. (1978). Mantle convection and the thermal structure of the plates. *Journal of Geophysical Research: Solid Earth*, *83*(B9), 4485–4496. https://doi.org/10.1029/JB083IB09P04485

Pichon, X. Le. (1968). Sea-floor spreading and continental drift. *Journal of Geophysical Research*, *73*(12), 3661–3697. https://doi.org/10.1029/JB073I012P03661

Ramberg, H. (1968a). Instability of layered systems in the field of gravity. I. *Physics of the Earth and Planetary Interiors*, *1*(7), 427–447. https://doi.org/10.1016/0031-9201(68)90014-9

Ramberg, H. (1968b). Instability of layered systems in the field of gravity. II. *Physics of the Earth and Planetary Interiors*, *1*(7), 448–474. https://doi.org/10.1016/0031-9201(68)90015-0

Schellart, W. P. (2004). Quantifying the net slab pull force as a driving mechanism for plate tectonics. *Geophysical Research Letters*, *31*(7). https://doi.org/10.1029/2004GL019528

Schlunegger, F., & Kissling, E. (2015). Slab rollback orogeny in the Alps and evolution of the Swiss Molasse basin. *Nature Communications 2015 6:1*, *6*(1), 1–10. https://doi.org/10.1038/ncomms9605

Schubert, G., Turcotte, D. L., & Olson, P. (2001). Mantle Convection in the Earth and Planets. *Mantle Convection in the Earth and Planets*. https://doi.org/10.1017/CBO9780511612879

Sears, J. W., St. George, G. M., & Winne, J. C. (2005). Continental rift systems and anorogenic magmatism. *Lithos*, *80*(1–4), 147–154. https://doi.org/10.1016/J.LITHOS.2004.05.009

Stern, R. J. (2004). Subduction initiation: spontaneous and induced. *Earth and Planetary Science Letters*, *226*(3–4), 275–292. https://doi.org/10.1016/J.EPSL.2004.08.007

Stern, R. J. (2018). The evolution of plate tectonics. *Philosophical Transactions of the Royal Society A: Mathematical, Physical and Engineering Sciences*, *376*(2132). https://doi.org/10.1098/RSTA.2017.0406

Stern, R. J., & Gerya, T. (2018). Subduction initiation in nature and models: A review. *Tectonophysics*, *746*, 173–198. https://doi.org/10.1016/J.TECTO.2017.10.014

Van Summeren, J., Conrad, C. P., & Lithgow-Bertelloni, C. (2012). The importance of slab pull and a global asthenosphere to plate motions. *Geochemistry, Geophysics, Geosystems*, *13*(2). https://doi.org/10.1029/2011GC003873

Turcotte, D. L., & Schubert, G. (2014). *Geodynamics 3rd edition | Structural geology, tectonics and geodynamics | Cambridge University Press*.

Uyeda, S., & Kanamori, H. (1979). Back-arc opening and the mode of subduction. *Journal of Geophysical Research: Solid Earth*, *84*(B3), 1049–1061. https://doi.org/10.1029/JB084IB03P01049

REFERENCES

Watts, A. B., Zhong, S. J., & Hunter, J. (2013). The Behavior of the Lithosphere on Seismic to Geologic Timescales. *Https://Doi.Org/10.1146/Annurev-Earth-042711-105457*, *41*, 443–468. https://doi.org/10.1146/ANNUREV-EARTH-042711-105457

Watts, A. B. (Anthony B., & Schubert, G. (2007). *Crust and lithosphere dynamics* (1st ed., Vol. 6). Elsevier.

Whipple, K. X., & Meade, B. J. (2006). Orogen response to changes in climatic and tectonic forcing. *Earth and Planetary Science Letters*, *243*(1–2), 218–228. https://doi.org/10.1016/J.EPSL.2005.12.022

Willis, K., Houseman, G. A., Evans, L., Wright, T., & Hooper, A. (2019). Strain localization by shear heating and the development of lithospheric shear zones. *Tectonophysics*, *764*(May), 62–76. https://doi.org/10.1016/j.tecto.2019.05.010

Yin, A., & Harrison, T. M. (2000). Geologic Evolution of the Himalayan-Tibetan Orogen. *Https://Doi.Org/10.1146/Annurev.Earth.28.1.211*, *28*, 211–280. https://doi.org/10.1146/ANNUREV.EARTH.28.1.211

Zhou, Y., Williams, R. J. R., Ramaprabhu, P., Groom, M., Thornber, B., Hillier, A., et al. (2021). Rayleigh–Taylor and Richtmyer–Meshkov instabilities: A journey through scales. *Physica D: Nonlinear Phenomena*. https://doi.org/10.1016/j.physd.2020.132838

Chapter 2.

COMPUTATIONAL FLUID DYNAMIC MODELLING

Computational fluid dynamics (CFD) is a branch of fluid mechanics that uses digital computers to quantitatively predict fluid-flow phenomena within the framework of some conservation laws governing the fluid motion. In CFD, the conservation laws, such as continuity, Navier-Stokes, and energy conservation, are solved numerically for a given geometry of the flow system, considering a set of intrinsic properties, and initial boundary conditions. One of the advantages of CFD is its ability to visualize intricate transient, complexly unsteady flow patterns in space and time. Additionally, this method enables one to quantitatively evaluate various physical quantities, such as velocity, pressure, temperature, and so forth at any point (space and time) in the flowing fluid medium. The CFD study is implemented employing different numerical approaches, e.g., finite difference, finite element, and volume of fluid methods. In this thesis, the finite element method (FEM) has been adopted to perform CFD-based geodynamic modelling of the present concern using the FEM code UNDERWORLD 2.0 (Mansour et al., 2020). The following sections provides a brief overview of the continuum mechanics approach in fluid mechanics and its application to CFD through the FEM schemes. This description also presents an outline of the numerical approaches, methods, and schemes.

2.1. *CONTINUUM MECHANICS APPROACH: BASIC PREMISES*

One of the most important assumptions in geodynamic problems is that all major rock units, such as the Earth's crust and mantle are considered as continua within the conceptual framework of continuum mechanics approach that describes the

21

macroscopic properties of materials phenomenologically without any formal connection to the atomic scale processes (Ranalli, 1997). For continuity on a macroscopic scale, the material under consideration evidently does not contain mass-free empty spaces or gaps (there can however, be pores or cavities that are filled with some substances, which constitute a continuum in the multiphase system). The physical properties in a continuum may vary in space as well as time, and their analysis demands continuous mathematical functions. They (field properties) are described by field variables, such as pressure, temperature, density, and velocity. There are three principal types of field variables:

a) scalars (e.g., density, pressure, temperature),

b) vectors (e.g., velocity, heat flux, mass flux),

c) tensors (e.g. stress, strain, strain rate).

Furthermore, continuity in geodynamic systems implies that the displacements in different media forming a continuum system must maintain the condition of compatibility, i.e., they cannot vary independently in space. In other words, the displacement must occur in a manner so that the spatial continuity must be maintained without creating macroscopic voids and gaps. This kind of continuous kinematic condition applies to fluid flows in the perspective of fluid mechanics (Kundu et al., 2015; Landau & Lifshitz, 1959). Since on geological timescales (million years) rocks behave as slowly creeping fluids (Braun et al., 2008; Carter, 1976; Griggs, 1939), a range of geodynamic processes for example, mantle convection, are often tackled in the theoretical perspective of fluid mechanics (geophysical fluid dynamics). It is thus, quite useful to translate the qualitative and intuitive notion of continuity into a quantitative mathematical formalism. This formalism, which takes

the form of continuity equation, specifies the conservation of mass and momentum during the displacement of a continuous medium and is frequently employed in numerical geodynamic modelling.

Prior to delving into the continuity equations, an important aspect of the mass conservation equation (and many other time-dependent conservation equations) needs an introduction of the Lagrangian versus Eulerian description of motion (Fig. 2.1). The Lagrangian frame of reference describes the motion of a set of material particles by taking their positions in space with time (*material description*). The Eulerian frame, on the other hand, is used to describe the motion at a fixed point in space, noting successive material particles occupying this spatial point at different times (*spatial description*). The Eulerian approach primarily deals with fields, e.g., velocity, pressure and temperature (that vary in time and space) independent to material particles, as often applicable to natural fluid systems. It simplifies the mathematical treatments to a large extent, providing partial differential equations for given fields. Consider the following example. The temporal density change in a flow can be written as $\frac{\partial \rho}{\partial t}$, which is the local rate $\left(\frac{\partial}{\partial t}\right)$ of density change obtained for a fixed point in the space, x_i. The total change in density can be obtained by adding a convective term, $\nabla.(\rho u_i)$. The equation for mass balance in an elementary fluid volume of Eulerian frame becomes,

$$\frac{\partial \rho}{\partial t} + \nabla.(\rho u_i) = 0 \tag{2.1}$$

Several equations in fluid mechanics containing time derivatives are written both in Lagrangian and Eulerian forms that differ from each other. Choosing to write an

equation in these two forms notably affects the way, advective transport (i.e., movement of material with the flow) terms are represented as will be seen throughout different derivations presented in this thesis work.
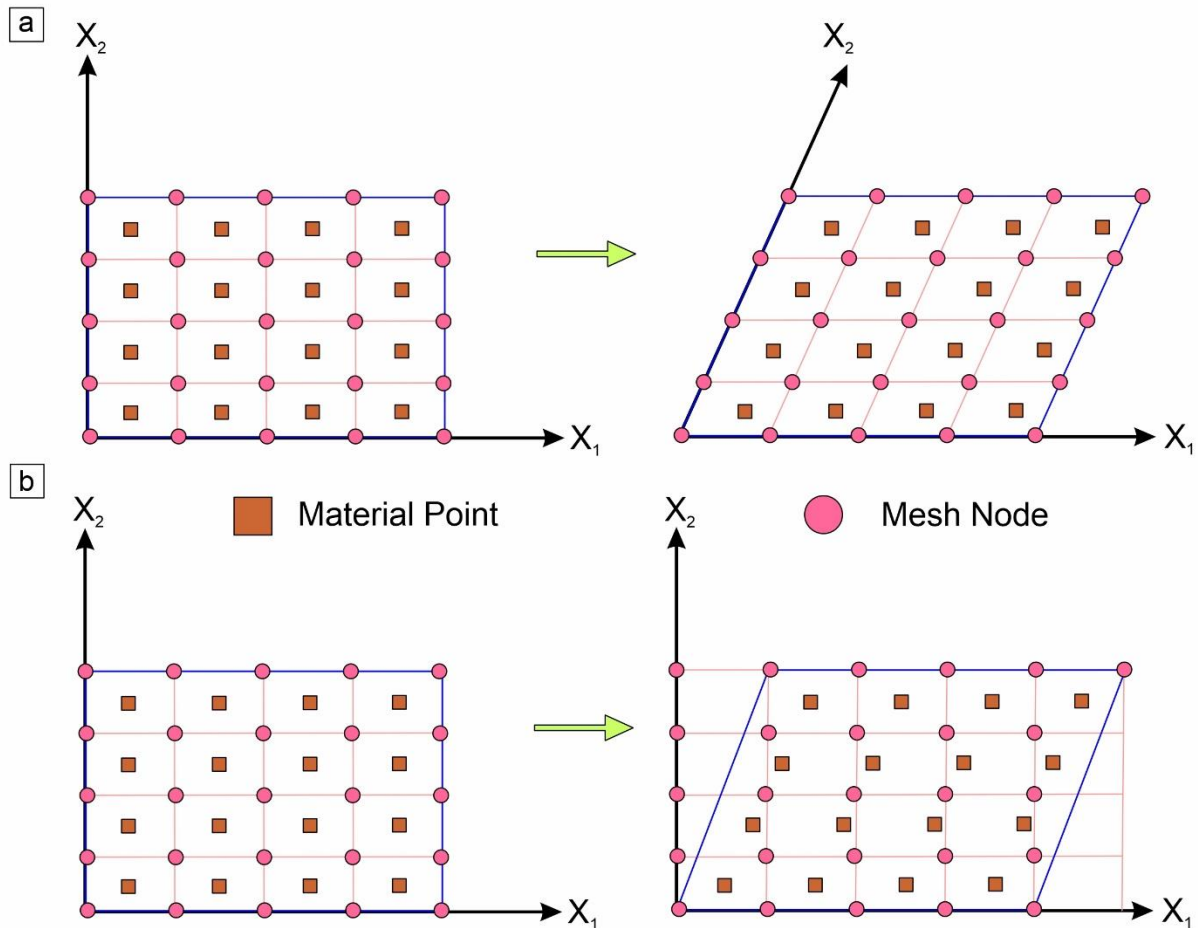
Figure 2.1: Lagrangian mesh (a) and Eulerian mesh (b)

The total mass of a fluid can neither be destroyed nor be created in most of the natural conditions, barring a few cases, like nuclear reactions and relativistic bodies. This basic premise allows one to track individual material particles in a flow field as they will never disappear or reappear as new material particles spontaneously. The mass conservation equation in fluid mechanics is based on the principle that mass of a specific collection of neighboring fluid particles remains constant. For an infinitesimal control volume fixed in space, the mass balance between inflow and outflow of fluid is thus equal to the rate of change in density of the control volume. Consider a fluid of volume V and density ρ is enclosed in space by a closed surface A.

The mass of fluid in the volume at any instant is $\int \rho dV$. Considering the net outward flow rate across the surface as $\int \rho u_i\, n_i dA$, the mass conservation equation can be written as

$$\frac{d}{dt}\int_V^{\cdot} \rho dV = \int_A^{\cdot} \rho u_i n_i dA \qquad (2.2)$$

Transforming the surface integral in Eq. (*2.2*) to volume integral, and taking the time derivative inside the integral, results in

$$\int_V^{\cdot} \left\{\frac{\partial \rho}{\partial t} + \nabla.(\rho u_i)\right\} dV = 0 \qquad (2.3)$$

Eq. (2.3) is valid for any chosen volume of fluid, only if it satisfies the following condition,

$$\frac{\partial \rho}{\partial t} + \nabla.(\rho u_i) = 0 \qquad (2.4)$$

Eq. (2.4) is known as the continuity equation, which can also be expressed in the following way.,

$$\frac{\partial}{\partial x_i}(\rho u_i) = \rho \frac{\partial u_i}{\partial x_i} + u_i \frac{\partial \rho}{\partial x_i} \qquad (2.5)$$

For an incompressible flow, Eqs. (2.4) and (2.5) yield the continuity equation as,

$$\nabla . u_i = 0, \tag{2.6}$$

which effectively signifies that the divergence of a flow field is zero at any given point.

For an infinitesimal fluid that moves along with the flow having a volume V and bounded by a material surface S, the momentum can be given as $\int_V \rho u_i \, dV$ for which the rate of momentum change becomes,

$$\frac{d}{dt} \int_V \rho u_i \, dV = \int_V dV \rho \frac{Du_i}{Dt} \tag{2.7}$$

This rate of change in momentum has to be equal to the net forces applied to the fluid element in all directions. The forces that act on any fluid element can be classified into two main types:

➢ Body forces: These are external forces to a body that bring in inertial changes in the body following Newton's law of motion. Every infinitesimal fluid element dV will experience the body force depending on the mass contained in the volume. For geodynamic problems, only body force that needs to be accounted for is the gravity (g_i).

➢ Surface forces: These are internal forces produced by interaction of materials particles on either side of a surface within a volume. Unlike body forces, this type of forces does not introduce any inertial change in the body. For any infinitesimal small fluid element dV, the net effect of these forces due to interactions with other infinitesimal fluid elements is exerted on the outer thin surface of the fluid volume. Similarly, each of the three surface planes around

the fluid element in 3D experiences a three-component force, resulting in a total of nine components. These components give rise to the stress tensor (σ_{ij}).

Therefore, total forces (body force + surface force) acting on the fluid element is given by,

$$\int_V dV \rho g_i = \int_S \sigma_{ij} \cdot dS_i = \int_V dV (\rho g_i + \nabla \cdot \sigma_{ij}) \qquad (2.8)$$

According to Newton's law of motion, the rate of change of momentum equals to the
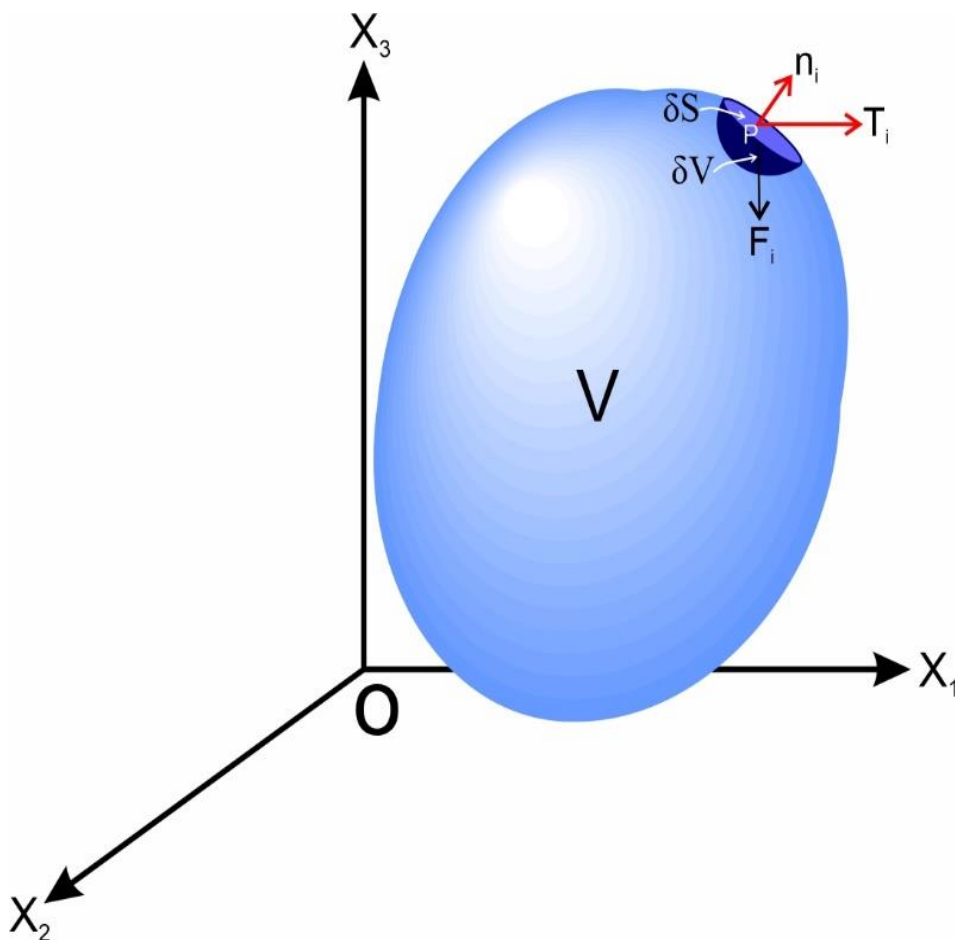
Figure 2.2: Forces acting on element of volume ΔV and surface area ΔS.

sum of body forces acting on the total fluid volume and surface forces acting on its

surface. This relation can be employed to obtain the momentum conservation equation. Therefore, combining Eq. (2.7) and (2.8) results in,

$$\rho \frac{Du_i}{Dt} = \rho g_i + \nabla \cdot \sigma_{ij} \tag{2.9}$$

$$\rho \frac{Du_i}{Dt} = \rho g_i + \frac{\partial \sigma_{ij}}{\partial x_j} \tag{2.10}$$

Equation (2.10) describes how a fluid body moves, with the term on the left-hand side of the equation represents the system's inertia. This equation is also referred to as *Cauchy's equation of motion*. As most natural geodynamic systems proceed at extremely slow rates, the resulting inertia can be considered zero or negligible, i.e., $\frac{Du_i}{Dt} = 0$.

For incompressible fluid flow the constitutive relation for stress tensor σ_{ij} versus strain-rate tensor $\dot{\epsilon}_{ij}$ is given by

$$\sigma_{ij} = -p\delta_{ij} + 2\mu\dot{\epsilon}_{ij}, \tag{2.11}$$

$$\sigma_{ij} = -p\delta_{ij} + \mu \left(\frac{\partial u_i}{\partial x_j} + \frac{\partial u_j}{\partial x_i} \right), \tag{2.12}$$

Substituting Eq. (2.12) into Eq. (2.10) we obtain

$$\rho \frac{Du}{Dt} = \rho g_x - \frac{\partial p}{\partial x} + \mu \left(\frac{\delta^2 u}{\partial x^2} + \frac{\delta^2 u}{\partial y^2} + \frac{\delta^2 u}{\partial z^2} \right), \tag{2.13}$$

$$\rho \frac{Dv}{Dt} = \rho g_y - \frac{\partial p}{\partial y} + \mu \left(\frac{\delta^2 v}{\partial x^2} + \frac{\delta^2 v}{\partial y^2} + \frac{\delta^2 v}{\partial z^2} \right), \tag{2.14}$$

$$\rho \frac{Dw}{Dt} = \rho g_z - \frac{\partial p}{\partial z} + \mu \left(\frac{\delta^2 w}{\partial x^2} + \frac{\delta^2 w}{\partial y^2} + \frac{\delta^2 w}{\partial z^2} \right), \tag{2.15}$$

These equations can be written as

$$\rho \frac{Du_i}{Dt} = \rho g_i - \nabla p + \mu \nabla^2 u_i \tag{2.16}$$

where ∇^2 is the Laplacian operator. For uniform density (ρ), we can simplify Eq. (2.16) by replacing the gravitational force term by a pressure gradient where $g_i = \nabla p_0$. Now defining $P = p - p_0$, we obtain

$$\rho \frac{Du_i}{Dt} - \nabla P + \mu \nabla^2 u_i \tag{2.17}$$

This is the incompressible form of the Navier-Stokes equation.

2.2. THEORY OF STRESS AND STRAIN-RATE TENSORS

Stress is the force per unit area, transmitted through a body by material particle interactions. The mathematical definition of stress can be arrived at by considering the interactions between contiguous parts of continuous bodies. Let a continuous medium occupy a volume V in Cartesian space, and let ΔV be an element of volume inside it (Fig. 2.2). As discussed in the previous section, this volume element is acted upon by two kinds of forces, i.e. body forces, per unit volume or unit mass, and surface forces acting on the surface ΔS bounding ΔV. The body force per unit mass F_i in geodynamic phenomena is the acceleration due to gravity. The surface forces act on a small surface element δS of ΔS with a unit vector n_i normal to ΔS. Let δF_i be the

surface force that the part of the body outside ΔS exerts on the part inside through δS. According to Newton's third law, an equal and opposite force is exerted by the material inside ΔS on the material outside. Assuming that ΔS tends to zero, a vector can be defined as

$$T_{(n)i} = \lim_{\Delta S \to 0} \frac{\delta F_i}{\delta S},$$

(2.18)

which represents the force per unit area acting on the surface with an orientation defined by its unit normal vector n_i. T_i defines traction. A traction vector field can be defined on any surface within a continuous medium, and is usually a continuous function of the coordinates.

A small parallelepiped is considered with faces in the coordinate planes and dimensions dx_1, dx_2, and dx_3 (Fig. 2.3). The tractions on the three faces shown in the figure can be resolved into their Cartesian components, one normal and two tangential to the face on which the traction acts:

$$T_{(1)i} = (\sigma_{11}, \sigma_{12}, \sigma_{13})$$

(2.19)

$$T_{(2)i} = (\sigma_{21}, \sigma_{22}, \sigma_{23})$$

(2.20)

$$T_{(3)i} = (\sigma_{31}, \sigma_{32}, \sigma_{33})$$

(2.21)

The nine components of the traction vector form a 3 x 3 matrix,

$$\sigma_{ij} = \begin{pmatrix} \sigma_{11} & \sigma_{12} & \sigma_{13} \\ \sigma_{21} & \sigma_{22} & \sigma_{23} \\ \sigma_{31} & \sigma_{32} & \sigma_{33} \end{pmatrix} \qquad (2.22)$$

σ_{ij} is defined as the stress tensor, the rank of which is 2.

We now shift our discussion to the kinematic (strain rate) description in fluids, which concerns time-dependent deformation. The primary kinematic quantity is the strain rate tensor that determines the response of a fluid. The fluid velocity (v_i) in the Eulerian reference frame is the total time derivative of the displacement (u_i),
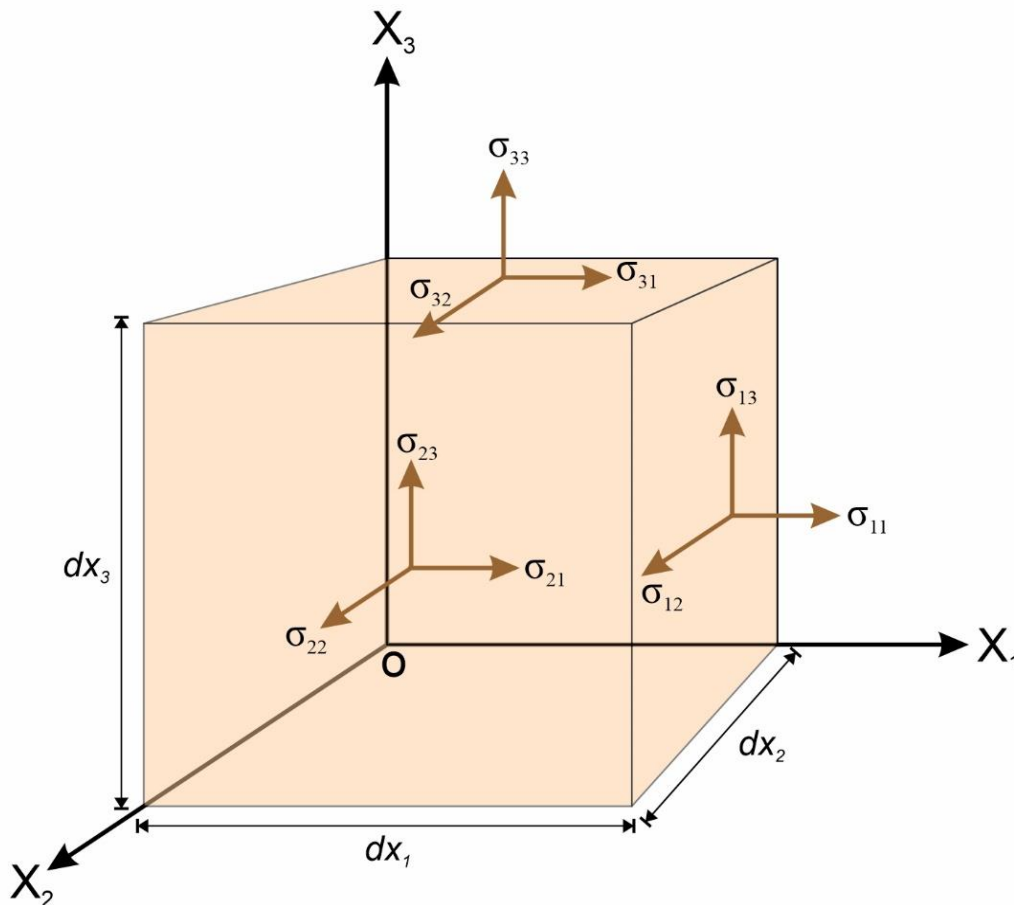
Figure 2.3: Stress components on three faces of infinitesimal parallelepiped of volume $dx_1 dx_2 dx_3$.

$$v_i = \frac{Du_i}{Dt} \tag{2.23}$$

Defining a velocity gradient tensor from Eq. (2.23) and neglecting the higher order terms results in

$$\frac{\partial v_i}{\partial x_j} = \frac{\partial}{\partial x_j}\left(\frac{\partial u_i}{\partial t} + v_k \frac{\partial u_i}{\partial x_k}\right) = \frac{\partial}{\partial t}\left(\frac{\partial u_i}{\partial x_j}\right) + v_k \frac{\partial}{\partial x_k}\left(\frac{\partial u_i}{\partial x_j}\right) = \frac{D}{Dt}\left(\frac{\partial u_i}{\partial x_j}\right) \tag{2.24}$$

The strain rate tensor $\dot{\epsilon}_{ij}$ can be expressed as

$$\dot{\epsilon}_{ij} = \frac{D\epsilon_{ij}}{Dt} = \frac{1}{2}\left\{\frac{D}{Dt}\left(\frac{\partial u_i}{\partial x_j}\right) + \frac{D}{Dt}\left(\frac{\partial u_j}{\partial x_i}\right)\right\} = \frac{1}{2}\left(\frac{\partial v_i}{\partial x_j} + \frac{\partial v_j}{\partial x_i}\right) \tag{2.25}$$

Strain rate tensor thus expresses the derivative of the strain tensor with respect to time, or as the symmetric component of the gradient (derivative with respect to position) of the flow velocity. Since the macroscopic motion of material is described by the strain rate tensor from a geometric point of view, it does not depend on the nature of the material, the forces, or stresses. . For any fluid, this tensor plays the most critical role to create viscous forces during the flow of a fluid. In 3D, the strain rate tensor ($\dot{\epsilon}_{ij}$) can be expressed as a 3×3 matrix in the following form

$$\dot{\epsilon}_{ij} = \begin{pmatrix} \dfrac{\partial v_1}{\partial x_1} & \dfrac{1}{2}\left(\dfrac{\partial v_1}{\partial x_2} + \dfrac{\partial v_2}{\partial x_1}\right) & \dfrac{1}{2}\left(\dfrac{\partial v_1}{\partial x_3} + \dfrac{\partial v_3}{\partial x_1}\right) \\ \dfrac{1}{2}\left(\dfrac{\partial v_2}{\partial x_1} + \dfrac{\partial v_1}{\partial x_2}\right) & \dfrac{\partial v_2}{\partial x_2} & \dfrac{1}{2}\left(\dfrac{\partial v_2}{\partial x_3} + \dfrac{\partial v_3}{\partial x_2}\right) \\ \dfrac{1}{2}\left(\dfrac{\partial v_3}{\partial x_1} + \dfrac{\partial v_1}{\partial x_3}\right) & \dfrac{1}{2}\left(\dfrac{\partial v_3}{\partial x_2} + \dfrac{\partial v_2}{\partial x_3}\right) & \dfrac{\partial v_3}{\partial x_3} \end{pmatrix} \tag{2.26}$$

2.3. RHEOLOGICAL CONSIDERATIONS

In classical mechanics, the mechanical state of a body is defined by means of kinematic and dynamic variables. The former refers to motion (i.e., displacement, velocity, acceleration, etc.), whereas the latter refers to various types of forces, as discussed in the previous section. These kinematic and dynamic parameters are always related by some fundamental laws of nature. For example, Newton's second law of motion relates a dynamic quantity (force) to a kinematic quantity
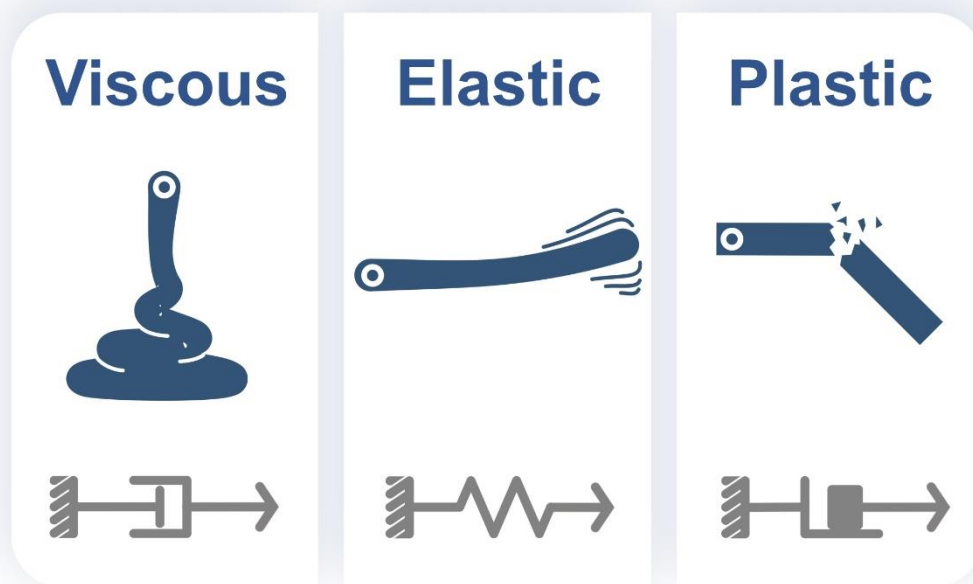
Figure 2.4: Three principal types of rheology used for modelling geodynamic systems.

(acceleration) through a proportionality constant m (mass of the body), which in Newtonian mechanics is a property of the body, independent to its mechanical state. Similar circumstances apply when formulating rheological constitutive equations, where the objective is to create fundamental relationships between dynamic and kinematic variables of continuum media, to assess and anticipate their meaning and implications (Fig. 2.4). The two most important classes of fluid in geodynamic modelling are:

> ➢ Newtonian fluids: They follow a linear relation between stress (σ_{ij}) and strain rate ($\dot{\epsilon}_{ij}$) tensors, implying that the viscosity (proportionality constant) does not vary with strain rate.

> ➢ Non-Newtonian fluids: They show a non-linear relation where the strain rate is proportional to the nth power of the applied stress. The nonlinear relationship means that the fluid changes its viscosity with strain rate.

2.3.1. NEWTONIAN RHEOLOGY

In case of a static fluid ($\dot{\epsilon}_{ij} = 0$) where stress tensor (σ_{ij}) is hydrostatic at all points, the constitutive equation is defined by,

$$\sigma_{ij} = -p\delta_{ij} \tag{2.27}$$

where p is the thermodynamic pressure and δ_{ij} is the Kronecker delta function such that $\delta_{ij} = 0$ when $i \neq j$ and $\delta_{ij} = 1$ when $i = j$. Once the viscous fluid moves to gain relative motion ($\dot{\epsilon}_{ij} \neq 0$), additional components of the stress (deviatoric stress, τ_{ij}) tensor come into play. The constitutive equation then modifies to:

$$\sigma_{ij} = -p\delta_{ij} + \tau_{ij} \tag{2.28}$$

In the case of Newtonian fluids, the relation between stress (σ_{ij}) and strain rate tensor ($\dot{\epsilon}_{ij}$) is linear, and the constitutive equation follows,

$$\sigma_{ij} = 2\mu\dot{\epsilon}_{ij} + \lambda\dot{\epsilon}_{kk}\delta_{ij} \tag{2.29}$$

Where $\dot{\epsilon}_{kk} = \nabla.v_i$, which represents the volumetric strain rate, μ is the dynamic viscosity and $\lambda = \left(\kappa - \frac{2}{3}\mu\right)$ is a scalar variable where κ is the coefficient of bulk viscosity. Combining Eqs. (2.28) & (2.29) results in

$$\tau_{ij} = p\delta_{ij} + 2\mu\dot{\epsilon}_{ij} + \lambda\dot{\epsilon}_{kk}\delta_{ij} \tag{2.30}$$

By setting $i = j$ in Eq, (2.23), a relation between two scalar variables follows,

$$\tau_{ij} = -3p + (2\mu + 3\lambda)\dot{\epsilon}_{kk} \tag{2.31}$$

The pressure term p can be expressed as a combination of diagonal stress tensor and volumetric strain rate as
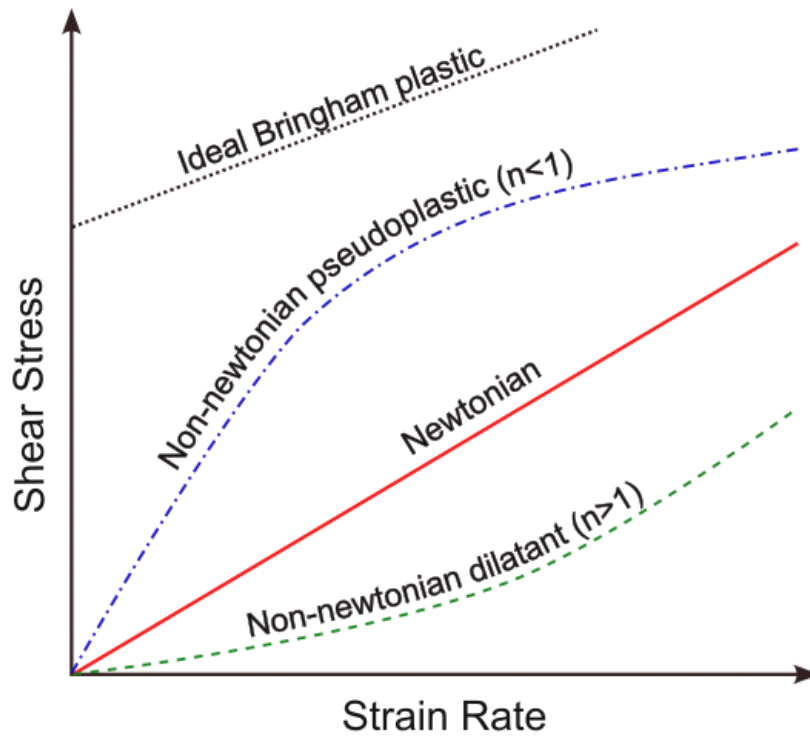
Figure 2.5: Rheological behavior of fluids, shear stress versus shear strain relation.

$$p = \frac{1}{3}\sigma_{ij} + \left(\frac{2}{3}\mu + \lambda\right)\nabla.v_i \tag{2.32}$$

A viscous fluid in motion ($\dot{\epsilon}_{ij} \neq 0$) may produce a stress tensor (σ_{ij}) with unequal diagonal terms proportional to μ. The mean pressure, $\bar{p}$ (different from thermodynamic pressure, p), can be defined by averaging the diagonal terms of stress tensor, as $\bar{p} = -\frac{1}{3}\sigma_{ij}$. Substituting this in Eq. (2.32) results in

$$p - \bar{p} = \left(\frac{2}{3}\mu + \lambda\right)\nabla.v_i \tag{2.33}$$

Eq. (2.33) is the general rheological law for incompressible Newtonian (linear) fluids. This linear relation is consistent with Newton's definition viscosity in a simple shear flow,

$$\tau = \mu\left(\frac{du}{dy}\right), \tag{2.34}$$

2.3.2. NON-NEWTONIAN RHEOLOGY

A non-Newtonian fluid has variable viscosity, and it's constitute equation can be expressed as,

$$\sigma_{ij} = A(\dot{\epsilon}_{ij})^n \tag{2.35}$$

where n is the stress exponent, and A is the empirical constant which is a function of pressure, temperature, and material properties. In Eq. (2.35), n determines the nature

36

of non-Newtonian behavior. For $n < 1$, the fluids show dilatant properties, whereas for $n > 1$ the behavior is pseudoplastic in nature (Fig. 2.5). For Newtonian fluids n = 1. The apparent viscosity of power-law fluid is obtained from

$$\mu = \frac{\sigma_{ij}}{\dot{\epsilon}_{ij}} = A(\dot{\epsilon}_{ij})^{n-1} \tag{2.36}$$

The most important non-linear stress-strain rate relation in geodynamic systems is the power- law creep equation (Karato & Wu, 1993; Ranalli, 1997), given by

$$\eta_{diff/disl} = A^{\frac{-1}{n}} \dot{\varepsilon}^{\frac{1-n}{n}} exp\left(\frac{E + PV}{nRT}\right) \tag{2.37}$$

Eq. (2.37) is used to model the rheology of earth's mantle and crust. T is the absolute temperature, P is the confining pressure, E is the activation energy and R is the gas constant. Due to the strong dependency of mantle rheology on temperature and stress and the nonlinear relation between flow velocity and temperature in the energy equation, these governing equations can be handled numerically using specific mathematical methods.

2.4. *NUMERICAL METHODS AND SCHEMES*

Numerical methods for solving partial differential equations (PDEs) are universal, which can be applied to solve for both continuous and discontinuous distributions of field variables (Gustafsson, 2008). The following groups of numerical approaches are commonly used in geodynamic modelling (Lynch, 2005; Van Zelst et al., 2022; Zhong et al., 2007):

➢ finite-difference methods (FDM)

> ➤ finite-volume methods (FVM)

> ➤ finite-element methods (FEM)

> ➤ spectral methods

In this section, these numerical schemes are briefly discussed to highlight their applicability in solving geodynamical problems numerically.

2.4.1. FINITE-DIFFERENCE METHOD

The application of finite-difference methods (FDM) in geodynamics started much earlier than the other methods. They are based on local discretization of the derivative operators based on a Taylor series expansion with an assigned order of accuracy about a given point (Zhong et al., 2007). The unknowns at each grid point depend on those of the neighboring points from the local Taylor expansion. For 2-D iso-viscous, geodynamic fluid flow within the Boussinesq approximation in FDM, a widely used formulation employs stream-function (Ψ) and vorticity (ω) to eliminate the pressure and velocity terms, and the governing equations (continuity of mass, momentum and energy) are written in terms of stream function (Ψ), vorticity (ω), and temperature (T) (Mckenzie et al., 1974). They can be written in time-dependent form as,

$$\nabla^2 \Psi = -\omega \tag{2.38}$$

$$\nabla^2 \Psi = R_a \frac{\partial T}{\partial x} \tag{2.39}$$

$$\frac{\partial T}{\partial t} = \nabla^2 T - \left(\frac{\partial \Psi}{\partial x} \frac{\partial T}{\partial z} - \frac{\partial \Psi}{\partial z} \frac{\partial T}{\partial x} \right) + \gamma \tag{2.40}$$

which automatically satisfies the continuity, x and z are the horizontal and vertical coordinates, respectively, with z vector pointing upward, and t is the time. It is to note that Eqs. (2.38) & (2.39) are given by a set of coupled second-order partial differential equations. Alternatively, these two could have combined them to form a single fourth-order partial differential equation in terms of Ψ, known as the biharmonic equation, as developed in the numerical scheme of Christensen (1984) using bicubic splines and also by (Schott & Schmeling, 1998) using FDs. In 2-D geodynamic flow problems, the so-called primitive variables (i.e., velocity and dynamical pressure) formulation can also be utilized by solving the coupled equations of mass and momentum conservations at each time step. However, due to the increased number of unknowns, this approach may require handling more numerical complexity and computing time. The examples of such formulations are available in Auth & Harder (1999) and Gerya & Yuen (2003, 2007).

2.4.2. FINITE-VOLUME METHOD

The finite volume method (FVM) is a numerical technique used to solve partial differential equations (PDEs) on a computational grid (Patankar, 2018). In FVM, the computational domain is subdivided into a set of control volumes or cells. These cells form a grid, and each cell represents a small region of the domain. The PDEs are then converted into a set of discrete algebraic equations by integrating them over each control volume. The key idea behind the finite volume method is the conservation principle. The method is based on the concept that the net flow of a conserved quantity into or out of a control volume must be balanced by the rate of change of that quantity within the volume. FV methods share some common features with FE and FD methods. The finite volume (FV) methods involve discretizing the PDEs by integrating

it over a control volume or cell and approximating lower-order differential operators at the boundaries of the cell (Patankar, 1980). According to Patankar (1980), the FV formulation can be seen as a particular instance of the weighted residual method in finite element (FE) analysis, where the weighting function is uniformly set to one within an element and zero outside of it. Similarly, both the FV and finite difference (FD) methods require approximating differential operators using values at grid points.

The basic idea of the FV method can be explained with the help of a simple example. Consider a 1-D heat conduction equation with heat source ζ:

$$\frac{d}{dx}\left(k\frac{dT}{dx}\right) + \zeta = 0 \tag{2.41}$$

where k represents the heat conductivity. This equation is integrated over a control-cell and the resulting equation is

$$\left(k\frac{dT}{dx}\right)_e + \left(k\frac{dT}{dx}\right)_w + \int_e^w \zeta dx = 0, \tag{2.42}$$

where e and w are the two ends of the control cell (Figure 1(b)). Introducing flux approximations at each end and the source term in Eq. (2.42) leads to

$$\frac{k_e(T_E-T_P)}{(\partial x)_e} + \frac{k_w(T_P-T_W)}{(\partial x)_w} + \bar{\zeta}\Delta x = 0, \tag{2.43}$$

where k_e and k_w represent the heat conductivity at cell boundaries, T_E, T_P, and T_W represent the temperatures at nodal points, $\bar{\zeta}$ signifies the averaged source in the

control- cell, and $\Delta x = [(\partial x)_e + (\partial x)_w]/2$ is the control-cell size. Eq. (2.43) represents a discrete equation in which the unknowns are the nodal temperatures associated with the specific control-cell. By applying this process to all control-cells, a system of equations is obtained, where the temperatures at all grid points are the unknowns, which is analogous to the finite difference (FD) method.

2.4.3. SPECTRAL METHOD

The spectral method is a popular numerical technique used to solve partial differential equations (PDEs) by representing the solution as a sum of basis functions that are Eigen functions of the underlying differential operators. This method is a traditional approach that draws its motivation from its widespread analytical use and intrinsic precision. It relies on the idea of expanding functions using orthogonal Eigen functions associated with the differential operators of the Laplace equation. This method operates within orthogonal curvilinear coordinate systems. In the context of mantle geodynamic problems, the horizontal variability can be described by employing a Fourier expansion for Cartesian geometry or spherical harmonics for the three-dimensional spherical shell. In terms of a symbol representation, this expansion can be expressed as,

$$F(x_1, x_2, x_3) = \sum_{ijk} a_{ijk} f(x_3) g(x_1) h(x_2) \tag{2.44}$$

where F refers to the field variable being expanded, a_{ijk} represents the spectral coefficient, x_3 is the vertical or radial coordinate, x_1 and x_2 are the horizontal coordinates, g and h are the implemented Eigen functions, and f is a function describing the vertical or radial dependence. It should be noted that f can be

determined by solving a two point boundary value or an orthogonal function expansion, or using the FDM (Cserepes et al., 1988; Cserepes & Rabinowicz, 1985; Gable et al., 1991; Glatzmaier, 2006; Machetel et al., 2006; Travis et al., 1990) level of accuracy compared to finite difference (FD) methods, even for comparable computational resources. The convergence performance of spectral methods can be evaluated by analyzing the decay rate of energy in the spectrum as the number of terms in the spectral expansion, as shown in Eq. (2.44), increases (Peyret & Taylor, 1983). In addition, spectral methods offer a couple of other notable advantages. Firstly, they are straightforward to implement as it is possible to simplify the problem into either an algebraic set or a set of weakly coupled ordinary differential equations, as discussed earlier. Secondly, by utilizing fast transform algorithms, e.g., the fast Fourier transform, spectral methods can be made highly efficient and fast even on single-processor computers.

Although there are several numerical schemes available presently to solve geodynamic fluid flow problems, the finite element method (FEM) has gained enormous popularity in the geodynamics community. The problems addressed in this thesis use mostly the FEM approach, which is discussed in detail in the following section.

2.5. FINITE ELEMENT MODELLING: METHODS AND APPLICATIONS

As discussed in the previous section, the physical laws of space and time-dependent geodynamic problems can be mathematically expressed in terms of partial differential equations (PDEs). For most of such geophysical problems and their geometries, these PDEs cannot be tackled using any analytical methods due to their inherent complexities. However, various discretization techniques can be used to deal

with the PDEs of the governing equations with some approximations. These discretization methods approximate the PDEs into numerical model equations, which is then solved numerically. Therefore, the solutions of the numerical model equations are, in reality, provide a close approximation of the real PDE solutions. The finite element method (FEM) is an efficient technique to compute such approximations numerically (May et al., 2013; Salomon, 2018; Thieulot & Bangerth, 2022). In the past several decades, FEM has received remarkable attention in solving numerical geodynamic problems for the following reasons:

- ➢ FEM can be easily applied to new equations with few intricacies.
- ➢ Meshes of complicated geometries can be created in FEM. Meshes can be constructed using triangles or quadrilaterals. They can be also be deformed and evolved with time.
- ➢ Several types of boundary conditions can be easily implemented in the model boundaries e.g. free surface boundary conditions.
- ➢ Jumps in material properties do not introduce any additional complexity.
- ➢ The programming complexity between 2D and 3D is minimal.
- ➢ FEM also has robust mathematical foundations which produces reliable and accurate results.

Consider a function u with a dependent variable (e.g., temperature, velocity, pressure etc.) in a PDE. The function u can be approximated by another function (u_h) which is a combination of basis function, that can be expressed as

$$u = u_h \text{ and } u_h = \sum_i u_i \psi_i \qquad (2.45)$$

where ψ_i refers to a basis functions and u_i is the coefficient of that basis function which approximates u to u_h. To provide further clarification, consider a 1D problem involving a rod that experiences non-uniform heating along its length, denoted by the variable x. In this scenario, u represents the temperature distribution along the x-axis. The linear basis functions used in this case have a value of 1 at their respective nodes and 0 at all other nodes. For this particular problem, the rod is divided into a total of seven elements, and the function u is defined within these elements to describe the temperature variation along the length of the rod.

2.5.1. FEM WEAK FORMULATIONS: TEST AND BASIS FUNCTIONS

Considering that the temperature distribution in a heat sink is given by the following equation,

$$\rho C_P \frac{\partial T}{\partial t} + \nabla \cdot (-k \nabla T) = g(T, t, x_k) \tag{2.46}$$

where the symbols ρ, C_P, and k represent the density, heat capacity, and thermal conductivity, respectively. The temperature, denoted as T, is the variable that depends on time, represented by t. The function g describes the heat source, which can vary based on the temperature (T), time (t), and spatial positions denoted by x_k ($x_k = (x, y, z)$). At steady state, where the time derivative of temperature field is zero, Eq. (2.46) for the model domain Ω becomes,

$$\nabla \cdot (-k \nabla T) = g(T, t, x_k) \text{ in } \Omega \tag{2.47}$$

Let us assume now that the temperature along one boundary, referred to as $(\partial \Omega_1)$, is given and known. Additionally, there is a heat flux normal to the other boundaries,

denoted as $(\partial \Omega_2)$, and for the remaining boundaries, $(\partial \Omega_3)$, there is no heat flux in the outward direction. Hence, the boundary conditions can be applied as follows:

$$T = T_0 \text{ on } \partial \Omega_1 \tag{2.48}$$

$$-k\nabla T \cdot n_k = h(T - T_a) \text{ on } \partial \Omega_2 \tag{2.49}$$

$$-k\nabla T \cdot n_k = 0 \text{ on } \partial \Omega_3 \tag{2.50}$$

where, h is the heat transfer co-efficient, and T_a is the ambient temperature. n_k denotes the outward unit normal vector to the boundary. In the next step, both sides of Eq. (2.46) is multiplied by a test function φ and integrated over the domain Ω, resulting in

$$\int_\Omega \nabla \cdot (-k\nabla T)\varphi dV = \int_A g\varphi dV, \tag{2.51}$$

so that the test function φ and the solution T are members of Hilbert spaces, which are function spaces with infinite dimensions and specific properties. Hilbert spaces can be envisioned as a collection of functions that possess certain desirable characteristics, allowing them to be manipulated in a manner similar to ordinary vectors in a vector space. In Hilbert spaces, it is possible to construct linear combinations of functions, where these functions have a well-defined length known as the norm. Additionally, the angle between these functions can be measured, analogous to Euclidean vectors. The finite element method offers an effective approach to transforming functions from an infinite dimensional function space into functions within a finite dimensional function space, ultimately converting them into

ordinary vectors within a vector space. This conversion allows one to utilize numerical methods to solve the resulting vectors efficiently. The weak formulation is derived by ensuring that Eq. (2.51) holds for all test functions within their respective test function space, as opposed to Eq. (2.46) being satisfied at all points within the domain Ω. A problem expressed in the form of Eq. (2.46) is known as *a pointwise formulation*. In the *Galerkin method*, it is assumed that the solution T belongs to the Hilbert space H, which is the same space as the test functions, denoted as $\varphi \in H$ and $T \in H$. Further, applying integration by parts (or Green's first identity) into Eq. (2.51) results in

$$\int_{\Omega} k\nabla T \cdot \nabla \varphi \, dV + \int_{\partial \Omega} -k\nabla T \cdot n_k \varphi \, dS = \int_{\Omega} g\varphi \, dV \qquad (2.52)$$

Eq. (2.52*)* represents the weak formulation or variational formulation of Eq. (2.51). It is referred to as weak because it relaxes the strict requirements of Eq. (2.51), where all terms in the partial differential equation (Eq. (2.51)) must be well-defined at all points in the domain Ω. Instead, the relationships presented in Eqs. (2.51) and (2.52) only necessitate equality in an integral sense. In the weak formulation, for instance, any discontinuity in the first derivative of the solution T is permissible as it does not impede integration. It can be demonstrated that the weak formulation, in conjunction with boundary conditions outlined in Eqs. (2.48) to (2.50), is directly connected to the solution obtained through the pointwise formulation. In cases, where the solution exhibits sufficient differentiability, meaning that well-defined second derivatives exist, the solutions obtained from the weak formulation and the pointwise formulation are equivalent. Constructing a weak formulation is the initial step in the finite element method. However, the weak formulation (Eq. (2.52)) cannot be directly

solved on a computer due to the infinite dimensionality of the test function φ. Hence, it is necessary to convert this weak formulation (Eq. (2.52)) into a finite-dimensional subspace in order to obtain an approximated weak formulation. This process is referred to as *discretization*, where the mathematical model equations are transformed into numerical model equations that can be solved using a computer. The Galerkin method is one of several techniques used for discretization within the framework of weak formulations.

Discretization (Fig. 2.7) refers to the process of finding an approximate solution to Eq. (2.52) within a finite-dimensional subspace of the Hilbert space H. In this approach, the approximate solution is represented as a linear combination of a set of *basis functions*, denoted as ψ_i, which are elements of the finite-dimensional subspace:

$$T_h(x_k) = \sum_i T_i \psi_i(x_k) \tag{2.53}$$

where T_i represent the unknown coefficients. Now, these basis functions are plugged into Eq. (2.52). Therefore, the discretized version of Eq. (2.52) for every test function ψ_i follows

$$\sum_i T_i \int_\Omega k \nabla \psi_i \cdot \nabla \psi_J dV + \sum_i T_i \int_{\partial\Omega} (-kT_i \nabla \psi_i) \cdot n_k \psi_J dS \tag{2.54}$$

$$= \int_\Omega g \left(\sum_i T_i \psi_i \right) \psi_J dV$$

Eq. (2.54) corresponds to a system of linear equations with the same dimension as the finite-dimensional function space. For instance, if we employ n test functions (ψ_J, where j ranges from 1 to n), = a system of n linear equations is obtained from Equation (2.54). In this system, there are also n unknown coefficients (T_i) as depicted in Eq. (2.53).

After the process of discretizing the system and applying the boundary conditions, the system of linear equations can be expressed in the form:

$$AT_h = b \qquad\qquad (2.55)$$

where, $T_h\{= (T_1, \dots., T_i, \dots., T_n)\}$ denotes the vector of unknowns. A refers to an $n \times n$ system matrix and b represents a vector with a dimension of n.

Until now, the approach has been applied using arbitrary function spaces. The primary objective of the Finite Element Method (FEM) is to select a finite-dimensional subspace that consists of local polynomial spaces, such as piecewise bi-linear functions. This choice allows for the straightforward assignment of basis functions or elements, which are discussed separately in section 3.2.3. In the previous examples (Eq. 3.10), the same set of functions were used as both test functions (ψ_J) and basis functions (ψ_i) for the discretization of model equations. However, the Petrov-Galerkin method presents an alternative finite element formulation in which the test functions differ from the basis functions. This method is commonly employed in convection-diffusion problems, where distinct basis functions may be utilized for various dependent variables. A typical scenario is encountered in solving the Navier-Stokes equations (Eq. 2.40), where the pressure can be approximated more smoothly

and easily than the velocity. Approaches in which the basis (and test) functions for different dependent variables belong to different function spaces are referred to as mixed finite element methods.
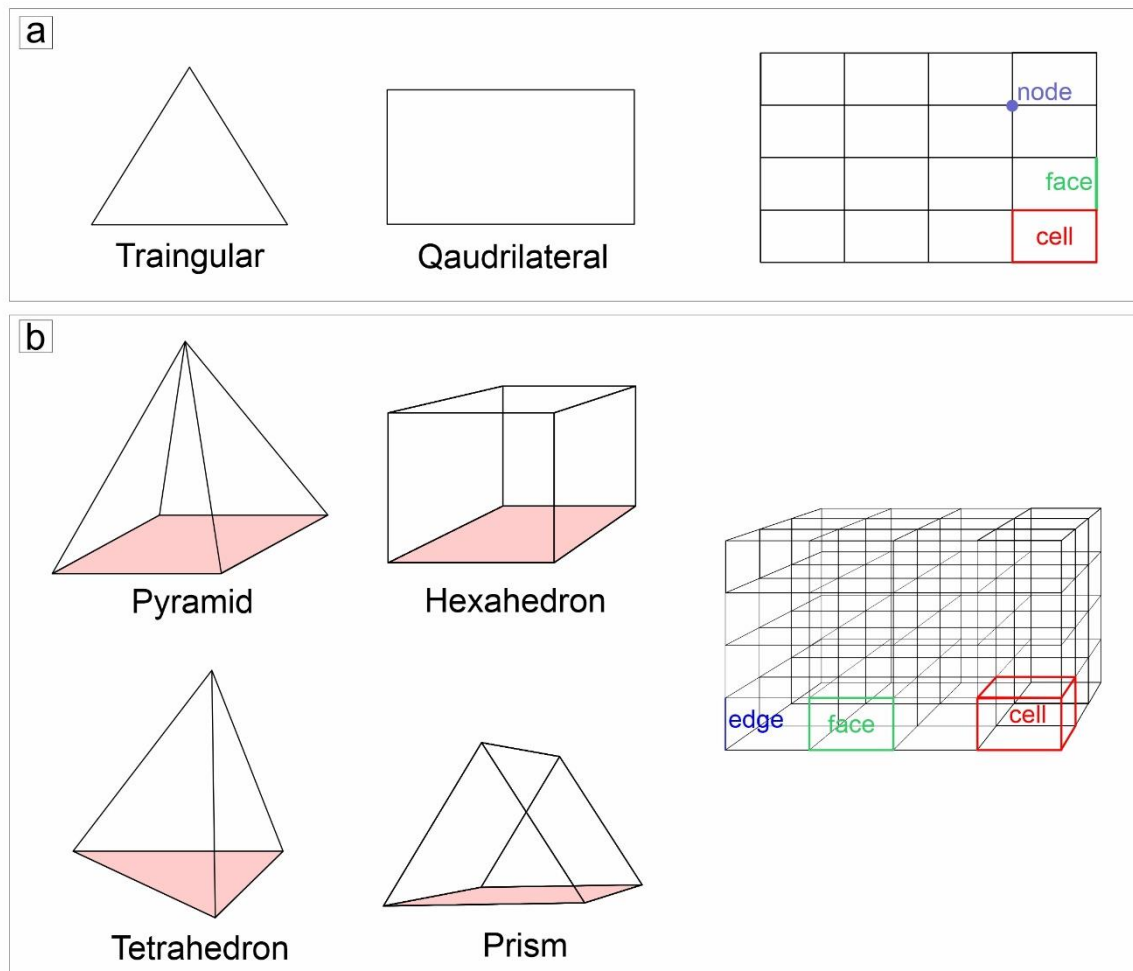
Figure 2.6: Types of mesh elements in a) 2D and b) 3D

2.5.2. MESH ELEMENTS

There are various approaches to define basis functions or elements in the Galerkin finite element formulation. In the following discussion, we will cover some commonly used elements in both 2D and 3D geometries. In 2D, triangular linear elements are widely employed for linear functions. These elements utilize basis functions that are defined based on the positions of the nodes. For structural mechanics analyses, as well as for boundary layer meshing in fluid mechanics and

heat transfer modeling, quadrilateral elements in 2D are often used (Fig. 2.6). For 3D geometries, the analogous counterparts to triangular and rectangular meshes are tetrahedral and hexahedral meshes, as depicted in Fig. 2.6b. When transitioning from hexahedral boundary layer elements to tetrahedral meshes, pyramidal elements are commonly used on top of the hexahedral boundary elements. Additionally, there can be second-order or quadratic elements, as illustrated in Fig. 2.6. These elements are characterized by curved surfaces or higher-order polynomial functions defined within them. The surfaces and edges of elements that face the domain boundary can be curved, while those facing the internal portion of the domain are typically lines or flat surfaces. However, it is also possible to define all edges and surfaces as curved. In the context of second-order elements, Lagrangian and serendipity elements are commonly used in both 2D and 3D. These elements provide enhanced accuracy and flexibility in representing curved surfaces and higher-order polynomial functions within the elements.

2.5.3. SOLUTION STRATEGIES

In Eq. (2.55), the matrix A and vector b are known. Once their values have been determined, T_h can be found either using a direct or iterative method. Direct methods aim to find an approximate solution of $T_h = A^{-1}b$ * through matrix factorization. These methods require a number of computational operations that depend on the size of the problem. The factorization process can be computationally expensive, and the approximate solution Th is obtained only when all the required operations for the factorization algorithm are completed. This means that the solution is approached in a single, large computational step. Commonly used direct solvers, such as MUMPS, PARDISO, and SPOOLES, are based on LU decomposition method. On the other hand,

iterative methods start with an initial guess of the solution and progressively improve it through successive iterations. Unlike direct methods, iterative algorithms can be stopped at any step of the iteration, and we can obtain the approximate solution T_h obtained up to that point. This allows for greater flexibility in controlling the convergence and accuracy of the solution.

In iterative methods, the solution is gradually approached, allowing us to observe the estimation of the error in the solution, which decreases as the number of iterations increases. In a well-conditioned problem, this convergence is typically monotonous. However, in poorly conditioned problems, the convergence can be slower. If the convergence curve of an iterative solver exhibits oscillations, it indicates that the problem is ill-conditioned or lacks sufficient constraints. There are various iterative solvers available, such as the conjugate gradient method, biconjugate
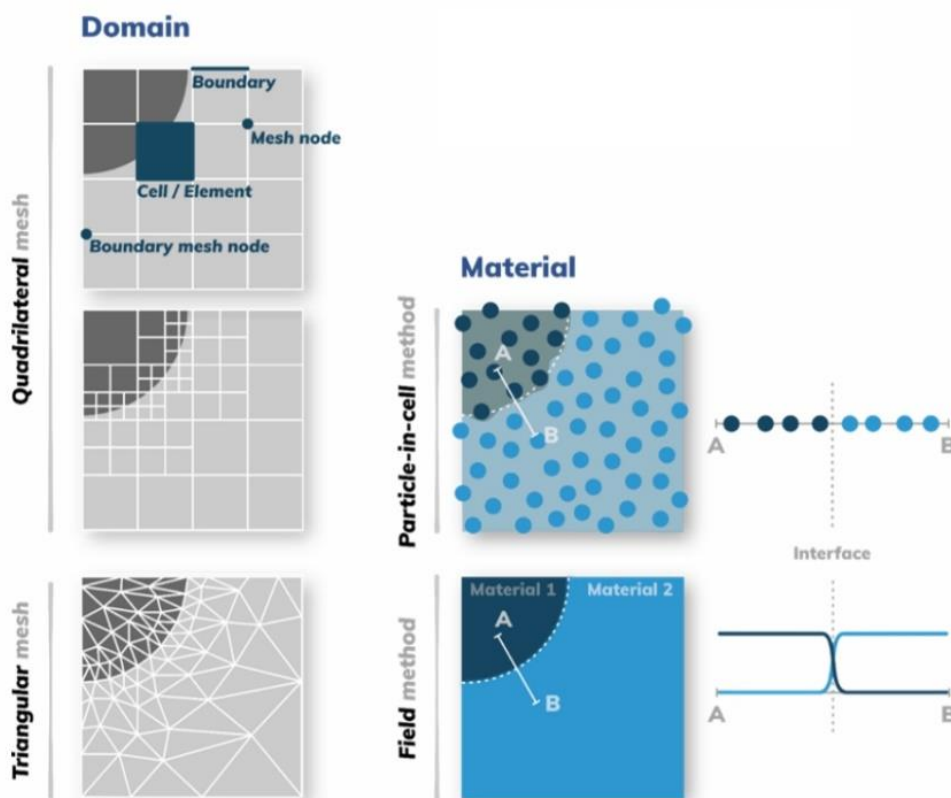
Figure 2.7: The systematic process of discretization in finite-element method

gradient stabilized method, and generalized minimum residual method. While these solvers have different names, they are conceptually similar.

When deciding between iterative and direct methods, several factors need to be considered. The first consideration is the application and the computational system being used. Direct methods are computationally expensive in terms of memory usage and computing time, making them preferable for small to medium-sized 2D and 3D applications. On the other hand, iterative methods require less memory and can outperform direct methods for large 3D applications. However, it should be noted that iterative methods are more difficult to tune and can pose challenges when working with matrices arising from multiphysics problems.

2.5.4. NUMERICAL CONVERGENCE

Numerical convergence is a method used to compare approximate solutions obtained from different mesh sizes. Typically, a very fine mesh is considered to provide the closest approximation to the actual solution. Thus, the error in the approximate solutions obtained from coarser meshes can be directly calculated. However, obtaining an approximate solution for a significantly fine mesh can be computationally challenging and expensive. Therefore, it is common practice to use a reasonably fine mesh for this purpose. With each mesh refinement, it becomes possible to estimate the change in the solution and its convergence towards the actual approximate solution. If the approximate solution is close to the convergence region, the change in solution should gradually decrease with each mesh refinement, bringing the approximate solution closer to the true solution.

Adaptive mesh refinement is another valuable technique in the finite element method. After computing the solution to the numerical equations, a posteriori local

error estimates are calculated. These error estimates are then used to create a denser mesh in regions where the error is large. A second approximate solution is subsequently computed using the refined mesh.

2.6. UNDERWORLD2: A PARTICLE-IN-CELL FEM CODE

Over several generations of computational development, specific software implementations of the aforementioned methods have emerged, giving rise to a diverse and continuously expanding family of tools. At the forefront of this progress is UNDERWORLD2 (Mansour et al., 2021; Moresi et al., 2007), representing the current state-of-the-art iteration. This powerful toolset supports 2D and 3D simulations using multigrid techniques and particle-in-cell features. UNDERWORLD2 combines a robust and modular C-level infrastructure (Quenette et al., 2007) with a user-friendly and highly extensible Python-based API. The implementation leverages MPI for parallelization capabilities, while *PETSc* is employed for the underlying solvers. Advanced users have the advantage of accessing and understanding the transparent layers of UNDERWORLD2. However, the Python layer is deliberately designed to foster fluidity, creativity, and model clarity. The Python interface provides encapsulated higher-level abstractions for various C assets, subtly encouraging good modeling practices among users. This design approach facilitates the development of customized applications (Mansour et al., 2020, 2021) and seamless integration of geodynamics codes with other modeling packages.

By fully exploiting Python's object-oriented character, the higher-level UNDERWORLD2 syntax encapsulates standard model features like meshes, swarms, variables, and solvers as independent instances of generalized classes, making it an intuitive and efficient tool for model construction and simulation tasks. Each object

within the system corresponds to C-level structures, which are organized under the *StGermain* interoperability framework for computational modeling (Quenette et al., 2007). The core algorithmic capabilities rely on the widely used PETSc code for partial differential equations. By default, the PETSc infrastructure prioritizes robustness over speed. However, at the Python level, a variety of options are exposed to allow users to reconfigure the solvers according to their preferences. UNDERWORLD2's design follows the principles of encapsulation and localization, minimizing the use of global attributes and strictly avoiding namespace pollution. As a result, the deletion of obsolete references, or 'garbage collection,' functions in a way that is intuitive to Python users. In most typical use cases, it is rarely necessary to do more than elementary due diligence to limit memory leaks. Nevertheless, when operating at large scales, unavoidable pointer entropy at the C-level has been observed to lead to problematic levels. This challenge has been addressed by judiciously reusing already instantiated objects and by employing subprocesses for the heaviest or lengthiest jobs, harnessing system-level garbage collection.

UNDERWORLD2 offers users a user-friendly interface to access *PETSc* options, with a strong focus on the inner solve method and tolerance selection. By default, the solver is configured as 'mg' (multigrid), which aligns with the previously described method. This default configuration is carefully designed to achieve a balance between speed, robustness, scalability, flexibility, and parallelization capabilities. However, UNDERWORLD2 also provides alternative solver configurations, such as 'mumps,' a multifrontal massively parallel sparse direct solver, and the 'lower-upper method' (LU). It's essential to note that selecting the appropriate configuration requires thorough benchmarking. It should not be assumed that the default configuration will

always yield optimal results for all cases. In particular, the tolerances need to be calibrated manually using convergence and power spectrum tests, as explained earlier. Setting excessively fine tolerances can needlessly prolong solver convergence, while overly generous tolerances can introduce numerical noise into the solution. The choice of tolerances plays a critical role in determining the inherent uncertainty of the model and should be approached with caution.

2.7. REFERENCES

Auth, C., & Harder, H. (1999). Multigrid solution of convection problems with strongly variable viscosity. *Geophysical Journal International*, *137*(3), 793–804. https://doi.org/10.1046/J.1365-246X.1999.00833.X/2/137-3-793-FIG011.JPEG

Braun, J., Thieulot, C., Fullsack, P., DeKool, M., Beaumont, C., & Huismans, R. (2008). DOUAR: A new three-dimensional creeping flow numerical model for the solution of geological problems. *Physics of the Earth and Planetary Interiors*, *171*(1–4), 76–91. https://doi.org/10.1016/J.PEPI.2008.05.003

Carter, N. L. (1976). Steady state flow of rocks. *Reviews of Geophysics*, *14*(3), 301–360. https://doi.org/10.1029/RG014I003P00301

Christensen, U. (1984). Convection with pressure- and temperature-dependent non-Newtonian rheology. *Geophysical Journal International*, *77*(2), 343–384. https://doi.org/10.1111/J.1365-246X.1984.TB01939.X

Cserepes, L., & Rabinowicz, M. (1985). Gravity and convection in a two-layer mantle. *Earth and Planetary Science Letters*, *76*(1–2), 193–207. https://doi.org/10.1016/0012-821X(85)90159-1

Cserepes, L., Rabinowicz, M., & Rosemberg-Borot, C. (1988). Three-dimensional infinite Prandtl number convection in one and two layers with implications for the Earth's gravity field. *Journal of Geophysical Research: Solid Earth*, *93*(B10), 12009–12025. https://doi.org/10.1029/JB093IB10P12009

Gable, C. W., O'Connell, R. J., & Travis, B. J. (1991). Convection in three dimensions with surface plates: Generation of toroidal flow. *Journal of Geophysical Research: Solid Earth*, *96*(B5), 8391–8405. https://doi.org/10.1029/90JB02743

Gerya, T. V., & Yuen, D. A. (2003). Rayleigh–Taylor instabilities from hydration and melting propel 'cold plumes' at subduction zones. *Earth and Planetary Science Letters*, *212*(1–2), 47–62. https://doi.org/10.1016/S0012-821X(03)00265-6

Gerya, T. V., & Yuen, D. A. (2007). Robust characteristics method for modelling multiphase visco-elasto-plastic thermo-mechanical problems. *Physics of the Earth and Planetary Interiors*, *163*(1–4), 83–105. https://doi.org/10.1016/j.pepi.2007.04.015

Glatzmaier, G. A. (2006). Numerical simulations of mantle convection: Time-dependent, three-dimensional, compressible, spherical shell. *Http://Dx.Doi.Org/10.1080/03091928808213626*, *43*(2), 223–264. https://doi.org/10.1080/03091928808213626

Griggs, D. (1939). Creep of Rocks. *The Journal of Geology*, *47*(3), 225–251. https://doi.org/10.1086/624775

Gustafsson, B. (2008). High Order Difference Methods for Time Dependent PDE. In *High Order Difference Methods for Time Dependent PDE*. Springer Berlin Heidelberg. https://doi.org/10.1007/978-3-540-74993-6

Karato, S. I., & Wu, P. (1993). Rheology of the Upper Mantle: A Synthesis. *Science*, *260*(5109), 771–778. https://doi.org/10.1126/SCIENCE.260.5109.771

Kundu, P. K., Cohen, I. M., & Dowling, D. R. (2015). Fluid mechanics: Sixth edition. In *Fluid Mechanics: Sixth Edition*. Elsevier. http://www.sciencedirect.com:5070/book/9780124059351/fluid-mechanics

Landau, L. D., & Lifshitz, E. M. (1959). Fluid Mechanics. In *Fluid Mechanics* (Vol. 6). http://www.sciencedirect.com:5070/book/9780080339337/fluid-mechanics

Lynch, D. R. (2005). Numerical partial differential equations for environmental scientists and engineers: A first practical course. In *Numerical Partial Differential Equations for Environmental Scientists and Engineers: A First Practical Course*. Springer US. https://doi.org/10.1007/B102052/COVER

Machetel, P., Rabinowicz, M., & Bernardet, P. (2006). Three-dimensional convection in spherical shells. *Http://Dx.Doi.Org/10.1080/03091928608210091*, *37*(1–2), 57–84. https://doi.org/10.1080/03091928608210091

Mansour, J., Giordani, J., Moresi, L., Beucher, R., Kaluza, O., Velic, M., Farrington, R., Quenette, S., & Beall, A. (2020). Underworld2: Python Geodynamics Modelling for Desktop, HPC and Cloud. *Journal of Open Source Software*, *5*(47), 1797. https://doi.org/10.21105/joss.01797

Mansour, J., Giordani, J., Moresi, L., Beucher, R., Kaluza, O., Velic, M., Farrington, R., Quenette, S., & Beall, A. (2021). *Underworld2: Python Geodynamics Modelling for Desktop, HPC and Cloud*. https://doi.org/10.5281/ZENODO.5209451

May, D. A., Schellart, W. P., & Moresi, L. (2013). Overview of adaptive finite element analysis in computational geodynamics. *Journal of Geodynamics*, *70*, 1–20. https://doi.org/10.1016/J.JOG.2013.04.002

Mckenzie, D. P., Roberts, J. M., & Weiss, N. O. (1974). Convection in the earth's mantle: towards a numerical simulation. *Journal of Fluid Mechanics*, *62*(3), 465–538. https://doi.org/10.1017/S0022112074000784

Moresi, L., Quenette, S., Lemiale, V., Mériaux, C., Appelbe, B., & Mühlhaus, H. B. (2007). Computational approaches to studying non-linear dynamics of the crust and

mantle. *Physics of the Earth and Planetary Interiors*. https://doi.org/10.1016/j.pepi.2007.06.009

Patankar, S. V. (2018). *Numerical Heat Transfer and Fluid Flow*. https://doi.org/10.1201/9781482234213

Peyret, R., & Taylor, T. D. (1983). Specialized Methods. *Computational Methods for Fluid Flow*, 125–139. https://doi.org/10.1007/978-3-642-85952-6_5

Quenette, S., Moresi, L., Sunter, P. D., & Appelbe, B. F. (2007). Explaining StGermain: An aspect oriented environment for building extensible computational mechanics modeling software. *Proceedings - 21st International Parallel and Distributed Processing Symposium, IPDPS 2007; Abstracts and CD-ROM*. https://doi.org/10.1109/IPDPS.2007.370400

Ranalli, G. (1997). Rheology of the lithosphere in space and time. *Geological Society Special Publication*. https://doi.org/10.1144/GSL.SP.1997.121.01.02

Salomon, C. (2018). Finite element modelling of the geodynamic processes of the Central Andes subduction zone: A Reference Model. *Geodesy and Geodynamics*, *9*(3), 246–251. https://doi.org/10.1016/J.GEOG.2017.11.007

Schott, B., & Schmeling, H. (1998). Delamination and detachment of a lithospheric root. *Tectonophysics*, *296*(3–4), 225–247. https://doi.org/10.1016/S0040-1951(98)00154-1

Thieulot, C., & Bangerth, W. (2022). On the choice of finite element for applications in geodynamics. *Solid Earth*, *13*(1), 229–249. https://doi.org/10.5194/SE-13-229-2022

Travis, B., Olson, P., & Schubert, G. (1990). The transition from two-dimensional to three-dimensional planforms in infinite-Prandtl-number thermal convection. *Journal of Fluid Mechanics*, *216*, 71–91. https://doi.org/10.1017/S0022112090000349

Van Zelst, I., Crameri, F., Pusok, A. E., Glerum, A., Dannberg, J., & Thieulot, C. (2022). 101 geodynamic modelling: How to design, interpret, and communicate numerical studies of the solid Earth. *Solid Earth*, *13*(3), 583–637. https://doi.org/10.5194/SE-13-583-2022

Zhong, S., Yuen, D. A., & Moresi, L. N. (2007). *Numerical Methods for Mantle Convection*.

Chapter 3.

THE DYNAMICS OF PLUMES IN A GLOBALLY FLOWING EARTH'S MANTLE

3.1. MANTLE PLUMES AND HOTSPOTS: AN INTRODUCTORY NOTE

Mantle plumes are recognized as the most effective geodynamic phenomena to drive focused upwelling of deep-mantle materials in Earth, and it is a well-accepted hypothesis that they originate as a result of RT instabilities in the thermal boundary layer (TBL) at the core-mantle boundary (CMB) (Burke et al., 2008; Morgan, 1972a; Nolet et al., 2007; Styles et al., 2011) and other regions at relatively shallower depths, such as melt-rich zones above sinking slabs in subduction zones (Gerya & Yuen, 2003; Ghosh et al., 2020) and transition zones (Brunet & Yuen, 2000; Kumagai et al., 2007). Such plumes are considered to be an integral part of Earth's convection process, despite several controversies have surrounded the plume hypothesis since it was first invoked to explain the origin of large-igneous provinces (LIPs) (Morgan, 1971, 1972a, 1972b). The plate tectonic theory in 1960s revolutionized the perception about Earth's dynamical phenomena, such as volcanism at plate boundaries. However, this theory hardly accounts for the origin of intra-plate LIPs and volcanic hotspots that serve as indicators of focused mantle upwelling. For example, the northwest-oriented lineament of Hawaiian Islands forming the volcanic chain was explained by the model of a rigid tectonic plate moving over a hotspot in Earth's asthenosphere, resulting in intra-plate magma production (Ballmer et al., 2011; Ribe & Christensen, 1999). It was later hypothesized that such a hotspot (Fig. 3.1) could form above a narrow, hot mantle plume rising from a deep mantle region (Foulger et al., 2006; Morgan, 1971, 1972a, 1972b). According to this model, mantle plumes were defined as narrow

thermal upwellings (Frazer & Korenaga, 2022; Korenaga, 2005a, 2005b) with a wide ~1,000-km head, trailing into a much thinner ~100-km conduit-like tail. In course of this conceptual development a connection between the deep mantle sources of plumes and the subduction-assisted recycling of old oceanic lithosphere into deep
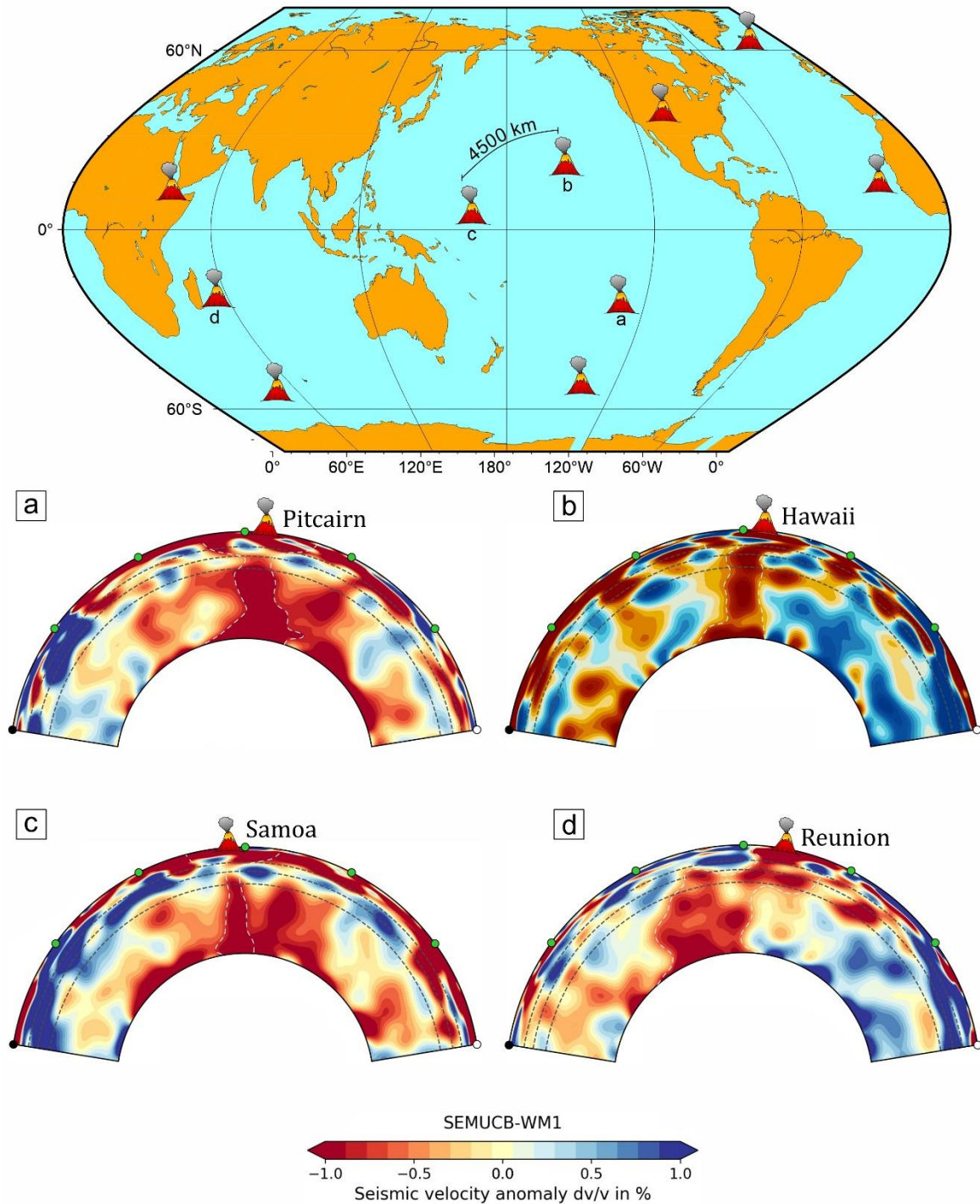
Figure 3.1: Global distribution of the major hotspots originating from deep-mantle plume sources. The seismic sections (lower panels) show the plume configurations in mantle beneath a) Pitcairn, b) Hawaii, c) Samoa, and d) Afar hotspots. Note that inter-hotspot distances are several thousand kilometres.

interiors was established (Koppers et al., 2021) that led to a complete picture of the convection cycle. The following questions, how many mantle plumes exist, at what depth in the mantle they originate, how long a plume can remain active, what is their petrological characteristics, and do geophysical and geochemical observations agree with each other, and what are the dynamics controlling plume ascent behaviour are yet to be fully explored.

Based on geophysical and geochemical evidences, geodynamicists came to a consensus that deep-mantle plumes are initiated by Rayleigh-Taylor instabilities in thermally, chemically or thermo-chemically buoyant layers at the core-mantle boundary (CMB) under buoyancy forces. Due to an excess temperature (~100-400 K) and quick decompression melting (Herzberg & Gazel, 2009; Schilling, 1991; Zhong & Watts, 2002), the ascending plume head eventually interact with the lithosphere, resulting in distinct (1-2 km) topographic reliefs on the Earth's surface (Campbell, 2007; Farnetani & Richards, 1994; Saunders et al., 2007). The magma generated by the melting at the lithospheric base, erupt to the surface in a few million years, covering an area of millions of square kilometers, i.e., LIPs (Black et al., 2021; Bryan & Ernst, 2008; Coffin & Eldholm, 1992, 1994). Geological records show that such LIP episodes have critical effects on the development of mineral deposits and biological evolution, including mass extinction (Xu et al., 2013, 2017; Li et al., 2017; Black et al., 2021). Subsequently, the plume tail also interacts with the overlying lithosphere, forming volcanic activities with time progression and abnormally high topography and heat flow on the Earth's surface, called the hotspot track (Richards et al., 1989; Courtillot et al., 2003; Campbell, 2007), such as the Hawaiian-Emperor volcanic island chain located in the Pacific plate (Fig. 3.1b). It is interesting to note that hotspot

distributions can be used to constrain global plate movement as the mantle plume is nearly stationary in the mantle's kinematic frame (Gordon and Jurdy, 1986; Molnar and Stock, 1987; Müller et al., 1993; Seton et al., 2012). Understanding plume dynamics enables us not only to comprehend the deep material exchange and energy transfer processes, but also to reconstruct the kinematic evolution of lithospheric plates and related geological phenomena, mineral deposit development, and long-term ecological/environmental changes on the Earth's surface.

3.2. GRAVITATIONAL INSTABILITY MODELS

Localized hot upwelling, like thermal plumes can be expected to be produced in the mantle of any other terrestrial planets, where convection occurs through bottom heating in a fluid with temperature-dependent viscosity and uniform composition. Such mantles are also capable of supporting a thermal boundary layer with concentrated heat production (Doornbos et al., 1986; Jarvis & Peltier, 1982; Lay et al., 1998; Spiliopoulos & Stacey, 1984), which in turn increases the probability of plume generation. Rising mantle plumes thus originate from the gravitational or thermochemical instabilities in the thermal boundary layers caused by density fluctuations resulting from thermal or chemical variations (G. F. Davies, 2005; Jellinek & Manga, 2004; Stacey & Loper, 1983; Steinberger & O'Connell, 1998). Understanding the mechanics of instability initiation at the thermal boundary layer is evidently critical to study the formation of deep-mantle plumes. This section presents a brief review of the geodynamic modelling studies that have aided in predicting the composition and behaviour of mantle plumes during their generation and ascent.

Scaled laboratory experiments and numerical simulations have provided significant insights into the ascent behaviour of mantle plumes (Ballmer et al., 2011;
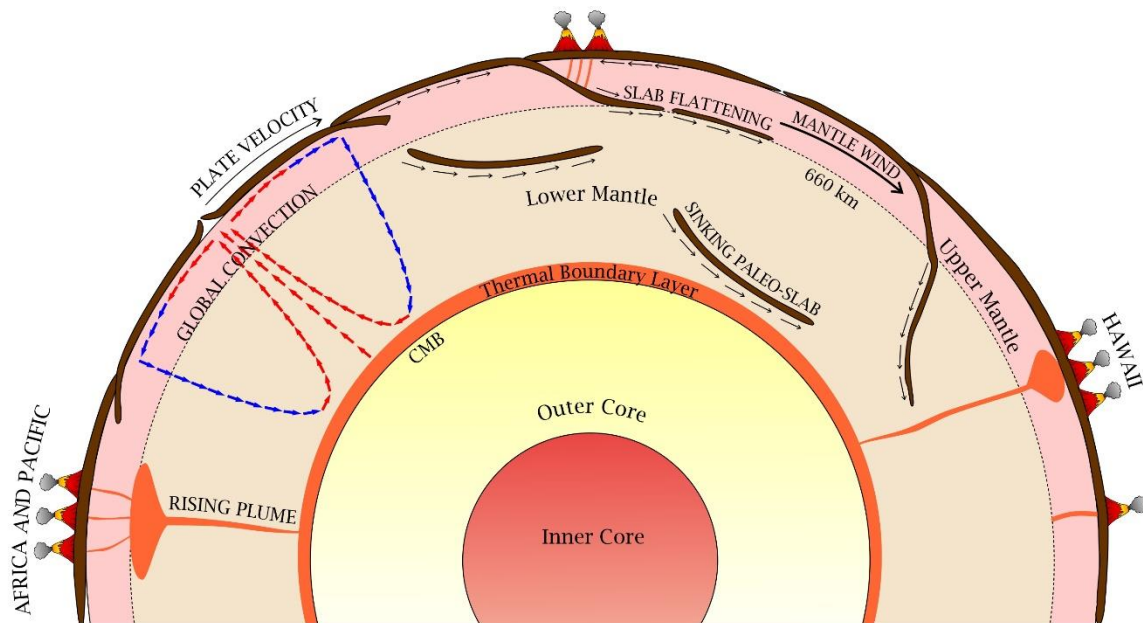
Figure 3.2: Schematic presentation of the Earth's interior showing major locations of plume generation in the mantle and associated volcanisms on the surface. Different types of mantle flows, such as convection-, sinking slab-, lithospheric plate-driven flows and mantle wind are also depicted. All deep-source plumes, forming hotspots, like the Hawaiian chain, originate from the thermal boundary layer (TBL) at the core-mantle boundary (CMB).

Bercovici & Kelly, 1997; Lowman et al., 2004; Olson & Singer, 1985; Whitehead & Luther, 1975). Jellinek et al., (2002) demonstrated from analogue experiments that, under a thermal equilibrium condition the dynamic topography in the TBL formed as a consequence of RT instabilities determines the relative spacing of upwelling zones. Similar laboratory experiments showed entrainment of surrounding materials by the bulbous plume heads during their ascent (van Keken et al., 1997). Several experimental studies have reported the transient behaviour of thermal plumes (Davaille & Vatteville, 2005) and their geometrical asymmetry as a function of source-layer inclination (Dutta et al. 2016). On the other direction, a number of CFD models, both 2D and 3D, have shown the formation of thermal plumes from the D'' layer in Earth's mantle (Frazer & Korenaga, 2022; Jones et al., 2016; Li & Zhong, 2017; Montague & Kellogg, 2000). For example, Montague & Kellogg (2000) showed from 2D numerical models with various combinations of the physical parameters that, a

dense basal layer may take an evolutionary path depending on its excess density. A layer of low density does not remain in continuous contact with the lower boundary of the model domain. With progressive time, the layer undergoes complete mixing with the rest of the mantle. However, a quasi-stable lower layer remains stable, but becomes convoluted into an uneven shape at its upper surface. Convection is promoted within the regions where the layer is extremely thick. The convection process is most favoured preferentially in regions of a high excess density, allowing the lighter layer to stabilize, provided the initial thickness is large enough (~200 km). This approach has set a new ground for the plume research to deal with complex ascent dynamics resulting from the interplay of multiple physical factors, e.g., viscoplastic rheology in the lower mantle (Davaille et al., 2018) and thermo-mechanical heterogeneities in TBL (Heyn et al. 2018). Additionally, the Earth's other tectonic units, such as mid-ocean ridges and subduction zones, may interact with the rising mantle plumes, and trigger a number of geological, geochemical, and geophysical phenomena through their mutual interactions (Ito et al., 2003; Betts et al., 2012; Koppers et al., 2021).

3.3. PROBLEM OF GLOBAL FLOW VERSUS GRAVITATIONAL INSTABILITY

Most of the earlier experimental, theoretical and numerical studies discussed in the previous section, conceptualized the plume dynamics within a framework of RT instability theory applicable for initially rest stratified fluid systems (Jellinek & Manga, 2004). The overlying heavy fluid chosen to represent the mantle is set to flow entirely under the destabilizing gravity effect of inverted density stratification. However, the assumption of an initially rest kinematic state is hardly valid in Earth's interior because the mantle regions are inherently under the influence of large-scale

global flows that originate from various geodynamic processes (Fig. 3.2), such as down-going slab movement, lithospheric plate motions, global convection and mantle winds (Bekaert et al., 2021). Plumes, irrespective of their thermal or thermo-chemical origin, therefore, evolve through kinematic interactions with the ambient mantle flows. However, how global mantle flows can modulate their ascent behaviour is still debated. Some workers (e.g., Korenaga 2005) have claimed that mantle plumes remain fixed in their spatial positions despite an active background flow in the mantle. They have supported their claim with seismic images of deep-mantle plumes. Another school holds a completely opposite view, claiming that deep-sourced plumes undergo horizontal deflections under the influence of global flows (e.g., Steinberger & O'Connell 1998), which are also demonstrated from laboratory experiments (Griffiths & Richards, 1989; Kerr et al., 2008; Kerr & Mériaux, 2004; Richards & Griffiths, 1989). However, none of these studies has attempted to address the most critical questions- in what way does a background flow influence the onset of RT instabilities for plume formation, and secondly, does the flow facilitate or dampen the instability growth? These unresolved issues form the central theme of this study.

Using a 2D finite element particle-in-cell numerical method, computational fluid dynamics (CFD) simulation experiments the present thesis investigates the problem of RT instability growth at the CMB in mantle subjected to a global horizontal flow. The CFD simulations are utilized to explore the existence of a threshold global velocity at which the instability can be completely suppressed, allowing no plume to grow from the buoyant basal layer.

3.4. NUMERICAL MODELLING OF MANTLE PLUMES

3.4.1 THEORETICAL APPROACH

In this study, CFD models are built in the framework of incompressible Stokes flow mechanics, using the mass and momentum conservation equations:

$$\nabla.\boldsymbol{u} = 0 \qquad\qquad (3.1)$$

$$-\nabla P + \nabla.\left(\mu_i(\nabla \boldsymbol{u} + \nabla^T \boldsymbol{u})\right) + \rho_i \boldsymbol{g} = 0, \qquad\qquad (3.2)$$

where, $\boldsymbol{u}$ is the velocity, μ_i is the viscosity of the medium i, P is the total pressure, $\boldsymbol{g}$ is the acceleration due to gravity, and ρ_i is the density of the medium i. The lower-mantle viscosity is assigned a constant average value to simplify the model setup, with an aim to find additional effects of global horizontal flows on plume formation in Earth's mantle. The average viscosity represents the layered mechanical structure as a single model layer. Earlier studies have provided different estimates for the lower-mantle viscosity, e.g., $\sim 10^{22}$ Pa s from geoid anomalies (Richards & Hager 1984), slightly
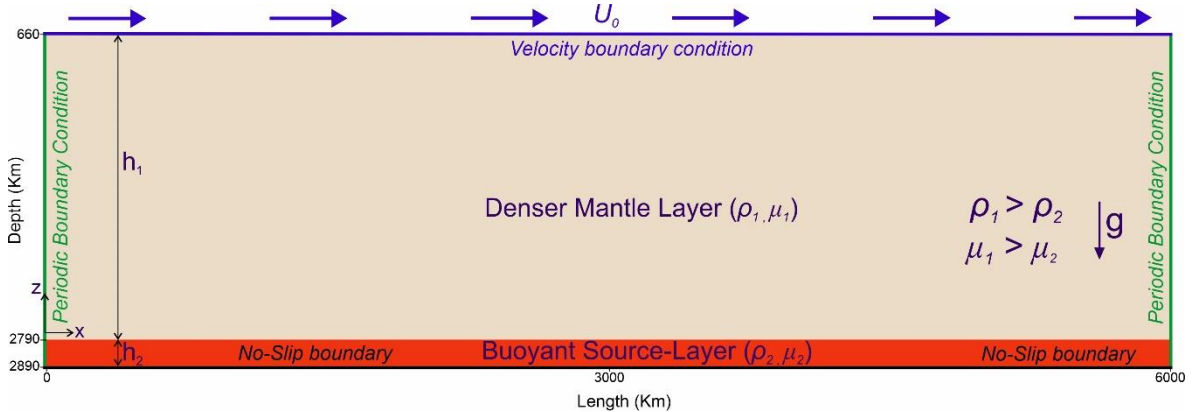
Figure 3.3: Consideration of the initial CFD model set-up and associated boundary conditions used for simulations of Rayleigh-Taylor instabilities in the lower mantle domain. Denser mantle (ρ_1) overlies a 100 km thick lighter (ρ_2) layer (source layer) at the model base. The model domain is discretized into elements with a mesh resolution of 1024 x 512. The side and the bottom walls are assigned periodic and no-slip boundary conditions, respectively. The top model boundary is imposed with a uniform horizontal velocity, which induces an initial global horizontal flow condition in the overlying denser mantle. g is the acceleration due to gravity.

66

higher than 10^{21} Pa s from postglacial rebound (Cathles, 1975; Spada et al., 1991). Numerical modelling, on the other hand, yields an estimate of $\sim 3\text{x}10^{22}$ Pa s from the slab sinking rates (Čížková et al., 2012). Considering these estimates, the average viscosity of the whole lower mantle is fixed at 10^{22} Pa s in the present model. This constant viscosity closely simulates the lower-mantle rheology, which is commonly assumed to be linearly viscous due to diffusion-dominated creep mechanisms, inferred from geophysical observations, such as absence of seismic anisotropy (Karato & Li, 1992, Ranalli 1995). The source-layer viscosity (μ_2) is however, varied in the range 10^{18} to 10^{21} Pa s (Nakada *et al.* 2012) to account for the mechanical effects of various lateral thermal and chemical heterogeneities at the base of lower mantle reported by several workers (D. R. Davies et al., 2012; Farnetani et al., 2018). The model introduces an initial perturbation $F(y)$ at the interface between the two fluid layers,

$$F(y) \;=\; D_o + \Delta A(\cos(kx)) \tag{3.3}$$

where D_o = 2790 km (initial depth of the interface), ΔA = 0.02 km, $k = 2\pi/\lambda$ and λ = 1200 km. To describe the simulation results, the source-layer viscosity (μ_2) is expressed in a normalized form, $\mu^* = \dfrac{\mu_1}{\mu_2}$, where μ_1 is the overlying mantle viscosity. Similarly, their density contrast (buoyancy factor) is non-dimensionalized in terms of Atwood number (A_T), expressed by:

$$A_T \;=\; \frac{\rho_1 - \rho_2}{\rho_1 + \rho_2} \tag{3.4}$$

where ρ_1 and ρ_2 are the densities of heavier overburden and lighter source-layer respectively. All the notations and their corresponding physical variables are

summarized in Table 3.1. A_T is varied in the range 0.01 to 0.04 (Nipin & Tomar, 2015).

The RTI wavelength (λ) is also normalized with source-layer thickness (h_2) as $\lambda^* = \frac{\lambda}{h_2}$.

3.4.2 MODEL SET-UP

Mantle plumes, initiated by Rayleigh Taylor Instability (RTI) are modelled in a domain containing a thin (h_2 = 100 km), low-density layer at the mantle base, overlain by a denser layer (h_1 = 2130 km thick mantle), where the model domain has a width, W = 6000 km (Fig. 3.3). The thin layer is chosen to mechanically replicate a buoyant boundary layer (described as *source layer* in the foregoing discussion) at the Core-Mantle boundary (CMB). The source layer faces gravity driven RTI due to density inversion, forming plumes in course of the instability evolution. A kinematic boundary condition is imposed at the upper model boundary to introduce a global flow in the model mantle, which is the prime concern of the present investigation (Fig. 3.3). The bottom wall is assigned a no-slip boundary condition, keeping the two side walls under a periodic boundary condition. The open-source finite element code of UNDERWORLD2 (http://www.underworldcode.org/) is used to solve the mass and momentum conservation equations (Eq. 3.1 and 3.2) for the CFD simulations. This code works within a continuum mechanics approximation, and has been extensively used to deal with a range of geological and geophysical problems (Mansour et al., 2020). As shown by previous workers (Moresi et al., 2007; Roy et al., 2021), the code discretizes the geometrical domain into a standard Eulerian finite element mesh and the domain is coupled with the particle-in-cell approach (Evans et al., 1957). This numerical approach is found to be effective to successfully discretize the material domain into sets of Lagrangian material points, which carry material properties that are history-dependent and can be tracked over the entire simulation run. The mass

and momentum conservation equations are solved to find the pressure and velocity conditions within the model domain. The physical properties of model materials, such as plume density and viscosity, are mapped using these advection equations through particle indexing. The numerical model domain is discretized into quadrilateral mesh elements comprising 1024 x 512 elements. Mesh refinement tests were performed to assess the mesh resolution effects on simulation results. To verify the applicability of the UNDERWORLD2 code in solving the problems of RT instability in a mechanical setting with large viscosity contrasts, experiments such as the Rayleigh–Taylor instability and falling block benchmarks are performed and compared to the solutions available in previous studies (van Keken et al. 1997; Thieulot 2011, 2014; Gerya 2019). The details of these benchmark tests are provided separately in Appendix A of this chapter.

3.5. MODEL RESULTS

3.5.1 DAMPENING EFFECTS OF HORIZONTAL GLOBAL FLOWS

The top model-boundary velocity (U_o) is systematically increased to evaluate the effects of global flows on the growth rates of instabilities in the source layer (estimated from the vertical ascent-velocity component of instability-driven domes). Following Ramberg's (1968) theoretical formulation, U_o is non-dimensionalized with the absolute value of instantaneous ascent velocity (v),

$$\frac{v}{\Delta A_{time}} = -K \frac{\rho_1 - \rho_2}{2\mu_2} h_2 g, \qquad (3.5)$$

where K is a constant that depends on the viscosity and the wavelength of the system under consideration. ΔA_{time} denotes the amplitude of interface perturbations calculated from numerical simulations at the moment (t $\sim$ 14 Ma) the instability starts
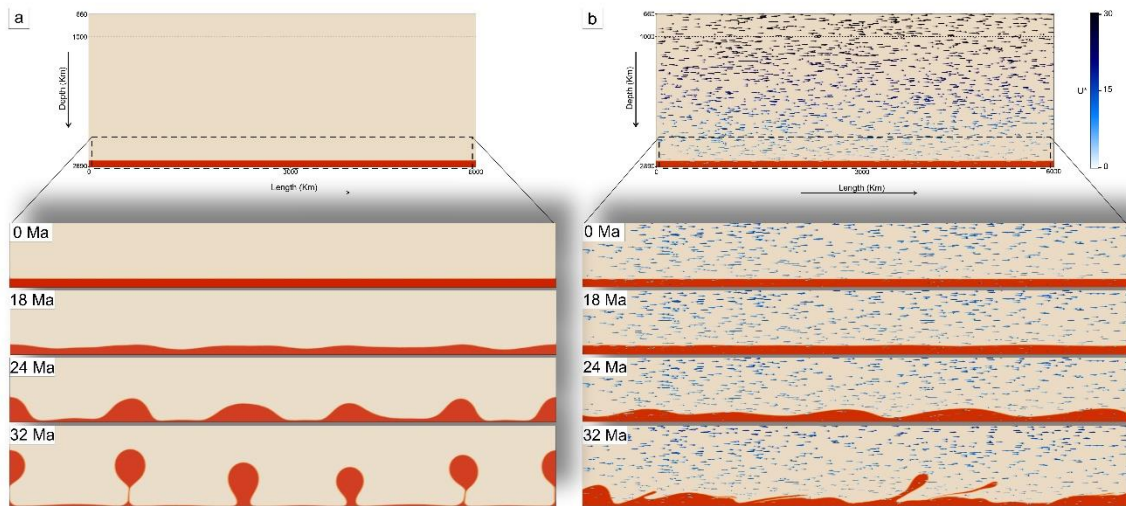
Figure 3.5: Progressive growth of Rayleigh-Taylor instabilities in CFD model simulations. a) Reference experiment with an initially rest mantle condition (U*= 0). b) Experiment with an initial horizontal global flow (U*=36) in the mantle. Notice in panel (b) at t = 32 Ma that the instability growth is significantly dampened by the global mantle flow. The color bar represents normalized flow velocity magnitudes.

to grow exponentially. The non-dimensional boundary velocity, $U^* = \frac{U_0}{|v|}$ was varied in

the range 0 to ~36, keeping A_T (= 0.02) and μ^* (=10^2) constant.

The reference experiment (Fig. 3.4a) run for an initially rest mantle condition

(U^*= 0) shows that the RT instabilities start to amplify with an appreciable rate (~0.8
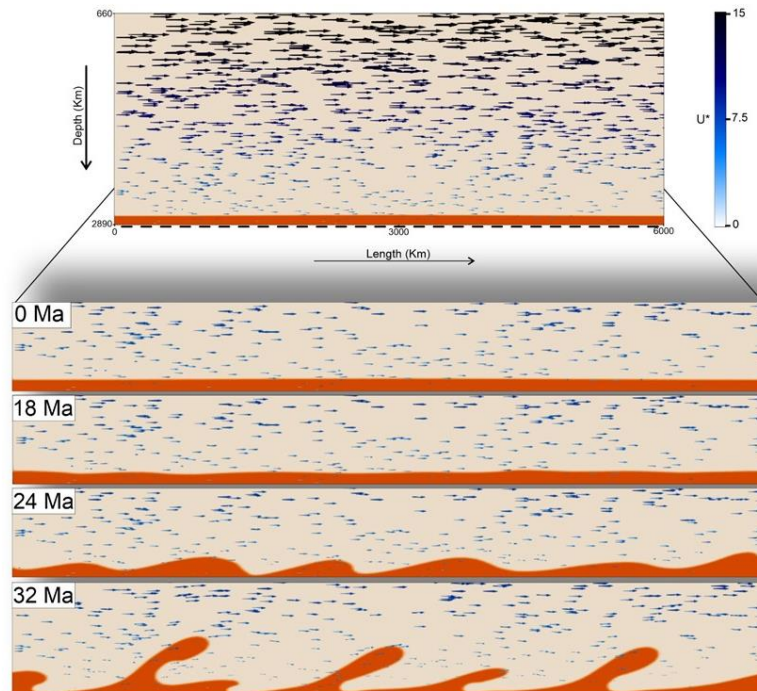
Figure 3.4: Progressive growth of Rayleigh-Taylor instabilities in CFD model simulations with an initial horizontal global flow (U*=18) in the mantle.

cm/yr) at a model run time, $t = \sim 14$ Ma. The instabilities then grow with exponentially increasing rates to form typical plume structures (bulbous heads trailing into narrow tails) at $t \sim 27$ Ma. At this stage, the plume heads ascend vertically through the mantle at the rates of 12 to 15 cm/yr, which is approximately in the same order of magnitudes obtained from the Stokes formula (Turcotte and Schubert, 2002). In a simulation with $U^* = \sim 18$ (Fig. 3.5) the global flow is found to dampen the instability growth in the initial stage, allowing them to grow at a relatively lower rate (~ 0.7 cm/yr) on a longer time scale ($t = \sim 18$ Ma), and the fastest growing instabilities attain a typical plume structure at $t = \sim 34$ Ma. The dampening effect strengthens further when $U^* = \sim 36$, where the instabilities grow in amplitude at much slower rates (~ 0.6 cm/yr at $t =$
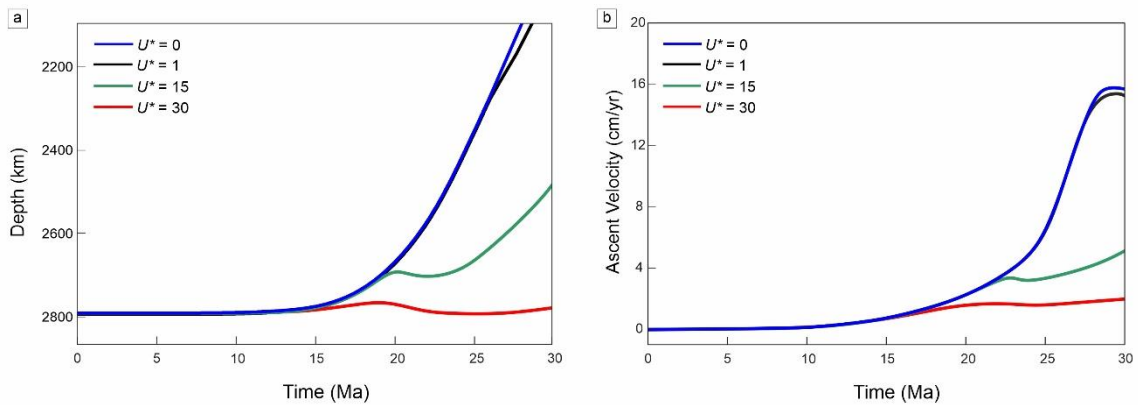
Figure 3.6: Graphical plots of a) plume ascent heights, and b) vertical ascent velocities of the fastest growing instabilities as a function of time for different normalized global flow-velocity magnitudes (U^*). For this set of simulations, $A_T = 0.02$ and $\mu^* = 10^2$ .Note that increasing U^* strongly influences the ascent heights and velocities at t > 18 Ma.

~ 18 Ma) (Fig. 3.4b) that becomes almost steady with time. Under this kinematic condition the instabilities eventually do not form any typical plume structure even after a very long model run time (t ~ 50 Ma) (Fig. 3.6).

The CFD simulation results described above clearly suggest that, under a given set of physical parameters, such as A_T, μ^* and layer thickness ratio, horizontal global flows in the mantle can act as a dampening factor in the RT instability dynamics to suppress the process of plume formation in the basal buoyant layer. Fig 3.6a and b

show reducing plume ascent heights and vertical ascent velocities of the fastest growing instabilities with increasing U^*.

3.5.2 ROLE OF SOURCE-LAYER BUOYANCY

A set of simulations is run by varying A_T in the range 0.01-0.04 for $U^* = 0$, keeping $\mu^* = 10^2$. For low buoyancy ($A_T = 0.01$), the instabilities start to significantly grow in amplitude (0.3 cm/yr) at $t = {\sim}24$ Ma, and the fastest growing waves (2 cm/yr)
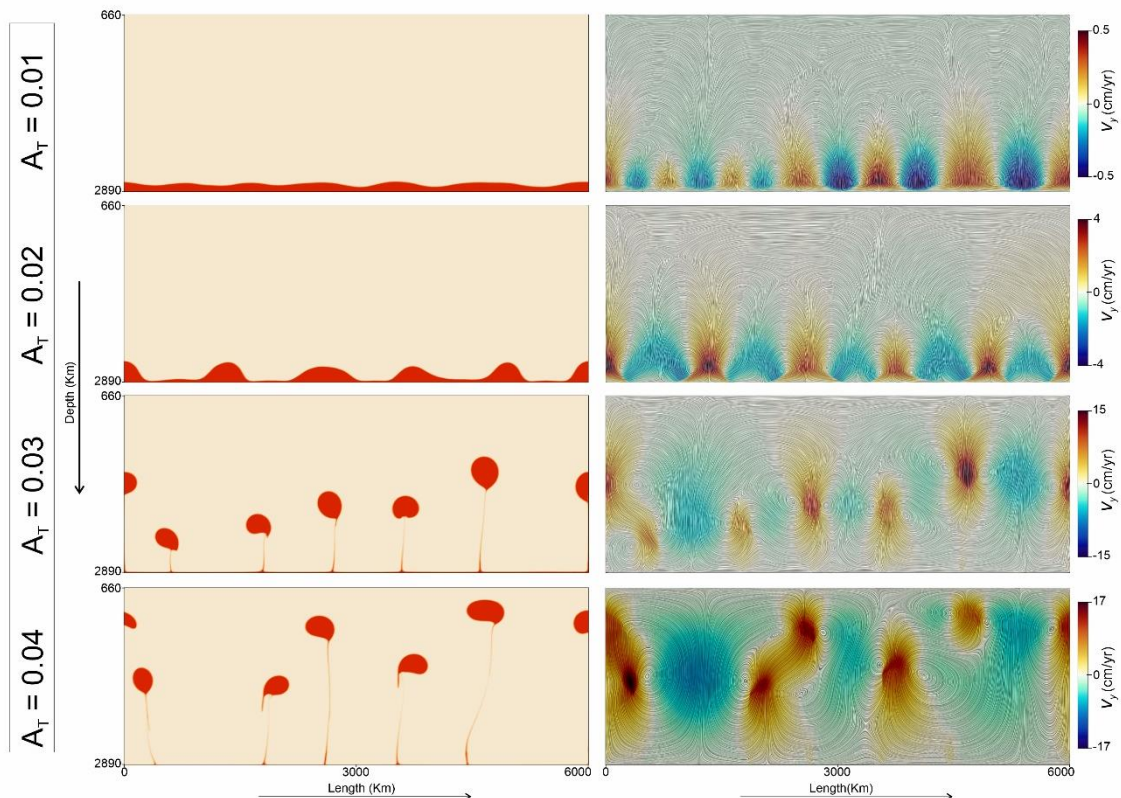
Figure 3.7: CFD simulations showing the effects of buoyancy factor (A_T) on a) Rayleigh-Taylor instability growth in the buoyant source layers (red colour) and b) the corresponding flow fields represented by streamlines. The colour contours depict the magnitudes of vertical velocity components. The snapshots of four different simulations presented in the row-wise panels correspond to a simulation time of 22 Ma.

form a typical head-tail structure of the plume at $t = {\sim}40$ Ma that continued to ascend vertically through the mantle layer. Increase in A_T greatly facilitates the RT instability growth as expected, and develops mature plume structures on much shorter time scales, for example, $t = {\sim}13$ Ma when $A_T = 0.03$. For a given simulation run time, the growth rate of instabilities increases with increasing A_T (Fig. 3.7), but showing little

variations in their wavelengths. Fig 3.10a and b present sets of graphical plots to show temporal variations of the ascent height of the fastest growing plumes and their ascent velocity, respectively as a function of A_T.

3.5.3   EFFECTS OF SOURCE-LAYER VISCOSITY

Another set of simulations is run by varying the viscosity ratio (μ^*) in the range $10^1 - 10^4$ for U^* =0, assigning A_T = 0.02. For a lower viscosity ratio (μ^* = 10^2), the
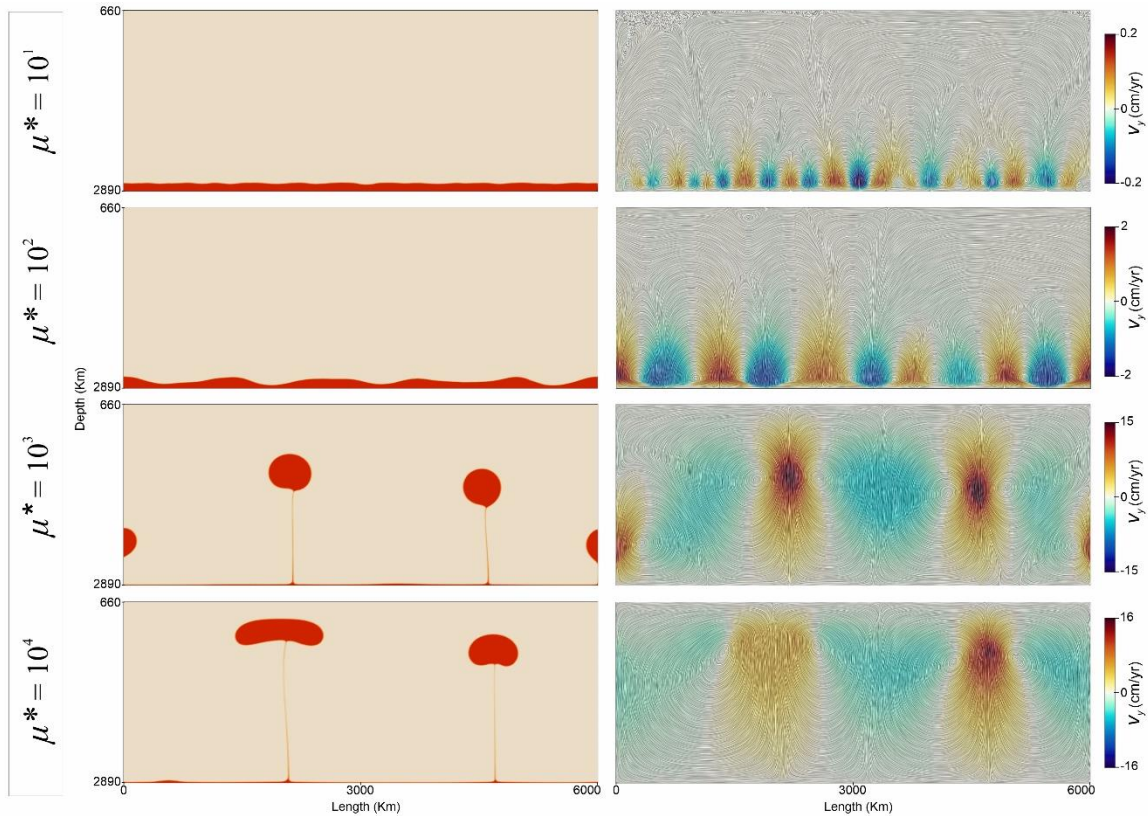
Figure 3.8: Effects of the normalized source-layer viscosity (μ^*) on a) Rayleigh-Taylor instability growth and b) the corresponding flow fields in CFD models. The colour contours depict the magnitudes of vertical velocity components. The snapshots of four different simulations presented in the row-wise panels correspond to a simulation time of 20 Ma.

instabilities are initiated with a non-dimensional wavelength, λ^* = 12 – 15, and they grow at significant rates (2 cm/yr) on a model run time, t = ~ 20 Ma (Fig. 3.8) and subsequently give rise to plume structures on a time scale of ~30 Ma. In addition to the fastest growing waves, several secondary waves evolve into plume structures at relatively shorter wavelengths (λ^* = 300 – 400).   Increase in μ^* facilitates the

instability growth rates and thereby reduces the time scale of plume formation (Fig. 3.8). For example, $\mu^* = 10^4$ yields fastest growing instabilities at $t = \sim 8$Ma, which form typical head-tail plume structures within a much shorter time scale ($t \sim 12$ Ma). The spacing of well-developed plumes calculated from these simulations show a nonlinear, but positive correlation with the overburden to source layer viscosity ratio (Fig. 3.9a). The effects of source-layer thickness, normalized to overburden thickness is also investigated, which reveals a similar increase of plume spacing with increasing source-layer thickness (Fig. 3.9b).
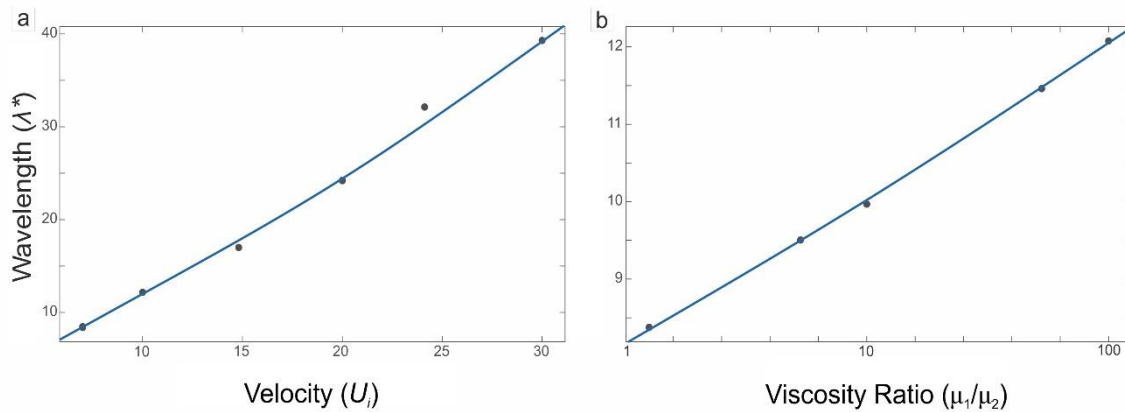
Figure 3.9: Normalized plume spacing as a function of (a) viscosity ratio (μ^*), and (b) normalized source layer thickness.

The vertical ascent height of plumes and their corresponding ascent velocities are summarily shown in graphic plots for different μ^* values (Figs. 3.10c, d). Interestingly, the inverse relations of plume ascent velocity with the source-layer viscosity obtained from the models have been reported in earlier studies (van Keken et al., 1997).
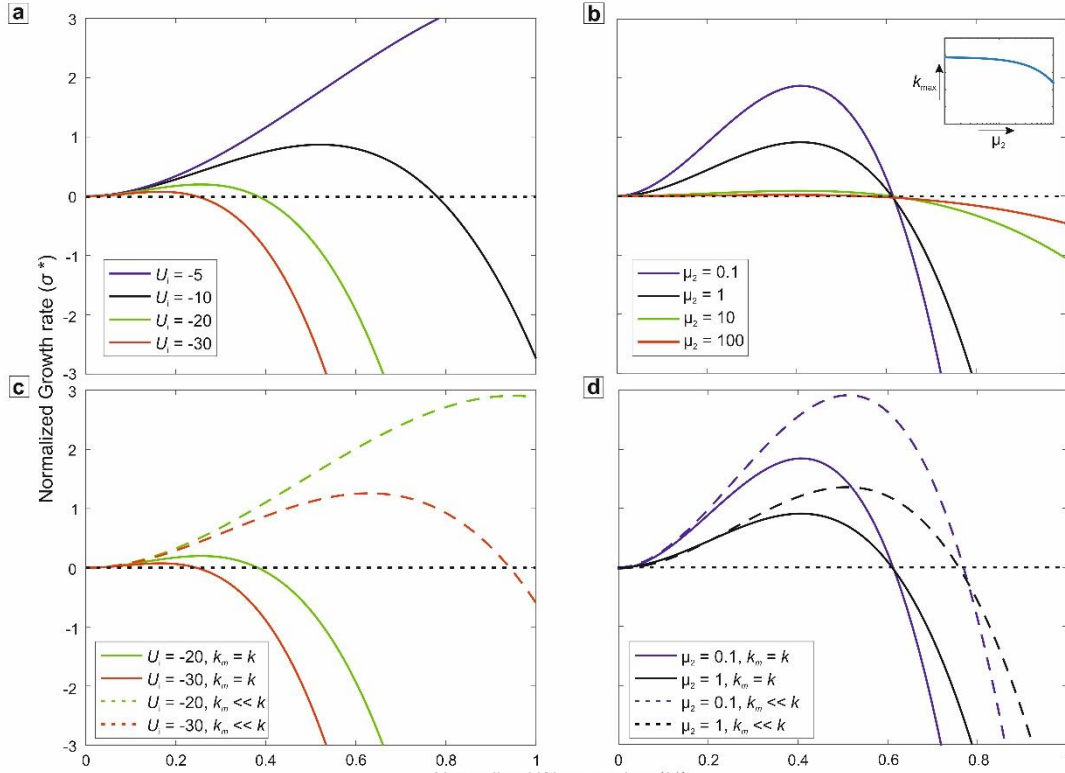
Figure 3.10: Time series analyses of the plume ascent heights and the vertical ascent velocities of the fastest growing instabilities for different A_T values in a) and b), keeping $\mu^* = 10^2$ and μ^* values in c) and d), keeping $A_T = 0.02$, respectively.

3.6. MODEL OUTCOMES: A SUMMARY

The model study primarily shows that an interface-parallel global flow velocity ((U^*) in horizontally stratified fluid layers of inverted densities significantly dampens the RT instabilities in the layered systems, where their growth rate is found to be inversely related to U^*. Under a given set of physical parameters, e.g., $A_T = 0.03$, $\mu^* = 10^2$, and $h_2 = 100km$, $U^* \geq 18$ can noticeably dampen the growth of RT instabilities, which completely cease to amplify into a plume structure at a threshold value of U^*. The model parameters chosen in this study yield the threshold $U^* = \sim 36$ (Fig. 4a, b). It is noteworthy that the threshold magnitude depends on the physical setting of the layered system defined by various parameters, such as Atwood number (A_T), viscosity ratio, source-layer thickness and initial geometrical heterogeneities (ΔA) at the layer interface. As an example, for a system with large value of A_T, a much higher threshold

U^* value is required to absolutely dampen the instability growth. Similar effects can occur in case of a layer system containing high-amplitude interfacial perturbations (i.e., large ΔA values). The CFD simulations also demonstrate that increase in either A_T or μ^* promotes the growth rate of a deep-source plume (Figs. **). Thus, for a mechanical setting with $A_T = 0.01$ and $\mu^* = 10^1$, instabilities that can amplify at a velocity of $\sim$0.2-0.3 cm/yr in a rest mantle condition, are effectively suppressed if the mantle flows attain a threshold condition ($U^* \geq 36$, i.e., 7-10 cm/yr in the absolute scale). This RT instability mechanics is applicable to several geodynamic settings, which is discussed in detail in context of the problem of unusually large inter-hotspot spacing in the next chapter, providing a new conceptual framework for the origin of sporadically distributed hotspots from deep-mantle sources.

Physical Variable	Symbol
Source-layer thickness	h_2
Overburden-layer thickness	h_1
Density of thin-layer	ρ_2
Density of Mantle	ρ_1
Density contrast	$\Delta\rho = (\rho_1 - \rho_2)$
Viscosity of thin-layer	μ_2
Viscosity of Mantle	μ_1
Horizontal velocity at the interface	U
Maximum horizontal flow at the interface	U_i
Normalized maximum horizontal flow at the interface	U_i^*
Strain rate	$\dot{\epsilon}$
Wavenumber of wave function	k_M
Wavenumber of perturbation	k
Angular frequency	ω
Growth rate	σ
Normalized growth rate	σ^*
Atwood Number	A_T
Total Pressure	P
Initial depth of the interface	D_o
Wavelength of initial perturbation	λ
Initial perturbation amplitude	ΔA
Top model-boundary velocity	U_i
Normalized top model-boundary velocity	U_i^*

Table 3.1: Different physical variables and their corresponding symbols used in this study.

APPENDIX A:

BENCHMARK 1: FALLING BLOCK EXPERIMENT

This straightforward benchmark test is performed to ensure the applicability of the UNDERWORLD2 code in numerical simulation of a mechanical system for a wide range of viscosity variations, comparing the velocity of an isolated square
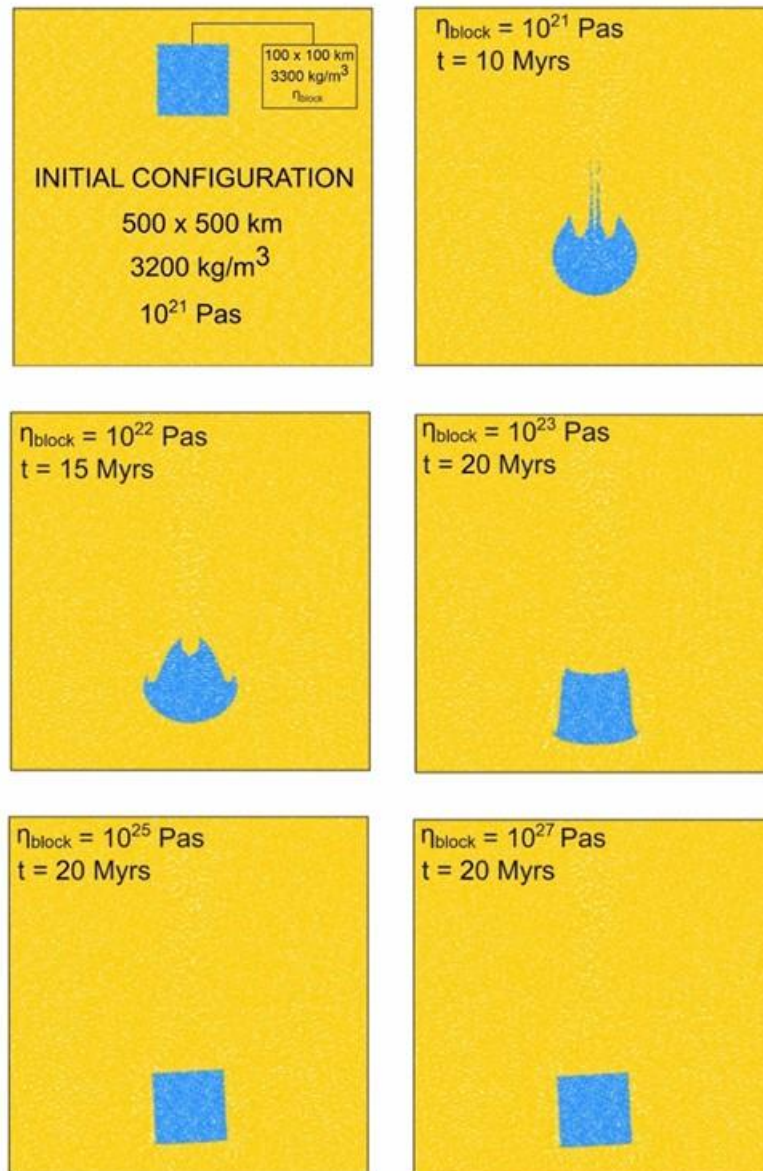
Figure A.1: Falling-block benchmark experiments. Initial model conditions are shown in the top left panel. Note that the degree of block deformation decreases with increasing block viscosity (indicated top left corner of each panel, which match well with the previous simulation results (Gerya, 2010; Thieulot, 2011)

viscous object (ρ_2, μ_{block}) of higher density that sinks in a low-viscosity medium of

lower density (ρ_1, μ_{medium}) under its own weigh. The numerical model domain represents a square with dimensions $L_x = L_y = 500$ km, where the square (100 km x 100 km) block is initially positioned with its centre at x = 250 km, y = 400 km (see Fig. A1). The simulation is carried out on a 51 x 51 elements grid, each element initially containing 30 x 30 particles. Free-slip boundary conditions are imposed on all sides of the model domain. The mechanical setting considered in this benchmark test differs from that of a benchmark test for Rayleigh – Taylor instabilities in a two-layer system. In the latter case the model has both the fluid layers extended to the model domain boundaries, whereas one-fluid object (denser in this case) is entirely surrounded by a lighter fluid in the falling block benchmark test.

The benchmark test results satisfy the following criteria: (i) reducing deformation of the block with increasing viscosity contrast (Fig. A1) and (ii) sinking velocity of the block being independent to its own viscosity at large viscosity ratios ($>10^4$), as performed in earlier benchmark studies (Gerya, 2019; Thieulot, 2011). The benchmark experiment thus validates the application of the UNDERWORLD2 code in the present study. This test also demonstrates the precision of the current numerical scheme, which is reflected in conservation of sharp initial edge/corner geometry of the object event after large deformations.

The benchmark tests were run on a wide range of the mechanical settings by varying the block viscosity, keeping the density ($\rho_1 = 3200$ kg/m^3) and viscosity (10^{21} Pa s) of the ambient medium constant. The details of following five experiments are presented in Fig. A1.

- ➢ Exp. 1: $\rho_2 = 3300$ kg/m^3, $\mu_2 = 10^{21}$ Pa s

➢ Exp. 2: ρ_2 = 3300 kg/m³, μ_2 = 10^{22} Pa s

➢ Exp. 3: ρ_2 = 3300 kg/m³, μ_2 = 10^{23} Pa s

➢ Exp. 4: ρ_2 = 3300 kg/m³, μ_2 = 10^{25} Pa s

➢ Exp. 5: ρ_2 = 3300 kg/m³, μ_2 = 10^{27} Pa s

From the numerical experiments, the block velocity is plotted as a function of the viscosity ratio ($\log \frac{\mu_{block}}{\mu_{medium}}$) (Fig. A2). The experimental data follow a well-defined characteristic curve, which further confirms the applicability of the UNDERWORLD2 code in accurately capturing the gravity driven motion of any object within a viscous medium on a wide spectrum of the mechanical setting.
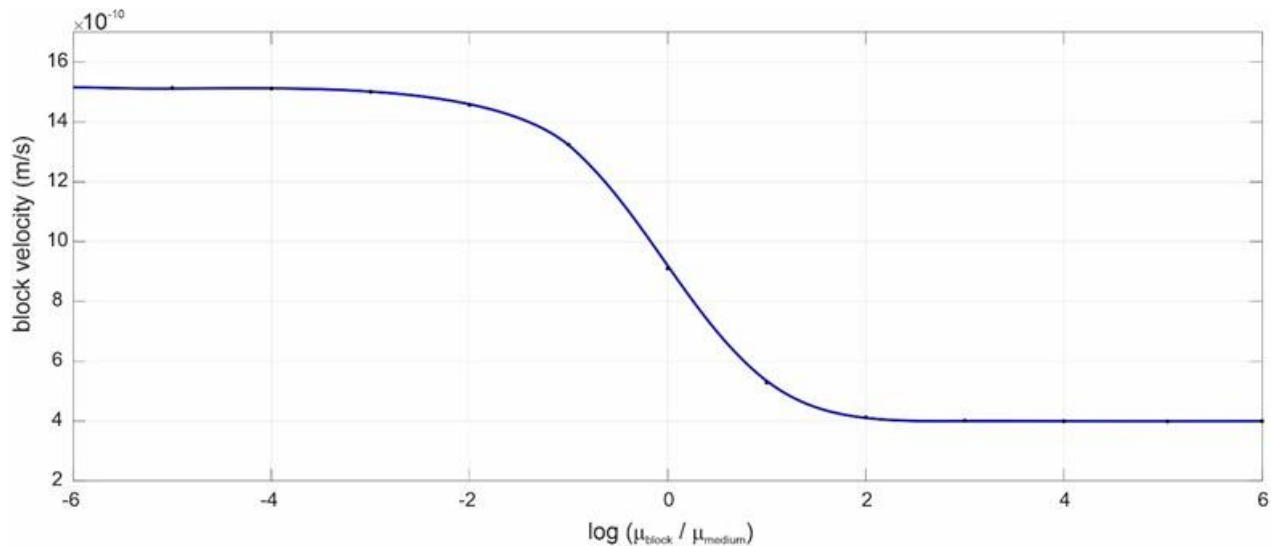
Figure A2: Calculated plot of the block-sinking velocity as a function of the block to host viscosity ratio ($\log \frac{\mu_{block}}{\mu_{medium}}$). This characteristic geometry of the curve is consistent with the available data (details in the text).

BENCHMARK 2: VAN KEKEN ET AL'S (1997) NUMERICAL EXPERIMENT

This benchmark test aims to reproduce the results of van Keken et al (1997), who validated numerical experiments on the Rayleigh-Taylor instability phenomenon in a two-layer fluid system with inverted density stratification (Fig. A3). They have used a range of numerical schemes, e.g., marker chain method. Several other authors

have also benchmarked this numerical problem using various techniques, such as tracers (Tackley and King, 2003), level set method (Hillebrand et al., 2014, Thieulot 2014), particle level set method (Samuel and Evonuk, 2010), phase field method (Bangerth and Heister, 2013). The present benchmark experiments consider nearly a square domain of unit height ($L_y = 1$) and a width (L_x) of 0.9142, containing a lighter viscous layer (ρ_2, μ_2) overlain by a denser layer (ρ_1, μ_1). The model introduces initial
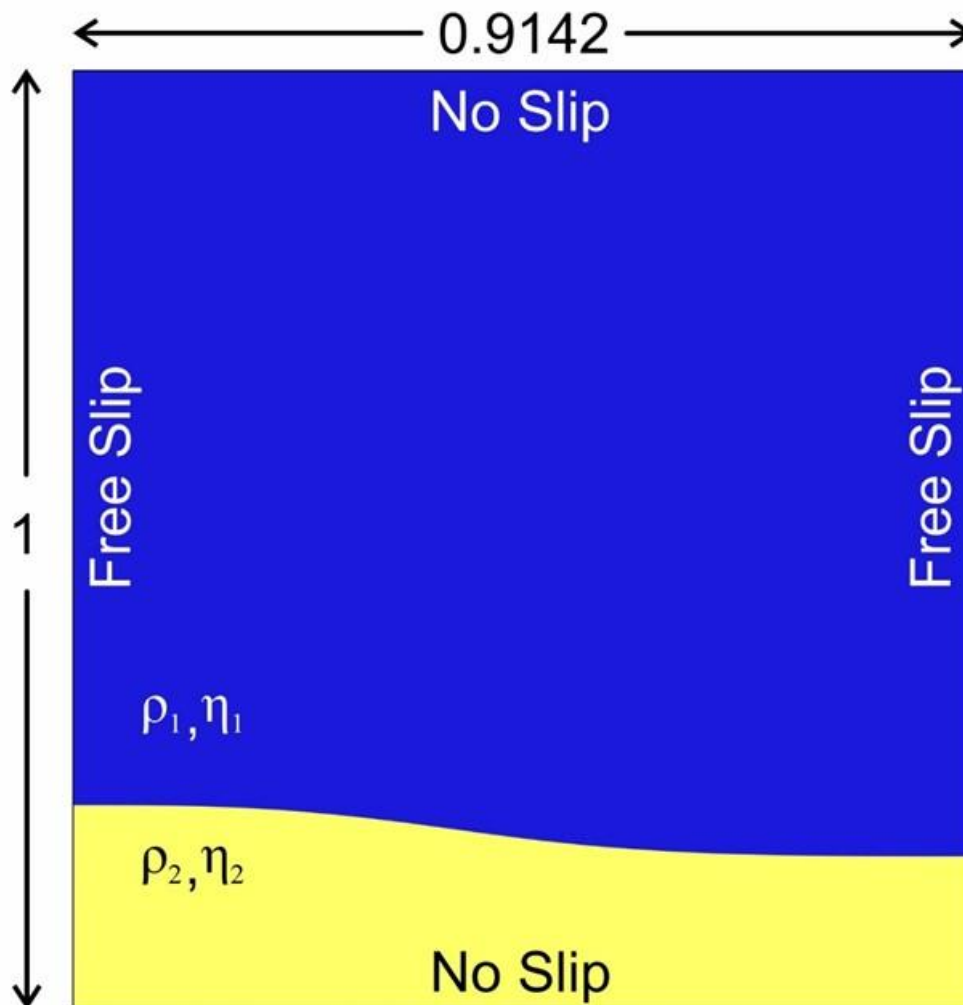
Figure A3: Initial model set-up and boundary conditions used for the Van Keken benchmark test.

geometrical perturbations at their interface in the form of waves defined by:

$$y(x) = 0.2 + 0.02\cos\left(\frac{\pi x}{\lambda}\right), \qquad (A2.1)$$

where λ (= 0.9142) denotes the wavelength of perturbations. The bottom lighter fluid is assigned density (ρ_2) = 1000 and viscosity (μ_2) = 100, and the density of the top heavier layer, ρ_1 = 1010, keeping $\mu_1 = \mu_2$. No-slip conditions are applied at the bottom and top boundaries of the box, whereas free-slip boundary conditions are imposed on both the lateral sides. In this benchmark study, a series of snapshots of the material field were taken at regular intervals to compare the corresponding results with those of van Keken et al., 1997. This study also compares the evolution of the root mean square velocity (v_{rms}) of the entire domain over time, specifically concentrating on the timing and the corresponding height of the first peak, which coincides with the rise of the first diapir. The v_{rms} of the system is given by,

$$v_{rms} = \sqrt{\frac{1}{V} \int \|v\|^2 \, dv}, \qquad\qquad (\text{A2.2})$$

 where V is the domain volume.

Method (Code)	Grid	Time	v_{rms} (max)	Source
Tracers (ELEFANT)	400x400	208.7	0.003093	Thieulot (2014)
Marker Chain	30x30	213.38	0.00300	PvK in Van Keken et al. (1997)
	50x50	211.81	0.003016	
	80x80	210.75	0.003050	
Particle-in-cell FEM	512x512	210.165	0.003102	This Study
	256x256	211.165	0.003107	
	128x128	214.124	0.003120	
	32x32	227.53	0.003144	

Table A1: Comparison of v_{rms}– model run time values obtained from different numerical methods.

T The time evolution of a system, obtained from the benchmark experiments, is shown in Fig. A4. The long-wavelength perturbations on the initial interface (Eq.
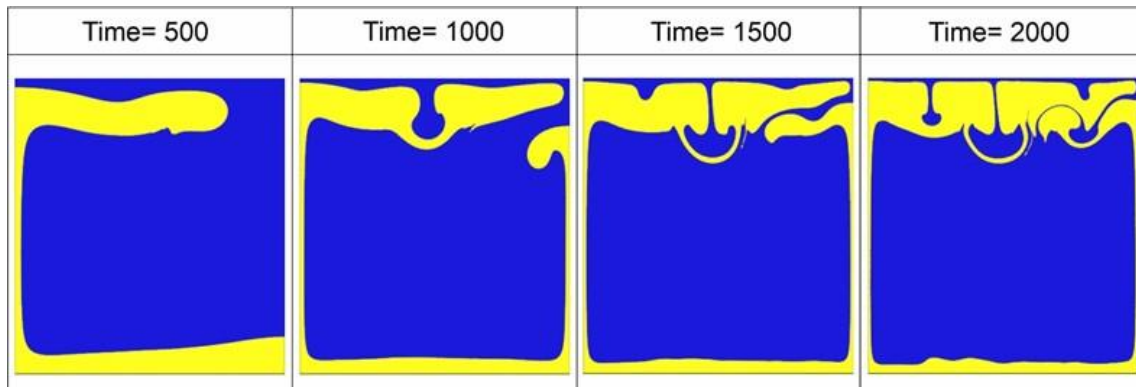
Figure A4: Time-series simulations of the Rayleigh-Taylor instabilities in the van Keken benchmark test with viscosity ratio = 1 (model run time indicated at the top of each panel).

A2.1) selectively grow and determine the rise of the first plume along the left edge of the domain (Fig. A4), followed by the rise of a second plume on the right edge. The benchmark test finally yields the evolved interface between the two fluids on a simulation run time, t = 2000 (Fig.A4), which closely matches with that of van Keken et al. (1997) shown in their Figure 2. Table A1 shows the comparison between
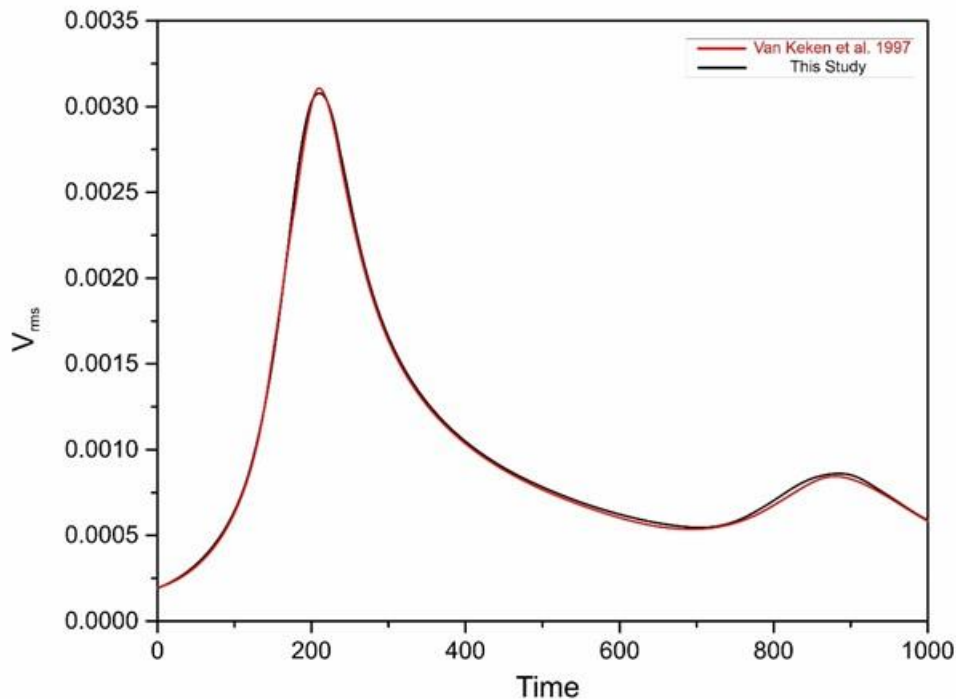
Figure A5: Comparison of the present van Keken test results (black) with the earlier plot (red line) given by van Keken et al., (1997). V_{rms} denotes the root mean square velocity.

v_{rms}/time values for different numerical methods. Fig. A5 presents the v_{rms} measurements for a 512 × 512 grids simulation, providing a comparison with those of van Keken et al. (1997). It is to note that the calculated curves match well in terms of the position and height of the peaks with theirs.

BENCHMARK 3: RAYLEIGH-TAYLOR INSTABILITY EXPERIMENT

This benchmark test is run based on the analytical solution of Ramberg (1968), which has been extensively used in numerical modelling (Gerya, 2009; Thieulot, 2011). The numerical model setup consists of an initial sinuous wave of geometrical perturbation
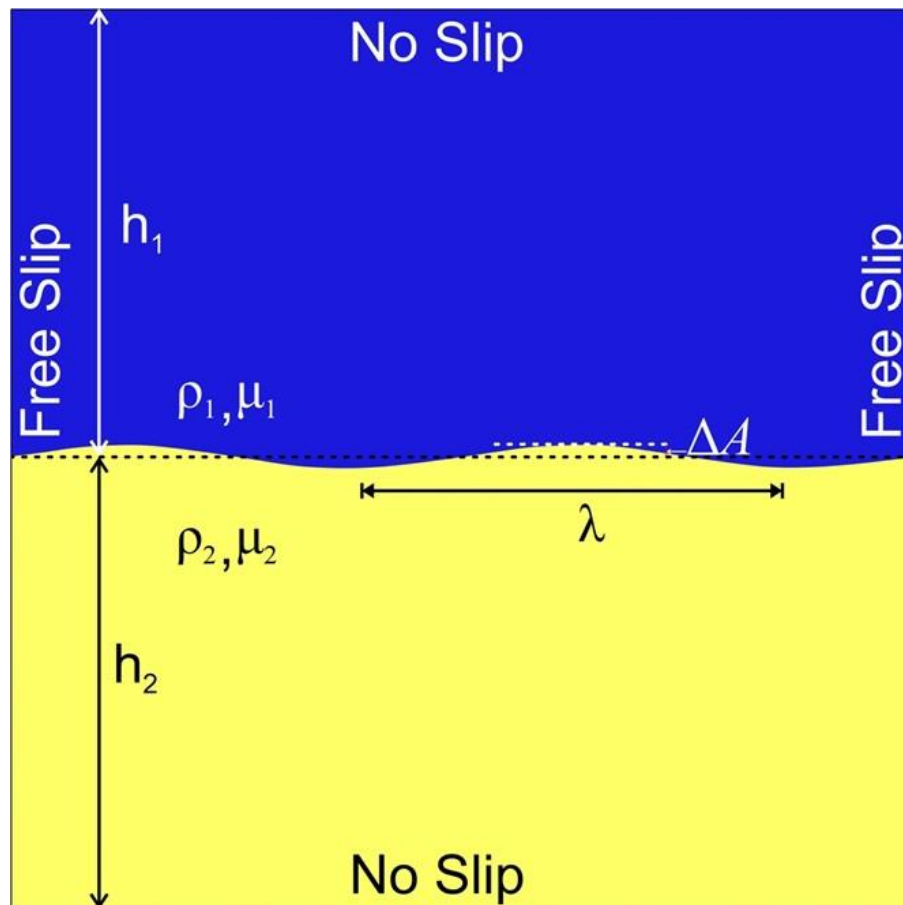
Figure A6: Initial model configuration and boundary conditions chosen for the Rayleigh-Taylor Instability benchmark test.

with a small initial amplitude (ΔA) and a wavelength ($\lambda = \frac{L_x}{2}$) at the boundary between the two layers (upper (μ_1, ρ_1) and lower (μ_2, ρ_2)) of thicknesses h_1 and h_2, respectively.

APPENDIX A:

A no-slip boundary condition is imposed at the top and the bottom of the box, while a free-slip condition on the lateral side walls. This study considers: ρ_1 = 3300 kg/m³, ρ_2 = 3300 kg/m³, μ_1 = 10^{21} Pa s, 10^{19} Pa s < μ_2 < 10^{27} Pa s, $h_1 + h_2 = L_y = 500$ km, similar to those used in Thieulot (2011).

After Ramberg's solution, the velocity of diapiric growth (v_y) follows,

$$\frac{v_y}{\Delta A} = -K \frac{\rho_1 - \rho_2}{2\mu_2} h_2 g ,\qquad\text{(A6)}$$

where the non-dimensional growth factor $(K) = -\dfrac{a_{12}}{b_{11}j_{22} - a_{12}i_{21}}$, and

$$\omega_1 = \frac{2\pi h_1}{\lambda} , \qquad \omega_2 = \frac{2\pi h_2}{\lambda},$$

$$b_{11} = \frac{\mu_1 2\omega_1{}^2}{\mu_2 \left(\cosh 2\omega_1 - 1 - 2\omega_1{}^2\right)} - \frac{2\omega_2{}^2}{\cosh 2\omega_2 - 1 - 2\omega_2{}^2},$$

$$a_{12} = \frac{\mu_1 (\sinh 2\omega_1 - 2\omega_1)}{\mu_2 \left(\cosh 2\omega_1 - 1 - 2\omega_1{}^2\right)} - \frac{\sinh 2\omega_2 - 2\omega_2}{\cosh 2\omega_2 - 1 - 2\omega_2{}^2},$$

$$i_{21} = \frac{\mu_1 \omega_2 (\sinh 2\omega_1 - 2\omega_1)}{\mu_2 \left(\cosh 2\omega_1 - 1 - 2\omega_1{}^2\right)} + \frac{\omega_2 (\sinh 2\omega_2 + 2\omega_2)}{\cosh 2\omega_2 - 1 - 2\omega_2{}^2},$$

$$j_{22} = \frac{\mu_1 2\omega_1{}^2 \omega_2}{\mu_2 (\cosh 2\omega_1 - 1 - 2\omega_1{}^2)} + \frac{2\omega_2{}^3}{\cosh 2\omega_2 - 1 - 2\omega_2{}^2},$$
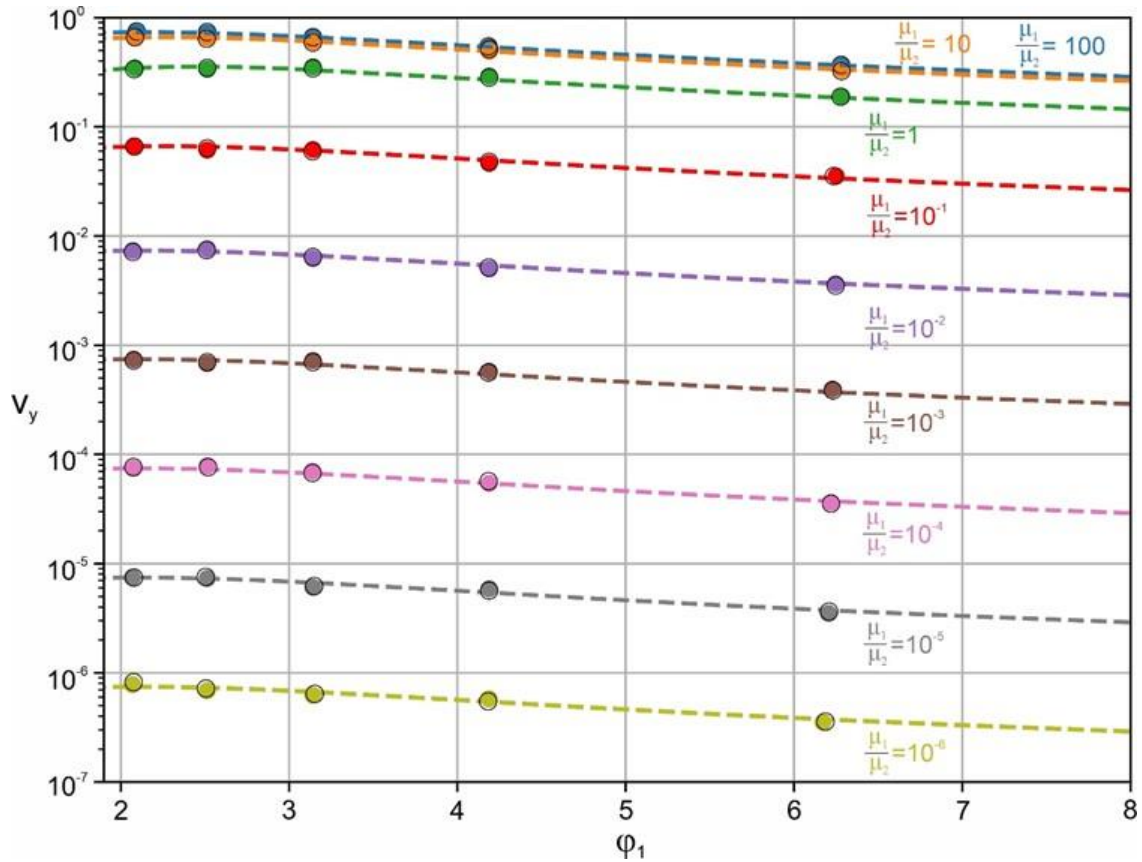
Figure A7: A comparative analysis of the present benchmark test results (symbols) for two different initial amplitudes (ΔA = s_y, ΔA = $\frac{s_y}{3}$) and the Ramberg's analytical solutions (dashed lines).

L_x is varied between 500 and 1500 km, leading to $\frac{2\pi}{3} \leq \omega_1 \leq 2\pi$. g is the acceleration due to gravity.

The benchmark test was run with a constant resolution of 75 x 75 elements for all the simulations. Two sets of measurements were measured, considering the perturbation amplitude: 1) $\Delta A = s_y$ and 2) $\Delta A = \frac{s_y}{3}$, where s_y ($=s_x$) is the size of an element. The results are presented in Fig. A7, which clearly reveals that, over a wide range of the viscosity ratio, the present model estimates agree well with the values obtained from the analytical solution (Eq. A3.1). This match validates the application

85

of the UNDERWORLD2 code to model the velocity fields of gravity driven flows in a

system with sharp and strong viscosity variations.

3.7 REFERENCES

Ballmer, M. D., Ito, G., van Hunen, J., & Tackley, P. J. (2011). Spatial and temporal variability in Hawaiian hotspot volcanism induced by small-scale convection. *Nature Geoscience 2011 4:7*, *4*(7), 457–460. https://doi.org/10.1038/ngeo1187

Bekaert, D. v., Gazel, E., Turner, S., Behn, M. D., de Moor, J. M., Zahirovic, S., Manea, V. C., Hoernle, K., Fischer, T. P., Hammerstrom, A., Seltzer, A. M., Kulongoski, J. T., Patel, B. S., Schrenk, M. O., Halldórsson, S. A., Nakagawa, M., Ramírez, C. J., Krantz, J. A., Yücel, M., … Barry, P. H. (2021). High 3He/4He in central Panama reveals a distal connection to the Galapagos plume. *Proceedings of the National Academy of Sciences of the United States of America*, *118*(47), e2110997118. https://doi.org/10.1073/PNAS.2110997118/SUPPL_FILE/PNAS.2110997118.SD03.XLSX

Bercovici, D., & Kelly, A. (1997). The non-linear initiation of diapirs and plume heads. *Physics of the Earth and Planetary Interiors*, *101*(1–2). https://doi.org/10.1016/S0031-9201(96)03217-7

Black, B. A., Karlstrom, L., & Mather, T. A. (2021). The life cycle of large igneous provinces. *Nature Reviews Earth & Environment 2021 2:12*, *2*(12), 840–857. https://doi.org/10.1038/s43017-021-00221-4

Brunet, D., & Yuen, D. A. (2000). Mantle plumes pinched in the transition zone. *Earth and Planetary Science Letters*, *178*(1–2), 13–27. https://doi.org/10.1016/S0012-821X(00)00063-7

Bryan, S. E., & Ernst, R. E. (2008). Revised definition of Large Igneous Provinces (LIPs). *Earth-Science Reviews*, *86*(1–4), 175–202. https://doi.org/10.1016/J.EARSCIREV.2007.08.008

Burke, K., Steinberger, B., Torsvik, T. H., & Smethurst, M. A. (2008). Plume Generation Zones at the margins of Large Low Shear Velocity Provinces on the core–mantle boundary. *Earth and Planetary Science Letters*, *265*(1–2), 49–60. https://doi.org/10.1016/J.EPSL.2007.09.042

Campbell, I. H. (2007). Testing the plume theory. *Chemical Geology*, *241*(3–4), 153–176. https://doi.org/10.1016/J.CHEMGEO.2007.01.024

Cathles, L. M. (1975). The viscosity of the earth's mantle. *Published in* ***1975*** *in Princeton NJ) by Princeton University Press*, 413. https://lib.ugent.be/catalog/rug01:001350016

Čížková, H., van den Berg, A. P., Spakman, W., & Matyska, C. (2012). The viscosity of Earth's lower mantle inferred from sinking speed of subducted lithosphere. *Physics of the Earth and Planetary Interiors*, *200–201*, 56–62. https://doi.org/10.1016/J.PEPI.2012.02.010

Coffin, M. F., & Eldholm, O. (1992). Volcanism and continental break-up: A global compilation of large igneous provinces. *Geological Society Special Publication*, *68*, 17–30. https://doi.org/10.1144/GSL.SP.1992.068.01.02

REFERENCE

Coffin, M. F., & Eldholm, O. (1994). Large igneous provinces: Crustal structure, dimensions, and external consequences. *Reviews of Geophysics*, *32*(1), 1–36. https://doi.org/10.1029/93RG02508

Davaille, A., Carrez, P., & Cordier, P. (2018). Fat Plumes May Reflect the Complex Rheology of the Lower Mantle. *Geophysical Research Letters*, *45*(3), 1349–1354. https://doi.org/10.1002/2017GL076575

Davaille, A., & Vatteville, J. (2005). On the transient nature of mantle plumes. *Geophysical Research Letters*, *32*(14), 1–4. https://doi.org/10.1029/2005GL023029

Davies, D. R., Goes, S., Davies, J. H., Schuberth, B. S. A., Bunge, H. P., & Ritsema, J. (2012). Reconciling dynamic and seismic models of Earth's lower mantle: The dominant role of thermal heterogeneity. *Earth and Planetary Science Letters*, *353–354*, 253–269. https://doi.org/10.1016/J.EPSL.2012.08.016

Davies, G. F. (2005). A case for mantle plumes. In *Chinese Science Bulletin* (Vol. 50, Issue 15, pp. 1541–1554). https://doi.org/10.1360/982005-918

Doornbos, D. J., Spiliopoulos, S., & Stacey, F. D. (1986). Seismological properties of D″ and the structure of a thermal boundary layer. *Physics of the Earth and Planetary Interiors*, *41*(4), 225–239. https://doi.org/10.1016/0031-9201(86)90002-6

Evans, M., Harlow, F., & Bromberg, E. (1957). *The Particle-In-Cell Method for Hydrodynamic Calculations*. https://apps.dtic.mil/sti/citations/ADA384618

Farnetani, C. G., Hofmann, A. W., Duvernay, T., & Limare, A. (2018). Dynamics of rheological heterogeneities in mantle plumes. *Earth and Planetary Science Letters*, *499*, 74–82. https://doi.org/10.1016/j.epsl.2018.07.022

Farnetani, C. G., & Richards, M. A. (1994). Numerical investigations of the mantle plume initiation model for flood basalt events. *Journal of Geophysical Research: Solid Earth*, *99*(B7), 13813–13833. https://doi.org/10.1029/94JB00649

Foulger, G. R., Fitton, J. G., Presnall, D. C., & Morgan, W. J. (2006). The great plume debate. *Eos, Transactions American Geophysical Union*, *87*(7), 76–80. https://doi.org/10.1029/2006EO070004

Frazer, W. D., & Korenaga, J. (2022). Dynamic topography and the nature of deep thick plumes. *Earth and Planetary Science Letters*, *578*. https://doi.org/10.1016/j.epsl.2021.117286

Gerya, T. (2009). Introduction to numerical geodynamic modelling. In *Introduction to Numerical Geodynamic Modelling* (Vol. 9780521887540). https://doi.org/10.1017/CBO9780511809101

Gerya, T. (2019). INTRODUCTION TO NUMERICAL GEODYNAMIC MODELLING, Second Edition. In *Introduction to Numerical Geodynamic Modelling, Second Edition*. https://doi.org/10.1017/9781316534243

Gerya, T. v., & Yuen, D. A. (2003). Rayleigh–Taylor instabilities from hydration and melting propel 'cold plumes' at subduction zones. *Earth and Planetary Science Letters*, *212*(1–2), 47–62. https://doi.org/10.1016/S0012-821X(03)00265-6

Ghosh, D., Maiti, G., Mandal, N., & Baruah, A. (2020). Cold Plumes Initiated by Rayleigh-Taylor Instabilities in Subduction Zones, and Their Characteristic Volcanic Distributions: The Role of Slab Dip. *Journal of Geophysical Research: Solid Earth*, *125*(8). https://doi.org/10.1029/2020JB019814

Griffiths, R. W., & Richards, M. A. (1989). The adjustment of mantle plumes to changes in plate motion. *Geophysical Research Letters*, *16*(5), 437–440. https://doi.org/10.1029/GL016I005P00437

Herzberg, C., & Gazel, E. (2009). Petrological evidence for secular cooling in mantle plumes. *Nature 2009 458:7238*, *458*(7238), 619–622. https://doi.org/10.1038/nature07857

Jarvis, G. T., & Peltier, W. R. (1982). Mantle convection as a boundary layer phenomenon. *Geophysical Journal International*, *68*(2), 389–427. https://doi.org/10.1111/J.1365-246X.1982.TB04907.X

Jellinek, A. M., Lenardic, A., & Manga, M. (2002). The influence of interior mantle temperature on the structure of plumes: Heads for Venus, Tails for the Earth. *Geophysical Research Letters*, *29*(11), 27–1. https://doi.org/10.1029/2001GL014624

Jellinek, A. M., & Manga, M. (2004). LINKS BETWEEN LONG-LIVED HOT SPOTS, MANTLE PLUMES, D″, AND PLATE TECTONICS. *Reviews of Geophysics*, *42*(3). https://doi.org/10.1029/2003RG000144

Jones, T. D., Davies, D. R., Campbell, I. H., Wilson, C. R., & Kramer, S. C. (2016). Do mantle plumes preserve the heterogeneous structure of their deep-mantle source? *Earth and Planetary Science Letters*, *434*, 10–17. https://doi.org/10.1016/j.epsl.2015.11.016

Kerr, R. C., Lister, J. R., Kerr, R. C., & Lister, J. R. (2008). Rise and deflection of mantle plume tails. *Geochemistry, Geophysics, Geosystems*, *9*(10), 10004. https://doi.org/10.1029/2008GC002124

Kerr, R. C., & Mériaux, C. (2004). Structure and dynamics of sheared mantle plumes. *Geochemistry, Geophysics, Geosystems*, *5*(12). https://doi.org/10.1029/2004GC000749

Koppers, A. A. P., Becker, T. W., Jackson, M. G., Konrad, K., Müller, R. D., Romanowicz, B., Steinberger, B., & Whittaker, J. M. (2021). Mantle plumes and their role in Earth processes. *Nature Reviews Earth & Environment 2021 2:6*, *2*(6), 382–401. https://doi.org/10.1038/s43017-021-00168-6

Korenaga, J. (2005a). Firm mantle plumes and the nature of the core-mantle boundary region. *Earth and Planetary Science Letters*, *232*(1–2), 29–37. https://doi.org/10.1016/j.epsl.2005.01.016

Korenaga, J. (2005b). Firm mantle plumes and the nature of the core-mantle boundary region. *Earth and Planetary Science Letters*. https://doi.org/10.1016/j.epsl.2005.01.016

Kumagai, I., Davaille, A., & Kurita, K. (2007). On the fate of thermally buoyant mantle plumes at density interfaces. *Earth and Planetary Science Letters*, *254*(1–2), 180–193. https://doi.org/10.1016/J.EPSL.2006.11.029

Lay, T., Williams, Q., & Garnero, E. J. (1998). The core–mantle boundary layer and deep Earth dynamics. *Nature 1998 392:6675*, *392*(6675), 461–468. https://doi.org/10.1038/33083

Li, M., & Zhong, S. (2017). The source location of mantle plumes from 3D spherical models of mantle convection. *Earth and Planetary Science Letters*, *478*, 47–57. https://doi.org/10.1016/J.EPSL.2017.08.033

Lowman, J. P., King, S. D., & Gable, C. W. (2004). Steady plumes in viscously stratified, vigorously convecting, three-dimensional numerical mantle convection models with mobile plates. *Geochemistry, Geophysics, Geosystems*, *5*(1). https://doi.org/10.1029/2003GC000583

Mansour, J., Giordani, J., Moresi, L., Beucher, R., Kaluza, O., Velic, M., Farrington, R., Quenette, S., & Beall, A. (2020). Underworld2: Python Geodynamics Modelling for Desktop, HPC and Cloud. *Journal of Open Source Software*, *5*(47), 1797. https://doi.org/10.21105/joss.01797

Montague, N. L., & Kellogg, L. H. (2000). Numerical models of a dense layer at the base of the mantle and implications for the geodynamics of D″. *Journal of Geophysical Research: Solid Earth*, *105*(B5), 11101–11114. https://doi.org/10.1029/1999jb900450

Moresi, L., Quenette, S., Lemiale, V., Mériaux, C., Appelbe, B., & Mühlhaus, H. B. (2007). Computational approaches to studying non-linear dynamics of the crust and mantle. *Physics of the Earth and Planetary Interiors*. https://doi.org/10.1016/j.pepi.2007.06.009

Morgan, W. J. (1971). Convection Plumes in the Lower Mantle. *Nature 1971 230:5288*, *230*(5288), 42–43. https://doi.org/10.1038/230042a0

Morgan, W. J. (1972a). Deep Mantle Convection Plumes and Plate Motions. *AAPG Bulletin*, *56*(2), 203–213. http://archives.datapages.com/data/bulletns/1971-73/data/pg/0056/0002/0200/0203.htm

Morgan, W. J. (1972b). Plate Motions and Deep Mantle Convection. *Memoir of the Geological Society of America*, *132*, 7–22. https://doi.org/10.1130/MEM132-P7

Nipin, L., & Tomar, G. (2015). Effect of viscosity contrast on plume formation in density stratified fluids. *Chemical Engineering Science*, *134*, 510–520. https://doi.org/10.1016/j.ces.2015.05.044

Nolet, G., Allen, R., & Zhao, D. (2007). Mantle plume tomography. *Chemical Geology*, *241*(3–4), 248–263. https://doi.org/10.1016/J.CHEMGEO.2007.01.022

Olson, P., & Singer, H. (1985). Creeping plumes. *Journal of Fluid Mechanics*, *158*. https://doi.org/10.1017/S0022112085002749

Ribe, N. M., & Christensen, U. R. (1999). The dynamical origin of Hawaiian volcanism. *Earth and Planetary Science Letters*, *171*(4), 517–531. https://doi.org/10.1016/S0012-821X(99)00179-X

Richards, M. A., & Griffiths, R. W. (1989). Thermal entrainment by deflected mantle plumes. *Nature 1989 342:6252*, *342*(6252), 900–902. https://doi.org/10.1038/342900a0

Richards, M. A., & Hager, B. H. (1984). Geoid anomalies in a dynamic earth. *J. Geophys. Res.*, *89*(B7), 5987–6002. https://doi.org/10.1029/jb089ib07p05987

Roy, A., Roy, N., Saha, P., & Mandal, N. (2021). Factors Determining Shear-Parallel Versus Low-Angle Shear Band Localization in Shear Deformations: Laboratory Experiments and Numerical Simulations. *Journal of Geophysical Research: Solid Earth*, *126*(10), e2021JB022578. https://doi.org/10.1029/2021JB022578

Saunders, A. D., Jones, S. M., Morgan, L. A., Pierce, K. L., Widdowson, M., & Xu, Y. G. (2007). Regional uplift associated with continental large igneous provinces: The roles of mantle plumes and the lithosphere. *Chemical Geology*, *241*(3–4), 282–318. https://doi.org/10.1016/J.CHEMGEO.2007.01.017

Schilling, J. G. (1991). Fluxes and excess temperatures of mantle plumes inferred from their interaction with migrating mid-ocean ridges. *Nature 1991 352:6334*, *352*(6334), 397–403. https://doi.org/10.1038/352397a0

Spada, G., Yuen, D. A., Sabadini, R., & Boschi, E. (1991). Lower-mantle viscosity constrained by seismicity around deglaciated regions. *Nature 1991 351:6321*, *351*(6321), 53–55. https://doi.org/10.1038/351053a0

Spiliopoulos, S., & Stacey, F. D. (1984). The earth's thermal profile: Is there a mid-mantle thermal boundary layer? *Journal of Geodynamics*, *1*(1), 61–77. https://doi.org/10.1016/0264-3707(84)90006-1

Stacey, F. D., & Loper, D. E. (1983). The thermal boundary-layer interpretation of D″ and its role as a plume source. *Physics of the Earth and Planetary Interiors*, *33*(1), 45–55. https://doi.org/10.1016/0031-9201(83)90006-7

Steinberger, B., & O'Connell, R. J. (1998). Advection of plumes in mantle flow: Implications for hotspot motion, mantle viscosity and plume distribution. *Geophysical Journal International*, *132*(2), 412–434. https://doi.org/10.1046/j.1365-246x.1998.00447.x

Styles, E., Goes, S., van Keken, P. E., Ritsema, J., & Smith, H. (2011). Synthetic images of dynamically predicted plumes and comparison with a global tomographic model. *Earth and Planetary Science Letters*, *311*(3–4), 351–363. https://doi.org/10.1016/J.EPSL.2011.09.012

Thieulot, C. (2011). FANTOM: Two- and three-dimensional numerical modelling of creeping flows for the solution of geological problems. *Physics of the Earth and Planetary Interiors*, *188*(1–2). https://doi.org/10.1016/j.pepi.2011.06.011

Thieulot, C. (2014). ELEFANT: a user-friendly multipurpose geodynamics code. *Solid Earth Discussions*, *6*(2).

van Keken, P. E., King, S. D., Schmeling, H., Christensen, U. R., Neumeister, D., & Doin, M.-P. (1997). A comparison of methods for the modeling of thermochemical convection. *Journal of Geophysical Research: Solid Earth*, *102*(B10), 22477–22495. https://doi.org/10.1029/97jb01353

Whitehead, J. A., & Luther, D. S. (1975). Dynamics of laboratory diapir and plume models. *Journal of Geophysical Research*, *80*(5). https://doi.org/10.1029/jb080i005p00705

Zhong, S., & Watts, A. B. (2002). Constraints on the dynamics of mantle plumes from uplift of the Hawaiian Islands. *Earth and Planetary Science Letters*, *203*(1), 105–116. https://doi.org/10.1016/S0012-821X(02)00845-2

Chapter 4.

EFFECTS OF GLOBAL FLOWS ON MANTLE PLUME GROWTH: THEORY

4.1. THEORETICAL FRAMEWORK OF RAYLEIGH-TAYLOR INSTABILITY

Rayleigh-Taylor (RT) instability, primarily driven by gravitational forces in inverted density stratification (i.e., a heavy fluid resting upon a relatively light fluid), governs a wide range of atmospheric and oceanic processes, e.g., global air circulation, cloud formation, oceanic currents as well as many interstellar, and planetary phenomena, e.g., supernova explosion and silicate-metal segregation. Lord Rayleigh and G.I. Taylor first theorized the RT instability growth rate from a linear stability analysis, considering the effects of inertial and body forces between two immiscible inviscid fluids (Rayleigh, 1882; Taylor, 1950). Since then, the RT theory continued to proliferate in diverse directions (Zhou, 2017a, 2017b; Zhou et al., 2019, 2021) with the addition of more and more physical variables, like surface tension (Mikaelian, 1996; Pullin, 1982), density gradient (Munro, 1988; Song et al., 2021), diffusion (Masse, 2007), temperature gradient and mass transfer (Gerashchenko & Livescu, 2016), effect of rotation (Baldwin et al., 2015) and magnetic field (Zrnić & Hendricks, 2003) to the theoretical treatment. A category of these variables (density gradient, temperature gradient, mass transfer, and diffusion) facilitates the growth of instabilities, whereas the others (surface tension, magnetic field, and rotational forces), in contrast, act as dampening agencies. A complete theory thus demands an account of both the driving and dampening factors to predict the dynamics of gravitational instabilities in natural systems as well as practical applications. The RT instability mechanics has been also extensively applied in solid earth geophysics to

theorize many important geodynamic processes (Turcotte & Schubert, 2002), such as salt dome formation in sedimentary basins (Louis-Napoleon et al., 2022; Miller & Behn, 2012; Ramberg, 1968a, 1968b, 1972), magma transport (Whitehead, 1986; Wilcock & Whitehead, 1991), intraplate orogenic collapse (Louis-Napoléon et al., 2020; Neil & Houseman, 1999), downwelling at the lithospheric base (Conrad & Molnar, 1997; Houseman & Molnar, 1997), silicate mantle-metallic core segregation in the Earth (Ida et al., 1987; Mondal & Korenaga, 2018). The success of these applications has greatly widened the research scope of mantle dynamics in the light of gravitational instabilities.

Several geological and geophysical phenomena, such as emplacement of large magmatic bodies (e.g., batholiths), volcanic activities, orogenesis, and isostatic adjustments involves subsurface flows caused by inverted density stratification (lower-density materials lying beneath higher-density fluids). The theory of gravitational instability in viscous layered systems has been a subject of in-depth mathematical treatment for several decades (Taylor (1950) Chandrasekhar (1955), Hide (1955), Danes (1964), Selig (1965), Biot et al. (1965), Ode (1966) and Ramberg (1968a, b)). Ramberg (1968a) provided a mathematical theory of instability in multi-clayered models, containing layers of varying densities. According to his theory, the upper surface of a low-density, viscous layer in the layered complex rises spontaneously in the form of waves, whose wavelength is controlled by a complex interaction of the thicknesses, rheological properties and densities of the participating layers.

Selig (1965) modified) the mathematical formulation of Danes (1964) to demonstrate the existence of explicit solutions for the problem of salt dome dynamics.
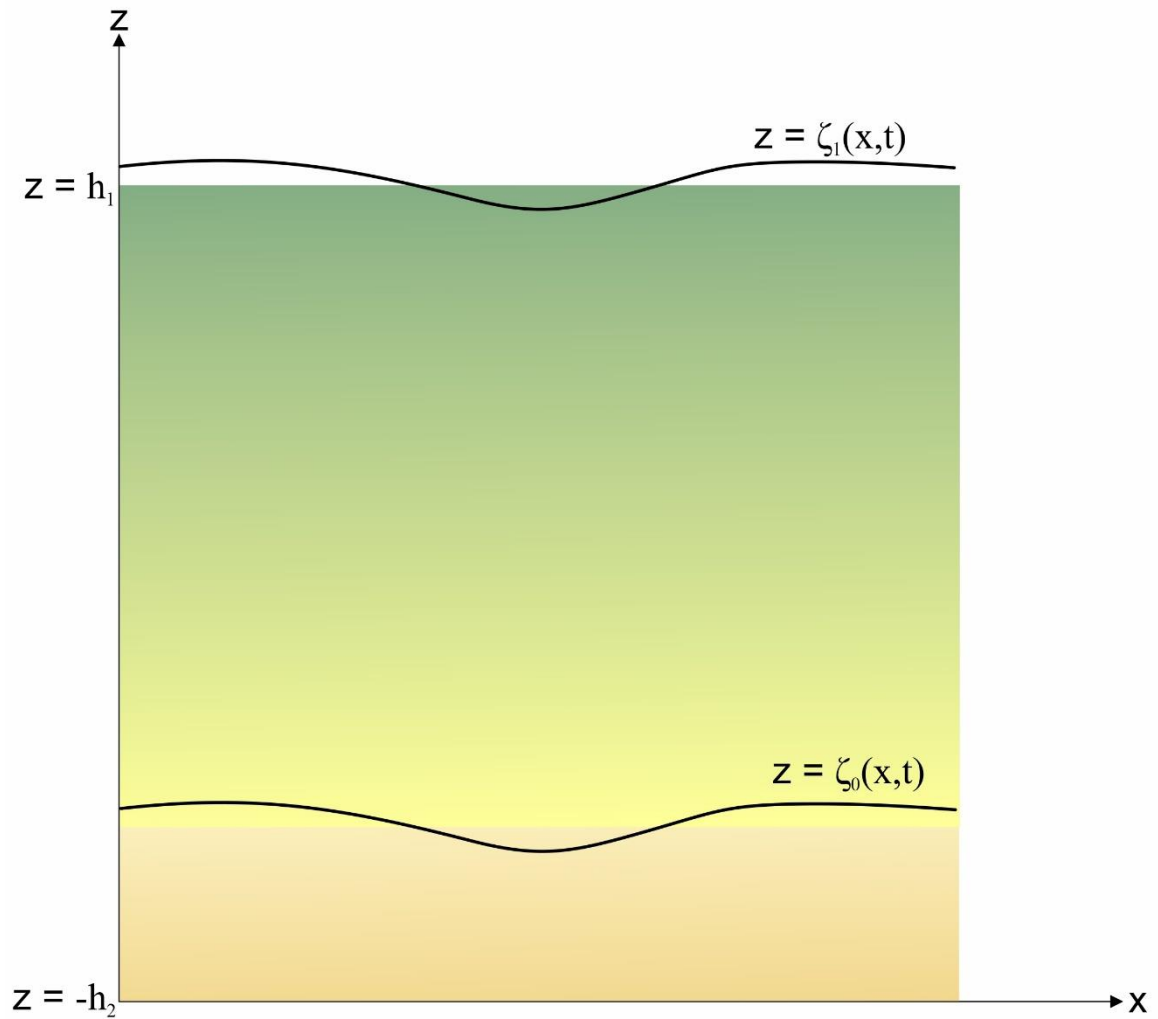
Figure 4.1: Geometry of the model (after Selig 1965)

Using a two-dimensional analytical model (Fig. 4.1), Selig (1965) derived a formula relating the rate of growth of the gravitational instability and its wavenumber with the physical and geometrical parameters of the system. He obtained mathematical derivations in the following way.

Considering the continuity condition, the equations of motion are expressed as,

$$\nabla^2 U = 0 \tag{4.1}$$

$$\nabla^2 \emptyset = 0 \tag{4.2}$$

$$\nu \nabla^2 \Psi = \frac{\partial \Psi}{\partial t} \tag{4.3}$$

95

$$\frac{\partial \emptyset}{\partial t} = \frac{p}{\rho} + U \tag{4.4}$$

where U is the gravitational potential, $\emptyset$ and Ψ are the scalar and vector potential respectively, p is the pressure, ν and ρ is the kinematic viscosity and density respectively, both of which are constant for each medium. The velocity is of the form:

$$v = -\nabla\emptyset + \nabla \times \Psi \tag{4.5}$$

and the stress components are given as:

$$p_{xy} = \rho\nu\left(\frac{\partial v_y}{\partial x} + \frac{\partial v_x}{\partial y}\right) \tag{4.6}$$

$$p_{xz} = \rho\nu\left(\frac{\partial v_z}{\partial x} + \frac{\partial v_x}{\partial z}\right) \tag{4.7}$$

$$p_{yz} = \rho\nu\left(\frac{\partial v_z}{\partial y} + \frac{\partial v_y}{\partial z}\right) \tag{4.8}$$

The following boundary conditions are applied: rigid boundary condition ($v = 0$) at the bottom of the lighter layer where $z = -h_2$, free boundary condition for $z = \xi_1$ at the top surface of the sediment, where normal and tangential viscous stresses are zero, and a continuity condition for the velocity and stress components at the interface between salt and sediment, where $z = \xi_0$ (Fig. 4.1)

The general solutions of equations (4.1) - (4.4) are:

$$\emptyset = (A_\emptyset e^{kz} + B_\emptyset e^{-kz}) \cos kx \, e^{\omega t} \tag{4.9}$$

$$\Psi = \boldsymbol{j}z \, (A_\Psi e^{kz} + B_\Psi e^{-kz}) \cos kx \, e^{\omega t} \tag{4.10}$$

Applying the method of separation of variables to the equations of motion, we have,

$$v_x = \{[(kA_\emptyset - A_\Psi) - kzA_\Psi]e^{kz} + [(kB_\emptyset - B_\Psi) + kzB_\Psi]e^{-kz}\} \sin kx\, e^{\omega t} \quad (4.11)$$

$$v_z = k\{-(kA_\emptyset + zA_\Psi)e^{kz} + (B_\emptyset - zB_\Psi)e^{-kz}\} \cos kx\, e^{\omega t} \quad (4.12)$$

p_{xz} and p_{zz} can be derived from equation (4.7). Similarly, p is calculated from equation *(4.4)*. Straightforward application of the boundary and matching conditions are then made. At the interface ($z = \xi_i(x,t)$) between the two fluids,

$$\frac{dz}{dt} = \frac{d\xi_i}{dt} + \frac{d\xi_i}{dx}\frac{dx}{dt} \quad (4.13)$$

As the flanks are not too steep, the term $\frac{d\xi_i}{dx}\frac{dx}{dt}$ can be neglected. For an early stage of instability growth, the velocity at the interface then follows,

$$v_z|_{z=\xi_i} = \frac{d\xi_i}{dt} \quad (4.14)$$

Equation *(4.14)* is used to calculate p_{zz} at the interface. Substituting all the boundary and matching conditions leads to a set of eight linear homogeneous equations. The determinant must be zero if the problem has nontrivial solutions. This mathematic approach ultimately gives rise to a relation between the wavenumber, k, and growth rate, ω, expressedas,

$$\omega = \frac{g(\rho_1 - \rho_2)}{4k}\frac{C_1}{C_2} \quad (4.15)$$

where

$$C_1 = \begin{vmatrix} 0 & 0 & 0 & 0 & e^{-kh_2} & -kh_2 e^{-kh_2} & e^{kh_2} & -kh_2 e^{kh_2} \\ 0 & 0 & 0 & 0 & e^{-kh_2} & (1-kh_2)e^{-kh_2} & -e^{kh_2} & (1+kh_2)e^{kh_2} \\ 1 & 0 & 1 & 0 & -1 & 0 & -1 & 0 \\ 1 & 1 & -1 & 1 & -1 & -1 & 1 & -1 \\ \rho_1 v_1 & \rho_1 v_1 & \rho_1 v_1 & -\rho_1 v_1 & -\rho_2 v_2 & -\rho_2 v_2 & -\rho_2 v_2 & \rho_2 v_2 \\ 1 & 0 & 1 & 0 & 1 & 0 & 1 & 0 \\ e^{kh_1} & kh_1 e^{kh_1} & e^{-kh_1} & kh_1 e^{-kh_1} & 0 & 0 & 0 & 0 \\ e^{kh_1} & (2+kh_1)e^{kh_1} & e^{-kh_1} & (-2+kh_1)e^{-kh_1} & 0 & 0 & 0 & 0 \end{vmatrix}$$

$$C_2 = \begin{vmatrix} 0 & 0 & 0 & 0 & e^{-kh_2} & -kh_2e^{-kh_2} & e^{kh_2} & -kh_2e^{kh_2} \\ 0 & 0 & 0 & 0 & e^{-kh_2} & (1-kh_2)e^{-kh_2} & -e^{kh_2} & (1+kh_2)e^{kh_2} \\ 1 & 0 & 1 & 0 & -1 & 0 & -1 & 0 \\ 1 & 1 & -1 & 1 & -1 & -1 & 1 & -1 \\ \rho_1\nu_1 & \rho_1\nu_1 & \rho_1\nu_1 & -\rho_1\nu_1 & -\rho_2\nu_2 & -\rho_2\nu_2 & -\rho_2\nu_2 & \rho_2\nu_2 \\ \rho_2\nu_2 & -(\rho_1\nu_1+\rho_2\nu_2) & \rho_2\nu_2 & -(\rho_1\nu_1+\rho_2\nu_2) & \rho_1\nu_1 & (\rho_1\nu_1+\rho_2\nu_2) & -\rho_1\nu_1 & (\rho_1\nu_1+\rho_2\nu_2) \\ e^{kh_1} & kh_1e^{kh_1} & e^{-kh_1} & kh_1e^{-kh_1} & 0 & 0 & 0 & 0 \\ e^{kh_1} & (2+kh_1)e^{kh_1} & e^{-kh_1} & (-2+kh_1)e^{-kh_1} & 0 & 0 & 0 & 0 \end{vmatrix}$$

With the simple observation that ω does not strongly depend on kh_2 if $h_2 > 10h_1$, an additional simplification can be introduced. Thus, considering $h_2 \to \infty$ and applying the boundary condition that $v = 0$, at $z = h_2$, we have

$$\omega = \frac{g(\rho_1 - \rho_2)}{2k(\rho_1\nu_1 + \rho_2\nu_2)}(1 - B^*) \tag{4.16}$$

where

$$B^* = \frac{2\rho_2\nu_2\{(\rho_1\nu_1+\rho_2\nu_2)(1+2kh_2+2k^2h_2{}^2)-(\rho_1\nu_1-\rho_2\nu_2)e^{-2kh_2}\}}{\{(\rho_1\nu_1+\rho_2\nu_2)e^{kh_2}-(\rho_1\nu_1-\rho_2\nu_2)e^{-kh_2}\}^2-4(\rho_1{}^2\nu_1{}^2-\rho_2{}^2\nu_2{}^2)k^2h_2{}^2}$$

The factor outside the parenthesis in equation *(4.16)* corresponds to the case $h_1 = h_2 \to \infty$. The term B^* can be interpreted as the influence of the finite thickness of the salt layer.

Non-dimensionalisation of equation *(4.16)* is done by considering $\nu = \frac{\rho_1\nu_1+\rho_2\nu_2}{\rho_1+\rho_2}$, such that

$$\Omega = \omega\left(\frac{\nu}{g^2}\right)^{\frac{1}{3}} \tag{4.17}$$

$$K = k\left(\frac{\nu^2}{g}\right)^{\frac{1}{3}} \tag{4.18}$$

$$X = kh_2 \tag{4.19}$$

$$H = \frac{kh_2}{K} \tag{4.20}$$

$$\mu = \frac{\rho_1 \nu_1}{\rho_2 \nu_2} \tag{4.21}$$

$$\alpha = \frac{\rho_1 - \rho_2}{\rho_1 + \rho_2} \tag{4.22}$$

These non-dimensionalized variables are used to obtain the following form

$$\Omega = \frac{\alpha H}{2X}\left\{1 - \frac{2(1 + 2X + 2X^2 - \frac{\mu - 1}{\mu + 1}e^{-2X})}{(\mu + 1)\left[\left(e^X - \frac{\mu - 1}{\mu + 1}e^{-X}\right)^2 - 4\frac{\mu - 1}{\mu + 1}X^2\right]}\right\} \tag{4.23}$$

The mode of maximum instability can be calculated from the equation $\frac{d\omega}{dk} = 0$. This

equation can be written down explicitly and the approximate solution k^* is obtained,

$$k^* = \frac{2.15}{h_2}\left(\frac{\rho_2 \nu_2}{\rho_1 \nu_1}\right)^{\frac{1}{3}} \tag{4.24}$$

$$\omega^* = \frac{0.33}{k^*}\left(\frac{g(\rho_1 - \rho_2)}{\rho_1 \nu_1 + \rho_2 \nu_2}\right)^{\frac{1}{3}} \tag{4.25}$$

Through this mathematical treatment Selig (1965) showed that the preferred mode k^* only depends mainly on the thickness of the undisturbed source layer and the ratio of the viscosities, μ. The density difference determines the speed of growth.

4.2. BASICS OF LINEAR STABILITY ANALYSIS

Linear stability analysis is generally used to predict the growth rate of instability as a function of wavenumber, taking into account a set of given physical parameters. The theory of Rayleigh-Taylor instabilities in the context of geological processes, as described in the preceding chapter has applied the concept of linear

stability analysis. The fundamentals of this mathematical method can be summarized in the following points:

i.   The governing equations for the particular problem being dealt with (e.g., Navier Stokes equation) is identified and tackled.

ii.   The mathematical treatment starts with the identification of a mean flow, which represents the unperturbed condition of the system. The mean flow field is then substituted into the governing equations to fully establish the pressure field and ensure that the flow is a solution to the governing equations.

iii.   The mathematical formulation then needs to account for a small perturbation to all of the flow and interface variables. This perturbed flow field is then substituted into the governing equation.

iv.   All non-linear terms are then neglected, retaining only the $\mathcal{O}(\varepsilon)$ terms to linearize the problem, and transform the governing equations with the perturbed variables of up to order ε.

v.   The boundary conditions are then applied to the set of derived equations. This results in a completely homogenous well-posed problem of governing equations with appropriate boundary conditions.

vi.   A normal mode assumption is made, where the flow variables are expanded in the form of appropriate Eigen functions. In this case, $e^{-i\omega t}$ for time and e^{ikx} for space. These normal mode expansions are then substituted into the linearized governing equations.

vii.   A set of ordinary differential equations is obtained in terms of y.

viii.   Substituting the solutions for the flow variables in the boundary conditions yields a dispersion relation of the form;

$$\omega = f(k), \text{ where } k \text{ is the wavenumber}$$

This dispersion relation is then used to find the effects of k and other variables of the governing equations on ω. In the following section, a linear stability analysis is developed to derive a dispersion relation of RT instabilities as a function of interface-parallel flow field in the overburden layer. This system is similar to the case of plume generation in the core-mantle boundary under the influence of horizontal flows in the mantle, as discussed in the previous chapter.
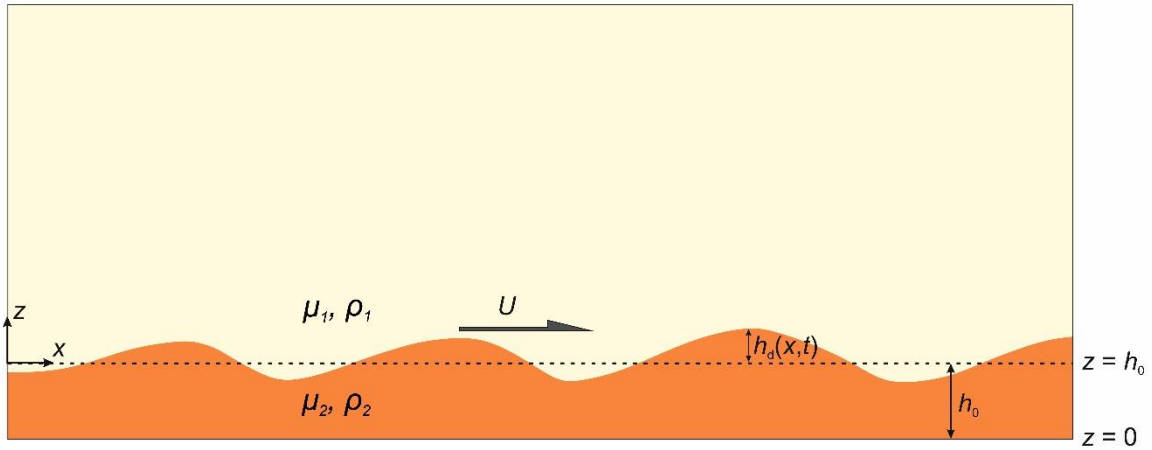
Figure 4.2: Theoretical consideration for the linear stability analysis: a thin buoyant layer (source layer) (density: ρ_2 and viscosity: μ_2) underlying a denser fluid layer (density: ρ_1 and viscosity: μ_1) (ambient mantle). Dashed and solid lines denote the initial source-layer configuration and the deformed interface geometry formed by RTI. h_o and h_d define the initial source-layer thickness and the vertical deflection at the interface, respectively. $U_i(x,t)$ represents the horizontal flow velocity at the interface.

4.3. GENERALIZED LINEAR STABILITY ANALYSIS

Consider a thin, mechanically distinct layer (source layer) above the CMB, lying below the mantle, subjected to a global horizontal flow, as illustrated in Fig 4.2. Here the theory is developed within a thin-layer approximation, which assumes layer thickness (h_2) much smaller than the length scale of the system (Bredow et al., 2017). The theoretical formulation uses a Cartesian coordinate system, *xz* with the z axis in

the vertical direction (positive upward). The thin layer is confined between $z = 0$ and $z = h_2(x, t)$ that represents the interface between the layer and the overlying mantle, respectively. The thin layer is assigned a negative density contrast relative to the overlying mantle region, and the entire system rests upon an undeformable substrate. Consider a layer parallel velocity condition at the interface $z = h_2(x, t)$ that forces materials in the thin layer to advect in the horizontal direction. The linear stability analysis is developed in the framework of mass and momentum conservation conditions, as in the CFD simulations. Considering incompressible fluid in the thin-layer, the mass conservation equation is expanded as,

$$\frac{\partial v}{\partial z} + \frac{\partial u}{\partial x} = 0, \tag{4.26}$$

where u and v denote the x- and z components of the flow velocity in the thin-layer, respectively. All the notations and their corresponding physical variables are summarized in Table 3.1. Applying the thin-layer approximation (Babchin et al., 1983), the momentum conservation conditions follow

$$\frac{\partial p}{\partial z} = -\Delta \rho g \tag{4.27}$$

and

$$\mu_2 \frac{\partial^2 u}{\partial z^2} - \frac{\partial p}{\partial x} = 0, \tag{4.28}$$

where p is the excess hydrostatic pressure, $\Delta \rho = \rho_1 - \rho_2$ is the density contrast between the denser overlying medium and the lighter thin layer at the base, and μ_2 is the thin-layer viscosity. The differential equations are solved using a set of boundary conditions (BCs) in the following way. The bottom surface is subjected to an impenetrable boundary condition:

$$v|_{z=0} = 0. \tag{4.29}$$

In addition, assuming a free-slip condition at this boundary, we have

$$\frac{\partial u}{\partial z}\bigg|_{z=0} = 0 \tag{4.30}$$

The layer-interface, on the other hand, is subjected to a differential normal stress condition, given by

$$p = p|_{z=h_2} + \Delta\rho g(z - h_2) \tag{4.31}$$

where $p|_{z=h_2}$ stands for the flow-induced normal stress at the mantle-thin layer interface, and the second term denotes buoyancy-induced pressure. To derive the horizontal velocity component in the thin layer, Eq. (4.31) is substituted in Eq. (4.28) to obtain the following second order differential equation.

$$\mu_2 \frac{\partial^2 u}{\partial z^2} - \frac{\partial}{\partial x}(-\Delta\rho g h_2 + p|_{z=h_2}) = 0 \tag{4.32}$$

On integration and after applying the boundary conditions (Eq. (4.29), (4.30)), the differential equation (4.32) yields

$$u = u|_{z=h_2} + \frac{1}{2\mu_2}\frac{\partial}{\partial x}(-\Delta\rho g h_2 + p|_{z=h_2})(z^2 - h_2{}^2) \tag{4.33}$$

The corresponding vertical component is derived from the mass conservation equation (Eq. (4.26)) after applying the impenetrable BC at $z = 0$ (Eq. (4.29)) as,

$$v|_{z=h_2} = u|_{z=h_2}\frac{\partial h_2}{\partial x} - \frac{\partial}{\partial x}\int_0^{h_2} u\,dz \tag{4.34}$$

Substituting Eq. (4.33) into this equation, we get

$$v|_{z=h_2} + h_2 \frac{\partial u|_{z=h_2}}{\partial x} - \frac{\partial}{\partial x}\left[\frac{h_2{}^3}{3\mu_2}\frac{\partial}{\partial x}\left(-\Delta\rho g h_2 + p|_{z=h_2}\right)\right] = 0 \qquad (4.35)$$

Considering the kinematic boundary condition at the interface,

$$\frac{\partial h_2}{\partial t} = v|_{z=h_2} - u|_{z=h_2}\frac{\partial h_2}{\partial x}, \qquad (4.36)$$

Eq. (4.35) yields,

$$\frac{\partial h_2}{\partial t} + \frac{\partial}{\partial x}\left(h_2 u|_{z=h_2}\right) - \frac{\partial}{\partial x}\left[\frac{h_2{}^3}{3\mu_2}\frac{\partial}{\partial x}\left(-\Delta\rho g h_2 + p|_{z=h_2}\right)\right] = 0. \qquad (4.37)$$

Eq. (4.37) defines the evolution of the interface, governed by the two competing forces: 1) non-hydrostatic pressure forces arising from the negative density contrast between the thin-layer and the mantle (3rd term) and 2) viscous forces due to the layer-parallel advective flow at the interface (2nd term). Let us now introduce a horizontal velocity at the interface as

$$u|_{z=h_2} = U_i(x,t) \qquad (4.38)$$

It is to note that the overlying horizontal mantle flows can be perturbed at some incipient geometrical irregularities on the thin layer, producing spatially and temporally heterogeneous layer-parallel flows close to the interface, as revealed from numerical simulations (Fig. 3.4). This theoretical problem is generalized by setting the boundary condition $u|_{z=h_2}$ as a function of x and t.

The vertical flows in the basal layer develop pure shear components at the interface, the rate of which can be expressed as (Hernlund & Bonati, 2019),

$$\dot{\epsilon} = -\left(\frac{\partial v}{\partial z}\right)\Bigg|_{z=0}. \qquad (4.39)$$

The corresponding normal stress at the interface follows,

104

$$p|_{z=h_2} = \mu_1 \dot{\epsilon}, \tag{4.40}$$

where μ_1 is the viscosity of the overburden layer. The boundary condition (Eq. (4.38)) represents a heterogeneous horizontal mantle flow condition as a function of x on the layer interface at a given instant. A sine wave function is chosen with a characteristic wavenumber k_M and a characteristic length-scale L to express the spatially varying horizontal interfacial flows. The later part of this section discusses the linear stability analysis in the perspective of different k_M versus k (instability wavelength) relations. Now, using the continuity equation (Eq. (4.26)) in Eq. (4.39), the expression of strain rate at the interface follows,

$$\dot{\epsilon} = -\frac{U_i(x,t)k_M}{2}\cos\left(\frac{k_M x}{2}\right) \tag{4.41}$$

Substitution of Eq. (4.41) in Eq. (4.40) yields the normal stress at the interface as a function of x.

Combining Eqs. ((4.37), (4.40) and (4.41)) leads to the final equation that expresses the geometrical evolution of the interface between the basal thin layer and the overlying mantle in the presence of a global horizontal flow:

$$\frac{\partial h_2}{\partial t} + \frac{\partial}{\partial x}(h_2 u|_{z=h_2}) + \frac{\partial}{\partial x}\left[\frac{h_2^3}{3\mu_2}\frac{\partial}{\partial x}\left(\Delta\rho g h_2 + \mu_1 \frac{U_i k_M}{2}\cos\left(\frac{k_M x}{2}\right)\right)\right]$$
$$= 0, \tag{4.42}$$

where U_i stands for the maximum horizontal flow magnitude at the interface, determined by the global horizontal flow velocity in the overlying mantle. At infinitesimal time the interfacial deflection (h_d) is assumed to be small enough such that $h_d \ll \varepsilon h_2$. Under this condition the linear terms determine the growth of instabilities at the interface in the system. The first term within the third bracket in

Eq. (4.42) represents the favoring force, where the density difference ($\Delta\rho$) facilitates the low-density fluid in the thin-layer to push vertically up against the overlying denser mantle. On the other hand, the second term represents the normal stress at the interface set by the large-scale horizontal flow that tends to dampen the instability growth under the boundary condition within the characteristic length (L).

To deal with the mathematical problem, the governing equations and the BCs are non-dimensionalized in the following way.

$$x^* = \frac{x}{L}, z^* = \frac{z}{h_0}, h^* = \frac{h_2}{h_0}, p^* = \frac{p}{\Delta\rho g h_0}, u^* = \frac{u\mu_2}{\Delta\rho g h_0^2},$$

$$v^* = \frac{v\mu_2}{\Delta\rho g h_0^2}\left(\frac{L}{h_0}\right), \qquad t^* = \frac{\Delta\rho g h_0^2}{\mu_2 L}t \tag{4.43}$$

where h_0 is the mean height of the interface. The governing equations then transform into:

$$\frac{\partial v^*}{\partial z^*} + \frac{\partial u^*}{\partial x^*} = 0, \tag{4.44}$$

$$\frac{\partial p^*}{\partial z^*} = 1 \tag{4.45}$$

$$\frac{\partial^2 u^*}{\partial z^{*2}} - \frac{\partial p^*}{\partial x^*} = 0, \tag{4.46}$$

and the BCs reduce to

$$v^*|_{z^*=0} = 0 \tag{4.47}$$

$$\left.\frac{\partial u^*}{\partial z^*}\right|_{z^*=0} = 0 \tag{4.48}$$

$$p^* = p^*|_{z^*=h^*} + (z^* - h^*) \tag{4.49}$$

106

With these new variables our interface evolution equation becomes

$$\frac{\partial h^*}{\partial t^*} + \frac{\partial}{\partial x^*}\left(h^* u^*\big|_{z^*=h^*}\right) + \left(\frac{h_0}{L}\right)\frac{\partial}{\partial x^*}\left[\frac{h^{*3}}{3}\frac{\partial}{\partial x^*}\left(h^* + p^*\big|_{z^*=h^*}\right)\right] = 0, \quad (4.50)$$

To derive the dispersion relation of an instability at the interface, consider a small perturbation on the mean height of the interface,

$$h_2(x,t) = h_0 + \varepsilon h_d(x,t), \quad (4.51)$$

where h_0 is the mean height of the interface and $h_d(x,t)$ represents the perturbation with $\varepsilon \ll 1$. Using Eq. (4.51) in Eq. (4.42) and keeping only the $\mathcal{O}(\varepsilon)$ terms, we find

$$\frac{\partial h_d}{\partial t} + \frac{\partial}{\partial x}\left(h_d u\big|_{z=h_2}\right) + \frac{\partial}{\partial x}\left[\frac{h_0^3}{3\mu_2}\Delta\rho g\frac{\partial h_d}{\partial x} + \frac{\mu_1}{\mu_2}\frac{h_0^2 h_d U_i k_M}{2}\cos\left(\frac{k_M x}{2}\right)\right]$$
$$= 0 \quad (4.52)$$

Note that any perturbation developed at the interface will simultaneously advect in the x-direction in response to the layer-parallel mantle flow. We can choose a spatio-temporal perturbation in the following form:

$$h_d(x,t) = C\exp i(kx - \omega t), \quad (4.53)$$

where C is a pre-factor, k is the perturbation wavenumber, and ω is the angular frequency. Substituting the expression of $h_d(x,t)$ in Eq. (4.52), and after some algebraic manipulation,

$$\omega = ku\big|_{z=h_2} - i\frac{\partial u\big|_{z=h_2}}{\partial x} + i\frac{h_0^3}{3\mu_2}\Delta\rho g k^2 + i\frac{h_0^2 k_M^3 U_i}{8}\frac{\mu_1}{\mu_2}\cos\left(\frac{k_M x}{2}\right)$$
$$\quad (4.54)$$
$$- \frac{h_0^2 k_M^2 k U_i}{4}\frac{\mu_1}{\mu_2}\sin\left(\frac{k_M x}{2}\right)$$

This equation provides a dispersion relation for interfacial instability in a complex form. Its imaginary part yields the growth rate as,

$$\sigma = -\frac{\partial u|_{z=h_2}}{\partial x} + \frac{h_0^3}{3\mu_2}\Delta\rho g k^2 + \frac{h_0^2 k_M^3 U_i}{8}\frac{\mu_1}{\mu_2}\cos\left(\frac{k_M x}{2}\right) \qquad (4.55)$$

Considering the mantle advection model, this equation takes the following form.

$$\sigma = \frac{k_M U_i}{2}\cos\left(\frac{k_M x}{2}\right) + \frac{h_0^3}{3\mu_2}\Delta\rho g k^2 + \frac{h_0^2 k_M^3 U_i}{8}\frac{\mu_1}{\mu_2}\cos\left(\frac{k_M x}{2}\right) \qquad (4.56)$$

The second term on the RHS of Eq. (4.56) favors the growth of the instability due the presence of density difference ($\Delta\rho$), the source layer viscosity in the same term on the other hand inhibits the instability growth. The first and third term on the RHS represents the dampening force of velocity. The first and third term on the RHS represents the dampening force of velocity. It is to note that the dispersion relation (Eq. (4.56)) in the absence of any external flow ($U_i^* = 0$) yields the same expression reported from previous stability analyses with thin-layer approximations (Brun et al., 2015; Ghosh, Maiti, & Mandal, 2020). In terms of non-dimensionalized variables, Eq. (4.56) takes the following form,

$$\sigma^* = \frac{k_M^* U_i^*}{2}\cos\left(\frac{k_M^* x^*}{2}\right) + \frac{k^{*2}}{3} + \frac{k_M^{*3} U_i^*}{8}\frac{\mu_1}{\mu_2}\cos\left(\frac{k_M^* x^*}{2}\right),$$

$$\qquad (4.57)$$

$$\sigma^* = \frac{\sigma\mu_2}{\Delta\rho g h_0} \,, k^* = k h_0$$

This generalized solution accounts for an initial kinematic heterogeneity (i.e., lateral flow gradient) at the interface between the two layers, which is implemented by choosing the velocity boundary condition as a function of x. Consequently, the growth of an interfacial instability depends on its location with respect to the heterogeneity configuration, and the growth rate in the dispersion relation becomes a function of x.

The foregoing sections will deal with the analytical solution (Eq. (4.57)) for $x^* = 0$ to show exclusively the effect of horizontal flow magnitude (U_i) on the instability development.

4.4. THEORETICAL RESULTS

This section uses Eq. (4.57) to study the effects of model parameters on the growth rate (σ^*) of Rayleigh-Taylor instabilities in the thin layer. Consider first an analysis with a condition of comparable k_M and k values ($k_M \sim k$), i.e., the length-scale
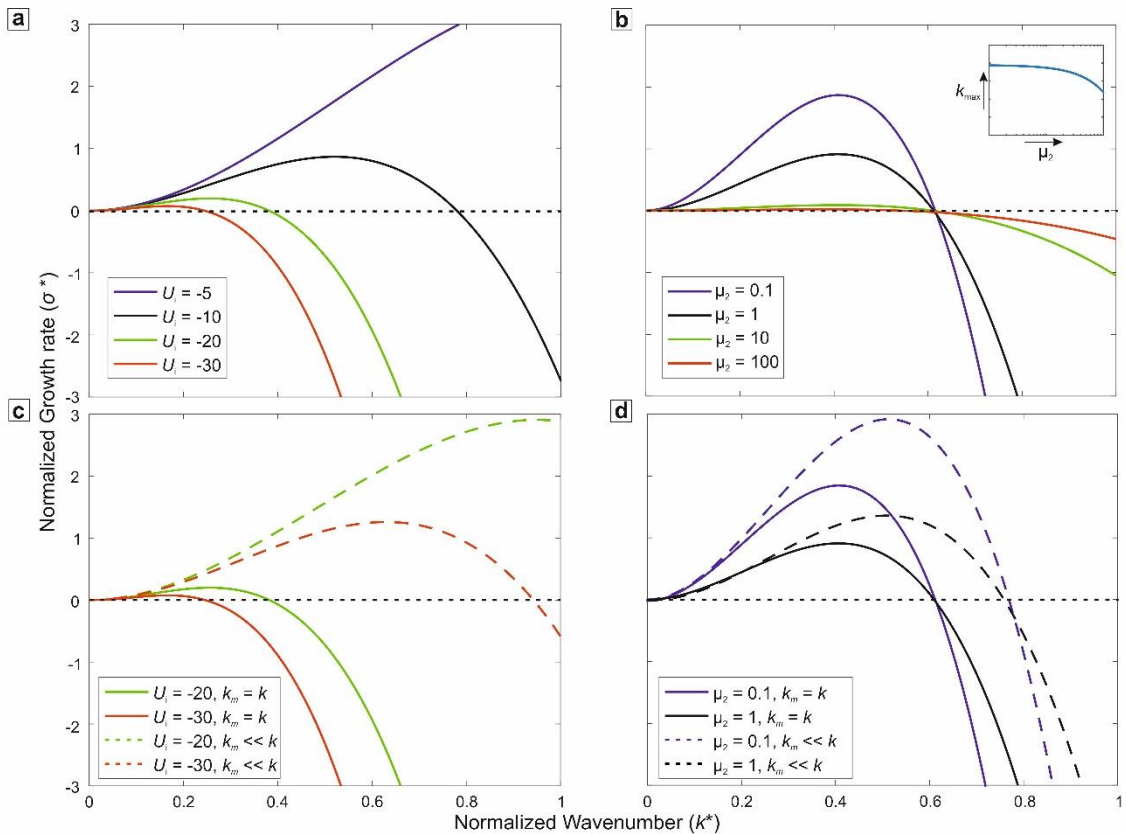
Figure 4.3: Normalized growth rates ($\sigma*$) versus normalized wavenumber (k^*) plots for different values of (a) the ambient mantle velocity (U_i), and (b) the source layer viscosity (μ_2) obtained from the linear stability analysis for $x = 0$ (decreasing wavenumber, i.e. increasing wavelength with μ_2 depicted in the inset). Normalized growth rates ($\sigma*$) versus normalized wavenumber (k^*) plots for different values of (c) ambient mantle velocity (U_i), and (d) source layer viscosity (μ_2) obtained from the linear stability analysis under the condition of $k_M = k$ and $k_M \ll k$.

of horizontal flow heterogeneity at the layer interface is close to that of instabilities growing in the thin-layer. The analysis is then extended for a condition, $k_M \ll k$, which implies the horizontal flow heterogeneity far exceeding the instabilities in

length scales. For $k_M \sim k$, increasing U_i^* (a non-dimensional form of U_i) facilitates the system to become more stable, as reflected from reducing amplitudes of the dispersion curve in Figure 4.3a. U_i^* also greatly influences the wavenumber (k) corresponding to the most unstable modes, forming an inverse relation of k with U_i^*. For example, $k = 0.5$ for $U_i^* = 10$, which drops to nearly 0.2 at $U_i^* = 30$. The theoretical results (Fig 4.3a) suggest that increasing horizontal flow velocity in the mantle favours interfacial instabilities to grow at longer wavelengths, and at the same time dampens their growth rates.

We now consider the second case, $k_M \ll k$ to show the effects of U_i^* on the modes of instability growth in the thin layer from two graphical plots for $U_i^* = 20$ and 30. These plots are compared with those for $k_M = k$ to find additional influence of the k_M versus k relation. Increase in U_i^* yields similar inverse impacts on both the maximum growth rates and their corresponding wave numbers, irrespective of $k_M \ll k$ or $k_M = k$ conditions. However, for a given U_i^* a transition from $k_M \ll k$ (Fig. 4.3c, dashed lines) to $k_M = k$ (Fig. 4.3a) condition greatly reduces the dominant wavenumber and its corresponding growth rate, implying that the latter condition is
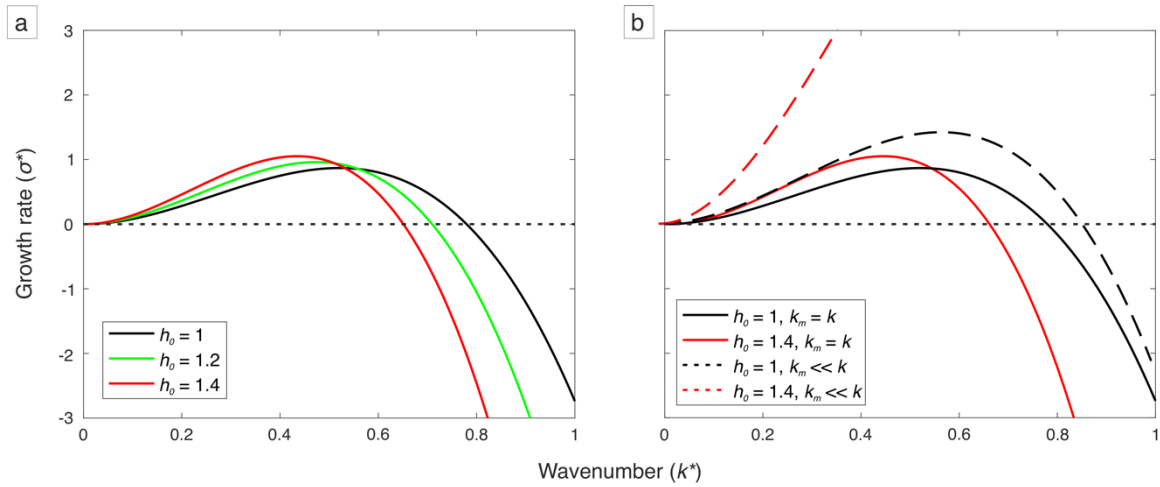
Figure 4.4: Normalized growth rates (σ^*) versus normalized wavenumber (k^*) plots for different values of source-layer thickness (h_0) for (a) $k_m = k$, and (b) for $k_m \ll k$.

less effective to produce instabilities in the basal thin layer.

The non-dimensional source-layer viscosity (μ_2) is another influential factor for the dispersion of various modes, as shown from a set of graphical plots in Figure 4.3b. For a given U_i and h_0, the plots indicate that increasing μ_2 while keeping the overburden layer viscosity (μ_1) constant, significantly dampens the growth rate of the RTIs (Fig. 4.3b, black and red lines). Secondly, the dominant wavelength of instabilities increases with decreasing source-layer viscosity (shown in the inset of Fig. 4.3b). The instabilities which grow against the prevalent gravitational forces, undergo significantly more resistance for higher values of source-layer viscosity, leading to the observed dampening effect of μ_2. (Fig. 4.3b, blue, green lines). The present linear stability analysis also accounts for the effects of source-layer viscosity for the two conditions: $k_M = k$ and $k_M \ll k$ (Fig. 4.3d). For a given source layer viscosity, μ_2, a change in the condition from $k_M = k$ and $k_M \ll k$ reduces the amplitude (maximum growth rate) of dispersion relations and their corresponding wavenumbers (Fig. 4.3d, dashed lines).

Using Eq. (4.57) this study investigated the evolution of interfacial instabilities as a function of the initial layer thickness (h_0). Increasing h_0 facilitates their growth rate because the destabilizing force (second term in the equation) is proportional to h_0^3. For extremely thin layers (low value of h_0), the long waves remain marginally stable or unstable (Fig. 4.4a). The short waves, in contrast, are always stabilized, primarily due to viscous effects of the thin-layer. Unlike the previous factors, increasing h_0 decreases the wavenumber corresponding to the most dominant mode that agrees well with the common observation that the wavelength of instabilities holds a positive correlation with layer thickness. For a given h_0 value, a switch over in the condition from $k_M = k$ to $k_M \ll k$ promotes the destabilizing state in the system

(Fig. 4.4b, dashed lines) both in terms of increasing growth rate and wavenumber (i.e., reducing wavelength).

4.5. APPLICABILTY OF THEORETICAL FINDINGS

This theoretical study primarily shows that an interface-parallel velocity in horizontally stratified fluid layers of inverted densities results in significant dampening of the RT instabilities in the layered systems, where their growth rate is found to be inversely related to the interface-parallel velocity magnitude (U_i^*). The results suggest that the global flow significantly influences the preferred wavelength at which RT instabilities can dominantly grow. Low layer-parallel velocities (e.g., $U_i^* \sim 10$) dampen selectively the short wavelength instabilities (i.e., of higher wavenumbers) (Fig. 4.5a). Consequently, ambient velocity fields, in general, facilitate
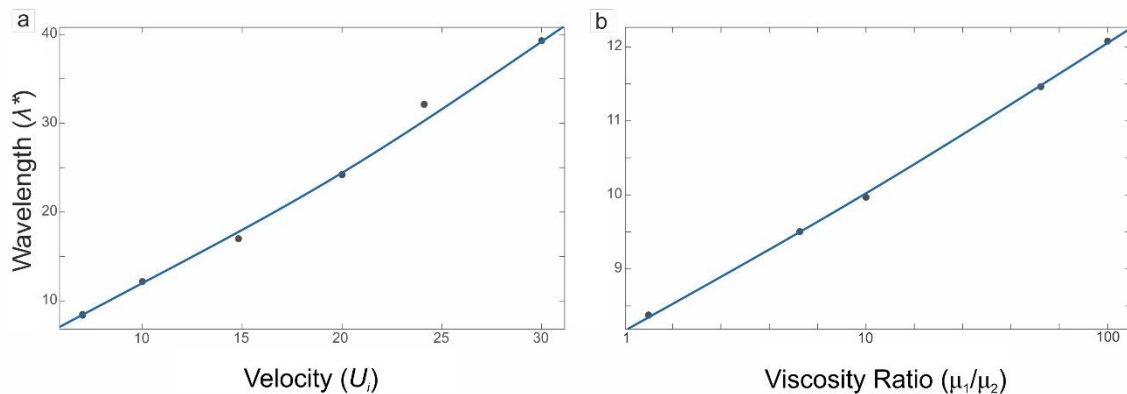
Figure 4.5: Variations of the instability wavelength (λ^*) with (a) global flow velocity (U_i), and (b) mantle-source layer viscosity ratio ($\frac{\mu_1}{\mu_2}$) from the linear stability analysis. All the variables are presented as non-dimensional quantities.

RT instabilities to grow on longer wavelengths in preference to those on shorter wavelengths. The theoretical prediction implies that the ambient mantle flows reduce the spatial frequency of plumes, allowing them to form at a large horizontal spacing, as reflected in the sporadic distributions of plume-driven hotspots (discussed in detail later).

The Atwood number (A_T) is also dealt with in this theoretical analysis, aiming to evaluate the effects of density contrast ($\Delta\rho = \rho_1 - \rho_2$) between the source layer and the overlying mantle. The density contrast is an important factor in the context of our present problem as the lower mantle is compositionally as well thermally heterogeneous (Davies et al., 2012; Farnetani et al., 2018), and such heterogeneities can eventually give rise to a large spatial variation in $\Delta\rho$. The results yield a positive relation of the instability growth rate with density ratio (Eq. (4.57)), as also predicted by earlier studies (van Keken et al., 1997). Increasing density ratio facilitates instabilities to amplify at fast rates (Fig. 3.10a, b). This finding allows us to hypothesize that inherent heterogeneities can be an important factor in preferential growth of mantle plumes initiated by RT instabilities. Thermo-chemical heterogeneities in mantle, e.g., TBL piling, can also result in lateral variations of the mantle viscosity, as reported from seismic tomographic studies (McNamara & Zhong 2004, Davaille & Romanowicz 2020). The analytical solution shows that the wavelength of RT instabilities increases nonlinearly with the mantle/source-layer viscosity ratio ($\frac{\mu_1}{\mu_2}$) (Fig. 4.5b), as shown in earlier studies (Lister & Kerr, 1989). The result suggests that the number of possible plume instabilities in a mantle region with large $\frac{\mu_1}{\mu_2}$ ratios would be low, but they will grow at fast rates as large $\frac{\mu_1}{\mu_2}$ ratios, i.e., low source-layer viscosity under a given mantle viscosity facilitate the growth rates, as evident from the dispersion relations shown in Fig. 4.3c.

Earlier theoretical and experimental studies have extensively investigated the evolution of mantle plumes originated from deep mantle sources by RT instabilities. However, how the presence of a global horizontal flow in the mantle that may originate from various geodynamic processes, such as thermal convection (Olson et

al. 1990), subducting slab driven shear flows (Čížková et al. 2012; van der Meer et al. 2018), and mantle winds (Tarduno et al. 2009) (Fig. 3.2), can influence the instability growth dynamics demands a quantitative analysis, which is the principal focus of this study. Previous model estimates suggest that subducting slabs sink in the lower mantle with velocity magnitudes in the range 4 -5 cm/yr at the top to 2-3 cm/yr at the bottom (van der Meer et al., 2018), whereas the maximum root-mean-square vector velocity field for whole mantle convection is estimated around 30 cm/yr (Rayleigh number in the order of 10^6). The global ambient flows in the overlying mantle can thus greatly influence the process of plume initiation at the TBL. In fact, some model studies have recently shown that such global flows can force ascending plumes to deflect from the vertical trajectories (Hassan et al., 2016; Kerr et al., 2008; Kerr & Mériaux, 2004), as documented from the seismic tomography of natural plumes, e.g., the Hawaiian plume is strongly deflected towards the west–southwest at around 1000 km depth (French & Romanowicz, 2015; Lei et al., 2020). However, these studies entirely focus on the interaction of mature plumes with global horizontal flows, giving little attention to the problem of plume initiation in a source layer, which fundamentally determines the possibility of plume formation in a geodynamic setting. The linear stability analysis suggests that the horizontal global flows in the mantle can critically control the initiation of plume instabilities in buoyant source layers. In extreme conditions they can completely suppress the instabilities, allowing no plume to evolve in the system. This RT instability mechanics is applicable to several other geodynamic settings, which is briefly discussed below.

Subduction zones are a typical geodynamic setting that commonly produce plumes, called cold plumes, initiated as RT instabilities in the buoyant melt-rich zones above the subducting slabs (Gerya et al., 2006; Ghosh, Maiti, Mandal, et al., 2020). In

this setting the subducting slabs typically set in a strong corner flow currents with appreciable magnitudes (~5-10 cm/yr), depending upon the subduction velocity that generally varies on a wide spectrum (4-20 cm/yr). Applying the model results, this study suggests that strong slab-parallel advection in the mantle wedge can dampen the RT amplification in the vertical direction, allowing those with high buoyancy factor to preferentially take part in instability driven plume generation. The transition zone (670 km) is another effective geodynamic setting for secondary plume formation from mega plumes, often stagnated at the transition zone (Brunet & Yuen, 2000). Many thermo-mechanical models and experiments indicate that the overlying lithospheric plate motion can globally induce horizontal flows in the upper mantle, where their magnitudes can be significantly large (8-10 cm/yr). According to the present model results, such lithosphere-induced flows can significantly counter to the destabilizing condition at the transition zone, reducing the possibility of plume formation. This model inference is also applicable for secondary plume generation from a super-plume beneath a drifting continental lithosphere, where the lithospheric motion can greatly suppress the RT instabilities in the melt-rich layers at the top of the super-plume.

Morgan (1971) in his seminal work proposed deep-mantle plumes as the principal source of primary magmatic hotspots, but their origin has remained a subject of great debate till date (Koppers et al., 2021). Later studies proposed a set of criteria in support of the deep-mantle hypothesis for hotspots: a) linear chain of volcanoes with monotonous age progression, b) flood basalt at the origin of this track, c) a large buoyancy flux, d) the presence of consistently high ratios of three to four helium isotopes, and e) occurrence of low shear-wave velocity (V_S) zones in the lower mantle. Based on these criteria, it has been possible to ascertain the following nine

hotspots of deep-mantle origin: Hawaii, Pitcairn, Samoa and Louisville (Jellinek & Manga, 2004; Koppers et al., 2021) in the Pacific hemisphere and Iceland, Afar, Reunion, Tristan and Kerguelen in the Indo-Atlantic hemisphere (Fig. 3.1). Their spatial distribution reveals that these hotspots are located at large distances from one another. For example, the Hawaii chain and the Samoan hotspot are located ~5000 km away from each other. Similarly, the Iceland and the Tristan hotspots maintain a spacing, more than 8000 km. On contrary, experimental and theoretical studies (Montague & Kellogg, 2000) show mantle plumes generated in the TBL at the CMB at much smaller wavelengths, lying in the range 1400 km to 1800 km. The plume frequency observed in experimental models evidently holds a clear disagreement with the spatial density of deep-mantle hotspots across the globe. This disagreement poses the following critical question- why are hotspots of deep-mantle plume origin so rare on the earth's surface?

One of the reasonable ways to address this question is to find some geodynamic processes that can inhibit plume initiation in the TBL above the CMB, allowing a few plumes to grow in the mantle and produce sporadic hotspots. The present study identifies global horizontal mantle flows as one of the potential dampening factors for mantle plume generation. The linear stability analysis shows that the RT instability growth rate becomes negligibly small ($\sigma \sim 0$) when the interface parallel flow velocity is significant ($U_i^* = \sim 20$). The same global flow effect is observed in the real scale CFD simulations shown in the previous chapter, where the growth rate drops significantly due to imposition of a global flow $U^* = >18$ (Fig. 3.5). The simulation results imply that mantle plumes to ascend to the surface in the flowing mantle states would require an unusually large time scale (>100 Ma). The mantle flows can also control their spatial frequency preferentially in the flow direction, as

revealed from the instability wavenumber (k) analysis as a function of U_i (Fig. 4.5). k corresponding to the fastest growing waves is reduced with increasing U_i. Applying this theoretical result to a real scale system, it appears that the wavelength of instabilities in a layer of 100 km thickness would be ~250 km in case of rest mantle condition, which multiplies by 10-14 times when the mantle is subjected to a global flow condition of 5 cm/yr. The instability theory presented in this study thus provides at least a clue to the problem of large spacing, i.e. low frequency of volcanic hotspots in the light of RT instability mechanics.

4.6. REFERENCES

Babchin, A. J., Frenkel, A. L., Levich, B. G., & Sivashinsky, G. I. (1983). Nonlinear saturation of Rayleigh-Taylor instability in thin films. *Physics of Fluids*, *26*(11). https://doi.org/10.1063/1.864083

Baldwin, K. A., Scase, M. M., & Hill, R. J. A. (2015). The inhibition of the Rayleigh-Taylor instability by rotation. *Scientific Reports*, *5*. https://doi.org/10.1038/srep11706

Bredow, E., Steinberger, B., Gassmöller, R., & Dannberg, J. (2017). How plume-ridge interaction shapes the crustal thickness pattern of the Réunion hotspot track. *Geochemistry, Geophysics, Geosystems*, *18*(8), 2930–2948. https://doi.org/10.1002/2017GC006875

Brunet, D., & Yuen, D. A. (2000). Mantle plumes pinched in the transition zone. *Earth and Planetary Science Letters*, *178*(1–2), 13–27. https://doi.org/10.1016/S0012-821X(00)00063-7

Brun, P. T., Damiano, A., Rieu, P., Balestra, G., & Gallaire, F. (2015). Rayleigh-Taylor instability under an inclined plane. *Physics of Fluids*, *27*(8). https://doi.org/10.1063/1.4927857

Conrad, C. P., & Molnar, P. (1997). The growth of Rayleigh-Taylor-type instabilities in the lithosphere for various rheological and density structures. *Geophysical Journal International*, *129*(1), 95–112. https://doi.org/10.1111/J.1365-246X.1997.TB00939.X

Davaille, A., & Romanowicz, B. (2020). Deflating the LLSVPs: Bundles of Mantle Thermochemical Plumes Rather Than Thick Stagnant "Piles." *Tectonics*, *39*(10), e2020TC006265. https://doi.org/10.1029/2020TC006265

Davies, D. R., Goes, S., Davies, J. H., Schuberth, B. S. A., Bunge, H. P., & Ritsema, J. (2012). Reconciling dynamic and seismic models of Earth's lower mantle: The dominant role of thermal heterogeneity. *Earth and Planetary Science Letters*, *353–354*, 253–269. https://doi.org/10.1016/J.EPSL.2012.08.016

Farnetani, C. G., Hofmann, A. W., Duvernay, T., & Limare, A. (2018). Dynamics of rheological heterogeneities in mantle plumes. *Earth and Planetary Science Letters*, *499*, 74–82. https://doi.org/10.1016/j.epsl.2018.07.022

French, S. W., & Romanowicz, B. (2015). Broad plumes rooted at the base of the Earth's mantle beneath major hotspots. *Nature 2015 525:7567*, *525*(7567), 95–99. https://doi.org/10.1038/nature14876

Gerashchenko, S., & Livescu, D. (2016). Viscous effects on the Rayleigh-Taylor instability with background temperature gradient. *Physics of Plasmas*, *23*(7), 072121. https://doi.org/10.1063/1.4959810

Gerya, T., Letters, D. Y.-E. and P. S., & 2003, undefined. (n.d.). Rayleigh–Taylor instabilities from hydration and melting propel "cold plumes" at subduction zones. *Elsevier*. Retrieved August 19, 2022, from https://www.sciencedirect.com/science/article/pii/S0012821X03002656?cas a_token=stS0ZI3ly9kAAAAA:kaqixXKfERHIhMpUKE3Rqp0Dlsp5s3dnJgI4rv-knCcwDR4XP5t3TxQ1U49XSaBTkskV_JDhonY

Ghosh, D., Maiti, G., & Mandal, N. (2020). Slab-parallel advection versus Rayleigh-Taylor instabilities in melt-rich layers in subduction zones: A criticality analysis. *Physics of the Earth and Planetary Interiors*, *307*. https://doi.org/10.1016/j.pepi.2020.106560

Ghosh, D., Maiti, G., Mandal, N., & Baruah, A. (2020). Cold Plumes Initiated by Rayleigh-Taylor Instabilities in Subduction Zones, and Their Characteristic Volcanic Distributions: The Role of Slab Dip. *Journal of Geophysical Research: Solid Earth*, *125*(8). https://doi.org/10.1029/2020JB019814

Hassan, R., Müller, R. D., Gurnis, M., Williams, S. E., & Flament, N. (2016). A rapid burst in hotspot motion through the interaction of tectonics and deep mantle flow. *Nature 2016 533:7602*, *533*(7602), 239–242. https://doi.org/10.1038/nature17422

Hernlund, J. W., & Bonati, I. (2019). Modeling Ultralow Velocity Zones as a Thin Chemically Distinct Dense Layer at the Core-Mantle Boundary. *Journal of Geophysical Research: Solid Earth*, *124*(8), 7902–7917. https://doi.org/10.1029/2018JB017218

Houseman, G. A., & Molnar, P. (1997). Gravitational (Rayleigh-Taylor) instability of a layer with non-linear viscosity and convective thinning of continental lithosphere. *Geophysical Journal International*, *128*(1), 125–150. https://doi.org/10.1111/J.1365-246X.1997.TB04075.X

Ida, S., Nakagawa, Y., & Nakazawa, K. (1987). The Earth's core formation due to the Rayleigh-Taylor instability. *Icarus*, *69*(2), 239–248. https://doi.org/10.1016/0019-1035(87)90103-5

Jellinek, A. M., & Manga, M. (2004). LINKS BETWEEN LONG-LIVED HOT SPOTS, MANTLE PLUMES, D″, AND PLATE TECTONICS. *Reviews of Geophysics*, *42*(3). https://doi.org/10.1029/2003RG000144

Kerr, R. C., Lister, J. R., Kerr, R. C., & Lister, J. R. (2008). Rise and deflection of mantle plume tails. *Geochemistry, Geophysics, Geosystems*, *9*(10), 10004. https://doi.org/10.1029/2008GC002124

REFERENCES

Kerr, R. C., & Mériaux, C. (2004). Structure and dynamics of sheared mantle plumes. *Geochemistry, Geophysics, Geosystems*, *5*(12). https://doi.org/10.1029/2004GC000749

Koppers, A. A. P., Becker, T. W., Jackson, M. G., Konrad, K., Müller, R. D., Romanowicz, B., Steinberger, B., & Whittaker, J. M. (2021). Mantle plumes and their role in Earth processes. *Nature Reviews Earth & Environment 2021 2:6*, *2*(6), 382–401. https://doi.org/10.1038/s43017-021-00168-6

Lei, W., Ruan, Y., Bozdağ, E., Peter, D., Lefebvre, M., Komatitsch, D., Tromp, J., Hill, J., Podhorszki, N., & Pugmire, D. (2020). Global adjoint tomography—model GLAD-M25. *Geophysical Journal International*, *223*(1), 1–21. https://doi.org/10.1093/GJI/GGAA253

Lister, J. R., & Kerr, R. C. (1989). The effect of geometry on the gravitational instability of a buoyant region of viscous fluid. *Journal of Fluid Mechanics*, *202*(577). https://doi.org/10.1017/S0022112089001308

Louis-Napoleon, A., Bonometti, T., Gerbault, M., Martin, R., & Vanderhaeghe, O. (2022). Models of convection and segregation in heterogeneous partially molten crustal roots with a VOF method – I: flow regimes. *Geophysical Journal International*, *229*(3), 2047–2080. https://doi.org/10.1093/GJI/GGAB510

Louis-Napoléon, A., Gerbault, M., Bonometti, T., Thieulot, C., Martin, R., & Vanderhaeghe, O. (2020). 3-D numerical modelling of crustal polydiapirs with volume-of-fluid methods. *Geophysical Journal International*, *222*(1), 474–506. https://doi.org/10.1093/GJI/GGAA141

Masse, L. (2007). Stabilizing effect of anisotropic thermal diffusion on the ablative Rayleigh-Taylor instability. *Physical Review Letters*, *98*(24), 245001. https://doi.org/10.1103/PHYSREVLETT.98.245001/FIGURES/5/MEDIUM

McNamara, A. K., & Zhong, S. (2004). Thermochemical structures within a spherical mantle: Superplumes or piles? *Journal of Geophysical Research: Solid Earth*, *109*(B7), 7402. https://doi.org/10.1029/2003JB002847

Mikaelian, K. O. (1996). Rayleigh-Taylor instability in finite-thickness fluids with viscosity and surface tension. *Physical Review E*, *54*(4), 3676. https://doi.org/10.1103/PhysRevE.54.3676

Miller, N. C., & Behn, M. D. (2012). Timescales for the growth of sediment diapirs in subduction zones. *Geophysical Journal International*, *190*(3), 1361–1377. https://doi.org/10.1111/J.1365-246X.2012.05565.X

Mondal, P., & Korenaga, J. (2018). The Rayleigh–Taylor instability in a self-gravitating two-layer viscous sphere. *Geophysical Journal International*, *212*(3), 1859–1867. https://doi.org/10.1093/GJI/GGX507

Montague, N. L., & Kellogg, L. H. (2000). Numerical models of a dense layer at the base of the mantle and implications for the geodynamics of D″. *Journal of Geophysical Research: Solid Earth*, *105*(B5), 11101–11114. https://doi.org/10.1029/1999JB900450

Morgan, W. J. (1971). Convection Plumes in the Lower Mantle. *Nature 1971 230:5288*, *230*(5288), 42–43. https://doi.org/10.1038/230042a0

Munro, D. H. (1988). Analytic solutions for Rayleigh-Taylor growth rates in smooth density gradients. *Physical Review A*, *38*(3), 1433. https://doi.org/10.1103/PhysRevA.38.1433

Neil, E. A., & Houseman, G. A. (1999). Rayleigh–Taylor instability of the upper mantle and its role in intraplate orogeny. *Geophysical Journal International*, *138*(1), 89–107. https://doi.org/10.1046/J.1365-246X.1999.00841.X

Pullin, D. I. (1982). Numerical studies of surface-tension effects in nonlinear Kelvin–Helmholtz and Rayleigh–Taylor instability. *Journal of Fluid Mechanics*, *119*, 507–532. https://doi.org/10.1017/S0022112082001463

Ramberg, H. (1968a). Instability of layered systems in the field of gravity. I. *Physics of the Earth and Planetary Interiors*, *1*(7), 427–447. https://doi.org/10.1016/0031-9201(68)90014-9

Ramberg, H. (1968b). Instability of layered systems in the field of gravity. II. *Physics of the Earth and Planetary Interiors*, *1*(7), 448–474. https://doi.org/10.1016/0031-9201(68)90015-0

Ramberg, H. (1972). Theoretical models of density stratification and diapirism in the Earth. *Journal of Geophysical Research*, *77*(5), 877–889. https://doi.org/10.1029/JB077I005P00877

Rayleigh. (1882). Investigation of the Character of the Equilibrium of an Incompressible Heavy Fluid of Variable Density. *Proceedings of the London Mathematical Society*, *s1-14*(1), 170–177. https://doi.org/10.1112/PLMS/S1-14.1.170

Song, Y., Wang, P., & Wang, L. (2021). Numerical investigations of Rayleigh–Taylor instability with a density gradient layer. *Computers & Fluids*, *220*, 104869. https://doi.org/10.1016/J.COMPFLUID.2021.104869

Taylor, G. (1950). The instability of liquid surfaces when accelerated in a direction perpendicular to their planes. I. *Proceedings of the Royal Society of London. Series A. Mathematical and Physical Sciences*, *201*(1065), 192–196. https://doi.org/10.1098/RSPA.1950.0052

Turcotte, D., & Schubert, G. (2002). *Geodynamics*. https://books.google.com/books?hl=en&lr=&id=-

REFERENCES

nCHlVuJ4FoC&oi=fnd&pg=PR11&ots=LqWMDVA6YQ&sig=agZlPRf7u0rI9Ryio3
A0xOiQo-M

van der Meer, D. G., van Hinsbergen, D. J. J., & Spakman, W. (2018). Atlas of the
underworld: Slab remnants in the mantle, their sinking history, and a new
outlook on lower mantle viscosity. *Tectonophysics*, *723*, 309–448.
https://doi.org/10.1016/J.TECTO.2017.10.004

van Keken, P. E., King, S. D., Schmeling, H., Christensen, U. R., Neumeister, D., & Doin,
M.-P. (1997). A comparison of methods for the modeling of thermochemical
convection. *Journal of Geophysical Research: Solid Earth*, *102*(B10), 22477–
22495. https://doi.org/10.1029/97jb01353

Whitehead, J. A. (1986). Buoyancy-driven instabilities of low-viscosity zones as
models of magma-rich zones. *Journal of Geophysical Research: Solid Earth*,
91(B9), 9303–9314. https://doi.org/10.1029/JB091IB09P09303

Wilcock, W. S. D., & Whitehead, J. A. (1991). The Rayleigh-Taylor instability of an
embedded layer of low-viscosity fluid. *Journal of Geophysical Research: Solid
Earth*, *96*(B7), 12193–12200. https://doi.org/10.1029/91JB00339

Zhou, Y. (2017a). Rayleigh–Taylor and Richtmyer–Meshkov instability induced flow,
turbulence, and mixing. I. In *Physics Reports* (Vols. 720–722).
https://doi.org/10.1016/j.physrep.2017.07.005

Zhou, Y. (2017b). Rayleigh–Taylor and Richtmyer–Meshkov instability induced flow,
turbulence, and mixing. II. In *Physics Reports* (Vols. 723–725).
https://doi.org/10.1016/j.physrep.2017.07.008

Zhou, Y., Clark, T. T., Clark, D. S., Gail Glendinning, S., Aaron Skinner, M., Huntington,
C. M., Hurricane, O. A., Dimits, A. M., & Remington, B. A. (2019). Turbulent
mixing and transition criteria of flows induced by hydrodynamic instabilities.
Physics of Plasmas, *26*(8). https://doi.org/10.1063/1.5088745

Zhou, Y., Williams, R. J. R., Ramaprabhu, P., Groom, M., Thornber, B., Hillier, A.,
Mostert, W., Rollin, B., Balachandar, S., Powell, P. D., Mahalov, A., & Attal, N.
(2021). Rayleigh–Taylor and Richtmyer–Meshkov instabilities: A journey
through scales. In *Physica D: Nonlinear Phenomena* (Vol. 423).
https://doi.org/10.1016/j.physd.2020.132838

Zrnić, D. S., & Hendricks, C. D. (2003). Stabilization of the Rayleigh-Taylor Instability
with Magnetic Feedback. *The Physics of Fluids*, *13*(3), 618.
https://doi.org/10.1063/1.1692967

Chapter 5.

EVOLUTION OF DOUBLE-SUBDUCTION SYSTEMS

5.1. SUBDUCTION ZONES: AN INTRODUCTORY NOTE

Plate tectonics is a complex dynamic process which drives convective down-welling of the cold heavy lithospheric layers, assisted by localization of weak zones that define narrow and rapidly deforming boundaries (Bercovici et al., 2015; Crameri & Tackley, 2016). The down-welling motion allowing the lithospheric slabs to sink back into the mantle. This process eventually results in fragmentation of the lithosphere into discrete blocks, described as tectonic plates. It is now generally accepted that the two main forces drive the plate motion: i) "ridge push" resulting from the upwelling of buoyant mantle materials at mid-ocean ridges (Bott, 1991; Forsyth & Uyeda, 1975a) and ii) "slab pull" caused by the negative buoyancy of dense, cold lithospheric slabs at subduction zones (Conrad & Lithgow-Bertelloni, 2002; Lithgow-Bertelloni & Richards, 1995). However, a line of studies (Forsyth & Uyeda, 1975b; Parsons & Richter, 1980) have claimed that ridge push accounts for only a small (< ~10%) fraction of the net driving forces, leaving slab pull as the dominant factor to fuel the plate tectonic engine. Consequently, understanding the subduction mechanics becomes the most critical challenge to explain the evolution of a plate tectonic system. The issue has taken a new turn as the subduction process governs the development of Earth's surface topography over geological time. Moreover, subduction zones act as potential locations of terrestrial seismic and planetary scale volcanic activities that render an enormous impact on Earth's climate.

5.2. SUBDUCTION DYNAMICS: A REVIEW

During the past several decades, the dynamics of lithospheric slab subduction, one of the most challenging and captivating geodynamic processes, has remained in the forefront of geodynamic research, leading to a remarkable progress in terms of both in-depth understanding of subduction dynamics and interpretations of various subduction-driven phenomena. The most attractive lines of subduction studies (Gerya, 2011, 2022) can be highlighted in the following three directions:

i.   Explanation of the major forces operating terrestrial plate tectonics, which are primarily responsible for shaping the evolution of Earth's external and internal structures through geological time.

ii.   Prediction of terrestrial seismic and volcanic activities that are primarily controlled by subduction zones.

iii.   Existing knowledge gaps in understanding the essential characteristics of subduction processes, largely due to lack of spatial-temporal geological and geophysical data.

Realistic subduction modelling, although technically challenging, has greatly facilitated the development of new numerical techniques (Gerya, 2011, 2022), enabling geoscientists to establish verifiable and predictive geodynamic models. The multi-physics nature of subduction-related problems indicates that numerical modelling is one of the most effective tools used to integrate natural observations, develop and test novel ideas, and eventually to gain a theoretical insight about the subduction mechanics. This section provides a review, summarising several important aspects of the existing concepts and related works based on numerical modelling approach.

The mechanics of subduction initiation (SI), although an intrinsic feature of the Earth's dynamics (Bercovici, 2003; Gurnis et al., 2004; Nikolaeva et al., 2010; Stern, 2004; Stern & Gerya, 2018), is still a great enigmatic issue and not well understood (e.g., Stern and Gerya, 2018; Crameri et al., 2020). Most of the currently active subduction zones initiated during the Cenozoic, primarily in intra-oceanic settings,
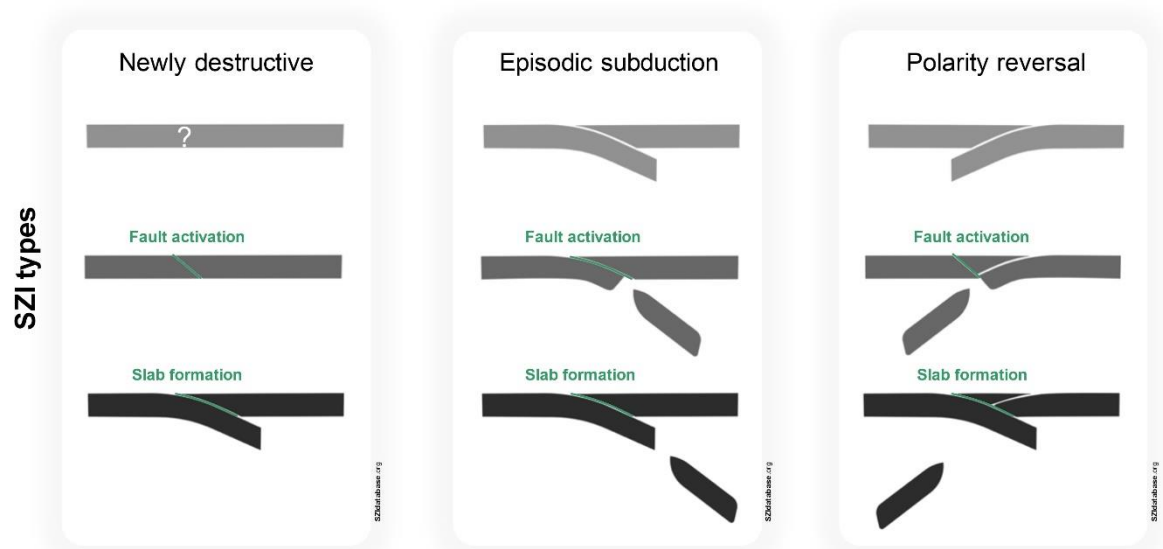
Figure 5.1: Visual representation of the three categories of subduction zone initiation (SZI) events. As described in Crameri et al., (2020), SZI events can be classified into three types. The first type is Newly Destructive, which occurs when a subduction fault forms either from an undisturbed portion of a tectonic plate or due to some weakness unrelated to subduction. The second type is Episodic Subduction, where a subduction fault re-establishes at the same location after a previous subduction zone has terminated, maintaining the same polarity. The third type is Polarity Reversal, which involves the formation of a new subduction fault with an opposite polarity compared to the fault in the previously terminated subduction zone.

suggesting the SI process as a geologically modern phenomenon in the history of plate tectonics (Crameri et al., 2020; Gurnis et al., 2004). Geodynamicists generally agree upon the hypothesis that the main force acting in a mature subduction system originates from negative buoyancy of the cold oceanic lithosphere (Davies, 1999; Korenaga, 2013; Vlaar & Wortel, 1976). On contrary, the driving forces involved in SI (Fig. 5.1) are more varied, and the mechanisms that govern SI are lined up along two main types (e.g., Stern, 2004; Stern and Gerya, 2018):

i. Induced: SI caused by ongoing plate motion, or its modification brought on by shifts in the force balance away from the SI location;

ii. Spontaneous: SI caused by forces originating only at the SI site.

Crameri et al. (2020) proposed the classification of SI mechanical settings based on the main governing forcing direction as either (but never exclusively) vertical (i.e., any combination of plate buoyancy force, the force from any surface load, and slab pull), or horizontal (i.e., some combination of tectonic force and horizontal viscous drag due to mantle-flow). It is, however, important to note that different SI scenarios may be possible in various regions, rather than a single mechanism. Geoscientists have proposed several potential subduction initiation settings, but some of them are witnessed in the present-day plate tectonics (Stern and Gerya, 2018; Crameri et al., 2020). Recent studies (e.g. Crameri et al. 2020) have provided key insights into the SI processes, which are summarized below.

i. In the context of modern plate tectonics of the Earth, it is unlikely that SI is only caused by plate buoyancy. The dynamic analysis thus accounts for horizontal and/or vertical forcing, as observed in natural settings.

ii. Subduction zones always form preferentially at or near a pre-existing plate weakness zone, such as a plate boundary, transform faults or fracture zones. Such weak zones can play a critical role in triggering the SI.

iii. The majority of SI events are found outside or near the borders of the Large Low Seismic Velocity Provinces (LLSVPs), indicating that both mantle upwelling and downwelling may largely contribute to the development of SI.

It is evident from the preceding discussions that different physical principles control the initiation of a subduction zone and its subsequent growth. The sustainability of a

subduction event is controlled by the sufficient slab pull (e.g., Vlaar and Wortel, 1976; Davies, 1999; Korenaga, 2013) and the presence of pressurized aqueous fluids along the subduction interface (Gerya et al., 2008; Van Dinther et al., 2013). In fact, activation of both these components requires an initiation stage (Dymkova & Gerya, 2013; Gurnis et al., 2004; C. E. Hall et al., 2003; Nikolaeva et al., 2010) that can be influenced by a variety of different horizontal and vertical forcing and weakening mechanisms (e.g., Stern and Gerya, 2018 and references therein; Crameri et al., 2020). In addition, rheological weakening due to shear heating (Kiss et al., 2020; Thielmann
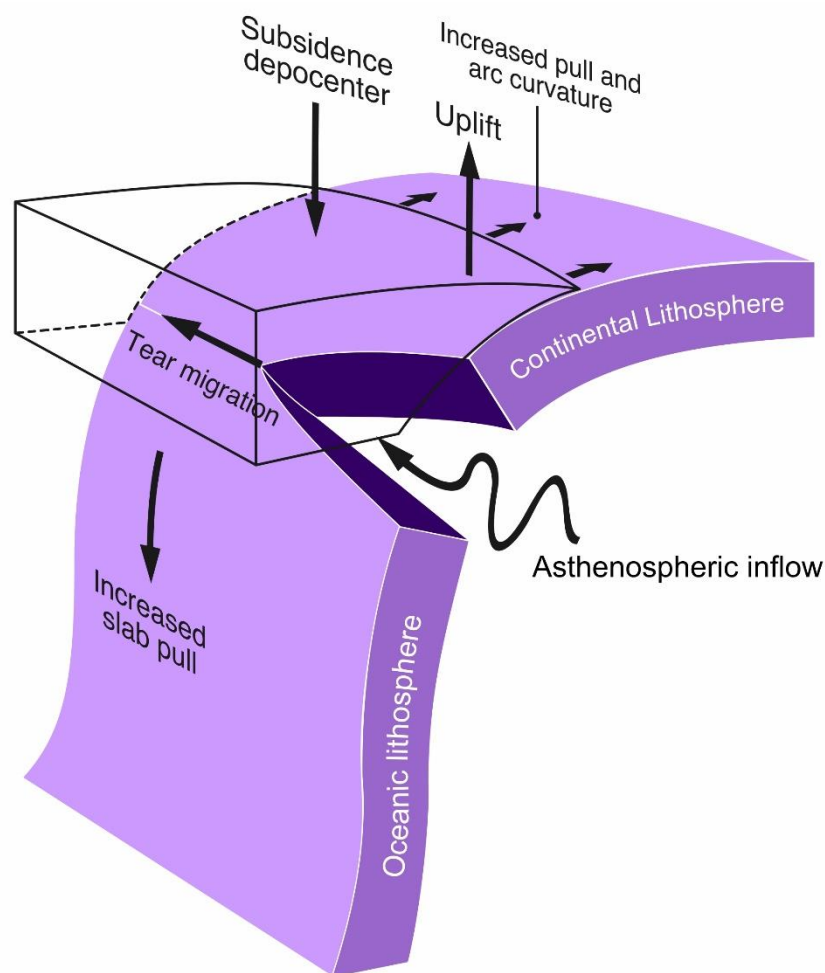
Figure 5.2: Illustration depicting the lateral advancement of slab detachment. There is an accumulation of forces pulling the slab as the subducted plate (slab) narrows, leading to a distinct pattern of sinking and rising of the Earth's surface. This pattern moves along the same direction as the plate's movement, causing the trench to retreat and allowing molten asthenospheric material to flow into the gap created by the detached slab.

127

& Kaus, 2012) and grain-size reduction (Bercovici & Mulyukova, 2021; Mulyukova & Bercovici, 2018) can also control "success" or "failure" of subduction initiation.

The opposite side of the subduction-research spectrum concerns the process that forces subduction to cease. This is an inevitable component of the terrestrial plate tectonics, which generally result from various geological conditions, such as collision of positively buoyant oceanic plateaus, continents, ridges, magmatic arcs, and seamount chains with active subduction zones (Gerya, 2011). Subduction termination is usually accompanied by several important geodynamic processes, continent-continent collision, continental crust subduction, and slab breakoff and/or tearing (Fig. 5.2). Several recent studies have delved deep into the mechanics of these processes with the help of numerical simulations. These numerical models have focused particularly on slab breakoff (also known as slab detachment) and slab tearing processes, including evolution of complex tectonic settings from 3D numerical models. Burkett & Billen (2010) developed the one of the first completely dynamic, 3D thermo-mechanical numerical models for the ridge-trench collision, demonstrating that detachment of a laterally-symmetric finite slab occurs almost instantaneously along strike due to the process of necking. Following that, van Hunen & Allen, (2011) presented 3D thermo-mechanical models featuring the transition from subduction to continental collision, which also accounted for additional lateral heterogeneities in the incoming plate. Similar to Burkett and Billen's (2010) models, homogeneous oceanic lithosphere exhibited a tendency to develop simultaneous necking and subsequent detachment, which shows an inherent preference to begin within the interior of the colder slab rather than at the warmer and weaker slab edges. Significant lateral asymmetry in a collision setting, on the other hand, has the potential to cause slab tearing that begins at one of the slab edges, to propagate

laterally (van Hunen and Allen, 2011). Li et al. (2013) studied the collision of a laterally bound continent with an ocean-continent subduction margin using 3D numerical models. They showed that the evolution of the oceanic subduction side (continuous retreating subduction) differed from that of the continental collision side (slab breakoff and topography uplift). In addition, their models also produced lateral extrusion of the thickened overriding crust from the collisional to the subduction side. The phenomenon of lateral extrusion is found in natural setting around the north-eastern part of the India-Asia collision zone (Li et al., 2013) and around the western edge of the Arabia-Asia collision zone.

Important aspects of subduction termination in laterally variable subduction systems that have recently been modelled include:

i.   Effects of active continental and/or oceanic transform boundaries (Duretz et al., 2014);

ii.   Role of the overriding plate thickness (Hertgen et al., 2020);

iii. Impact of lateral flow in the asthenospheric (Sternai et al., 2014);

iv.   Influence of continental underplating following slab breakoff (Magni et al., 2017);

v.   Effects of backarc extension due to continental collision (Magni et al., 2014);

vi.   Role of subduction migration and continental accretion (Moresi et al., 2014);

vii. Development of surface topography in continental collision zones (Chen et al., 2017; Pusok & Kaus, 2015); and several other topics.

Moresi et al. (2014) demonstrated from numerical modelling the growth of continental margins by accretion of continental ribbons. Their study suggests that the dynamics after the continental block accretion are governed by spontaneous lateral

rollback of an arcuate trench, migrating perpendicular to the direction of plate convergence. This model explains the pre-Carboniferous evolution of the southern Tasmanides (Moresi et al., 2014). In fact, given the inherent complexity of subduction systems, the numerical modelling approaches seem to be the most effective means for handling subduction problems that demand integration of natural observations, laboratory tests, and analytical theories.

5.3. MULTIPLE SUBDUCTION SYSTEMS: CATEGORIES AND THEIR FEATURES

As discussed above, single subduction dynamics has been extensively studied with numerical models both in 2-D and 3-D. However, subduction systems are much complex due to interplay of two or more subduction zones, where the plates subduct simultaneously resulting in additional complications to the subduction dynamics. A particular architecture of double subduction develops when two slabs are situated spatially close enough to interact with one another. The study of multi-slab systems is particularly useful to gain insights into the interaction of the subducting slabs with the asthenosphere and other surface plates because they develop dynamic pressure that can influence the asthenospheric flows, slab dip and forces influencing plate coupling beyond those observed commonly in single subduction systems.

Natural examples from seismic tomography have revealed three conceivable double subduction configurations: i) "out dip", ii) "in dip", and iii) "same dip" (Fig.5.3a). The Molucca Sea Subduction Zone (Fig.5.3b) is an example of a typical divergent out-dip double subduction system (Zhang et al., 2017) where the Molucca Sea plate subducted below the Eurasian plate on one side and the Philippines Sea plate on the other. The Caribbean and the Philippines Subduction systems (Fig.5.3b), on the other hand, are excellent natural examples of in-dip subduction system

(Dasgupta & Mandal, 2018, 2022). Previous double-subduction studies have used numerical modelling to look into a number of crucial elements of these intricate systems. For example, Mishin et al. (2008) demonstrated that the interaction between the two subduction zones is influenced by the relative rates of the plates, the age of the slabs, and the length of the intermediate plate. Burkett & Gurnis (2013) examined
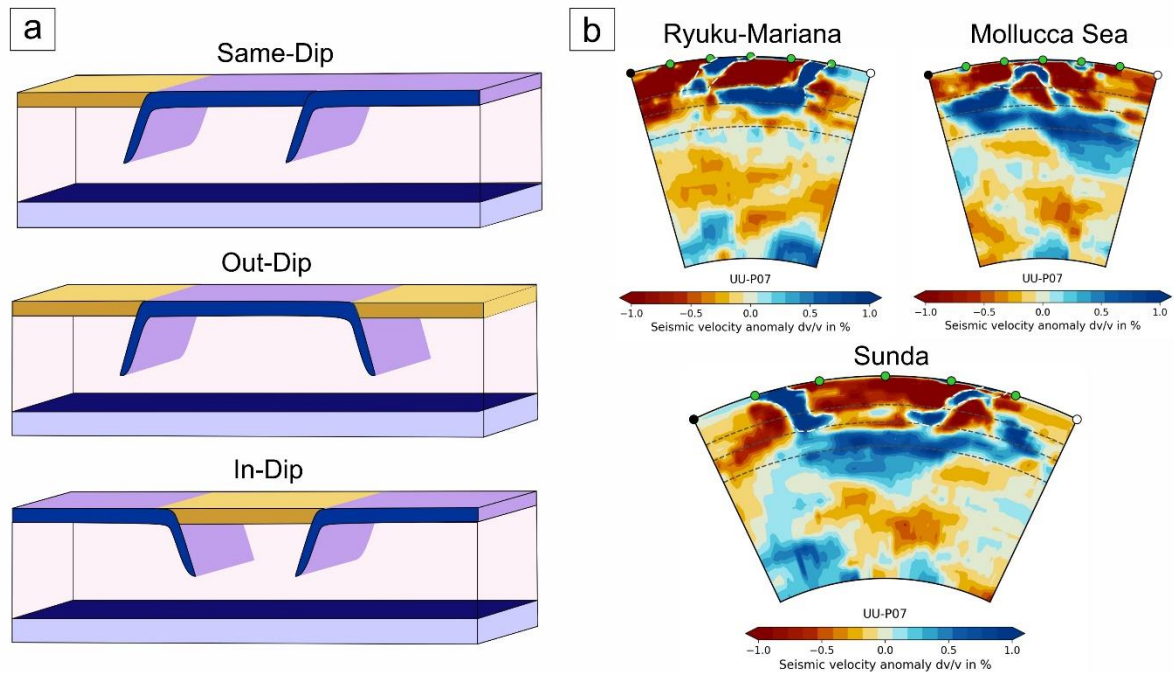
Figure 5.3: Illustrations showing a) the three different types of double subduction systems and b) their natural counterparts observed from seismic tomography.

the conditions in which a slab is stalled in the mantle, as documented from the western North American tectonics using a double subduction model configuration. Similarly, using 2-D double subduction models, Čížková and Bina (2015) hypothesized that the IBM trench is advancing as a result of the Ryukyu subduction zone's effects, while Faccenna et al., (2018) suggested that the conversion of the retreating IBM trench to advancing motion occurred due to the reestablishment of double subduction following a break-off episode of the Ryukyu slab. On the other hand, Jagoutz et al. (2015) and Holt et al. (2018) employed 3-D numerical models to

demonstrate the contrasting behaviors of two nearby slabs in terms of slab-dip and trench motions, with application to India-Eurasia and IBM-Ryukyu systems.

5.4. MECHANICS OF SAME-DIP DOUBLE-SUBDUCTION PROCESSES

The main focus of this chapter, however, is on the formation and evolution of same-dip double subduction: a geodynamic regime which develops when two oceanic plate dipping in the same direction proceed to subduct synchronously (Mishin et al., 2008; Pusok & Stegman, 2019). Episodes of this same-dip double subduction are common in both ancient and modern plate tectonic systems and are, particularly involved in the history of the Himalayan collision zone (Burg, 2011; Burg et al., 2006), and that of South East Asia leading to the formation of the active Izu-Bonin-Marianas and Ryukyu arcs (Faccenna et al., 2018; Hall, 1996). Same-dip double subduction systems have been previously modelled using various numerical (Pusok & Stegman, 2020; Holt et al., 2018, Mishin et al., 2008) and analytical techniques (Holt et al., 2017; Jagoutz et al., 2015). These studies have examined the models of multi-slab subduction systems in both 2-D and 3-D and also compared their results with natural cases from both past and present. However, despite significant advancement in modelling techniques and geophysical observations, the same-dip double subduction process remains poorly understood, and questions regarding the dynamics of this process remain mostly unanswered in terms of the physical factors controlling its initiation, evolution, and stability.

The present study deals with the interconnected evolution of two spatially separated subduction zone resulting in a coupled subduction processes. Time-dependent and self-consistently evolving particle-in-cell finite element numerical models are employed to analyse the conditions that promote the initiation and

stabilization of a second subduction zone, and convert a single subduction system into a self-sustaining double subduction system and vice-versa. The imprints that dynamic variations in the double subduction evolution have on slab Moho and slab top temperature are also investigated in this study. Such imprints found in geological record can help to identify paleo double subduction systems. Finally, we will compare the model findings with real-world scenarios of same-dip double subduction systems.

5.4.1. MODELLING APPROACH

The UNDERWORLD2 code (Mansour et al., 2021) is used to build numerical, time-evolving, dynamically consistent thermomechanical subduction models in 2-D
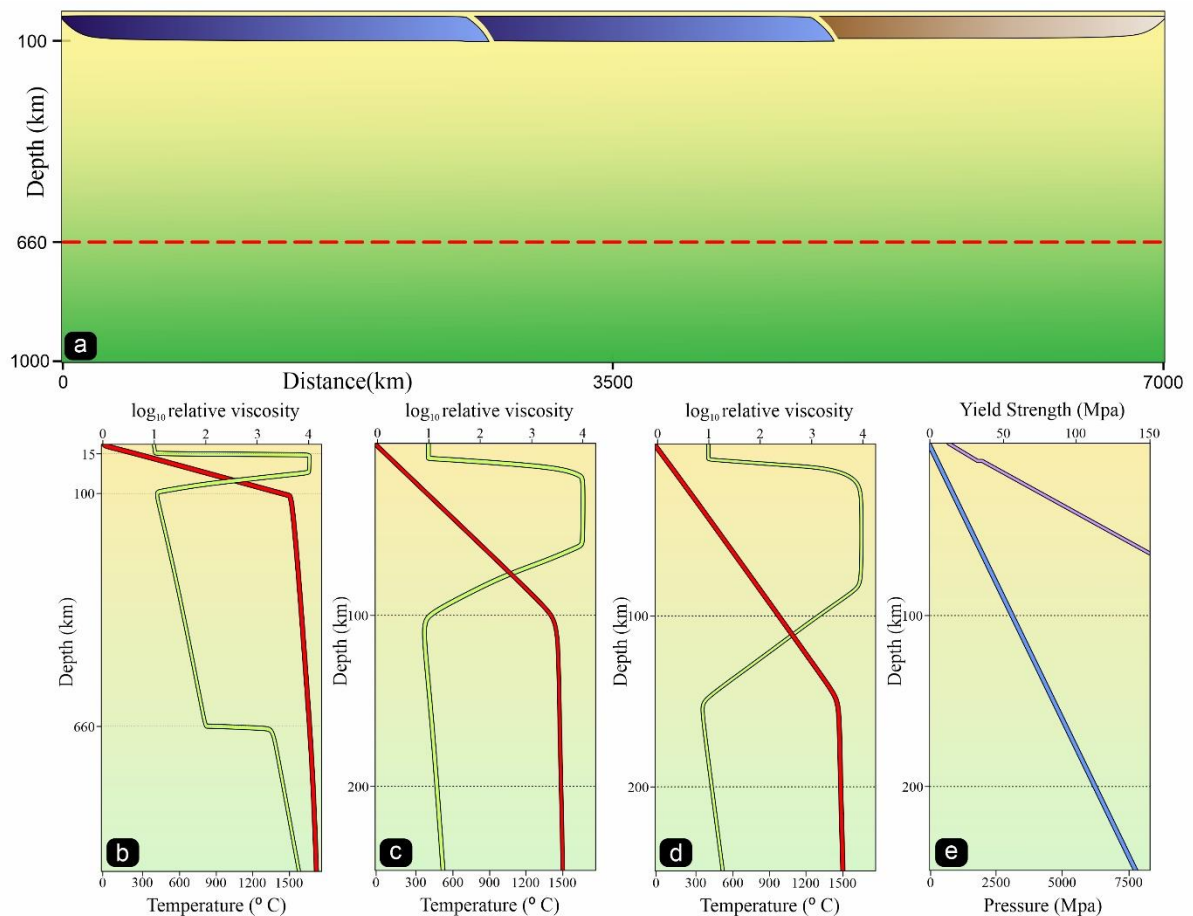
Figure 5.4: (a) The model setup and boundary conditions considered for CFD simulations, which shows the whole domain and initial setup of model employed for simulating same-dip double subduction in oceanic setting. Detailed illustrations representing the viscosity and temperature profiles of b) the complete model domain, c) oceanic lithosphere, and d) continental lithosphere utilized in the models. The viscosity values are relative to the asthenosphere value of 10^{20} Pa s. e) The strength plots exhibiting depth-dependent variations, showcasing increasing strength (purple) and pressure (blue).

Cartesian domains. The simulations presented in this work reflect an incompressible Boussinesq fluid flow at low Reynolds Number where the inertial forces are neglected. This flow driven by internal buoyancy anomalies is described by the continuity and momentum conservation equations (3.1) and (3.2) explained in Chapter 3. Applying the appropriate boundary conditions, the unknown parameters are solved by the Stokes and continuity equations in a pre-defined 2-D Cartesian domain. The 2-D domain is further divided into smaller quadrilateral elements resulting in a mesh resolution of 512 elements in the vertical direction which provides an element width of ~3 km, and a particle density of 50 tracers per element. These Lagrangian tracer particles are used to advect the material properties which are mapped to quadrature points using nearest-neighbour interpolation (Sandiford & Moresi, 2019).

The progressive evolution of the subduction models presented in this study are inherently dynamic, implying the absence of any external forces or velocities applied to the overall system. In this section, the geometrical, mechanical, thermal and rheological properties of our subduction models, are described in detail. Figure 5.4a provides an overview of the model domain, including the initial and boundary conditions used for running the numerical simulations. The depth of the model domain is fixed at 1000 km, with an aspect ratio of 7. The upper and lower boundaries are kept as mechanically free slip (zero tangential stress) whereas the two sidewalls are assigned a periodic condition. The thermal evolution of the subduction system represents the balance between heat transfer as a consequence of fluid motion, thermal diffusion, and heat generation within the system, represented by (assuming incompressibility):

$$\rho C_p \frac{DT}{Dt} = \nabla . q + \rho Q \tag{5.1}$$

where Q is the internal heat production rate and T is the temperature. Diffusion rates are described by Fourier's law, which satisfies the condition:

$$q = -k\nabla T' \tag{5.2}$$

where k is the conductivity and T′ is the non-adiabatic temperature. Using the Boussinesq approximation and combining Eqs. (5.1) and (5.2) we get,

$$\frac{\partial T}{\partial t} + u.\nabla T' = \kappa \nabla^2 T' + \frac{Q}{C_p} \tag{5.3}$$

where $\kappa = \frac{k}{\rho C_p}$, represents the thermal diffusivity. T' is replaced by the adiabatic temperature (T) of the system as a function of depth (z) obtained from the relation:

$$T = T' + z\left(\frac{\partial T}{\partial z}\right) = T' + z\left(\frac{\alpha g T_p}{C_p}\right) \tag{5.4}$$

where T_p is the mantle potential temperature and α = 3 × 10^{-5} K^{-1} is the coefficient of thermal expansion. Considering C_p = 1260 J/kg/K for the earth's mantle, a resultant adiabatic temperature gradient of 0.4 K/km is added to the nonadiabatic temperature of the mantle. The energy conservation equation (5.3) is solved in UNDERWORLD2 using the Semi-Lagrangian Crank-Nicholson (SLCN) method (Spiegelman & Katz, 2006), which builds on the potencies of the Crank-Nicolson scheme for diffusion and the semi-Lagrangian scheme for advection. This method is shown to be unconditionally stable, allowing for much larger time-step sizes. The energy equation has constant (Dirichlet) and zero-flux (Neumann) on the top and bottom boundaries

respectively. The surface temperature is initialised to 0° C whereas the model basal temperature is initially kept at 1900° C.

The initial flat geometries of the lithospheric plates are characterised by half space cooling profiles corresponding to their assigned ages, a thermal diffusivity value of 10^{-6} m²/s, and a mantle potential temperature of 1400° C. The density parameters within the model are function of the assigned temperature which essentially links the thermal properties and their evolution to the momentum equation. The equation of state for the case of density variations due to temperature is defined as,

$$\rho = \rho_r\big(1 - \alpha(T - T_p)\big) \tag{5.5}$$

where $\rho_r = 3300$ kg/m³ is the reference mantle density at the mantle potential temperature. The implementation of the Boussinesq approximation ensures that all effects of density change is neglected except its buoyancy effects.

The asthenosphere rheology of the subduction models is implemented in the form a composite creep law, which incorporates the combined effects of diffusion creep (η_{diff}), dislocation creep (η_{disl}), and plastic yielding (η_{yield}). The plastic strain rates represent brittle failure near the surface in low pressure conditions and low-temperature plasticity within the slab at significantly higher pressure. The creep laws governing the behaviour of mantle silicates demonstrate an Arrhenius temperature and pressure dependence, controlled by activation volume V and the activation energy E (Hirth & Kohlstedt, 2004), resulting in the following diffusion/dislocation viscosity:

$$\eta_{diff/disl} = A^{\frac{-1}{n}} \dot{\varepsilon}^{\frac{1-n}{n}} exp\left(\frac{E + PV}{nRT}\right) \tag{5.6}$$

where A where is a pre-factor, n is the stress exponent (diffusion creep = 1, dislocation creep = 3.5), R is the gas constant and P is the lithostatic pressure. It is usually observed that mantle material yields under increased lithostatic pressure by stress-limiting mechanisms such as Peierls' creep (Kameyama et al., 1999). In addition, reduction of material strength is promoted as a consequence of brittle yielding (Byerlee et al., 1978; Kohlstedt et al., 1995) near the surface. These two yielding mechanisms are combined into a simplified plastic rheology (van Hunen and Allen, 2011), for which the viscosity is described as:

$$\eta_{yield} = \frac{\tau_{yield}}{2\dot{\varepsilon}} \qquad (5.7)$$

and τ_{yield} is obtained from the relation:

$$\tau_{yield} = min\ (C + \mu P,\ \tau_{max}) \qquad (5.8)$$

where C (= 20 MPa) is the initial cohesion , μ (= 0.1) is the friction coefficient, and τ_{max} is the cut-off yield stress value. An effective model viscosity (η_{eff}) is obtained by calculating the harmonic mean of the different type of viscosity as:

$$\frac{1}{\eta_{eff}} = \frac{1}{\eta_{diff}} + \frac{1}{\eta_{disl}} + \frac{1}{\eta_{yield}} \qquad (5.9)$$

The activation volumes (V) and energies (E) values are consistent with the experimental estimates determined for dry olivine (Karato & Wu, 1993). The value of pre- factor (A) in the upper mantle is chosen based on the findings that a) shallow part of the upper mantle manifests an effective viscosity in the order of 10^{20} Pa s (Hager, 1990), and b) the presence of seismic anisotropy illustrates that dislocation creep is dominant throughout a significant portion of the mantle (Becker, 2006). The lower mantle is considered to be much more viscous than the upper mantle and is allowed

137

to deform only through diffusion creep mechanism. The lower mantle diffusion creep pre-factor is computed to produce a lower mantle diffusion creep viscosity of 3×10^{22} (Čížková et al., 2012) at 660 km depth which increases with depth. All the viscosity structures in form of profiles are summarised in Fig. 5.4

The top crustal layer, which is assigned a constant viscosity of 1×10^{20} Pa s yields following Eq. (5.7) to mimic the effects of brittle failure at the surface. The cohesion is however assumed to be 10 MPa so as to simulate a crust with much less yield strength than that of the lithosphere. The weak crustal layer plays an important role in decoupling the subducting slab from the over- riding plate and facilitate plate convergence. The mantle lithosphere strength is determined by the upper viscosity cut-off values (1×10^{24} Pa s) except for regions where plastic yielding is activated. In the case of the overriding plate (OP), this upper limit is increased slightly (2.5×10^{24} Pa s) in order to mimic its stiffness. Both the crust and the lithosphere are devoid of any internal rheological layering and the effects of elastic deformation is neglected entirely. Passive tracers are added to the compositional field in regions of interest to track plate motion and deformation.

Previous studies (Bercovici & Ricard, 2012; Mulyukova & Bercovici, 2019) have shown that spontaneous initiation of slab subduction can be caused across pre-existing lithospheric weakness like transform faults. Owing to the lack of any consensus on the mechanisms for subduction initiation (i.e., strain weakening), a weak zone is generally introduced in the model lithosphere to initiate subduction. In this study, subduction is enabled by a narrow weak zone of 10 km width having a uniform viscosity of 10^{20} Pa s extended to the lithospheric base, which efficiently decouples the SP from the OP. This method not only enables convergent plate to

decouple without any complexities of slab dehydration and mantle wedge hydration and weakening, but also has no effect on the slab break-off processes.

In order to investigate the effects of continental structures on the evolution of a double subduction system, 150-km deep continental block consisting of a 40-km thick continental crust is incorporated with the oceanic plates, which has a 600 kg/m³ lower compositional density than the mantle material under the same temperature. The rheological and thermal parameters assigned to the continental blocks are summarized in the Figure 5.4d. The equations and parameters utilized for solving the numerical simulations are based dimensionless equivalents of the governing equations. All the numerical parameters used in the models are scaled to their dimensionalized or non-dimensionalized forms using the UNDERWORLD2 scaling module. All models are first solved non-dimensionally and are subsequently scaled to their equivalent real physical units using reference values. T. The scaling coefficients derived from the base units of length (Kl), mass (Km), time (Kt) and temperature (KT) are Kl = l, Km = $\rho_{ref} \times Kl^3$, Kt = 1 / ($\frac{\eta_{ref} \times Kl}{Km}$) and KT = T_p , respectively. The implementation of the scaling strategy was to keep buoyancy force responsible for the subduction of oceanic lithosphere to a non-dimensional value of 1 to aid the solver efficiency.

5.4.2. MODEL TYPES

Three different initial settings of tectonic plates are considered to model same-dip double-subduction systems, with an objective to study their spatio-temporal dynamics and thermal evolution. Each of these initial setting accounts for locally lithospheric weaknesses in a specific arrangement with or without mechanically strong continental blocks. The first type of model (referred to as oceanic plate model)

replicates a simple oceanic plate tectonic setting, consisting of a 120 Ma old, flat lying oceanic lithosphere with an initial length of 5000 km (Fig. 5.5a). Two narrow mechanically weak zones are introduced to the lithospheric slabs in the initial model at distances of 2500 km and 5000 km with a dip of 30° and 20°, respectively. The weak zone at 2500 km characterizes an intraplate lithosphere-scale fault that develops in large oceanic plates, similar to the present-day Wharton Basin (Stevens et al., 2020). The second type of model represents an ongoing subduction system, where an oceanic plate has already been subducted halfway into the upper mantle, carrying a continental block (length: 400 km and thickness: ~150 km). The block is assumed to form a weak interface with the adjoining oceanic plate, possibly from the inter-plate 3D differential stress localization (Fig. 5.6a). On the opposite side, it is separated from an 80 Ma old oceanic lithosphere by a dipping (30°) weak zone. The third model, which aims to reproduce a continent-continent collision setting, initially consists of a flat-lying, 1200 km long 80 Ma old oceanic lithosphere, and two continental blocks (thickness: 150 km and length: 1500 km), separated by an oceanic basin. This oceanic plate forms a narrow weak channel at the contact with the overriding strong continental plate (Fig. 5.7a). The continental blocks are compositionally buoyant relative to the underlying asthenosphere (Fig. 5.4d).

5.5. MODEL RESULTS

This section presents results obtained from the three different models, with a special focus on their characteristic temperature and pressure evolutionary patterns.

5.5.1. OCEANIC PLATE SETTING

In this type of tectonic architecture, plastic yielding localizes preferentially at one of the pre-existing lithospheric weaknesses (Fig.5.5a), resulting in an unstable mechanical state of the flat-lying oceanic plate to trigger and initiate the back subduction zone (BSZ). The subduction initiation is coupled with formation of a spreading centre (divergent tectonics) that eventually acts as a new active site of
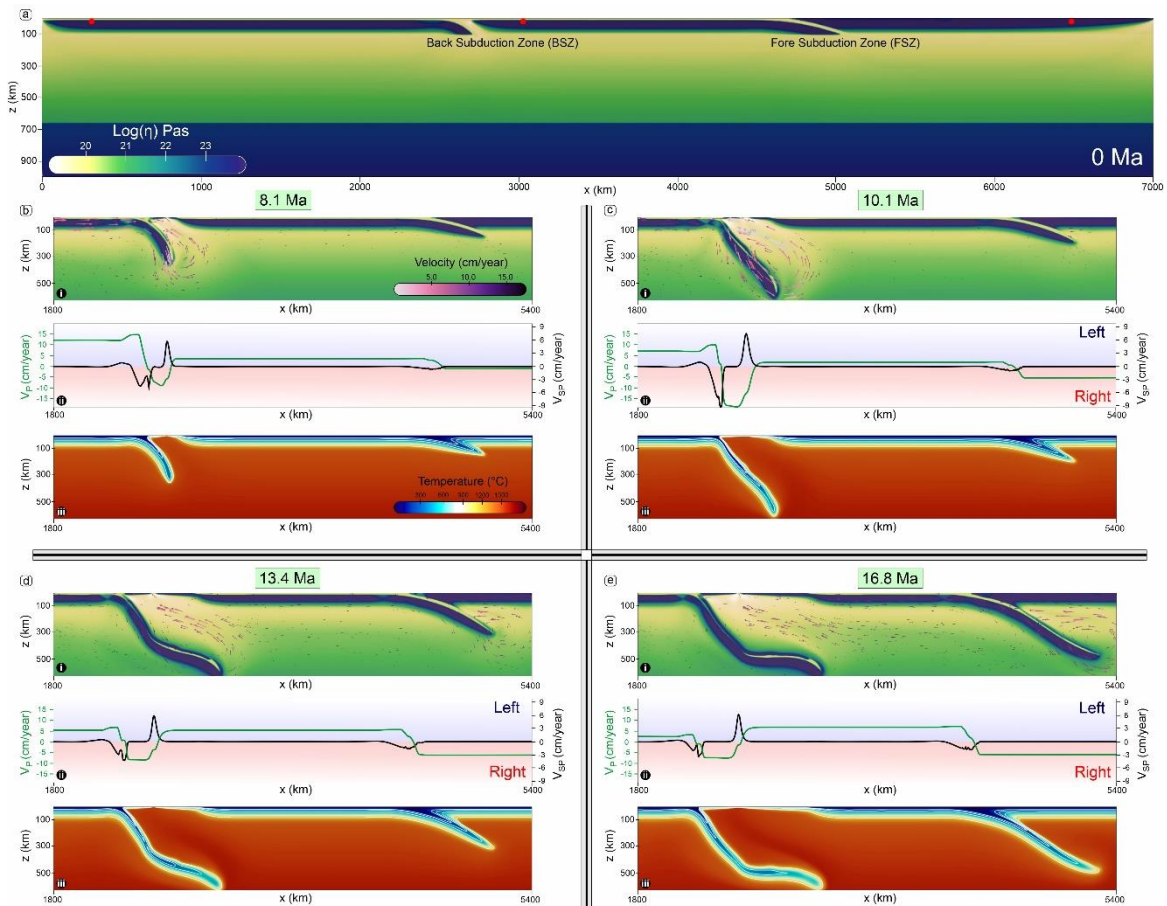
Figure 5.5: Evolution of the double subduction model in an oceanic setting. Panels show: (a) the initial viscosity field of the complete numerical model domain, (b)-(e) evolution of the i) viscosity and velocity fields, ii) plate velocities (green) and subduction velocity (black), and iii) temperature field, zoomed into a region around the subduction zone for four time-steps corresponding to the back subduction initiation (t= 8.1 Ma), back subduction free sinking (t= 10.1 Ma), frontal subduction initiation (t= 13.4 Ma) and mature double subduction (t = 16.8 Ma) phases.

oceanic plate generation. At ~ 6 Ma, the newly generated lithosphere constitutes a well-developed overriding plate (OP) structure in the subduction zone. This phase of the tectonic setting evolves in a typical single-subduction dynamics, allowing the

proto-slab to subduct to a depth of ~300 km with a convergence rate (V_C) of ~ 13 cm/yr (with respect to its adjoining overriding oceanic plate) on a model run time of 8.1 Ma (Fig 5.5b). The BSZ oceanic plate, which is tectonically the most active unit at this stage, approaches the trench with a velocity (V_P) of ~+12 cm/year (+ sign denotes movement towards right), although the trench itself retreats with a velocity (V_{LT}) of ≈-2.5 cm/yr. The plate convergence velocity (V_C) accelerates further with increase in the total negative buoyancy to attain a maximum value of ~15 cm/year at ~9 Ma (Fig. 5.8a) and the BSZ slab dip (at 125 km depth) steepen to ~45°. At a model run time of 10.1 Ma, the slab encounters the lower mantle at a depth of 660 km and decelerates ($V_P \approx 7.5$ cm/yr) due to higher viscous resistance offered by the strong lower mantle. This slab-lower mantle interaction also forces the oceanic plate to slow down its convergence motion ($Vc \approx 12$ cm/year) (Fig. 5.8a), prompting the other proto-slab to activate its subduction motion and result in the initiation of the fore subduction zone (FSZ) (Fig. 5.5c). At this stage of plate evolution the tectonic setting transforms into a typical double-subduction configuration, albeit with significant asymmetry in terms of both slab geometry and kinematics, where the FSZ slab shows much shallower dip (20° at 125 km depth) and lower convergence velocity ($V_c^{RS} \approx 7$ cm/yr) than the back subducting slab. In addition, the BSZ trench retreats significantly faster ($V_{LT} \approx 9$ cm/yr) than the FSZ trench ($V_{RT} \approx 2.5$ cm/yr). The cumulative effects of double-subduction motion facilitate the convergence velocity (Vc) that declined after ~9 Ma (Fig. 5.8a) due to the slab-lower mantle interaction.

The double-subduction system always maintains an active state of the spreading centre, which in turn continues to produce new lithospheric materials in the oceanic setting. At around ~13.4 Ma, the BSZ verges to a declining stage, marked by a significant drop in V_P (~ 5 cm/yr), although its trench continues to retreat with V_{LT} ~

3 cm/yr. In contrast, the FSZ continues to remain active, where the subducting slab sinks rapidly into the upper mantle to facilitate the convergence plate velocity ($V_P \approx 5$ cm/year) as well as the trench retreat velocity ($V_{RT} \approx 7$ cm/year). However, the double-subduction system cumulatively shows a decreasing trend of the net convergence plate velocity ($V_c \approx 11$ cm/yr). At ~16.8 Ma, the back subducting slab leans back as V_{LT} (≈ 3.5 cm/year) exceeds V_P (≈ 2.5 cm/year) and the double-subduction evolves a steady state condition of the BSZ in terms of V_c and slab dip (~55°). On the opposite side however, the oceanic plate associated with the fore subduction zone attains a maximum velocity $V_P \approx 6.5$ cm/year, which is significantly higher than the back subducting plate velocity. The FSZ slab then moves through the entire upper mantle to encounter the lower mantle and eventually slows down its velocity. The corresponding trench continues to retreat with $V_{RT} = 6$ cm/yr, which subsequently surpasses the FSZ plate velocity in course of the subduction evolution (>20 Ma). The total convergence velocity attains a steady configuration with a constant velocity of ≈ 8.5 cm/year which continues to the end of the model run.

Subduction-induced mantle circulation that evolves with the double subduction process critically controls the dynamic conditions in convergent margins. In the initiation stage of the BSZ, the slab-driven flow has both vertical and horizontal components, forming a flow vortex circulating with its centre around the subducting slab. The vortex remains active till ~10Ma, and weakens as the BSZ slab decelerates on its encounter with the 660 km discontinuity. The vortex location then shifts to the FSZ slab and the flow intensifies with time. At ~13Ma, the double-subduction system sets in a strong slab-parallel upward flow beneath the spreading centre. This sub-lithospheric flow strengthens further on combination with the back flow generated

by the fore subducting slab (Fig 5.5e-i), and acts as a robust mantle-material feeding system to the spreading centre, which facilitates the lithospheric accretion rates.

5.5.2. *MICROCONTINENT - OCEANIC PLATE SETTING*

The micro-continent-bearing oceanic plate setting consists of an already initiated subduction in the front (FSZ: fore subduction zone) and the lithospheric weakness between the microcontinent and the oceanic plate results in the initiation of the back subduction zone (Fig. 5.6a). This results in the formation of a double-subduction system at an early stage ($\sim$ 6 Ma) of the model run, as evident from a convergence velocity V_C = $\sim$5 cm/yr (Fig. 5.8b). The subduction zones, however, grow at different rates, where the FSZ subduction is much more active than the BSZ. This difference in the subduction rates leads to an activation of a rift between the FSZ oceanic plate and the microcontinent. The rift subsequently acts as a spreading centre, allowing upwelling of the underlying mantle material to the surface and generate new oceanic lithosphere between the continental and the fore oceanic plates. At $\sim$ 6.1 Ma, the BSZ proto-slab subducts to a depth of $\sim$200 km into the upper mantle, and this subduction motion forces the continental block to act as an OP, moving trench-ward at a velocity $V_P \approx$ -7 cm/year. The formerly passive continental margin consequently transforms into an active convergent tectonic setting. The FSZ slab, on the other side, continues to subduct freely into the upper mantle, setting the entire plate to move at a high velocity ($V_P \approx$+10 cm/yr) (Fig. 5.6b). During this phase of tectonic evolution both the trenches retreat, but with contrasting velocities; the BSZ trench retreats at a much faster rate ($V_{LT} \approx$ -6.5 cm/yr) than the FSZ ($V_{RT} \approx$ -3.8 cm/yr). The convergence velocity (V_C) between the main OP and the BSZ slab is $\approx$7 cm/year, which increases to attain a high value ($V_C \approx$13 cm/yr) on a model run time of $\sim$9 Ma (Fig. 5.8b). The fore

oceanic slab reaches the lower mantle at ~ 10.5 Ma, and begins to slow down its velocity ($V_P \approx +7$ cm/yr) as it encounters higher viscous forces in the 660 km transition zone. The BSZ slab, however, continues to subduct through the upper mantle and maintains the back oceanic plate movement at a velocity of ≈ +8 cm/year. The BSZ trench at the same time retreats, but with a reduced velocity ($V_{LT} \approx$ -5 cm/yr), whereas

Figure 5.6: Evolution of the double subduction model in presence of a continental block. Panels show: (a) the initial viscosity field of the complete numerical model domain, (b)-(e) evolution of the i) viscosity and velocity fields, ii) plate velocities (green) and subduction velocity (black), and iii) temperature field, zoomed into a region around the subduction zone for four time-steps corresponding to the fore subduction free sinking (t= 6.1 Ma), back subduction free sinking (t= 10.5 Ma), mature double subduction (t= 15.9 Ma) and fore subducting slab detachment (t = 28.6 Ma) phases.

the FSZ trench continues to retreat at a steady rate (V_{RT} ≈ +4 cm/year). The convergence velocity is high (V_C ≈13 cm/year) although it begins to show a diminishing trend after this period. On a model run time of ~15.9 Ma, both the subducting oceanic slabs lower their dips to become almost flat, and significantly

reduce the plate velocities ($V_P \approx$ +2.5 cm/yr and $\approx$ +3.5 cm/yr for FSZ and BSZ slabs, respectively). The relatively buoyant juvenile (~15 Ma) lithosphere, formed at the spreading centre, eventually reaches the FSZ trench and its subduction accelerates the retreat motion ($V_{RT} \approx$+7.5 cm/year). This motion reduces its slab dip from 30° to ~26° (Fig. 5.6d), which starts to increase exponentially after ~18 Ma. The BSZ trench retreat velocity (V_{LT}) increases to -5.5 cm/yr during this period. At ~25 Ma, the FSZ slab undergoes break-off at the location of maximum tensile stresses developed by the negative buoyancy induced slab pull.

In this double-subduction system the spreading centre located between the two trenches remains active, continuously adding new lithosphere to accommodate the increasing space between the continental block and the fore oceanic plate. At ~28.6 Ma, the spreading centre, however, becomes almost inactive as the upwelling process is replaced by slab-driven horizontal flows in the mantle region between the two subducting plates. The entire newly formed lithosphere is coherently coupled with the main OP, as revealed from the plate velocity ($V_P \approx$ -5 cm/year). The double subduction system ceases to exist due to the absence of slab pull force at the FSZ trench and transforms into a single subduction system.

5.5.3. MULTIPLE-CONTINENTAL PLATE SETTING

The modelling of a multiple-continental setting primarily aims to investigate the influence of continental plates on the process of subduction initiation and evolution, leading to the formation of a double-subduction system. The model run shows that subduction localize preferentially along the lithospheric weakness and initiates the fore subduction zone (FSZ), leaving the trailing weak zone at the continent-oceanic plate interface almost inactive (Fig. 5.7b). At this stage (~ 4 Ma)

146

the system follows mostly single-subduction dynamics, allowing the FSZ slab to penetrate into the upper mantle to a depth of ~ 200 km. This plate velocity (V_P) increases to $\sim+7.5$ cm/year on a model run time of 8.5 Ma (Fig. 5.7b). The velocity field indicates that the lithospheric plates move coherently as a single unit to subduct
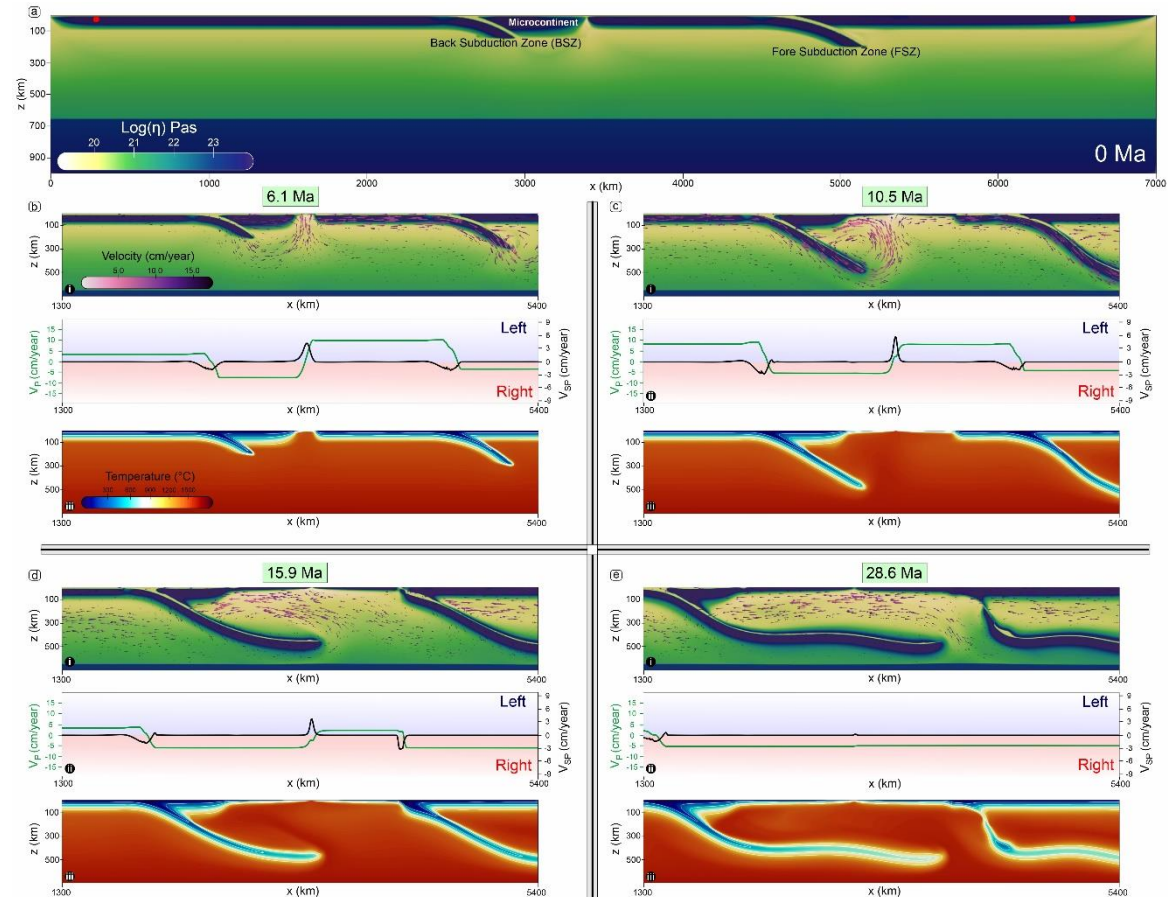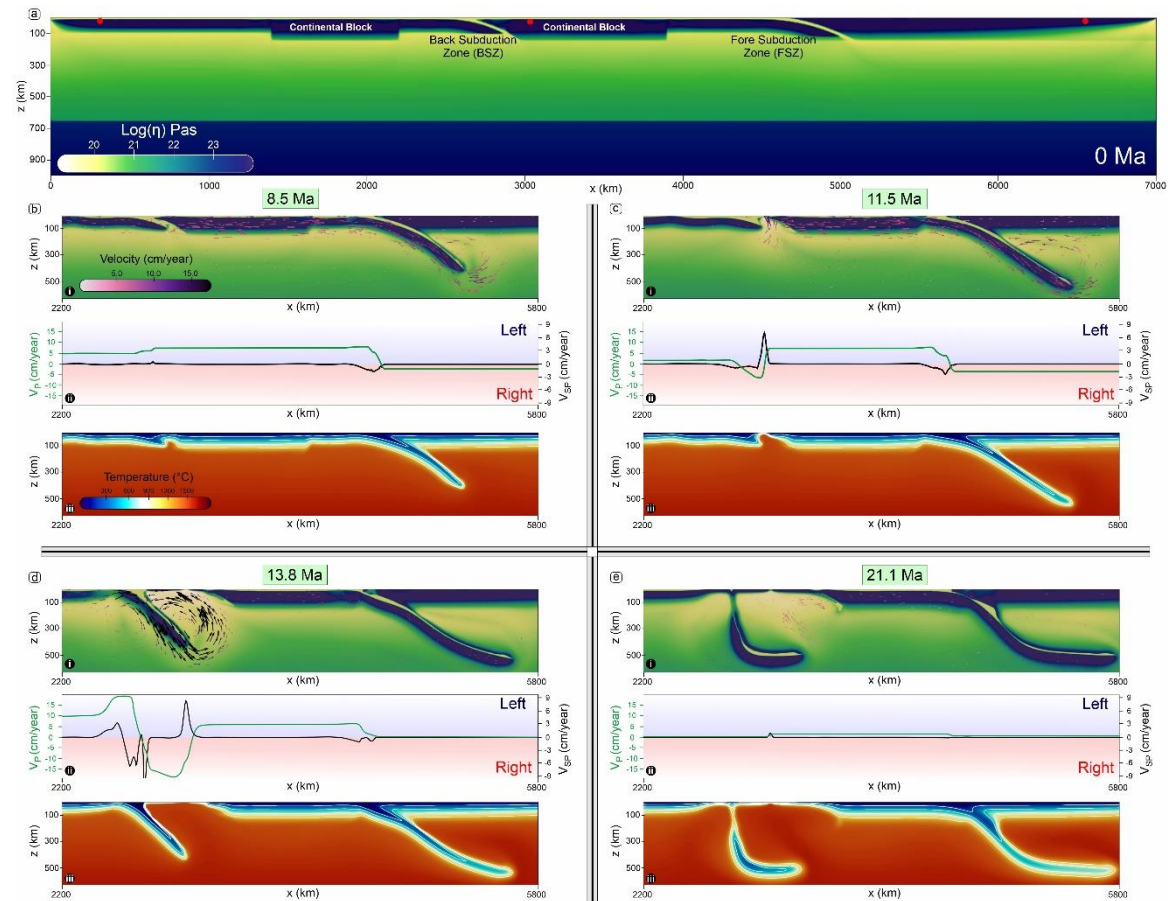

Figure 5.7: Evolution of the double subduction model in presence of multiple continental plates. Panels show: (a) the initial viscosity field of the complete numerical model domain, (b)-(e) evolution of the i) viscosity and velocity fields, ii) plate velocities (green) and subduction velocity (black), and iii) temperature field, zoomed into a region around the subduction zone for four time-steps corresponding to the fore subduction free sinking (t= 8.5 Ma), continental collision (t= 11.5 Ma), back subduction initiation(t= 13.8 Ma) and back subducting slab detachment (t = 21.1 Ma) phases.

beneath the FSZ trench although a lithospheric weakness is present in between them ($V_P \approx +5$ cm/year for back oceanic plate). This implies that the FSZ entirely determines the dynamics of the system at an early stage. The fore oceanic plate progressively accelerates its motion to attain a convergence rate ($V_c^{RS} \approx 8$ cm/year, Fig. 5.8c solid blue line) with respect to the OP at $\sim$11.5 Ma. At this stage the subduction system

undergoes a remarkable kinematic transformation, leading to plate decoupling at the back lithospheric weakness that eventually triggers mantle upwelling and accretion of new lithospheric materials to form a thin overriding plate. This decoupling decelerates the back plate motion ($V_P \approx +1$ cm/year) and brings it almost to a halt. In contrast, the fore slab continues to maintain a high plate velocity ($V_P \approx +7.5$ cm/year)
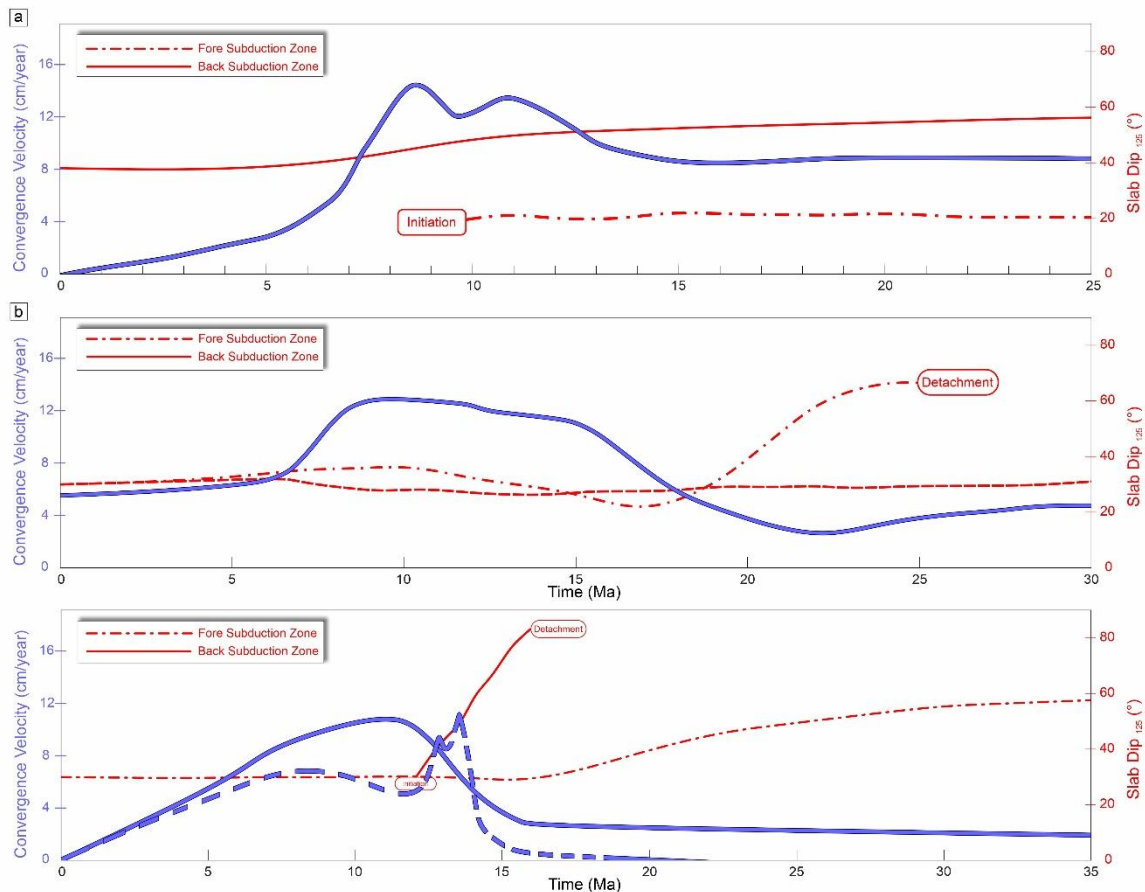
Figure 5.8: Temporal evolution of subduction zone convergence rates and shallow slab dips (at depth = 125 km) of fore and back subducting slabs, for double subduction in a) oceanic setting, b) microcontinent - oceanic plate setting and, c) multiple continental plate setting.

and a high convergence rate (V_c^{RS} = +7.5 cm/year), along with a moderate trench retreat rate ($V_{RT} \approx$ -3.5 cm/yr). At ~ 12.5 Ma, the back subducting slab gains significant a slab-pull velocity ($V_{SP} \approx$ -10 cm/year), which consequently causes the back subduction zone (BSZ) to initiate. The proto-slab continues to move through the upper mantle, setting the convergence velocity rapidly accelerate to attain a value of ~11 cm/year at 13.8 Ma. On the other side, the FSZ slab reaches the 660-km transition

zone and slows down its overall sinking velocities. The continental block in this plate reaches the trench and collides with the overriding plate, switching a reversal in the trench motion to advance at a rate $V_{RT} \approx +2$ cm/yr. The collision event also reduces the plate velocity ($V_P \approx +5$ cm/yr) as well as the convergent velocity ($V_c^{RS} \approx 4.5$ cm/yr) at ~15 Ma. The BSZ eventually fails to compete with the FSZ as it faces steepening of the slab dip (> 65° at 125 km), which is followed by slab-detachment. The continental block, which has lower compositional density, i.e. positive buoyancy, plays an instrumental role to facilitate triggering the slab detachment at ~ 16 Ma. In course of the double-subduction evolution (~21.1 Ma), the plate velocities drastically drop to ~ 2.5 cm/year and the tectonic setting transforms into a single subduction system.

5.5.4. *THERMAL EVOLUTION OF DOUBLE-SUBDUCTION SYSTEMS*

The present thermo-mechanical models are utilized also to study the thermal evolution in an oceanic double-subduction system (cf., (Holt & Condit, 2021) , with a focus on the crustal bottom (oceanic slab Moho) and the surface (oceanic slab top) depths (D_{MOHO} and D_{TOP}) intersected by an isotherm ($T = 450$ °C). Calculated D_{MOHO} and D_{TOP} bound the depth range expected to be recorded from exhumed crustal rocks for a particular temperature. In the oceanic plate setting, low convergence rates (< 4 cm/yr) are accompanied by high slab-Moho (T_{MOHO}) and slab-top temperatures (T_{TOP}) in the BSZ initiation stage, yielding $D_{MOHO} \approx 48$ km (corresponding $P = 1.6$ GPa) and $D_{TOP} \approx 20$ km (corresponding $P = 0.7$ GPa) (Fig. 5.9a). The model predicted slab temperatures are consistent with several petrological interpretations of warm subduction conditions (Agard et al., 2018, 2020; Cloos, 1985). Model results also show that both the slab-Moho and -top in the BSZ undergo rapid cooling during the period (~9 Ma) of its initiation, followed by a phase of more protracted cooling.

Considering the slab top at a depth of 100 km, the cooling occurs at a rate of ~ 35 °C/Ma in the first 8.5 Ma time, and then steeply reduces to ~12 °C/Ma (Fig. 5.9b). This can also be observed by the progressive increase in the slab top isotherm depth throughout the 25 Ma of back subduction evolution (Fig. 5.9a). As e.g. the isotherm starts from an initial depth of ≈12 km, and reaches a depth of ≈52 km by the time of our mature subduction snapshot. The thermal evolution of slab Moho is more complex than the corresponding slab top, as the Moho undergoes additional rapid cooling (~ 140 °C/Ma) following the phase of moderate cooling (~22 °C/Ma) at the time of subduction initiation. The thermal state of this rapid slab sink is transient, persisting for 4 to 5 Ma, and is more pronounced at greater depth, as an example, the 450°C isotherm at the Moho is dragged down to $D_{MOHO} \approx 240$ km, which exceeds the
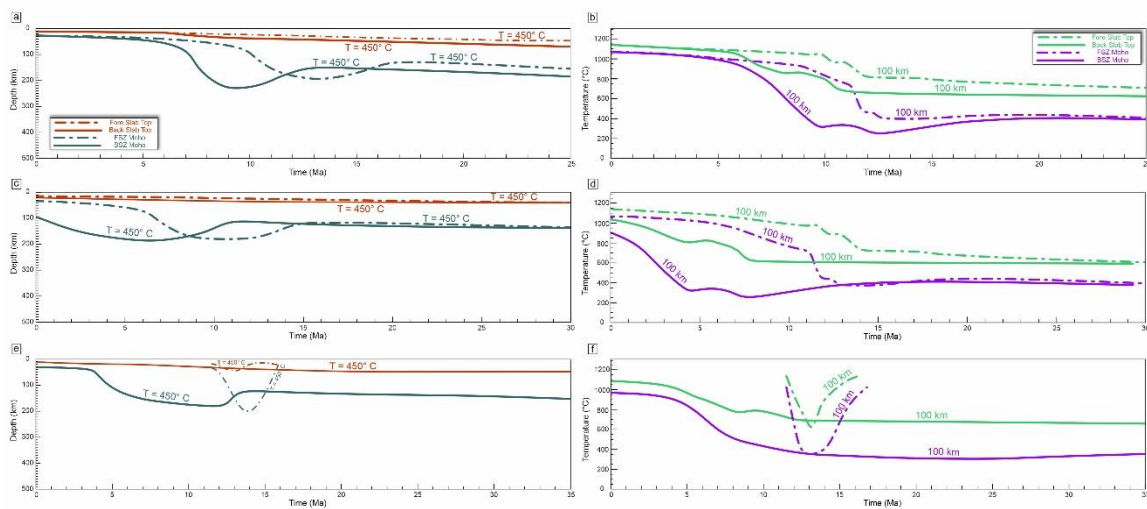
Figure 5.9: Temporal evolution of the depth of the 450°C isotherm along the slab top and slab Moho for double subduction in a) oceanic plate setting, c) microcontinent - oceanic plate setting and, e) multiple continental plate setting, and the temperature at a depth of 100 km along the slab top and slab Moho for double subduction in b) oceanic setting, d) microcontinent - oceanic plate setting and, f) multiple continental plate setting.

background cooling trend by ~100 km (Fig. 5.9a). The cooling phase ends as the subduction slows down, leaving the slab Moho temperatures to increase with time. The fore subduction zone (FSZ) evolves similarly compared to the BSZ. The calculated $D_{MOHO} \approx 42$ km and $D_{TOP} \approx 12$ km in the FSZ initiation stage (Fig 5.9a), changes to D_{MOHO}

≈176 km and D_{TOP} ≈22 km at ~14 Ma as the fore subducting slab moves through the upper mantle. The fore slab Moho also undergoes rapid cooling (120 °C/Ma) from ~8Ma to ~14 Ma after which the slab begins to gain temperature as it slows down due to the interaction with the 660 km boundary.

The other two models showed the temperature evolution almost similar to the above discussed oceanic setting model. I also evaluated the heat flow rates and their spatio-temporal patterns in the oceanic double-subduction setting. Excluding the variability due to local effects, such as shallow magmatic intrusion, the surface heat flow increases by about 50 mW/m² from forearc to arc (Tanaka et al., 2004; Wada et al., 2008). The present models yield a similar pattern of surface heat flow (~55 mW/m²) (Fig. 5.10).
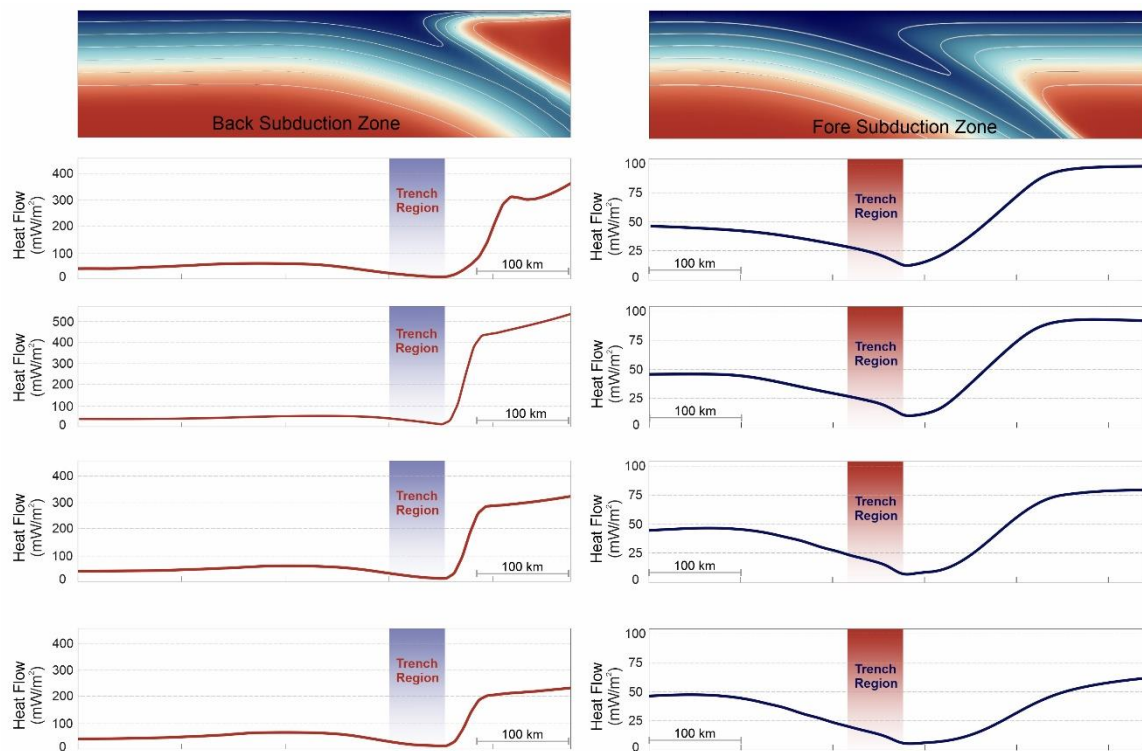
Figure 5.10: Temporal evolution of surface heat flow values for double subduction in oceanic plate setting with zoomed in calculations shown for both back and fore subduction zone.

5.6. NATURAL DOUBLE-SUBDUCTION SYSTEMS: CASE STUDIES

Temporal changes in the thermal structure and the tectonic architecture of double subduction systems observed in the numerical models can be compared to different natural subduction zones where two plates subduct in close proximity to each other. In this section, dynamics of such natural double subduction zones are discussed in the light of our numerical model findings.

5.6.1. MAJOR DOUBLE-SUBDUCTION SYSTEMS

A classical natural example of a double-subduction system is the Izu-Bonin-Mariana (IBM) subduction and Ryukyu subduction zone in the western Pacific Ocean. The Izu-Bonin-Mariana (IBM) and Ryukyu trenches involve the subduction of two separate oceanic plates leading to the formation of double subduction architecture in an oceanic setting (Čížková & Bina, 2015; Faccenna et al., 2018). In the IBM region, the Pacific Plate subducts beneath the Philippine Sea Plate, while in the Ryukyu region, the Philippine Sea Plate subducts beneath the Eurasian Plate. This double subduction system contributes to the complex tectonic activity and geodynamic processes occurring in the Izu-Bonin-Mariana and Ryukyu regions. The IBM double-subduction system is known for its associated volcanic activity, with the formation of volcanic arcs, back-arc basins, and deep-sea trenches. The system has played a significant role in the formation of the Izu-Bonin-Mariana Island Arc, which includes volcanic islands such as the Marianas Trench, and has been instrumental in the study of plate tectonics and subduction zone processes. The Philippine Sea Plate is surrounded by subduction zones and has formed through sea-floor spreading and back-arc spreading along multiple axes. The oldest section, known as the West Philippine Basin, developed between 54 to 30 million years ago (Ma). Subsequently,

spreading occurred in the Shikoku and Parece-Vela basins from around 30 Ma to 15 Ma, with three distinct stages of spreading observed. This change in spreading direction may be attributed to the clockwise rotation of the Philippine Sea Plate. The spreading rates ranged from 2 to 3 cm/yr to 5-6 cm/yr, resulting in a total retreat of the Izu-Bonin trench by approximately 1000 km along its northern portion. The third episode of extension, which is ongoing, occurred behind the Mariana Trough and began around 7 Ma. The evolution of this subduction system is complex due to variations in subduction initiation and cessation, as well as the northward migration of the Ryukyu-Izu Bonin triple junction. Subduction at the Izu-Bonin-Mariana Trench began approximately 54 Ma, with the northward migration of the triple junction leading to the Pacific Plate initiating subduction in the northern Ryukyu region, which was later replaced by the Philippine Sea Plate. The subduction of the Philippine Sea Plate was interrupted by the entrance of the Gagua Ridge, a paleotransform plate boundary, into the trench. This led to a slab break-off event. After the slab break-off, subduction of the Philippine Sea Plate resumed along the Ryukyu Trench, forming the present-day Ryukyu subduction system. Around 10 million years ago, there was a fundamental change in the kinematics of trench motion, transitioning from eastward retreat to westward advancement of the Izu-Bonin-Mariana Trench. The total westward advance of the trench since then is estimated to be approximately 70 km. Paleomagnetic data suggests clockwise rotation and northward drift of the Philippine Sea Plate, indicating trench advance over the past 5 million years. The timing of the triple junction between Ryukyu, Izu, and Japan can be inferred from paleomagnetic data, indicating westward movement since around 3 million years ago.

5.6.2. EVOLUTION OF THE ANDAMAN SUBDUCTION SYSTEM

In the case of the Andaman Subduction System (Fig. 5.11), the currently active subduction occurs at the northern flank of the Java trench where the oceanic part of the Indian Plate subducts at a low angle to the arc-trend beneath a small continental block as the overriding plate (Fig. 5.6). This continental fragment, which is a detached part of the larger Indian Plate occurs parallel to the volcanic arc, forming the Andaman
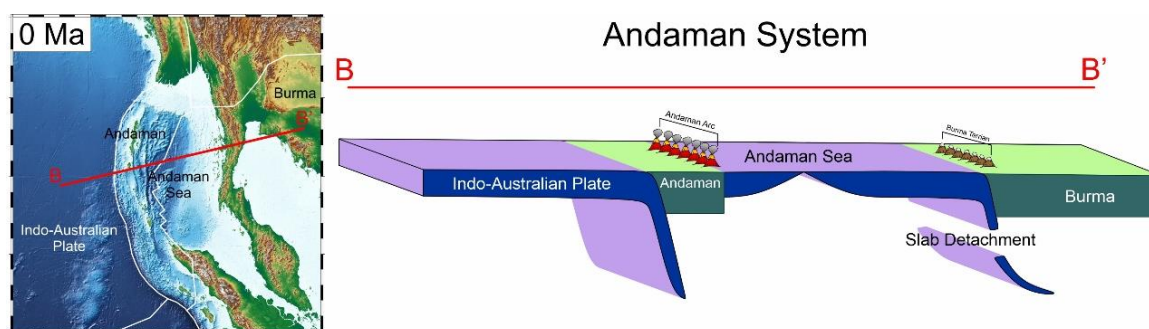
Figure 5.11: Map of the Andaman subduction zone and its vicinity with a cross section along BB' showing slab geometries and distances between subduction systems and the Andaman micro-continent.

Island Chain. The Pliocene-Holocene volcanism in the inner arc of the Java Trench suggests that the subduction has remained active since the late Miocene (Acharyya et al., 1990). The Andaman Sea, a manifestation of extensional tectonics and other similar basins in this region also opened up in the late Miocene (Curray, 2005). The Andaman Ophiolites occur in a flat-lying arrangement, showing a close spatial association with a zone of negative gravity anomalies that suggest their occurrence as rootless sub-horizontal bodies. Moreover, the ophiolite suits range in age between late Mesozoic and early Eocene, much older than the Andaman Sea crust. These evidences indicate that the Andaman and other related ophiolites farther north in this convergent zone were derived from a suture to the east during late Oligocene time and emplaced as nappes during the middle Eocene. The geochronological order indicates the existence of a second subduction zone at the time of late-Miocene subduction (continuing to present day) and opening of the Andaman Sea (P. K. Khan

& Chakraborty, 2005). The micro-continent- oceanic plate model (Fig. 5.6) ideally represent such a tectonic evolution in SE Asia. The FSZ replicates the mid-Eocene subduction event where the Indo-Australian oceanic lithosphere continued to subduct beneath the Burma Plate (equivalent to the stiffer OP in the model). The model setup produces a spreading centre (extensional zone) as a consequence of some pre-existing lithospheric flaws, switching a remarkable change in the course of the general single subduction system. The opening of this extensional zone led to the late Miocene emergence of the Andaman Sea basin. The microcontinental fragment (Andaman continental block in nature) eventually decoupled itself from the ongoing subducting slab, and initiated a second subduction in the same region, as observed in our model run time of ~6 Ma. The newly formed subduction can be compared with the presently active Indo-Australian oceanic subduction below the Java Trench. The model suggests that both the subduction remained active for a considerable time (~24 Ma), and facilitated the Indo-Australian Plate motion relative to the Burma Plate. With time, the younger oceanic lithosphere formed at the Andaman Sea spreading centre drifted to the trench close to the Burma Plate and resulted in oceanic slab detachment as the lithosphere failed to gain density required for the mid-Eocene subduction.

5.6.3 EVOLUTION OF THE INDIAN SUBDUCTION SYSTEM

The Trans-Tethyan intra-oceanic system evolved through multiple subduction episodes in the Neo-Tethys during the Cretaceous to Early Tertiary period. This system consisted of a north-dipping oceanic slab of the Kshiroda Plate subducting beneath the southern margin of Eurasia (Yin & Harrison, 2000) and a second, intra-oceanic subduction, where the northern oceanic part of the India Plate subducted

beneath the Kshiroda Plate (Fig. 5.12). Geological, geochemical, and paleomagnetic studies of the tectonic units i.e., forearc sequences and oceanic melange sequences, ophiolite sequences (Aitchison et al., 2000; Bouilhol et al., 2013; R. Hall, 2012; Yin & Harrison, 2000; Zaman & Torii, 1999) in the Himalayas that grew during the India-Eurasia convergence substantially suggest the occurrence of a pair of nearly parallel, northward dipping subduction zones between the Indian and Eurasian plates during the Early Cretaceous period. Tomographic evidence of the two remnant slabs (Van Der Voo et al., 1999) observed beneath the Indian plate further support the existence of the same slab-dip facing double-subduction system. The convergence history, derived from the plate reconstructions and paleomagnetic interpretations (Cande et
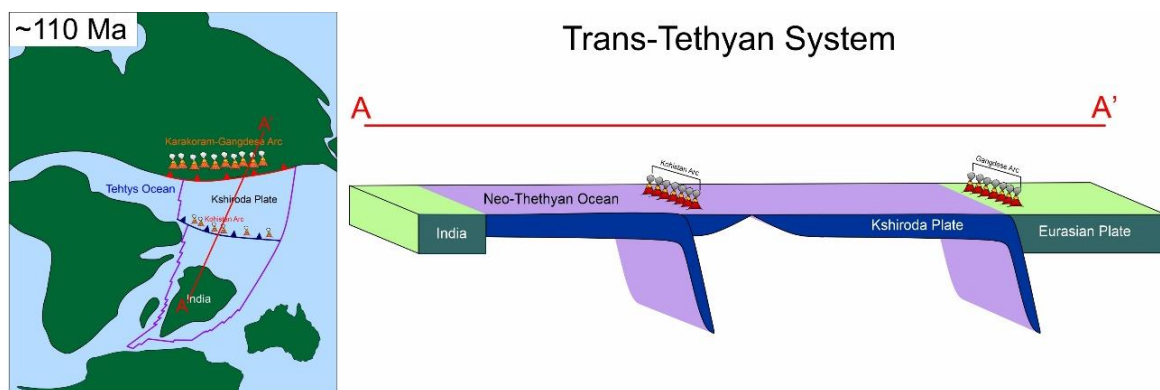
Figure 5.12: Sketch showing the reconstructions of Neo-Tethyan plate boundaries at ~110 Ma with a cross section along AA' showing slab geometries and distances between the two prominent subduction systems giving rise to the double subduction process.

al., 2010; Cande & Stegman, 2011; Copley et al., 2010; Van Hinsbergen et al., 2011) reveal that, during the Indo-Eurasian convergence the Indian Plate had a rapid northward drift moving at rates > 10 cm/year from 70 Ma to 45 Ma (Copley et al., 2010; Molnar & Stock, 2009), which subsequently reduced to 7.5 cm/year at ~40 Ma that marks the timing of India-Eurasia collision (Maiti et al., 2021). The oceanic plate model presented in Section 5.5.1. provides new insights into the geodynamic and thermal evolution of the Trans-Tethyan intra-oceanic system. The subducting oceanic plates in the model BSZ and FSZ represent the frontal oceanic part of the Indian Plate

and the Kshiroda Plate respectively is association with the Eurasian overriding plate. Pre-existing lithosphere-scale weaknesses, such as transform faults or oceanic fracture zones between the Kshiroda and the Indian Plate nucleated the subduction initiation at the leading edge of the Indian oceanic lithosphere, almost synchronously accompanied by opening of a proto back-arc extensional zone. The subduction event resulted in arc formation, preserved as the Kohistan-Ladakh Arc in the Himalaya-Tibet Mountain system (Bouilhol et al., 2013). A correlation of the arc initiation timing with the paleomagnetic data reveal that the Kohistan–Ladakh Arc rocks and ophiolites in the Tsangpo-suture zone formed nearly at the equator position (Aitchison et al. 2000, Zaman, H. & Torii, M, 1999). After ~4 - 5 Ma from the intra-oceanic subduction initiation, the passive margin between the Kshiroda and Eurasian
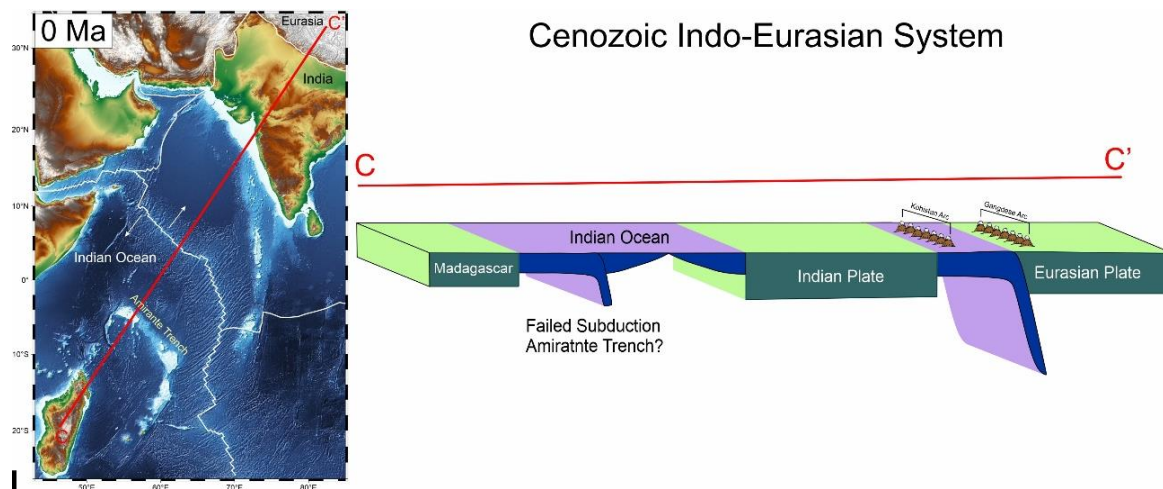
Figure 5.13: Map showing the present day Indo-Eurasia collisional system with a cross section along CC' showing slab geometries and distances between the subduction systems.

Plates became active to form a second subduction (FSZ) (Fig. 5.5), which gave rise to the Gangdese-Karakoram continental arc. The paleomagnetic data of magmatic rocks indicate that the arc formed at a latitudinal position ~20°–25° N, suggesting a distance of ~2500 km from the Kohistan Arc, which is consistent with the present model estimates. The model convergence history reveals a period of rapid convergence with velocities > ~15 cm/year for a period of ~8 Ma before reducing to ~9 cm/year in the

later phase of the model run. This two-stage kinematic evolution is also in agreement with the Cretaceous convergence history of the Indo-Eurasian system prior to the Early Cenozoic slowdown (Molnar & Stock, 2009).

The India-Eurasia convergence during the Cenozoic period had a collision between the continental Indian with the Kohistan arc (Burg 2011) and subsequently, with the Gangdese-Karakoram continental arc, resulting in the closure of the Neo-Tethyan basin. The opening of the Carlsberg Ridge in the Indian Ocean basin characterises the region south of the Indian continent (Fig. 5.13). The multiple continent – oceanic plate model perfectly reproduces the Cenozoic Indo-Eurasian collisional tectonic history. It is noteworthy the model aims to reproduce the collision of the Indian continental plate with the Kohistan Arc (*ca* >60 Ma) (Ding et al., 2005; S. D. Khan et al., 2009; Yin, 2006) when the oceanic subduction below Eurasia was active. Interestingly, the Carlsberg ridge had a fast spreading in during late Cretaceous (Merkouriev & Sotchevanova, 2003), which is observed in our model that forms a spreading ridge and a second subduction in the ridge's vicinity. Based on our model results, we propose that the subduction occurred at the present-day position of the Amirante Trench- a trough-like feature, approximately 600 km long in the western Indian Ocean. Geological and geophysical studies show evidence of partial or limited subduction within the trench (Miles, 1982). As observed in our model, the subduction was active in this region for ~4 Ma, which ceased to remain active following the slab detachment under the influence of a continental block (analogous to the Madagascar continental fragment in nature). The collision between the Indian and Eurasian continents led to a dramatic shift from retreating to advancing trench motion and a decrease in the Carlsberg ridge spreading rate, both of which are compatible with the model results.

5.7. GEOLOGICAL IMPLICATIONS OF DOUBLE-SUBDUCTION TECTONICS

5.7.1. DOUBLE-SUBDUCTION EVOLUTION BY FEEDBACK MECHANISMS

Convergent plate tectonics often evolve in a complex manner, forming multiple subduction zones that mutually interact with one another during the convergent motion (Dasgupta & Mandal, 2022; Faccenna et al., 2018; Holt et al., 2017; Mishin et al., 2008; Pusok & Stegman, 2019). From numerical model experiments this study shows that a double-subduction system can grow spontaneously from pre-existing weak zones (Bercovici & Ricard, 2014) in the lithospheric plates under slab-pull dynamics. The two subduction zones in such systems, however, evolve in a competing mode, one suppressing the other, ultimately leading to their unequal development on a million year timescale. To elaborate this discussion, consider our double-subduction model for an oceanic plate setting presented in Section 5.5.1. The model shows synchronous initiation of subduction at two lithospheric weak zones, but one of them preferentially becomes the most active zone (subduction velocity: ~11 cm/yr), suppressing the other slab motion to remain significantly weak (~1.5 cm/yr). This competing double-subduction dynamics causes the second subduction to become more active once the first subducting slab encounters the lower mantle at 660 km. The retarding slab motion, coupled with a trench retreat motion in one subduction has a feedback effect on the second subduction in accelerating slab motion (~1.5 cm/yr to ~6 cm/yr).

The other two model settings show similar feedback effects on the development of double-subduction systems. In the microcontinent-bearing oceanic plate setting the double subduction processes operate almost equally (Fig. 5.6), forming a spreading centre between the two subduction zones. However, the new lithosphere

formed in the spreading centre causes the fore subduction zone (FSZ) to undergo slab detachment, which in turn facilitates the slab motion in the back subduction zone (BSZ). The multiple continental plate setting also shows a time-dependent interaction between the BSZ and FSZ during their evolution. The FSZ slab motion hardly allows the BSZ to become significantly active until the slab encounters the lower mantle to slow down its motion. The BSZ slab starts to actively sink when the BSZ almost reaches the upper-lower mantle boundary after a time of ~11 Ma. The feedback direction reverses as the BSZ experiences slab detachment due to resistance offered the continent in the subducting oceanic plate. Thus, the model examples discussed here suggest that the same-dip double-subduction systems generally evolve with a feedback relation between the two subduction zones which mutually interact with one another.

5.7.2. INFLUENCE OF CONTINENTAL HETEROGENEITIES

Double-subduction systems maintain the slab-pull and ridge-push force balance more complexly than single-subduction systems, and the complexity originates mainly from the effects of inter-slab interactions in plate bending and viscous dissipations in the mantle, coupled with additional factors, contrasting plate ages, plate dimensions, rheology, and inter-slab distance (Mishin et al., 2008; Cížková & Bina 2015; Holt et al., 2017). This study identifies the presence of microcontinental blocks or continental plates in oceanic plate tectonic settings as an additional influential factor in the dynamics and stability of a double-subduction system. Microcontinents are mostly surrounded by oceanic crusts, and they form by extension and breakup of continental masses, followed by plate boundary relocations. Jan-Mayen in the north-east Atlantic Ocean (Gaina et al., 2009; Peron-Pinvidic et al.,

2012b, 2012a), Andaman in the Indian Ocean (Bandyopadhyay et al., 2020) and a number of small isolated islands around Australia (Gaina et al., 2003) are typical examples of microcontinents. Our double-subduction model suggests that such microcontinents play a vital role in localizing a spreading centre (location of new lithosphere generation) between the two subduction zones. The spreading centre, however, remain active for a specific time span (~28 Ma), and its activity weakens following the slab detachment in the FSZ.

The model results suggest that an oceanic plate setting in the absence of any continental blocks can readily form double-subduction, initiated by pre-existing lithospheric weak zones in the plate setting. However, the presence of a buoyant continental fragment prevents selectively the subduction zones in front of this plate to mature with time, and forces the system to evolve unequally at the two trenches. Similarly, a multiple-continental assemblage reduces the convergence rates due to their buoyancy and continent-arc collision effects, described as *transference* by Stern (2004) to show the accretion-assisted continental growth mechanism. The reducing convergence rates result in tensile stresses in the subducting slab, eventually leading to slab detachment (Fig. 5.7). This model study indicates that microcontinental blocks can greatly influence the evolution of subduction processes, as reported from several natural subduction systems, such as the northern Luzon, the Puysegur (New Zealand) and the Andaman subduction zones (Bandyopadhyay et al., 2020; Zhu et al., 2023). The microcontinents provide a potential location of passive continental margin that transforms into a tectonically active region by subduction initiation. Due to their lower mechanical strength, as compared to large continental plates they localize subduction and facilitate the process to occur at faster rates.

5.7.3. SUBDUCTION-DRIVEN SPREADING CENTRES: LOCATION OF NEW PLATE GENERATION

Oceanic plates subduct beneath overriding plates of different mechanical characteristics, ranging from neutrally or positively buoyant thick continental plate to negatively buoyant thin oceanic plates. In single-subduction type of convergent boundaries the slab rollback is often accommodated by trench-ward movement of the overriding plate. In the case of double-subduction in oceanic plate setting, trench retreats at fast rates, hardly in balance with trench-ward overriding plate motion. This unbalanced kinematic state gives rise to opening at the trench, which eventually act as a spreading centre to form new lithosphere plates at the convergent boundary. The present numerical models show the importance of spontaneous formation of back-arc spreading centres in the subduction initiation between two oceanic plates. The initiation phase records oceanic plate subduction beneath newly formed lithosphere at high rates, as compared to that beneath the stiffer overriding plate, setting in different evolutionary paths of the P-T conditions for the two cases (Fig. 5.9a).

The model findings demonstrate that spreading centres crucially control the subduction dynamics in transforming a double- to a single-subduction system. The microcontinent- oceanic plate setting model shows the development of large tensile stresses in the region between the older subducting plate and the newly formed lithosphere at the trench, which causes the older slab to experience detachment. The slab detachment then stops the subduction activity, leaving the other subduction active. Spreading centres also play an important role in the onset of convergent setting and promotes decoupling in a large oceanic plate (e.g. *Exp-Oc_Oc*). Such tectonic processes are observed in natural systems, for example, the Cocos-Nazca

spreading centre where the spreading centre formed by splitting of the oceanic lithosphere, giving rise to the Farallon plate break up in the early Miocene.

5.8 REFERENCES

Acharyya, S. K., Ray, K. K., & Sengupta, S. (1990). Tectonics of the ophiolite belt from Naga Hills and Andaman Islands, India. *Proceedings of the Indian Academy of Sciences - Earth and Planetary Sciences*, *99*(2), 187–199. https://doi.org/10.1007/BF02839389/METRICS

Agard, P., Plunder, A., Angiboust, S., Bonnet, G., & Ruh, J. (2018). The subduction plate interface: rock record and mechanical coupling (from long to short timescales). *Lithos*, *320–321*, 537–566. https://doi.org/10.1016/J.LITHOS.2018.09.029

Agard, P., Prigent, C., Soret, M., Dubacq, B., Guillot, S., & Deldicque, D. (2020). Slabitization: Mechanisms controlling subduction development and viscous coupling. *Earth-Science Reviews*, *208*, 103259. https://doi.org/10.1016/J.EARSCIREV.2020.103259

Aitchison, J. C., Badengzhu, Davis, A. M., Liu, J., Luo, H., Malpas, J. G., McDermid, I. R. C., Wu, H., Ziabrev, S. V., & Zhou, M. fu. (2000). Remnants of a Cretaceous intra-oceanic subduction system within the Yarlung–Zangbo suture (southern Tibet). *Earth and Planetary Science Letters*, *183*(1–2), 231–244. https://doi.org/10.1016/S0012-821X(00)00287-9

Bandyopadhyay, D., van Hinsbergen, D. J. J., Plunder, A., Bandopadhyay, P. C., Advokaat, E., Chattopadhaya, S., Morishita, T., & Ghosh, B. (2020). *Andaman Ophiolite: An Overview*. 1–17. https://doi.org/10.1007/978-3-030-39843-9_1

Becker, T. W. (2006). On the effect of temperature and strain-rate dependent viscosity on global mantle flow, net rotation, and plate-driving forces. *Geophysical Journal International*, *167*(2), 943–957. https://doi.org/10.1111/J.1365-246X.2006.03172.X/2/M_167-2-943-EQ018.JPEG

Bercovici, D. (2003). The generation of plate tectonics from mantle convection. *Earth and Planetary Science Letters*, *205*(3–4), 107–121. https://doi.org/10.1016/S0012-821X(02)01009-9

Bercovici, D., & Mulyukova, E. (2021). Evolution and demise of passive margins through grain mixing and damage. *Proceedings of the National Academy of Sciences of the United States of America*, *118*(4), e2011247118. https://doi.org/10.1073/PNAS.2011247118/SUPPL_FILE/PNAS.2011247118.SAPP.PDF

Bercovici, D., & Ricard, Y. (2012). Mechanisms for the generation of plate tectonics by two-phase grain-damage and pinning. *Physics of the Earth and Planetary Interiors*, *202–203*, 27–55. https://doi.org/10.1016/J.PEPI.2012.05.003

Bercovici, D., Tackley, P. J., & Ricard, Y. (2015). The Generation of Plate Tectonics from Mantle Dynamics. *Treatise on Geophysics: Second Edition*, *7*, 271–318. https://doi.org/10.1016/B978-0-444-53802-4.00135-4

Bott, M. H. P. (1991). Ridge push and associated plate interior stress in normal and hot spot regions. *Tectonophysics*. https://doi.org/10.1016/0040-1951(91)90003-B

Bouilhol, P., Jagoutz, O., Hanchar, J. M., & Dudas, F. O. (2013). Dating the India–Eurasia collision through arc magmatic records. *Earth and Planetary Science Letters*, *366*, 163–175. https://doi.org/10.1016/J.EPSL.2013.01.023

Burg, J. P. (2011). The asia-kohistan-india collision: Review and discussion. *Frontiers in Earth Sciences*, *4*, 279–309. https://doi.org/10.1007/978-3-540-88558-0_10/COVER

Burg, J. P., Jagoutz, O., Dawood, H., & Shahid Hussain, S. (2006). Precollision tilt of crustal blocks in rifted island arcs: Structural evidence from the Kohistan Arc. *Tectonics*, *25*(5). https://doi.org/10.1029/2005TC001835

Burkett, E., & Gurnis, M. (2013). Stalled slab dynamics. *Lithosphere*, *5*(1), 92–97. https://doi.org/10.1130/L249.1

Burkett, E. R., & Billen, M. I. (2010). Three-dimensionality of slab detachment due to ridge-trench collision: Laterally simultaneous boudinage versus tear propagation. *Geochemistry, Geophysics, Geosystems*, *11*(11). https://doi.org/10.1029/2010GC003286

Byerlee, J., Mjachkin, V., Summers, R., & Voevoda, O. (1978). Structures developed in fault gouge during stable sliding and stick-slip. *Tectonophysics*. https://doi.org/10.1016/0040-1951(78)90068-9

Cande, S. C., Patriat, P., & Dyment, J. (2010). Motion between the Indian, Antarctic and African plates in the early Cenozoic. *Geophysical Journal International*, *183*(1), 127–149. https://doi.org/10.1111/J.1365-246X.2010.04737.X/2/183-1-127-TBL007.JPEG

Cande, S. C., & Stegman, D. R. (2011). Indian and African plate motions driven by the push force of the Réunion plume head. *Nature 2011 475:7354*, *475*(7354), 47–52. https://doi.org/10.1038/nature10174

Chen, L., Capitanio, F. A., Liu, L., & Gerya, T. V. (2017). Crustal rheology controls on the Tibetan plateau formation during India-Asia convergence. *Nature Communications*. https://doi.org/10.1038/ncomms15992

Čížková, H., & Bina, C. R. (2015). Geodynamics of trench advance: Insights from a Philippine-Sea-style geometry. *Earth and Planetary Science Letters*, *430*, 408–415. https://doi.org/10.1016/J.EPSL.2015.07.004

Čížková, H., van den Berg, A. P., Spakman, W., & Matyska, C. (2012). The viscosity of Earth's lower mantle inferred from sinking speed of subducted lithosphere. *Physics of the Earth and Planetary Interiors*, *200–201*, 56–62. https://doi.org/10.1016/J.PEPI.2012.02.010

Cloos, M. (1985). Thermal evolution of convergent plate margins: Thermal modeling and reevaluation of isotopic AR-ages for Blueschists in the Franciscan Complex of California. *Tectonics*, *4*(5), 421–433. https://doi.org/10.1029/TC004I005P00421

Conrad, C. P., & Lithgow-Bertelloni, C. (2002). How mantle slabs drive plate tectonics. *Science*, *298*(5591), 207–209. https://doi.org/10.1126/SCIENCE.1074161/SUPPL_FILE/CONRADSOM.PDF

Copley, A., Avouac, J. P., & Royer, J. Y. (2010). India-Asia collision and the Cenozoic slowdown of the Indian plate: Implications for the forces driving plate motions. *Journal of Geophysical Research: Solid Earth*, *115*(B3), 3410. https://doi.org/10.1029/2009JB006634

Crameri, F., Magni, V., Domeier, M., Shephard, G. E., Chotalia, K., Cooper, G., Eakin, C. M., Grima, A. G., Gürer, D., Király, Á., Mulyukova, E., Peters, K., Robert, B., & Thielmann, M. (2020). A transdisciplinary and community-driven database to unravel subduction zone initiation. *Nature Communications 2020 11:1*, *11*(1), 1–14. https://doi.org/10.1038/s41467-020-17522-9

Crameri, F., & Tackley, P. J. (2016). Subduction initiation from a stagnant lid and global overturn: new insights from numerical models with a free surface. *Progress in Earth and Planetary Science*, *3*(1), 1–19. https://doi.org/10.1186/S40645-016-0103-8/FIGURES/10

Curray, J. R. (2005). Tectonics and history of the Andaman Sea region. *Journal of Asian Earth Sciences*, *25*(1), 187–232. https://doi.org/10.1016/J.JSEAES.2004.09.001

Dasgupta, R., & Mandal, N. (2018). Surface topography of the overriding plates in bi-vergent subduction systems: A mechanical model. *Tectonophysics*, *746*, 280–295. https://doi.org/10.1016/J.TECTO.2017.08.008

Dasgupta, R., & Mandal, N. (2022). Role of double-subduction dynamics in the topographic evolution of the Sunda Plate. *Geophysical Journal International*, *230*(1), 696–713. https://doi.org/10.1093/GJI/GGAC025

Ding, L., Kapp, P., & Wan, X. (2005). Paleocene–Eocene record of ophiolite obduction and initial India-Asia collision, south central Tibet. *Tectonics*, *24*(3), 1–18. https://doi.org/10.1029/2004TC001729

Duretz, T., Gerya, T. V., & Spakman, W. (2014). Slab detachment in laterally varying subduction zones: 3-D numerical modeling. *Geophysical Research Letters*, *41*(6), 1951–1956. https://doi.org/10.1002/2014GL059472

Dymkova, D., & Gerya, T. (2013). Porous fluid flow enables oceanic subduction initiation on Earth. *Geophysical Research Letters*, *40*(21), 5671–5676. https://doi.org/10.1002/2013GL057798

Faccenna, C., Holt, A. F., Becker, T. W., Lallemand, S., & Royden, L. H. (2018). Dynamics of the Ryukyu/Izu-Bonin-Marianas double subduction system. *Tectonophysics*, *746*, 229–238. https://doi.org/10.1016/J.TECTO.2017.08.011

Forsyth, D., & Uyeda, S. (1975a). On the Relative Importance of the Driving Forces of Plate Motion*. *Geophysical Journal of the Royal Astronomical Society*, *43*(1), 163–200. https://doi.org/10.1111/J.1365-246X.1975.TB00631.X

Forsyth, D., & Uyeda, S. (1975b). On the Relative Importance of the Driving Forces of Plate Motion*. *Geophysical Journal of the Royal Astronomical Society*, *43*(1), 163–200. https://doi.org/10.1111/J.1365-246X.1975.TB00631.X

Gaina, C., Gernigon, L., & Ball, P. (2009). Palaeocene-Recent plate boundaries in the NE Atlantic and the formation of the Jan Mayen microcontinent. *Journal of the Geological Society*, *166*(4), 601–616. https://doi.org/10.1144/0016-76492008-112/ASSET/92E86D01-60A2-45C0-881D-91B4E2BFEE06/ASSETS/GRAPHIC/601FIG10.JPEG

Gaina, C., Müller, R. D., Brown, B., & Ishihara, T. (2003). Microcontinent formation around Australia. *Special Paper of the Geological Society of America*, *372*, 405–416. https://doi.org/10.1130/0-8137-2372-8.405

Gerya, T. (2011). Future directions in subduction modeling. *Journal of Geodynamics*, *52*(5), 344–378. https://doi.org/10.1016/J.JOG.2011.06.005

Gerya, T. (2022). Numerical modeling of subduction: State of the art and future directions. *Geosphere*, *18*(2), 503–561. https://doi.org/10.1130/GES02416.1

Gerya, T. V., Connolly, J. A. D., & Yuen, D. A. (2008). Why is terrestrial subduction one-sided? *Geology*, *36*(1), 43–46. https://doi.org/10.1130/G24060A.1

Gurnis, M., Hall, C., & Lavier, L. (2004). Evolving force balance during incipient subduction. *Geochemistry, Geophysics, Geosystems*, *5*(7), 7001. https://doi.org/10.1029/2003GC000681

Hager, B. H. (1990). Mantle viscosity: a comparison of models from postglacial rebound and from the geoid, plate driving forces, and advected heat flux. *Glacial Isostasy, Sea-Level and Mantle Rheology*, 493–513. https://doi.org/10.1007/978-94-011-3374-6_23/COVER

REFERENCES

Hall, C. E., Gurnis, M., Sdrolias, M., Lavier, L. L., & Müller, R. D. (2003). Catastrophic
initiation of subduction following forced convergence across fracture zones.
Earth and Planetary Science Letters, *212*(1–2), 15–30.
https://doi.org/10.1016/S0012-821X(03)00242-5

Hall, R. (1996). Reconstructing Cenozoic SE Asia. *Geological Society Special
Publication*, *106*, 153–184. https://doi.org/10.1144/GSL.SP.1996.106.01.11

Hall, R. (2012). Late Jurassic–Cenozoic reconstructions of the Indonesian region and
the Indian Ocean. *Tectonophysics*, *570–571*, 1–41.
https://doi.org/10.1016/J.TECTO.2012.04.021

Hertgen, S., Yamato, P., Guillaume, B., Magni, V., Schliffke, N., & van Hunen, J. (2020).
Influence of the Thickness of the Overriding Plate on Convergence Zone
Dynamics. *Geochemistry, Geophysics, Geosystems*, *21*(2), e2019GC008678.
https://doi.org/10.1029/2019GC008678

Hirth, G., & Kohlstedt, D. (2004). Rheology of the Upper Mantle and the Mantle
Wedge: A View from the Experimentalists. *Geophysical Monograph Series*, *138*,
83–105. https://doi.org/10.1029/138GM06

Holt, A. F., & Condit, C. B. (2021). Slab Temperature Evolution Over the Lifetime of a
Subduction Zone. *Geochemistry, Geophysics, Geosystems*, *22*(6), e2020GC009476.
https://doi.org/10.1029/2020GC009476

Holt, A. F., Royden, L. H., & Becker, T. W. (2017). The dynamics of double slab
subduction. *Geophysical Journal International*, *209*(1), 250–265.
https://doi.org/10.1093/GJI/GGW496

Huw Davies, J. (1999). Simple analytic model for subduction zone thermal structure.
Geophysical Journal International, *139*(3), 823–828.
https://doi.org/10.1046/J.1365-246X.1999.00991.X/3/139-3-823-
FIG005.JPEG

Jagoutz, O., Royden, L., Holt, A. F., & Becker, T. W. (2015). Anomalously fast
convergence of India and Eurasia caused by double subduction. *Nature
Geoscience 2014 8:6*, *8*(6), 475–478. https://doi.org/10.1038/ngeo2418

Kameyama, M., Yuen, D. A., & Karato, S. I. (1999). Thermal-mechanical effects of low-
temperature plasticity (the Peierls mechanism) on the deformation of a
viscoelastic shear zone. *Earth and Planetary Science Letters*, *168*(1–2), 159–172.
https://doi.org/10.1016/S0012-821X(99)00040-0

Karato, S. I., & Wu, P. (1993). Rheology of the Upper Mantle: A Synthesis. *Science*,
260(5109), 771–778. https://doi.org/10.1126/SCIENCE.260.5109.771

Khan, P. K., & Chakraborty, P. P. (2005). Two-phase opening of Andaman Sea: a new seismotectonic insight. *Earth and Planetary Science Letters*, *229*(3–4), 259–271. https://doi.org/10.1016/J.EPSL.2004.11.010

Khan, S. D., Walker, D. J., Hall, S. A., Burke, K. C., Shah, M. T., & Stockli, L. (2009). Did the Kohistan-Ladakh island arc collide first with India? *GSA Bulletin*, *121*(3–4), 366–384. https://doi.org/10.1130/B26348.1

Kiss, D., Candioti, L. G., Duretz, T., & Schmalholz, S. M. (2020). Thermal softening induced subduction initiation at a passive margin. *Geophysical Journal International*, *220*(3), 2068–2073. https://doi.org/10.1093/GJI/GGZ572

Kohlstedt, D. L., Evans, B., & Mackwell, S. J. (1995). Strength of the lithosphere: Constraints imposed by laboratory experiments. *Journal of Geophysical Research: Solid Earth*, *100*(B9), 17587–17602. https://doi.org/10.1029/95JB01460

Korenaga, J. (2013). Initiation and Evolution of Plate Tectonics on Earth: Theories and Observations. *Https://Doi.Org/10.1146/Annurev-Earth-050212-124208*, *41*, 117–151. https://doi.org/10.1146/ANNUREV-EARTH-050212-124208

Lithgow-Bertelloni, C., & Richards, M. A. (1995). Cenozoic plate driving forces. *Geophysical Research Letters*, *22*(11), 1317–1320. https://doi.org/10.1029/95GL01325

Li, Z. H., Xu, Z., Gerya, T., & Burg, J. P. (2013). Collision of continental corner from 3-D numerical modeling. *Earth and Planetary Science Letters*, *380*, 98–111. https://doi.org/10.1016/J.EPSL.2013.08.034

Magni, V., Allen, M. B., van Hunen, J., & Bouilhol, P. (2017). Continental underplating after slab break-off. *Earth and Planetary Science Letters*, *474*, 59–67. https://doi.org/10.1016/J.EPSL.2017.06.017

Magni, V., Faccenna, C., van Hunen, J., & Funiciello, F. (2014). How collision triggers backarc extension: Insight into Mediterranean style of extension from 3-D numerical models. *Geology*, *42*(6), 511–514. https://doi.org/10.1130/G35446.1

Maiti, G., Roy, A., Sen, J., & Mandal, N. (2021). Impact of Decelerating India-Asia Convergence on the Crustal Flow Kinematics in Tibet: An Insight From Scaled Laboratory Modeling. *Geochemistry, Geophysics, Geosystems*, *22*(11), e2021GC009967. https://doi.org/10.1029/2021GC009967

Mansour, J., Giordani, J., Moresi, L., Beucher, R., Kaluza, O., Velic, M., Farrington, R., Quenette, S., & Beall, A. (2021). *Underworld2: Python Geodynamics Modelling for Desktop, HPC and Cloud*. https://doi.org/10.5281/ZENODO.5209451

Merkouriev, S. A., & Sotchevanova, N. A. (2003). *Structure and evolution of the Carlsberg Ridge: Evidence for non-stationary spreading on old and modern spreading centres*. Current Science. https://www.jstor.org/stable/24108663

Miles, P. R. (1982). Gravity models of the Amirante Arc, western Indian Ocean. *Earth and Planetary Science Letters*, *61*(1), 127–135. https://doi.org/10.1016/0012-821X(82)90045-0

Mishin, Y. A., Gerya, T. V., Burg, J. P., & Connolly, J. A. D. (2008). Dynamics of double subduction: Numerical modeling. *Physics of the Earth and Planetary Interiors*, *171*(1–4), 280–295. https://doi.org/10.1016/J.PEPI.2008.06.012

Molnar, P., & Stock, J. M. (2009). Slowing of India's convergence with Eurasia since 20 Ma and its implications for Tibetan mantle dynamics. *Tectonics*. https://doi.org/10.1029/2008TC002271

Moresi, L., Betts, P. G., Miller, M. S., & Cayley, R. A. (2014). Dynamics of continental accretion. *Nature 2014 508:7495*, *508*(7495), 245–248. https://doi.org/10.1038/nature13033

Mulyukova, E., & Bercovici, D. (2018). Collapse of passive margins by lithospheric damage and plunging grain size. *Earth and Planetary Science Letters*, *484*, 341–352. https://doi.org/10.1016/J.EPSL.2017.12.022

Mulyukova, E., & Bercovici, D. (2019). The Generation of Plate Tectonics From Grains to Global Scales: A Brief Review. *Tectonics*, *38*(12), 4058–4076. https://doi.org/10.1029/2018TC005447

Nikolaeva, K., Gerya, T. V., & Marques, F. O. (2010). Subduction initiation at passive margins: Numerical modeling. *Journal of Geophysical Research: Solid Earth*, *115*(B3). https://doi.org/10.1029/2009JB006549

Parsons, B., & Richter, F. M. (1980). A relation between the driving force and geoid anomaly associated with mid-ocean ridges. *Earth and Planetary Science Letters*, *51*(2), 445–450. https://doi.org/10.1016/0012-821X(80)90223-X

Peron-Pinvidic, G., Gernigon, L., Gaina, C., & Ball, P. (2012a). Insights from the Jan Mayen system in the Norwegian-Greenland Sea-II. Architecture of a microcontinent. *Geophysical Journal International*, *191*(2), 413–435. https://doi.org/10.1111/J.1365-246X.2012.05623.X/2/191-2-413-FIG017.GIF

Peron-Pinvidic, G., Gernigon, L., Gaina, C., & Ball, P. (2012b). Insights from the Jan Mayen system in the Norwegian–Greenland sea—I. Mapping of a microcontinent. *Geophysical Journal International*, *191*(2), 385–412. https://doi.org/10.1111/J.1365-246X.2012.05639.X

Pusok, A. E., & Kaus, B. J. P. (2015). Development of topography in 3-D continental-collision models. *Geochemistry, Geophysics, Geosystems*, *16*(5), 1378–1400. https://doi.org/10.1002/2015GC005732

Pusok, A. E., & Stegman, D. R. (2019). Formation and Stability of Same-Dip Double Subduction Systems. *Journal of Geophysical Research: Solid Earth*, *124*(7), 7387–7412. https://doi.org/10.1029/2018JB017027

Sandiford, D., & Moresi, L. (2019). Improving subduction interface implementation in dynamic numerical models. *Solid Earth*. https://doi.org/10.5194/se-10-969-2019

Spiegelman, M., & Katz, R. F. (2006). A semi-Lagrangian Crank-Nicolson algorithm for the numerical solution of advection-diffusion problems. *Geochemistry, Geophysics, Geosystems*, *7*(4). https://doi.org/10.1029/2005GC001073

Sternai, P., Jolivet, L., Menant, A., & Gerya, T. (2014). Driving the upper plate surface deformation by slab rollback and mantle flow. *Earth and Planetary Science Letters*, *405*, 110–118. https://doi.org/10.1016/J.EPSL.2014.08.023

Stern, R. J. (2004). Subduction initiation: spontaneous and induced. *Earth and Planetary Science Letters*, *226*(3–4), 275–292. https://doi.org/10.1016/J.EPSL.2004.08.007

Stern, R. J., & Gerya, T. (2018). Subduction initiation in nature and models: A review. *Tectonophysics*, *746*, 173–198. https://doi.org/10.1016/J.TECTO.2017.10.014

Stevens, D. E., McNeill, L. C., Henstock, T. J., Delescluse, M., Chamot-Rooke, N., & Bull, J. M. (2020). A complete structural model and kinematic history for distributed deformation in the Wharton Basin. *Earth and Planetary Science Letters*, *538*, 116218. https://doi.org/10.1016/J.EPSL.2020.116218

Tanaka, A., Yamano, M., Yano, Y., & Sasada, M. (2004). Geothermal gradient and heat flow data in and around Japan (I): Appraisal of heat flow from geothermal gradient data. *Earth, Planets and Space*, *56*(12), 1191–1194. https://doi.org/10.1186/BF03353339/METRICS

Thielmann, M., & Kaus, B. J. P. (2012). Shear heating induced lithospheric-scale localization: Does it result in subduction? *Earth and Planetary Science Letters*, *359–360*, 1–13. https://doi.org/10.1016/J.EPSL.2012.10.002

Van Der Voo, R., Spakman, W., & Bijwaard, H. (1999). Tethyan subducted slabs under India. *Earth and Planetary Science Letters*, *171*(1), 7–20. https://doi.org/10.1016/S0012-821X(99)00131-4

Van Dinther, Y., Gerya, T. V., Dalguer, L. A., Mai, P. M., Morra, G., & Giardini, D. (2013). The seismic cycle at subduction thrusts: Insights from seismo-thermo-

mechanical models. *Journal of Geophysical Research: Solid Earth*, *118*(12), 6183–6202. https://doi.org/10.1002/2013JB010380

Van Hinsbergen, D. J. J., Kapp, P., Dupont-Nivet, G., Lippert, P. C., Decelles, P. G., Torsvik, T. H., Hinsbergen, V., Kapp, P., Dupont-Nivet, G., Lippert, P. C., Decelles, P. G., & Torsvik, T. H. (2011). Restoration of Cenozoic deformation in Asia and the size of Greater India. *Tectonics*, *30*(5), 5003. https://doi.org/10.1029/2011TC002908

van Hunen, J., & Allen, M. B. (2011). Continental collision and slab break-off: A comparison of 3-D numerical models with observations. *Earth and Planetary Science Letters*, *302*(1–2), 27–37. https://doi.org/10.1016/j.epsl.2010.11.035

Vlaar, N. J., & Wortel, M. J. R. (1976). Lithospheric aging, instability and subduction. *Tectonophysics*, *32*(3–4), 331–351. https://doi.org/10.1016/0040-1951(76)90068-8

Wada, I., Wang, K., He, J., & Hyndman, R. D. (2008). Weakening of the subduction interface and its effects on surface heat flow, slab dehydration, and mantle wedge serpentinization. *Journal of Geophysical Research: Solid Earth*, *113*(B4), 4402. https://doi.org/10.1029/2007JB005190

Yin, A. (2006). Cenozoic tectonic evolution of the Himalayan orogen as constrained by along-strike variation of structural geometry, exhumation history, and foreland sedimentation. *Earth-Science Reviews*, *76*(1–2), 1–131. https://doi.org/10.1016/J.EARSCIREV.2005.05.004

Yin, A., & Harrison, T. M. (2000). Geologic Evolution of the Himalayan-Tibetan Orogen. *Https://Doi.Org/10.1146/Annurev.Earth.28.1.211*, *28*, 211–280. https://doi.org/10.1146/ANNUREV.EARTH.28.1.211

Zaman, H., & Torii, M. (1999). Palaeomagnetic study of Cretaceous red beds from the eastern Hindukush ranges, northern Pakistan: palaeoreconstruction of the Kohistan–Karakoram composite unit before the India–Asia collision. *Geophysical Journal International*, *136*(3), 719–738. https://doi.org/10.1046/J.1365-246X.1999.00757.X

Zhang, Q., Guo, F., Zhao, L., & Wu, Y. (2017). Geodynamics of divergent double subduction: 3-D numerical modeling of a Cenozoic example in the Molucca Sea region, Indonesia. *Journal of Geophysical Research: Solid Earth*, *122*(5), 3977–3998. https://doi.org/10.1002/2017JB013991

Zhu, M., Yan, Z., Pastor-Galán, D., Chen, L., Miao, L., Zhang, F., Li, S., & Yang, S. (2023). Do microcontinents nucleate subduction initiation? *Geology*, *51*(7), 668–672. https://doi.org/10.1130/G51222.1

Chapter 6.

GRAVITATIONAL COLLAPSE OF THE TIBETAN PLATEAU

6.1. INDIA-ASIA COLLISION TECTONICS

The deformation and crustal-flow kinematic history of Tibet, reconstructed from various geological records, indicate an interesting tectonic scenario in the past. Since the beginning of Indo-Eurasian collision at ~50 Ma to ~19±3 Ma it was dominated by NNE-SSW directed contractional deformations (thrust faulting) both in its interior and southern margins (Y. Li et al., 2015a; C. Wang et al., 2014). During this time period, the plateau had most of its crustal thickening to build the present-day raised topography with an average elevation of 5 km by 26 Ma (DeCelles et al., 2007). It is still ambiguous whether the topographic uplift took place uniformly or varied in space and time during this period. Several workers have proposed a non-coeval uplift hypothesis to explain the growth of the Tibetan plateau along east-west as well as north-south directions (Chung et al., 1998; Tapponnier et al., 2001; C. Wang et al., 2008). According to the outward growth model ((C. Wang et al., 2008)), the plateau grew southward and northward from an initially elevated proto-Tibetan plateau (presently Lhasa and Qiangtang blocks), which had already attained a topographic elevation of 3-4 km by ~40 Ma (Kapp et al., 2005; Murphy et al., 1997). On the other hand, compilation of thermochronological data along N-S transect of the plateau (Y. Li et al., 2015a) suggests, although central Tibet might have attained its elevated topography to some extent before 40 Ma, the plateau underwent an overall northward progressive contraction and uplift after the onset of India-Asia collision. The most striking event, the plateau witnessed during the collision, is marked by a dramatic transformation in its tectonic deformation pattern at around 19±3 Ma. At

this stage ESE-WNW extension was onset in central and southern Tibet (Y. Li et al., 2015a; C. Wang et al., 2014) with the ongoing NE-SW contraction in the orogen margins. This tectonic transition is evident from initiation of a series of N-S trending high-angle normal faults or rifts (Fig. 6.1a) in central and southern Tibet (Cooper et al., 2015; Ge et al., 2015). The extensional tectonics is shown to have continued till the
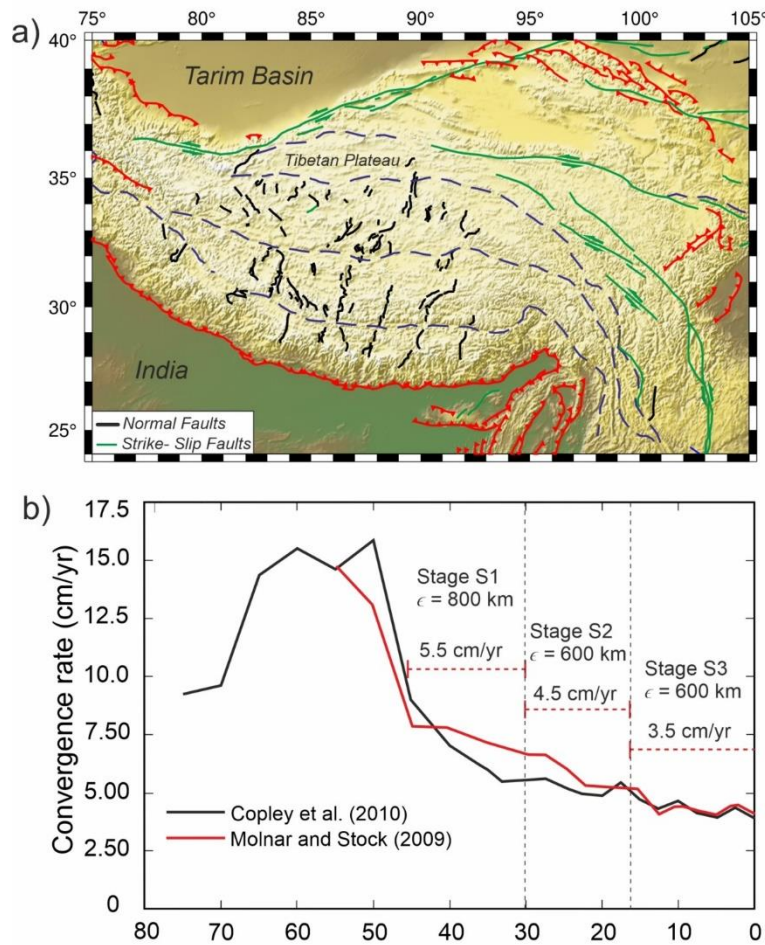
Figure 6.1: a) Tectonic map of the Tibetan plateau showing spatial distribution of normal and strike-slip faults. b) India-Asia convergence velocity curve through time. The total India-Asia convergence length and duration have been divided in three Stages (1 to 3) where in each stage we have assumed an average indentation velocity.

present-day with a west to east younging trend in rift initiation (Y. Li et al., 2015a). During this period the contractional tectonics shifted its focus from the interior of the Tibetan plateau to its margins ((Y. Li et al., 2015b; Maiti & Mandal, 2021)), including the regions of the Himalayan wedge (Main Central Thrust, 23-13 Ma; Main Boundary

Thrust, 12-8 Ma; Main Frontal Thrust, 5-0 Ma) (Huyghe et al., 2001; Meigs et al., 1995; Montemagni et al., 2018; Najman, 2006; Soucy La Roche et al., 2018). On the other side, the north-eastern (Northern Qilian Shan thrust, 9-0 Ma) and eastern (Longmen Shan thrust, 10-0 Ma) margins of Tibet underwent fresh contractional deformation pulses at this late Cenozoic stage (Clark et al., 2005; E. Wang et al., 2012; Xu & Kamp, 2000; S. Yang et al., 2007). The central plateau thrust belts are eventually not major contributors to the present-day Tibetan tectonics (Y. Li et al., 2015a), as reflected from the earthquake focal mechanism solutions (Copley et al., 2011). In fact, the earthquake records indicate contraction deformations (thrust activities) to localize preferentially in the southern, north-eastern, and eastern margins of the Tibetan plateau, leaving its interior dominated by normal and strike-slip faulting (Fig. 6.2). The thrust activities in central and southern Tibet became remarkably weak, but not totally inactive. For example, some recent studies have reported active thrusts from Gangdese (Taylor et al., 2021) and Qimen Tagh regions (Wu et al., 2020, 2021). Geological data suggest that the N-S extensional tectonics (i.e., STDS) initiated at around 23 Ma and remained active to as late as 11 Ma (Fig. 6.4; Kellett et al., 2009; 2013). The E-W extensional tectonics, on the other hand, initiated relatively at a later phase (ca. 19 Ma) of the India-Asia collision, and continued to operate till present-day, as warranted by a number of geological proxies, such as neotectonic faults (Armijo et al., 1986), offset quaternary deposits in the in the Ama Drime Massif and central Himalaya (Jessup et al., 2008), and geophysical signatures, such as earthquake fault plane solutions (Andronicos et al., 2007) and GPS data (Zheng et al., 2017).

6.2. EASTWARD CRUSTAL FLOWS IN THE TIBETAN PLATEAU

The tectonic transition, NNE-SSW shortening during the initial phase of collision (~50 to 19±3 Ma) to a dominant ESE-WNW extension at around 19±3 to 0 Ma in central and southern Tibet, is widely accepted and strongly backed by extensive geological evidences, e.g., fault kinematics (Fig. 6.3) and sedimentary basin formation (Blisniuk et al., 2001; Cooper et al., 2015; Ge et al., 2015; Mitsuishi et al., 2012; Styron et al., 2013). But, what kind of geodynamic models can best describe such spatiotemporal variations of crustal deformation in the Tibetan plateau has remained an open-ended issue. A variety of models have been proposed to explain different modes of the Cenozoic crustal deformation pattern in the plateau and their relationship to topographic upliftment. The major models are: i) intracontinental deformation of the plateau by rigid block indentation, and lateral crustal extrusion along large scale strike-slip faults (Tapponnier et al., 1982, 2001), ii) underplating of Indian crust beneath the Tibetan plateau as far as northern Qiangtang block, leading to crustal thickening and rapid surface upliftment in the plateau (Powell, 1986), iii) distributed crustal thickening by continuous north-south shortening of the entire
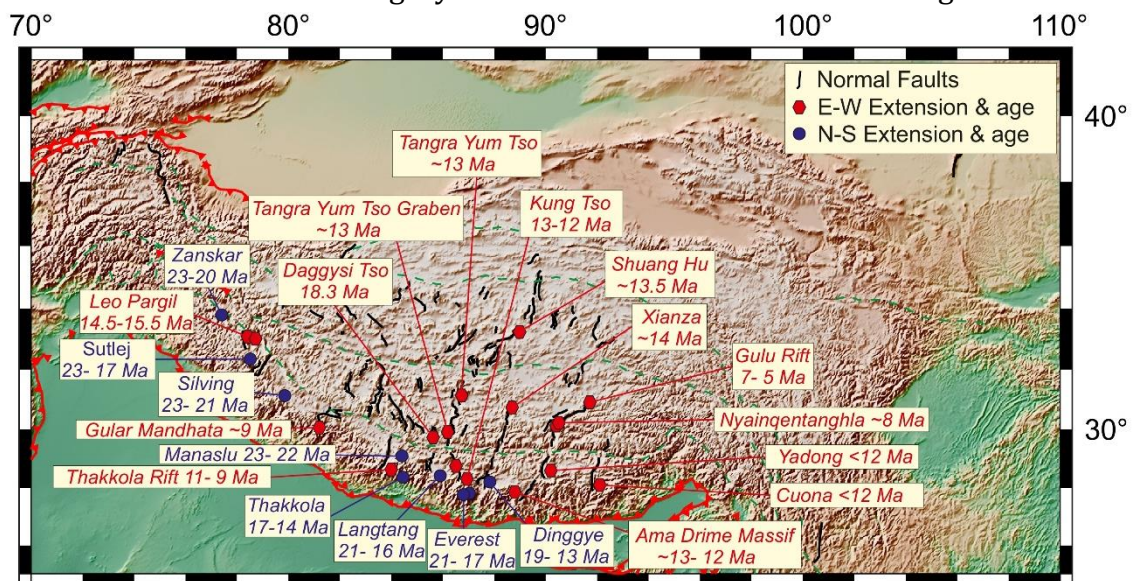
Figure 6.2: Visual representation of the E-W trending faults in the central and south-central region and the initiation time of major structures formed due to E-W and N-S extension of the Tibetan Plateau.

176

plateau (Philip England & Houseman, 1986), iv) convective removal of the Tibetan mantle lithosphere and Miocene upliftment of the Tibetan plateau (Molnar et al., 1993), v) lower crustal channel flow dynamics for low-relief in the interior of the plateau and steep topography in its eastern and southern margin (Bird, 1991; Clark & Royden, 2000; Zhao & Morgan, 1987), and vi) an outward growth model from a pre-existing proto-Tibetan plateau (Murphy et al., 1997; C. Wang et al., 2008). (Yin, 2000) proposed a completely different geodynamic model to explain E-W extension in the late Cenozoic time. According to his model, slab rollback of the western pacific plate gave rise to a regional lithospheric extension in entire southeast Asia, leading to Tibetan and Baikal rifting, and Shanxi graben formation. Despite a strong divergence in the prevailing views, it is generally accepted, based on the spectacular records of Tibet's long-term evolution history, that the evolution of plateau topography had an intricate relationship with the continental scale deformation episodes in Tibetan crust (DeCelles et al., 2002; P. England & Houseman, 1989). Recent tectonic models have shown that the lateral crustal heterogeneities, such as rigid Tarim and Sichuan basins in the Asian plate have strongly influenced the topographic uplift and the long-term crustal deformations in the Tibetan plateau (Chen et al., 2017; A. E. Pusok & Kaus, 2015; Y. Yang & Liu, 2013).

Paleomagnetic data and plate reconstructions suggest that the India-Asia collision slowed the convergence rates, from 15 cm/yr at 50 Ma to 3.5 cm/yr at the present-day (Fig. 6.1b) (Copley et al., 2010; Molnar & Stock, 2009; Adina E. Pusok & Stegman, 2020). Such a decelerating convergence motion had the potential to reduce the tectonic forcing upon the deforming Asian plate, resulting in the gravitational collapse of the elevated plateau in the course of collision (Maiti et al., 2020; Rey et al.,

2001). Copley and McKenzie's theoretical model (2007) predicts this gravitational collapse as the driving factor in setting the present-day extensional tectonics in Tibet. On the other hand, several workers suggested eastward gravitational spreading of the whole Tibetan lithosphere, confined between two rigid blocks (Indian craton in the south and the Tarim and Qaidam basins in the north) controlled the rifting and strike slip faulting in the Tibetan plateau (Bajolet et al., 2015; Fournier et al., 2004; Yin & Taylor, 2011). From laboratory models Bajolet et al. (2013) showed that the symmetric lateral extrusion between two rigid colliding plates, coupled with a late
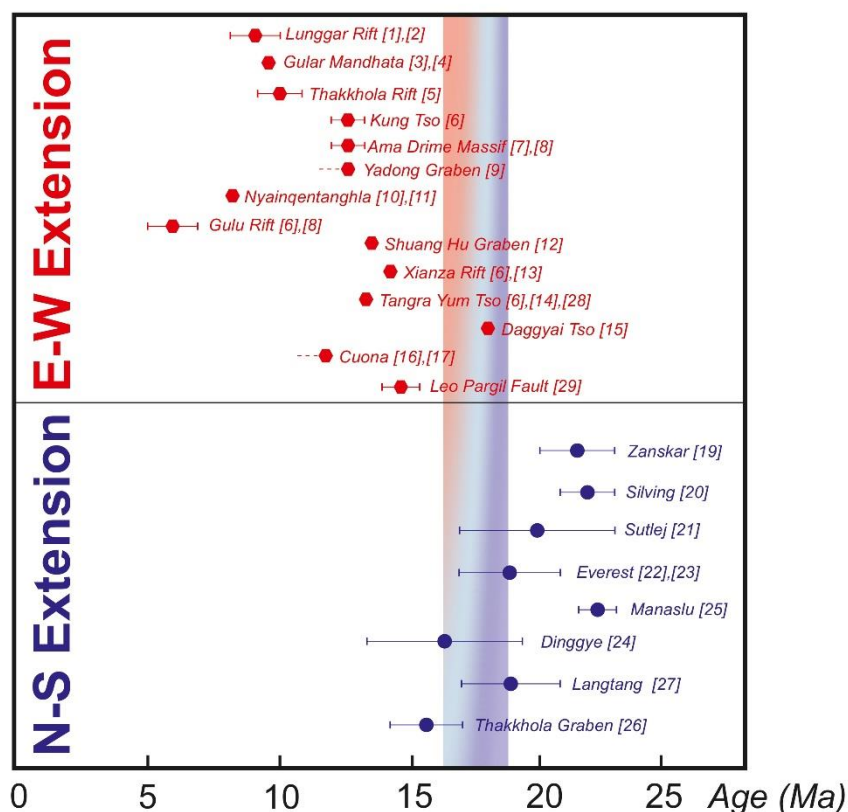
Figure 6.3: Age distribution of N-S and E-W extensional faults which shows that N-S extensional faults are older than E-W extensional faults and they form ~7 Ma temporally overlapping period.

stage gravity collapse of the thickened crust modulated Tibetan tectonics, including the syntaxis formation on the eastern and western flanks of Tibet. This model agrees with Fournier et al.'s (2004) study, suggesting a free or weakly confined eastward boundary of Tibet as a necessary condition for eastward gravitational spreading of

the Tibetan crust. However, these earlier numerical and analogue experiments mostly ignored the temporally varying India-Asia collisional kinematics in their models, setting the experimental runs at a constant boundary condition, either with an average convergence velocity of 5 cm/yr (Beaumont et al., 2001; Y. Yang & Liu, 2013) or an average indentation rate of ~3.5 cm/yr (W. P. Schellart et al., 2019) for the entire 50 Ma collision event. Furthermore, most of the laboratory models did not account for lateral crustal heterogeneities, particularly rigid Tarim and Sichuan basins situated in the north-western and easternmost regions of Tibet, respectively. Numerical simulations of (P. England & Houseman, 1989) took into account the effects of decreasing collision force, expressed in terms of Argand number, but their study excludes any possible effects of the lateral crustal heterogeneities (Tarim and Sichuan basins) around the Tibetan plateau. Despite a remarkable progress of tectonic modelling in recent time, it is yet to address the following questions- did the temporally varying collision kinematics play a critical role in the tectonic evolution of Tibet, and if so, what were the complementary effects of the lateral crustal heterogeneities? These issues constitute the central theme of this thesis chapter.

6.3. EXPERIMENTAL DESIGN AND APPLICATIONS OF PIV ANALYSIS

A classical indentation tectonic model is adopted to perform analogue experiments of the India-Asia collision in laboratory (Fournier et al., 2004; Schellart et al., 2019; Tapponier et al., 1982). The experiments were designed to study the Tibetan plateau deformation in the last ~50 Ma as a function of the three collisional kinematic states discussed in the preceding section. The experimental results are used to constrain the decelerating India-Asia collision rate as a critical collision kinematics required for setting the eastward crustal flow in Tibet. The laboratory

model results help in explaining the crustal velocity pattern, topography, and strain fields in space and time.

6.3.1. MODEL SETUP

The continental lithosphere is often modelled as a fluid continuum of Newtonian or power-law rheology to describe its large-scale deformation behaviour on million years' time scales (Philip England & McKenzie, 1982). As the horizontal length scale of the continuum system (Tibetan plateau) far exceeds the lithospheric
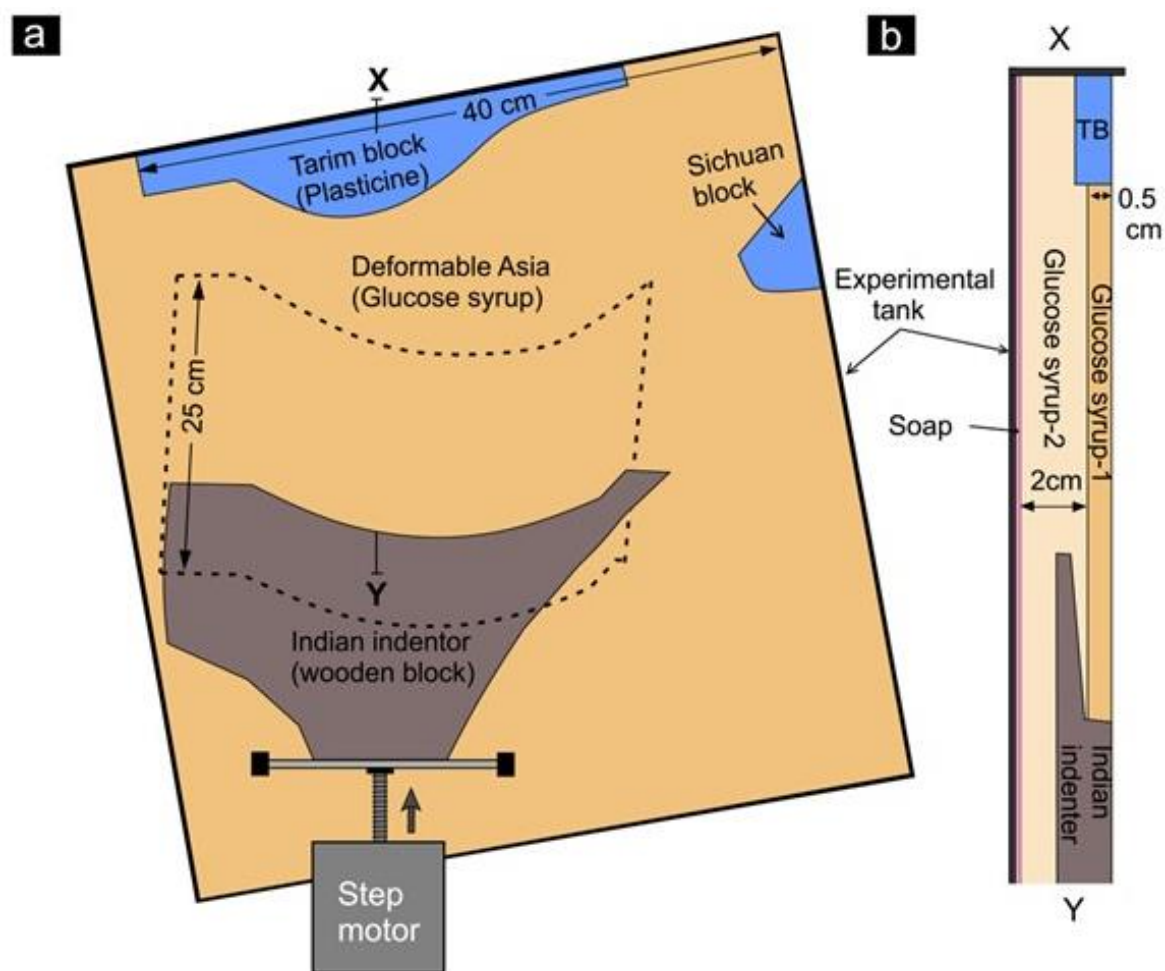
Figure 6.4: A schematic diagram of the top view of the laboratory model setup of India-Asia indentation experiment.

thickness, several workers have developed their tectonic models within a framework of thin viscous sheet

(TVS) approximation (Bischoff & Flesch, 2018; Houseman & England, 1986; Y. Yang & Liu, 2013). The TVS approximation ((Philip England & McKenzie, 1982)) simplifies depth-wise rheological variations in the lithosphere by considering a vertically averaged and approximated lithospheric rheology, and treats the system as a single continuum medium. A two-layer continuum model was chosen to perform scaled laboratory experiments on Tibet.

In the model, the continental deformation in the Asian domain has been enforced by imposing external velocities in the Indian indenter, attached to a step motor (Fig. 6.5). To investigate exclusively the effects of reducing convergence rate on the mode of Tibetan crustal deformations, a kinematic model boundary condition was chosen by externally controlling the velocities at the model boundaries. This kinematic approach to modelling is similar to those used in many earlier India-Asia collision models (Bischoff & Flesch, 2018; Cook & Royden, 2008; W. P. Schellart et al., 2019; Y. Yang & Liu, 2013). The northern boundary (leading) of the Indian indenter represents the contact between the Indian plate and the Himalaya-Tibetan plateau. A recent analysis of the seismic tomography and earthquake locations data suggests that underthrusting of the Indian plate beneath the Tibetan plateau reaches up to a horizontal distance of ~300-500 km north of the Himalayan front (Craig et al., 2020). To include this subduction induced simple shear beneath the Asian plate, the Indian indenter was designed to allow a part of it to underthrust for about 350 km north of the mountain front (Fig. 6.5).

Several important additional features have been incorporated in the present analogue model; one of them replicates the lateral crustal heterogeneities i.e., rigid Tarim and Sichuan basins, situated in the northern and the eastern margins of the Tibetan plateau, respectively. They act as a region of mechanically strong lithosphere (Clark et al., 2005; Dewey et al., 1988), as predicted from observations of fast seismic velocities down to a depth of 200 km (C. Li et al., 2006), measurements of low heat flow-rate (Y. Wang, 2001), and present-day GPS velocity data (Gan et al., 2007; Liang et al., 2013; Zhang et al., 2004). On the other hand, an arcuate plate boundary of the Indian plate was also considered. It is noteworthy that all the previous analogue India-Asia collision models used the Indian indenter ideally rectangular in shape, forming a straight plate contact. But, the present-day southern margin of the Tibetan plateau, i.e., India-Asia contact, is strongly curved. The plate reconstructions and rotations measured from palaeomagnetic data (as summarized in (Van Hinsbergen et al., 2011) suggest that this arcuate geometry existed since the onset of continent-continent collision in this region. (Copley, 2012) has shown how this curved plate contact influenced the gravitational spreading of the Tibetan plateau in the late stage of the orogeny. The present study primarily aims to investigate the entire tectonic evolution of the plateau, including its late-stage gravity collapse, and thus considers such a curved plate contact to model the India-Asia collision system.

6.3.2. MATERIAL PROPERTIES AND SCALING

The analogue model was scaled to the natural prototype setting, keeping geometric similarity of the model domain, similarity in the temporal variation of collision kinematics, and downscaling of the crustal and mantle rheology (King Hubbert, 1937; Ribe & Davaille, 2013; Wouter P. Schellart & Strak, 2016). To model the India-Asia collision system, a length scale factor (nature to model ratio): $l_r = 1.25$

$\times 10^{-7}$ was used. This scaling yields a model dimension of 40 cm to represent an approximately 3200 km east-west length of the Tibetan plateau. Similarly, a 40 km thick crustal lithosphere in the initial model is represented as 0.5 cm thick viscous layer. The model crustal lithosphere rests over an initially 2 cm thick layer, which represents a sub-crustal mantle region. The whole setup was contained within an experimental tank. At the contact between the model base and the basal plate of the experimental tank, liquid soap (viscosity $\sim$0.5 Pa s) was applied to minimize friction to the model.

Model materials with different rheological properties were chosen to appropriately scale the crustal lithosphere and underlying sub-crustal mantle region in the experiments. A glucose syrup (syrup-1) of constant density (ρ_{cl} = 1406 ± 3 kg/m³) and viscosity (μ_{cl} = 305 ± 5 Pa s) was used to model the whole (40 km thick) crustal-lithosphere as a single continuum, representing its depth-averaged physical properties in the corresponding natural prototype (viscosity: 3×10^{21} Pa s; density: 2780 kg/m³) (Jiménez-Munt et al., 2008). The model to nature scaling factors for viscosity (μ_r) and density (ρ_r) are found to be 10^{-19} and $\sim$0.5, respectively. Another variety of glucose syrup was used (syrup-2) with different density and viscosity (μ_{sm} = 28 ± 5 Pa s; ρ_{sm} = 1510 ± 5 kg/m³) to simulate the sub-crustal mantle region (viscosity: $\sim 10^{20}$ Pa s; density: 3200 kg/m³) (Jiménez-Munt et al., 2008). To obtain the right density of glucose syrup-2, water soluble sodium carbonate ($Na_2CO_3 . 10\ H_2O$, ρ = 2.53 gm/cm³) was mixed with a low-viscosity glucose syrup (μ = 10 ± 3 Pa s and ρ = 1392 ± 5 kg/m³). The lower μ_{sm} and higher ρ_{sm} of syrup-2 than that of syrup-1 allows the base of the crustal lithosphere to deform vertically and maintain an isostatic equilibrium of the model topography during the experimental run.

Commercial plasticine mixed with oil (viscosity = 3 ×10^5 Pa s; density = 1.5 gm/cc) (Zulauf & Zulauf, 2004) was used to represent rigid Tarim and Sichuan basins in the model as it is relatively much stronger than the glucose syrup-1. The viscosity ratio in the model is then in the order of ~10^3, which agrees well with the numerical estimates of the viscosity ratio (~10^2 to 10^3) between rigid Tarim basin and Tibetan upper crust (Clark & Royden, 2000; Flesch et al., 2001).

Considering an extremely slow motion in the geodynamic setting, the dynamic scaling must satisfy the following relation (Marques & Mandal, 2016),

$$\mu_r = \rho_r \times l_r \times t_r \qquad (6.1)$$

Eq. (6.1) yields a time ratio: $t_r = 1.6 \times 10^{-12}$. That means, 1 Ma time in nature equals to ~50 seconds in the scaled model. Now, using the relation:

$$U_r = l_r/t_r, \qquad (6.2)$$

the velocity ratio in our model is: $U_r = 7.813 \times 10^4$. According to this scaling factor, Indian plate's indentation velocity of 5.5, 4.5, and 3.5 cm/yr in nature equates to 8.17, 6.69, and 5.20 mm/min in the model, respectively. The total model runtime in our experiments was ~42 minutes, which is equivalent to ~50 Ma in nature.

6.3.3. RECORDING OF EXPERIMENTAL RUNS

For a quantitative analysis of the model crustal flow velocity and topography development in each experiment, a particle image velocimetry (PIV) system was used, which consisted of four synchronized cameras systematically aligned around the experimental box: three at the top and one at the side of the model set-up (Fig. 6.6).
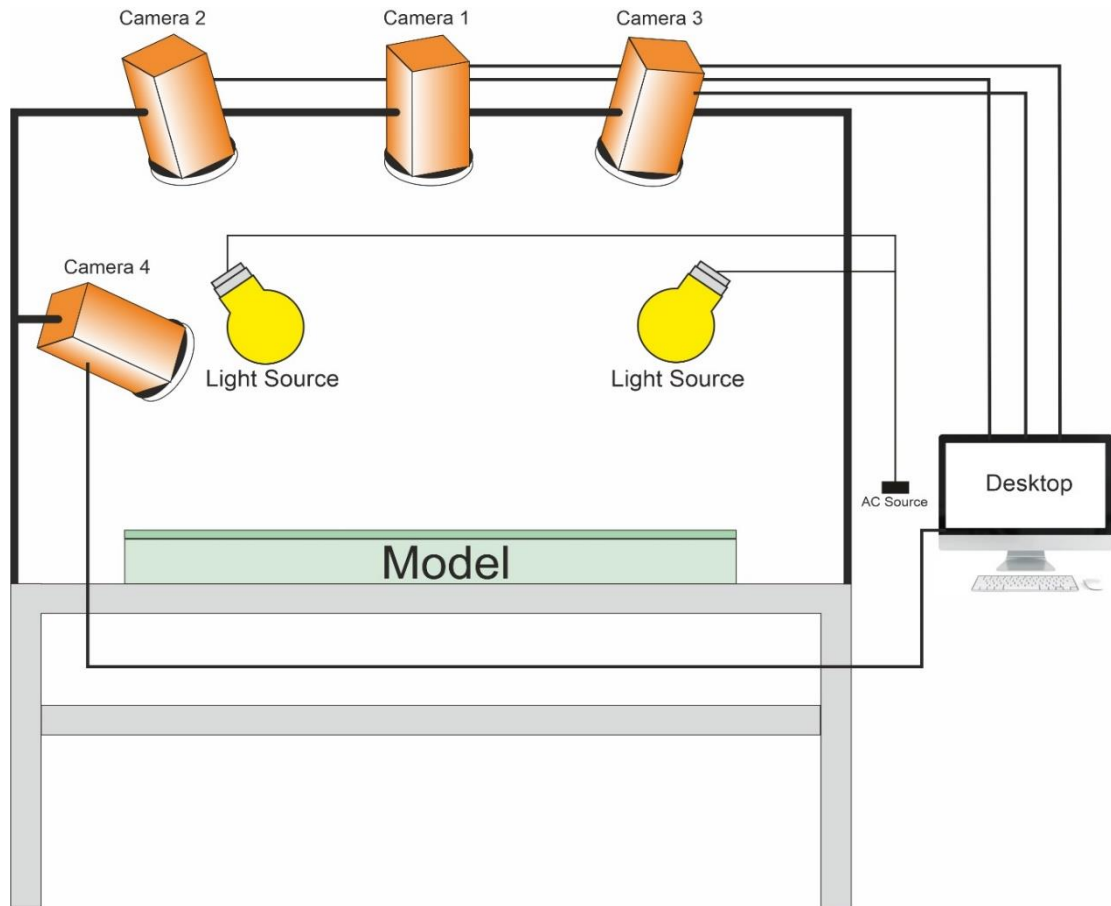
Figure 6.5: Experimental setup for PIV and topography analysis.

The top cameras were placed ~80 cm above the set-up table, with 10° -15° angles between them to capture sharp images (Galland et al., 2016). All four cameras were standard DSLR (Digital single-lens reflex) cameras (Nikon D3400 24.2 MP) with a shutter speed of 1/125 and a focal length of 24mm. The operation of these four cameras was synchronized with the help of open-source software, *digiCamControl* in a single computer system.

Characterization of velocity vectors in this study was executed using PIVLab (Thielicke & Stamhuis, 2010), an image correlation algorithm written in MATLAB. Cross correlation was performed on temporally successive image pairs, which were captured with top view cameras. The correlation consisted of 2 passes with the 1st pass comprised of a preliminary 64×64 pixel interrogation zone for a coarse

velocity calculation, followed by a 32 × 32 smaller interrogation zone for finer vector resolution. The velocity vectors were then exported in .vtk format in order to compute the strain rate tensors (Eq. S5) in Paraview.

$$\dot{\varepsilon}_{ij} = \frac{1}{2}\left(\frac{\partial u_i}{\partial x_j} + \frac{\partial u_j}{\partial x_i}\right) \tag{6.3}$$

The Compute Derivatives tab in Paraview calculates the 9 component tensor:

$$\begin{bmatrix} \dfrac{\partial u}{\partial x} & \dfrac{\partial u}{\partial y} & \dfrac{\partial u}{\partial z} \\ \dfrac{\partial v}{\partial x} & \dfrac{\partial v}{\partial y} & \dfrac{\partial v}{\partial z} \\ \dfrac{\partial w}{\partial x} & \dfrac{\partial w}{\partial y} & \dfrac{\partial w}{\partial z} \end{bmatrix}$$

Several such quantitative analyses were performed of the model observations to study the effect of the India-Asia convergence kinematics on the Tibetan Plateau.

In this study, the multi-faceted and precise software MicMac (Galland et al. 2016; Rupnik et al. 2017) was used that applies photogrammetry in *SfM* algorithms to generate DEMs and 3D point clouds. The suitability of MicMac for laboratory models of geological processes has been tested by many previous workers. (Girod 2012; Galland et al. 2016). It is a free open-source code distributed under the *CeCILL-B* license. The main steps of the photogrammetric workflow in this study using MicMac are the following:

➢ During an experimental run four photographs of the model were simultaneously captured at an instant, keeping the cameras (24.1 MP DSLR Nikon D5600) at different angles (Fig. 6.6). All images were post-processed with the photogrammetric software MicMac to compute tie points (Tapioca).

➤ The tie points were used to compute both the viewing angle and camera positions, and the distortion model of the cameras' optics (Tapas).

➤ The 3D transformation between the arbitrary system (Relative Orientation) and the georeferenced system were achieved with the help of ground control points (GCPBascule).

➤ A depth map was prepared using all the images to create a 3D model through densification (Malt).

➤ A point cloud was generated (Nuage2Ply) and further cleaned in *MeshLab*. The X, Y, Z coordinates of the point clouds were then plotted to produce the topographic graphs.

For each time step of the model run, the four synchronous images taken by the four cameras are processed with MicMac to produce a high-resolution DEM and an orthorectified image. Using the orthorectified images has an advantage as they accurately depict the model surface by implementing optical corrections of the distortion resulting from the lens and camera tilt. The orthorectified imaging technique is remarkably effective to measure distances and angles with high accuracy. The DEMs from the successive snaps of a model run gave a detailed time-series configuration of the evolving surface topography. This approach was adapted mainly for a quantitative analysis of the topographic evolution in the Tibetan Plateau.

6.4. PIV-BASED MODEL CRUSTAL FLOW PATTERNS

The primary aim of the laboratory model experiments is to explore the possible effects of decreasing convergence/indentation velocity (Molnar & Stock, 2009) on the crustal flow and deformation patterns in Tibet. Three types of experiments were performed, and their results were compared to find this kinematic

effect. Type 1 experiment simulated a steady fast-rate collisional kinematics, setting the indentation rate (I_{FAST}) at a constant value of 5.5 cm/yr. Type 2 experiment simulated a steady, but slow-rate collisional kinematics with a constant indentation rate (I_{SLOW}) of 3.5 cm/yr, which represents the average indentation rate. In the Type 3 experiment, an unsteady collisional kinematics was generated, beginning with a fast indentation rate of 5.5 cm/yr, but decelerating (I_{DEC}) to 3.5 cm/yr with time. This experiment exactly represents the reducing India-Asia convergence velocity reported in the literature (Copley et al., 2010; Peter Molnar & Stock, 2009). In all the three types of experiments, the Indian indenter's leading edge was positioned at a distance around 1800-2000 km south from its present-day position. The total indentation of 1800-2000 km in the model is expressed in percentage as ϵ = 100%.

6.4.1. TYPE 1 MODEL EXPERIMENT: STEADY FAST-RATE COLLISION

In this experiment of steady fast-rate (I_{FAST} = 5.5. cm/yr) collision at ϵ = 30% convergence the model produced an NNE directed high velocity (5 cm/yr) crustal flow field in southern Tibet, gradually weakening nearly to 0 cm/yr in the northern margin of Tibet. When ϵ = 50%, the NNE directed flow field grew northward, setting strong flow velocities ($\sim$4 cm/yr) in the central Tibetan region. But, the northernmost part of the plateau still remained nearly undisturbed. At ϵ = 70%, the northward crustal flow interacted with the rigid Tarim basin situated in the north, and started to deflect towards north-eastern Tibet. The crustal flow velocities also showed a strong spatial heterogeneity, $\sim$5 cm/yr dominantly in southern and central Tibet, whereas $\sim$ 3 cm/yr in northern Tibet. This velocity gradient clearly suggests NNE-SSW contractional deformations in a large part of Tibet. At ϵ =100%, i.e., after the completion of total $\sim$2000 km Indian indentation to the present-day condition, the

entire Tibetan plateau continued to evolve with dominant NE-SW contractional deformations, maintaining crustal flow velocities nearly 5 cm/yr in southern Tibet, ~3.5 cm/yr in central Tibet, and ~2.5 cm/yr in northern and north-eastern Tibet. During the entire stage of collisional event, the model did not produce any clockwise rotation of the crustal flows around eastern Himalayan syntaxis (EHS), as observed in the present-day Tibet.

The principal strain axes were plotted on the second invariant of strain-rate tensor maps to study the spatio-temporal variations of crustal deformation in Type 1 model experiments. The plots show intense deformation (high strain rates ~4.5 ×10^{-8} yr^{-1}) localization preferentially near the leading edge of the Indian indenter in the initial stage (ϵ = 30%) of India-Asia collision. With progressive collision the high strain-rate zone propagated northward. During ϵ = 30% to 70% convergence the northern and the north-eastern regions of Tibet had crustal shortening at strain rates of 6 to 2.0 ×10^{-8} yr^{-1}. The principal strain axes plot suggests that the entire collisional event underwent contractional deformations broadly in the NNE-SSW direction.

The topographic analysis reveals that at 30% convergence, the plateau developed a northward topographic slope of 0.02°, suggesting a higher uplift rate in southern Tibet, compared to the northern region. At this stage the plateau gained virtually no topographic slope (0.01°) in the east-west direction. For ϵ = 70%, the northward slope steepened further to 0.1°, but the E-W topographic slope remains almost steady at 0.02°. Increasing convergence resulted in a topographic modification, marked by the increase of the northward topographic slope from 0.1° to 0.6° when ϵ = 100%.

6.4.2. TYPE 2 MODEL EXPERIMENT: STEADY SLOW-RATE COLLISION

The Type 2 experiment was similarly run at a steady, but relatively slow rate (I_{SLOW} = 3.5 cm/yr) to cover the total ~2000 km convergence. The model run at ϵ = 32% produced high crustal flow velocities (3.5 cm/yr) in the southern Tibetan region, where the flow had broadly a NNE-ward trend. However, central and northern Tibet were left virtually undisturbed, showing little or no crustal flow. At ϵ = 50% the high-velocity (~3 cm/yr) crustal flow regime in the southern region propagated northward to set a strong crustal flow (~2 cm/yr) in central Tibet. The northern part of Tibet also became kinematically active, but with significantly low velocities (~1 cm/yr). After ϵ = 70% strong high-velocity crustal flows still dominated in southern (~3 cm/yr) and central Tibet (~2 cm/yr), and at the same time the flows in northern Tibet - strengthened by increasing their velocity to ~1.4 cm/yr. The rigid Tarim basin deflected crustal-flows towards north-eastward, but at much lower magnitudes, as compared to that observed in the Type 1 experiment. At the completion of experimental run (i.e., ϵ = 100%) the model maintained the same kinematic state of crustal flows with slightly reduced magnitudes (~3 cm/yr in southern Tibet and ~1.8 cm/yr in northern Tibet). This Type-2 experiment also failed to produce the clockwise turning crustal-flow field around EHS of the present-day Tibet.

The second invariant mapping of strain-rate tensor from Type 2 model experiments reveals that intense contractional deformations localized at the rate of 2.0 ×10^{-8} yr^{-1} in front of the Indian indenter during the initial stage of convergence (ϵ = 32%). In course of the convergence motion (ϵ = 30% to 70%) the deformation front propagated northward, inducing grossly NE-SW contraction at 2.4 ×10^{-8} yr^{-1} in central Tibet. At ϵ = 100%, high strain rates (1.2 to 2.4 ×10^{-8} yr^{-1}) localized preferentially in

central and north-western Tibet, leaving the northern and north-eastern regions of Tibet virtually undeformed.

The model run at ϵ = 30% produced a gentle northward slope (0.02º), but negligibly small (0.009º) eastward slope. With increasing convergence, the northward topographic slope of Tibet steepened from 0.02° to 0.03° when ϵ = 70%. Meanwhile, the eastward topographic slope had a small value, ∼ 0.01°. On completion of the experimental run (ϵ =100%), the model Tibet attained a N-S slope of 0.05°, whereas the E-W slope increased to 0.02°.

To highlight the main findings from the two steady-state collision experiments (Type 1 and Type 2), irrespective of fast or slow convergence rates, the collision did not produce eastward crustal flows or clockwise rotation of the crustal flow field around EHS in model Tibet at any stage of the convergence event. None of them gave rise to the present-day E-W extensional strain in central Tibet, as revealed from GPS observations. Therefore, another experiment was run with decelerating convergence rates, as applicable for the India-Asia collision event (Copley et al., 2010; Peter Molnar & Stock, 2009).

6.4.3. TYPE 3 MODEL EXPERIMENT: DECELERATING COLLISION

To perform this unsteady collision experiment, the convergence velocity (I_{DEC}) was reduced stepwise in three stages, approximated to the decreasing India-Asia convergence velocity shown in Fig. 6.7a. In stage S1 (ϵ = 0 to 40%; I_{DEC} = 5.5 cm/yr), the model produced a strongly heterogeneous NNE-directed crustal-flow regime at ϵ = 30%. The flow occurred at high velocities (∼5 cm/yr) in southern Tibet, but decreased to almost zero at the northern boundary (Fig. 6.7a-i). In stage S2 (ϵ = 41 to

70%; I_{DEC} = 4.5 cm/yr), the flow regime propagated northward to induce crustal flow velocity ~ 4.2 cm/yr in central plateau at ϵ = 50%. The model produced flows also in northern Tibet, although at much lower rates (~1.5 cm/yr) (Fig. 6.7a-ii). At this stage the rigid Tarim basin acted as a mechanical barrier, and reduced the effective width of the western Tibetan plateau to make it much narrower than its eastern flank. This west to east variation in the mechanical setting caused the crustal flows to take a north-east ward turn in the eastern parts of Tibet (Fig. 6.7a-iii). In stage S3 (ϵ = 71 to 100%; I_{DEC} = 3.5 cm/yr) of collision, the model showed a remarkable change in the crustal flow pattern (Fig. 6.7a-iv). Southern Tibet underwent NNE-directed flows with an average rate of 3.5 cm/yr, which reduced to ~2 cm/yr in north-eastern Tibet with an azimuthal change grossly to ENE. Secondly, the flow field developed a distinct region of east-directed crustal flows with magnitudes of 1.5 to 2 cm/yr in the central and southern parts of the plateau (Fig. 6.7a-iv), which was not observed in the steady collision experiments. Interestingly, the eastward crustal flow, after facing resistance from the mechanically strong Sichuan basin in the east, took a clockwise turn to channelize through the passage in between the Eastern Himalayan Syntaxis (EHS) and Sichuan basin, and escaped southward, forming a fan-like front. This region accelerated the crustal flows, with velocity magnitudes reaching ~3 cm/yr (Figure 6.7a-iv). At the final stage (ϵ =100%), the model produced a crustal-flow pattern strikingly similar to the present-day GPS velocity field (Liang et al., 2013; Zhang et al., 2004).

In the initial stage (ϵ = 30%) of collision the Type 3 model showed localization of high strain rates (3.2×10^{-8} yr^{-1}) in front of the leading Indian indenter edge. With on-going collision (ϵ = 30% to 70%) the deformation front propagated northward to

increase the strain rates in central and NW Tibet at 3.2 to 4×10^{-8} yr^{-1}. At $\epsilon = 100\%$, southern, north-western, and north-eastern Tibet became active locations for deformations with high strain rates (2 to 3.2 $\times 10^{-8}$ yr^{-1}). Interestingly, at this stage
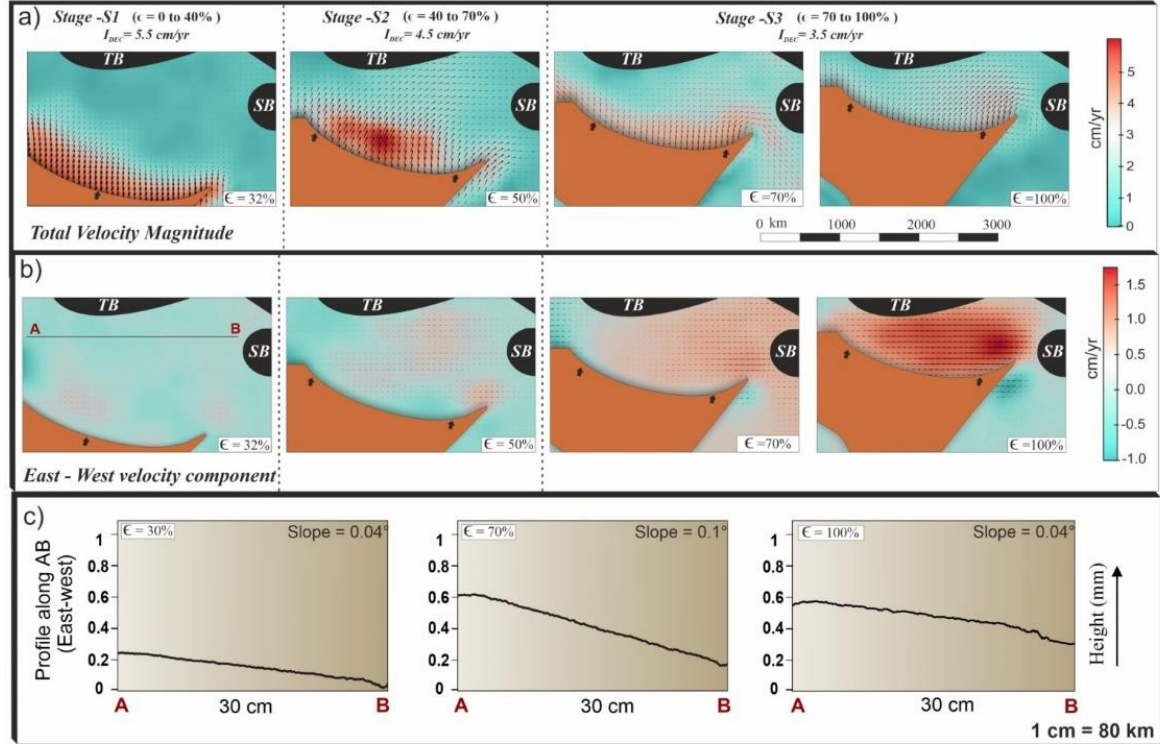
Figure 6.6: a) Change in crustal flow pattern measured from the analogue model as India-Asia convergence velocity reduces through time. b) East-west velocity component of the total velocity field. Note that East-West velocity component increases significantly when indentation velocity reduces to present day average of 3.5 cm/yr at stage S3. c) Evolution of east-west topographic gradient in the model Tibetan plateau.

the region between EHS and Sichuan basins also started to deform at high strain rates (3.2 to .8 $\times 10^{-8}$ yr^{-1}). On the other end, central Tibet was dominated by ESE-WNW extensional strains of 0.8 to 2.2 $\times 10^{-8}$ yr^{-1}.

The decelerating collision kinematics led to characteristic topographic evolution in model Tibet. In stage S1 ($\epsilon =30\%$) the southern plateau gained higher topographic elevation to form a gentle northward slope of 0.03°, and almost an equal slope of 0.04° in the E-W direction (Fig. 6.7c-i). Towards the end of stage S2 ($\epsilon = 70\%$), the model plateau underwent a remarkable topographic modification, setting steep topographic slopes both in the northward (0.07°) and eastward (0.1°) directions (Fig.

6.7c-ii). The eastward topographic gradient directed the gravitational collapse of the elevated plateau to facilitate crustal flows from western and central Tibet towards the south-eastern and north-eastern region. At the end of stage S3 (ϵ =100%), the topographic gradients reduced both along the N-S (0.02°) and E-W (0.04°) directions (Fig. 6.7c-iii).

6.5. N-S VERSUS E-W EXTENSIONAL TECTONICS: AN OVERVIEW

The results obtained from the analogue models are compared to the 2D thermomechanical numerical model results (Maiti and Mandal, 2021), which suggest that during the early phase of fast India-Asia collision the downgoing motion of the subducting Indian plate (subduction velocity, U_s = 8 cm/yr) produced a high lubrication dynamic pressure in the Himalayan wedge and facilitated burial of buoyant crustal rocks into the wedge. The magnitudes of lubrication dynamic pressure started to drop with reducing subduction velocity, and the collision system eventually attained a threshold condition and under this critical state of low dynamic pressure, the Himalayan wedge failed to transmit sufficient contractional stress to support the elevated topography of the overriding Tibetan lithosphere produced in the fast collision phase, and resulted in gravitational collapse in the uplifted and thickened Tibetan crust. The collapse of the Tibetan plateau started to occur preferentially at the southern margin of Tibet, which forced the deep-crustal materials in the Himalayan wedge to extrude in the form of a spontaneously developed extrusion channel, bounded by two oppositely directed shear zones with a normal sense of shear on the top and a thrust sense of shear at the bottom. The normal sense of shear in the model is located close to the Himalaya-Tibet suture zone, and represents the N-S extensional tectonics, as manifested in the form of STDS fault

systems at the southern margin of Tibet (Carosi et al., 2018). Thus, the comparison between the numerical (Maiti and Mandal, 2021) and analogue modelling approach integrates the following crucial issues within a single geodynamic framework: 1) the underlying dynamics of N-S and E-W crustal extensions in Tibet, 2) the role of temporally retarding India-Asia collision in the extensional tectonics, and 2) the influence of rigid crustal blocks, such as Tarim and Sichuan basins in the evolution of 3D Tibetan topography with eastward topographic slopes that set in the present-day eastward crustal flows in the Tibetan plateau. The 2D numerical model suggests that the Himalayan wedge dynamics entirely controlled the N-S extension in the Himalaya-Tibet system, where the retarding India-Asia convergence kinematics played a mediated role, as explained in the following. According to the lubrication model, the downward movement of subducting Indian plate at a high velocity produced a large dynamic pressure in the wedge (Maiti and Mandal, 2020; Maiti et al., 2021), which enabled the wedge to support the overriding lithospheric load and at the same time transferred compressive stresses into the overriding Tibet. With decreasing plate velocity, the dynamic pressure started to decline, as predicted from the lubrication mechanics (Maiti and Mandal, 2020) and became sufficiently low so that the wedge failed to support the elevated Tibetan topography and initiated gravitational collapse at the southern margin of Tibet. The gravitational collapse, in turn, forced the deep-crustal materials in the Himalayan wedge to extrude in the southward direction that developed a N-S extensional tectonic setting. This N-S extension in the southern margin of Tibet was the first response to the reducing collision rate, the effect of which took a considerable time to influence the differentially uplifted western and eastern Tibetan topography and to initiate the eastward crustal flows. The wedge dynamic

model explains a time difference of 4 to 5 Ma between the initiation timings of N-S and E-W extensional events.

To summarize, this study substantiates the topography-induced gravitational collapse theory for the Tibetan plateau to explain the extensional crustal deformations in the Himalaya-Tibet system (Cook & Royden, 2008; Copley & Mckenzie, 2007). However, coupled dynamics is required to explain the extension across and along the orogen, i.e. N-S and E-W, respectively. It is the drop in dynamic pressure in the Himalayan wedge that dictated the N-S extension in southern Tibet, whereas the topography-driven gravity current developed due to the eastward topographic gradient set in the E-W extension in central Tibet. However, the two tectonic events did not occur exactly in the same time frame; the N-S extension (22 – 11 Ma) ceased to operate as the dynamic pressure regained its initial state with ongoing topographic collapse, but the E-W extension (18-4 Ma) continued to take place in response to the eastward topographic slope under the present-day convergence kinematics. Therefore, reducing Indian plate's indentation velocity actually controlled the coupled extensional dynamics. Far-field tectonic stresses or convective instability might have provided additional influences on extensional tectonics (Schellart et al., 2019). But, a complete synthesis of model results points to that a combined effect of the crustal heterogeneity and the reducing Indian indentation velocity is necessary and sufficient to explain the E-W extension.

6.6. REFERENCES

Bajolet, F., Chardon, D., Martinod, J., Gapais, D., & Kermarrec, J. J. (2015). Synconvergence flow inside and at the margin of orogenic plateaus: Lithospheric-scale experimental approach. *Journal of Geophysical Research: Solid Earth*. https://doi.org/10.1002/2015JB012110

Beaumont, C., Jamieson, R. A., Nguyen, M. H., & Lee, B. (2001). Himalayan tectonics explained by extrusion of a low-viscosity crustal channel coupled to focused surface denudation. *Nature*. https://doi.org/10.1038/414738a

Bird, P. (1991). Lateral extrusion of lower crust from under high topography, in the isostatic limit. *Journal of Geophysical Research*, *96*(B6), 275–286. https://doi.org/10.1029/91jb00370

Bischoff, S. H., & Flesch, L. M. (2018). Normal faulting and viscous buckling in the Tibetan Plateau induced by a weak lower crust. *Nature Communications*. https://doi.org/10.1038/s41467-018-07312-9

Blisniuk, P. M., Hacker, B. R., Glodny, J., Ratschbacher, L., Bi, S., Wu, Z., et al. (2001). Normal faulting in central Tibet since at least 13.5 Myr ago. *Nature*. https://doi.org/10.1038/35088045

Chen, L., Capitanio, F. A., Liu, L., & Gerya, T. V. (2017). Crustal rheology controls on the Tibetan plateau formation during India-Asia convergence. *Nature Communications*. https://doi.org/10.1038/ncomms15992

Chung, S. L., Lo, C. H., Lee, T. Y., Zhang, Y., Xie, Y., Li, X., et al. (1998). Diachronous uplift of the Tibetan plateau starting 40 Myr ago. *Nature*. https://doi.org/10.1038/29511

Clark, M. K., & Royden, L. H. (2000). Topographic ooze: Building the eastern margin of Tibet by lower crustal flow. *Geology*. https://doi.org/10.1130/0091-7613(2000)28<703:TOBTEM>2.0.CO;2

Clark, M. K., House, M. A., Royden, L. H., Whipple, K. X., Burchfiel, B. C., Zhang, X., & Tang, W. (2005). Late Cenozoic uplift of southeastern Tibet. *Geology*. https://doi.org/10.1130/G21265.1

Cook, K. L., & Royden, L. H. (2008). The role of crustal strength variations in shaping orogenic plateaus, with application to Tibet. *Journal of Geophysical Research: Solid Earth*. https://doi.org/10.1029/2007JB005457

Cooper, F. J., Hodges, K. V., Parrish, R. R., Roberts, N. M. W., & Horstwood, M. S. A. (2015). Synchronous N-S and E-W extension at the Tibet-to-Himalaya transition in NW Bhutan. *Tectonics*. https://doi.org/10.1002/2014TC003712

Copley, A. (2012). The formation of mountain range curvature by gravitational spreading. *Earth and Planetary Science Letters*. https://doi.org/10.1016/j.epsl.2012.07.036

REFERENCES

Copley, A., & Mckenzie, D. (2007). Models of crustal flow in the India-Asia collision zone. *Geophysical Journal International*. https://doi.org/10.1111/j.1365-246X.2007.03343.x

Copley, A., Avouac, J. P., & Royer, J. Y. (2010). India-Asia collision and the Cenozoic slowdown of the Indian plate: Implications for the forces driving plate motions. *Journal of Geophysical Research: Solid Earth*. https://doi.org/10.1029/2009JB006634

Copley, A., Avouac, J. P., & Wernicke, B. P. (2011). Evidence for mechanical coupling and strong Indian lower crust beneath southern Tibet. *Nature*. https://doi.org/10.1038/nature09926

Craig, T. J., Kelemen, P. B., Hacker, B. R., & Copley, A. (2020). Reconciling Geophysical and Petrological Estimates of the Thermal Structure of Southern Tibet. *Geochemistry, Geophysics, Geosystems*, *21*(8). https://doi.org/10.1029/2019GC008837

DeCelles, P. G., Robinson, D. M., & Zandt, G. (2002). Implications of shortening in the Himalayan fold-thrust belt for uplift of the Tibetan Plateau. *Tectonics*. https://doi.org/10.1029/2001TC001322

DeCelles, P. G., Quade, J., Kapp, P., Fan, M., Dettman, D. L., & Ding, L. (2007). High and dry in central Tibet during the Late Oligocene. *Earth and Planetary Science Letters*. https://doi.org/10.1016/j.epsl.2006.11.001

Dewey, J. F., Shackleton, R. M., Chengfa, C., & Yiyin, S. (1988). The tectonic evolution of the Tibetan Plateau. *Philosophical Transactions of the Royal Society of London. Series A, Mathematical and Physical Sciences*. https://doi.org/10.1098/rsta.1988.0135

England, P., & Houseman, G. (1989). Extension during continental convergence, with application to the Tibetan Plateau. *Journal of Geophysical Research*. https://doi.org/10.1029/jb094ib12p17561

England, Philip, & Houseman, G. (1986). Finite strain calculations of continental deformation: 2. Comparison with the India-Asia Collision Zone. *Journal of Geophysical Research: Solid Earth*. https://doi.org/10.1029/jb091ib03p03664

England, Philip, & McKenzie, D. (1982). A thin viscous sheet model for continental deformation. *Geophysical Journal of the Royal Astronomical Society*. https://doi.org/10.1111/j.1365-246X.1982.tb04969.x

Flesch, L. M., Haines, A. J., & Holt, W. E. (2001). Dynamics of the India-Eurasia collision zone. *Journal of Geophysical Research: Solid Earth*. https://doi.org/10.1029/2001jb000208

Fournier, M., Jolivet, L., Davy, P., & Thomas, J. C. (2004). Backarc extension and collision: An experimental approach to the tectonics of Asia. *Geophysical Journal International*. https://doi.org/10.1111/j.1365-246X.2004.02223.x

Galland, O., Bertelsen, H. S., Guldstrand, F., Girod, L., Johannessen, R. F., Bjugger, F., et al. (2016). Application of open-source photogrammetric software MicMac for

monitoring surface deformation in laboratory models. *Journal of Geophysical Research: Solid Earth*. https://doi.org/10.1002/2015JB012564

Gan, W., Zhang, P., Shen, Z. K., Niu, Z., Wang, M., Wan, Y., et al. (2007). Present-day crustal motion within the Tibetan Plateau inferred from GPS measurements. *Journal of Geophysical Research: Solid Earth*. https://doi.org/10.1029/2005JB004120

Ge, W. P., Molnar, P., Shen, Z. K., & Li, Q. (2015). Present-day crustal thinning in the southern and northern Tibetan Plateau revealed by GPS measurements. *Geophysical Research Letters*. https://doi.org/10.1002/2015GL064347

Van Hinsbergen, D. J. J., Kapp, P., Dupont-Nivet, G., Lippert, P. C., Decelles, P. G., & Torsvik, T. H. (2011). Restoration of Cenozoic deformation in Asia and the size of Greater India. *Tectonics*. https://doi.org/10.1029/2011TC002908

Houseman, G., & England, P. (1986). Finite strain calculations of continental deformation: 1. Method and general results for convergent zones. *Journal of Geophysical Research: Solid Earth*. https://doi.org/10.1029/jb091ib03p03651

Huyghe, P., Galy, A., Mugnier, J. L., & France-Lanord, C. (2001). Propagation of the thrust system and erosion in the Lesser Himalaya: Geochemical and sedimentological evidence. *Geology*. https://doi.org/10.1130/0091-7613(2001)029<1007:POTTSA>2.0.CO;2

Jiménez-Munt, I., Fernàndez, M., Vergés, J., & Platt, J. P. (2008). Lithosphere structure underneath the Tibetan Plateau inferred from elevation, gravity and geoid anomalies. *Earth and Planetary Science Letters*. https://doi.org/10.1016/j.epsl.2007.11.045

Kapp, P., Yin, A., Harrison, T. M., & Ding, L. (2005). Cretaceous-Tertiary shortening, basin development, and volcanism in central Tibet. *Bulletin of the Geological Society of America*, *117*(7–8), 865–878. https://doi.org/10.1130/B25595.1

King Hubbert, M. (1937). Theory of scale models as applied to the study of geologic structures. *Bulletin of the Geological Society of America*, *48*(10), 1459–1520. https://doi.org/10.1130/GSAB-48-1459

Li, C., van der Hilst, R. D., & Toksöz, M. N. (2006). Constraining P-wave velocity variations in the upper mantle beneath Southeast Asia. *Physics of the Earth and Planetary Interiors*. https://doi.org/10.1016/j.pepi.2005.09.008

Li, Y., Wang, C., Dai, J., Xu, G., Hou, Y., & Li, X. (2015a). Propagation of the deformation and growth of the Tibetan-Himalayan orogen: A review. *Earth-Science Reviews*. https://doi.org/10.1016/j.earscirev.2015.01.001

Li, Y., Wang, C., Dai, J., Xu, G., Hou, Y., & Li, X. (2015b). Propagation of the deformation and growth of the Tibetan–Himalayan orogen: A review. *Earth-Science Reviews*, *143*, 36–61. https://doi.org/10.1016/J.EARSCIREV.2015.01.001

Liang, S., Gan, W., Shen, C., Xiao, G., Liu, J., Chen, W., et al. (2013). Three-dimensional velocity field of present-day crustal motion of the Tibetan Plateau derived from GPS measurements. *Journal of Geophysical Research: Solid Earth*. https://doi.org/10.1002/2013JB010503

REFERENCES

Maiti, G., & Mandal, N. (2021). Early Miocene Exhumation of High-Pressure Rocks in the Himalaya: A Response to Reduced India-Asia Convergence Velocity. *Frontiers in Earth Science*, *9*, 66. https://doi.org/10.3389/FEART.2021.632806/BIBTEX

Maiti, G., Mandal, N., & Misra, S. (2020). Insights into the dynamics of an orogenic wedge from lubrication theory: Implications for the Himalayan tectonics. *Tectonophysics*. https://doi.org/10.1016/j.tecto.2020.228335

Marques, F. O., & Mandal, N. (2016). Post-buckling relaxation of an elastic layer and its geological relevance: Insights from analogue experiments in pure shear. *Tectonophysics*. https://doi.org/10.1016/j.tecto.2015.12.004

Meigs, A. J., Burbank, D. W., & Beck, R. A. (1995). Middle-late Miocene (>10 Ma) formation of the Main Boundary Thrust in the western Himalaya. *Geology*. https://doi.org/10.1130/0091-7613(1995)023<0423:MLMMFO>2.3.CO;2

Mitsuishi, M., Wallis, S. R., Aoya, M., Lee, J., & Wang, Y. (2012). E-W extension at 19Ma in the Kung Co area, S. Tibet: Evidence for contemporaneous E-W and N-S extension in the Himalayan orogen. *Earth and Planetary Science Letters*. https://doi.org/10.1016/j.epsl.2011.11.013

Molnar, P., & Stock, J. M. (2009). Slowing of India's convergence with Eurasia since 20 Ma and its implications for Tibetan mantle dynamics. *Tectonics*. https://doi.org/10.1029/2008TC002271

Molnar, P., England, P., & Martinod, J. (1993). Mantle dynamics, uplift of the Tibetan Plateau, and the Indian Monsoon. *Reviews of Geophysics*. https://doi.org/10.1029/93RG02030

Montemagni, C., Iaccarino, S., Montomoli, C., Carosi, R., Jain, A. K., & Villa, I. M. (2018). Age constraints on the deformation style of the south tibetan detachment system in garhwal himalaya. *Italian Journal of Geosciences*. https://doi.org/10.3301/IJG.2018.07

Murphy, M. A., Yin, A., Harrison, T. M., Dürr, S. B., Chen, Z., Ryerson, F. J., et al. (1997). Did the Indo-Asian collision alone create the Tibetan plateau? *Geology*. https://doi.org/10.1130/0091-7613(1997)025<0719:DTIACA>2.3.CO;2

Najman, Y. (2006). The detrital record of orogenesis: A review of approaches and techniques used in the Himalayan sedimentary basins. *Earth-Science Reviews*. https://doi.org/10.1016/j.earscirev.2005.04.004

Powell, C. M. A. (1986). Continental underplating model for the rise of the Tibetan Plateau. *Earth and Planetary Science Letters*. https://doi.org/10.1016/0012-821X(86)90102-0

Pusok, A. E., & Kaus, B. J. P. (2015). Development of topography in 3-D continental-collision models. *Geochemistry, Geophysics, Geosystems*. https://doi.org/10.1002/2015GC005732

Pusok, Adina E., & Stegman, D. R. (2020). The convergence history of India-Eurasia records multiple subduction dynamics processes. *Science Advances*. https://doi.org/10.1126/sciadv.aaz8681

Rey, P., Vanderhaeghe, O., & Teyssier, C. (2001). Gravitational collapse of the continental crust: Definition, regimes and modes. *Tectonophysics*. https://doi.org/10.1016/S0040-1951(01)00174-3

Ribe, N. M., & Davaille, A. (2013). Dynamical similarity and density (non-) proportionality in experimental tectonics. *Tectonophysics*. https://doi.org/10.1016/j.tecto.2013.06.005

Schellart, W. P., Chen, Z., Strak, V., Duarte, J. C., & Rosas, F. M. (2019). Pacific subduction control on Asian continental deformation including Tibetan extension and eastward extrusion tectonics. *Nature Communications*. https://doi.org/10.1038/s41467-019-12337-9

Schellart, Wouter P., & Strak, V. (2016). A review of analogue modelling of geodynamic processes: Approaches, scaling, materials and quantification, with an application to subduction experiments. *Journal of Geodynamics*, *100*, 7–32. https://doi.org/10.1016/j.jog.2016.03.009

Soucy La Roche, R., Godin, L., Cottle, J. M., & Kellett, D. A. (2018). Preservation of the Early Evolution of the Himalayan Middle Crust in Foreland Klippen: Insights from the Karnali Klippe, West Nepal. *Tectonics*. https://doi.org/10.1002/2017TC004847

Styron, R. H., Taylor, M. H., Sundell, K. E., Stockli, D. F., Oalmann, J. A. G., Möller, A., et al. (2013). Miocene initiation and acceleration of extension in the South Lunggar rift, western Tibet: Evolution of an active detachment system from structural mapping and (U-Th)/He thermochronology. *Tectonics*. https://doi.org/10.1002/tect.20053

Tapponnier, P., Peltzer, G., Le Dain, A. Y., Armijo, R., & Cobbold, P. (1982). Propagating extrusion tectonics in Asia: new insights from simple experiments with plasticine. *Geology*. https://doi.org/10.1130/0091-7613(1982)10<611:PETIAN>2.0.CO;2

Tapponnier, P., Zhiqin, X., Roger, F., Meyer, B., Arnaud, N., Wittlinger, G., & Jingsui, Y. (2001). Oblique stepwise rise and growth of the tibet plateau. *Science*. https://doi.org/10.1126/science.105978

Taylor, M., Forte, A., Laskowski, A., & Ding, L. (2021). Active uplift of southern tibet revealed. *GSA Today*, *31*(8). https://doi.org/10.1130/GSATG487A.1

Thielicke, W., & Stamhuis, E. (2010). Pivlab-time-resolved digital particle image velocimetry tool for matlab. *… under the BSD License, Programmed with MATLAB*. https://doi.org/doi:10.6084/m9.figshare.1092508

Wang, C., Zhao, X., Liu, Z., Lippert, P. C., Graham, S. A., Coe, R. S., et al. (2008). Constraints on the early uplift history of the Tibetan Plateau. *Proceedings of the National Academy of Sciences of the United States of America*. https://doi.org/10.1073/pnas.0703595105

Wang, C., Dai, J., Zhao, X., Li, Y., Graham, S. A., He, D., et al. (2014). Outward-growth of the Tibetan Plateau during the Cenozoic: A review. *Tectonophysics*. https://doi.org/10.1016/j.tecto.2014.01.036

Wang, E., Kirby, E., Furlong, K. P., Van Soest, M., Xu, G., Shi, X., et al. (2012). Two-phase growth of high topography in eastern Tibet during the Cenozoic. *Nature Geoscience*. https://doi.org/10.1038/ngeo1538

Wang, Y. (2001). Heat flow pattern and lateral variations of lithosphere strength in China mainland: Constraints on active deformation. *Physics of the Earth and Planetary Interiors*. https://doi.org/10.1016/S0031-9201(01)00251-5

Wu, C., Li, J., Zuza, A. V., Liu, C., Liu, W., Chen, X., et al. (2020). Cenozoic cooling history and fluvial terrace development of the western domain of the Eastern Kunlun Range, northern Tibet. *Palaeogeography, Palaeoclimatology, Palaeoecology*, *560*(August), 109971. https://doi.org/10.1016/j.palaeo.2020.109971

Wu, C., Zuza, A. V., Li, J., Haproff, P. J., Yin, A., Chen, X., et al. (2021). Late Mesozoic–Cenozoic cooling history of the northeastern Tibetan Plateau and its foreland derived from low-temperature thermochronology. *GSA Bulletin*, (March). https://doi.org/10.1130/b35879.1

Xu, G., & Kamp, P. J. J. (2000). Tectonics and denudation adjacent to the Xianshuihe Fault, eastern Tibetan Plateau: Constraints from fission track thermochronology. *Journal of Geophysical Research: Solid Earth*. https://doi.org/10.1029/2000jb900159

Yang, S., Chen, H., & Cheng, X. (2007). Deformation characteristics and rules of spatial change for the Northern Qilianshan thrust belt. *Earth Science Frontiers*, *14*(5), 211–221. https://doi.org/10.3321/j.issn:1005 -2321.2007.05.021

Yang, Y., & Liu, M. (2013). The indo-asian continental collision: A 3-D viscous model. *Tectonophysics*. https://doi.org/10.1016/j.tecto.2013.06.032

Yin, A. (2000). Mode of Cenozoic east-west extension in Tibet suggesting a common origin of rifts in Asia during the Indo-Asian collision. *Journal of Geophysical Research: Solid Earth*. https://doi.org/10.1029/2000jb900168

Yin, A., & Taylor, M. H. (2011). Mechanics of V-shaped conjugate strike-slip faults and the corresponding continuum mode of continental deformation. *Bulletin of the Geological Society of America*. https://doi.org/10.1130/B30159.1

Zhang, P. Z., Shen, Z., Wang, M., Gan, W., Bürgmann, R., Molnar, P., et al. (2004). Continuous deformation of the Tibetan Plateau from global positioning system data. *Geology*. https://doi.org/10.1130/G20554.1

Zhao, W. -L, & Morgan, W. J. (1987). Injection of Indian crust into Tibetan lower crust: A two-dimensional finite element model study. *Tectonics*. https://doi.org/10.1029/TC006i004p00489

Zulauf, J., & Zulauf, G. (2004). Rheology of plasticine used as rock analogue: The impact of temperature, composition and strain. *Journal of Structural Geology*. https://doi.org/10.1016/j.jsg.2003.07.005

Chapter 7.

MECHANISMS OF SHEAR FAILURE IN LITHOSPHERE

7.1. LARGE-SCALE FAILURE OF LITHOSPHERIC SLABS IN SUBDUCTION ZONES

Geophysical and seismic evidences suggest that subducting lithosphere generally have finite dimensions laterally as well as down the slab dip.. They often have lateral terminal points where positively buoyant continental masses encounter the trench, resulting in cessation of the subduction process. This kind of kinematic state can trigger slab breakoff phenomena, such as detachment, tearing and shearing of the lithosphere slabs (Fig. 7.1), as discussed briefly in Chapter 5. The breaking processes require not only significant down-ward pull forces, but also and involves complex rheological and kinematic transformations (Duretz et al., 2011; Duretz et al., 2013; Yoshioka and Wortel, 1995). The slab-breakoff model, as first proposed by Davies and von Blanckenburg, 1995 accounts for buoyancy-driven detachment of subducted oceanic lithosphere from the light continental lithosphere following continental collision. This model explains post-collisional magmatism and exhumation of high-pressure rocks in the European Alps.

In the past three decades a wide range of numerical and analogue models appeared in the literature (Yoshioka and Wortel, 1995, Wong A Ton and Wortel, 1997, Regard et al., 2005, Regard et al., 2008, Duretz and Gerya, 2013); all of them primarily aim to investigate the physical mechanism of slab detachment. Several studies evaluated the possible effects of slab breakoff on crucial geological processes, such as surface uplift and erosion, exhumation of high-pressure rocks, thermal disturbances, and heat sources (van de Zedde and Wortel, 2001, Buiter et al., 2002, Gerya et al., 2004, Zlotnik et al., 2008, van Hunen and Allen, 2011). Further. Some workers

explained specific tectonic events, e.g., ridge-trench collision   in the light of such models (Burkett and Billen, 2010). Another direction of studies, mostly based on numerical models enumerate topographic response to slab breakoff events and predict surface uplift rates on a wide range, varying from as low as 0.1 km/Ma to as
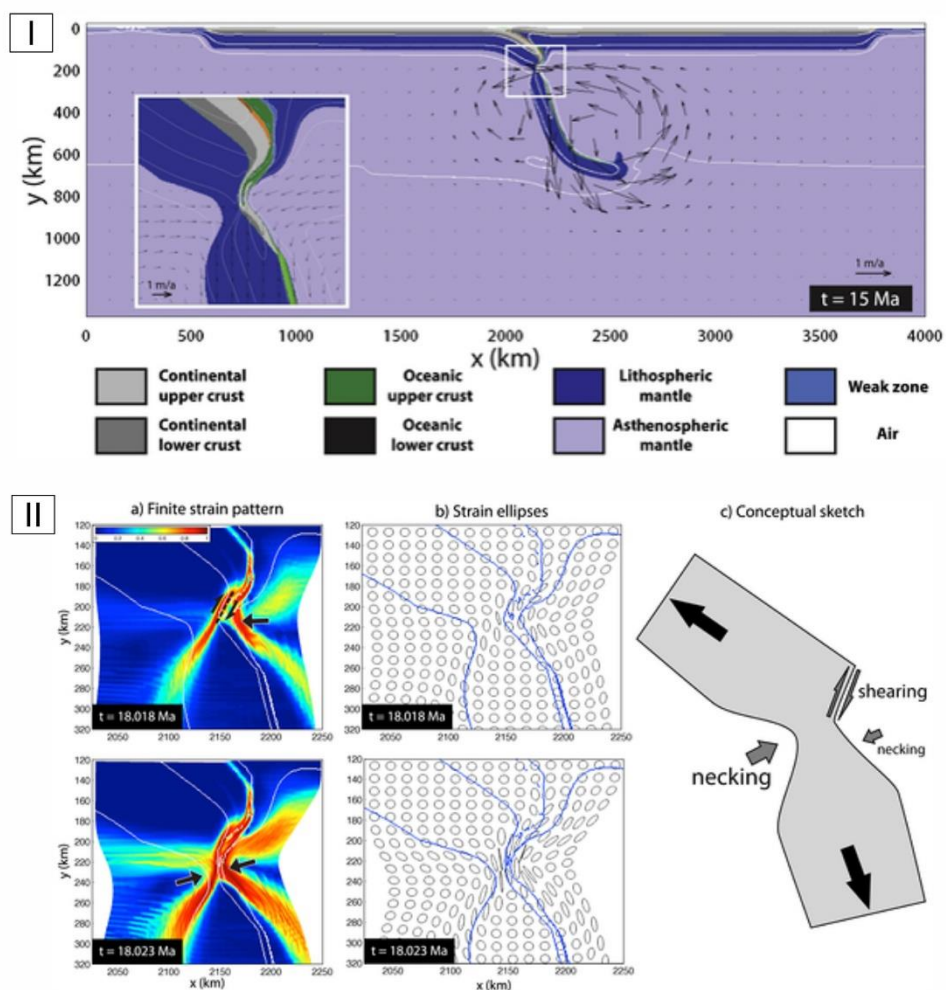
Figure 7.1: The process of slab detachment as shown by Duretz et al., 2012; I) simulation demonstrating intermediate depth slab detachment. The model is dynamically driven by the slab pull and the ridge push exerted by the mantle on the left and right sides of the model domain, II) model results showing a) accumulation of finite strain at the detachment zone, b) strain ellipses corresponding to the two stage intermediate depth slab detachment, and c) Conceptual sketch showing the interplay of localized shear deformation and distributed necking in the detachment process.

high as 2.65 km/Ma (Andrews and Billen, 2009, Duretz et al., 2011).

It is now a well- accepted hypothesis that slab detachment in continental-oceanic settings originate from the failure under tensile stresses generated by the

opposite actions of the subducting continental lithosphere (positive buoyancy) and the previously subducted oceanic slab (negative buoyancy). The two major consequences of slab detachment can be summarized as: (1) flow of hot asthenosphere into the detachment location, and (2) a complete or partial loss of the slab pull force in the upper plate. The first case is frequently invoked to explain several tectonic processes, like exhumation of deep-lithospheric materials under high pressure [Andersen et al., 1991; Babist et al., 2006; Xu et al., 2010], variations in surface uplift rates [Rogers et al., 2002; Morley and Back, 2008] and in the sedimentary record [Mugnier and Huyghe, 2006], orogenic extension [Zeck, 1996], or frequent variations in plate motions [Austermann et al., 2011]. The second case, on the other hand, is typically considered as an effective mechanism to advect heat from lithospheric to sub crustal level [van de Zedde and Wortel, 2001], resulting in partial melting and plutonism [Davies and von Blanckenburg, 1995; Ferrari, 2004; Altunkaynak and Can Genç, 2004]. Some workers have suggested that the long-term crustal recycling processes can be influenced by the entrainment of continental material following a slab detachment event in the mantle [Hildebrand and Bowring, 1999].

Understanding the dynamics of shear failure in lithospheric slabs is thus, an important direction of geophysical research, where the process of strain localization plays a critical role in determining the complex failure mechanisms. Strain localization can be defined as an instability phenomenon, occurring in deformable materials subjected to some energy dissipative behavior. This instability results in sharp jumps in the gradients of displacement or velocity fields across a narrow zone of finite thickness, which often leads to rupture failure (material discontinuity) in the

continua. These narrow zones of intense shear strain localization are termed as *shear bands* (Rice 1985; Rudnicki & Rice, 1975). In ductile materials, shear bands can grow in number to increase their population density and produce shear zones, characterized by arrays of different types of shear bands. The next section presents a comprehensive review of the earlier numerical, experimental and theoretical studies on the origin, mode, orientation and geometry of shear bands in ductile shear zones.

7.2. SECONDARY SHEAR BANDS IN SHEAR ZONES: A REVIEW
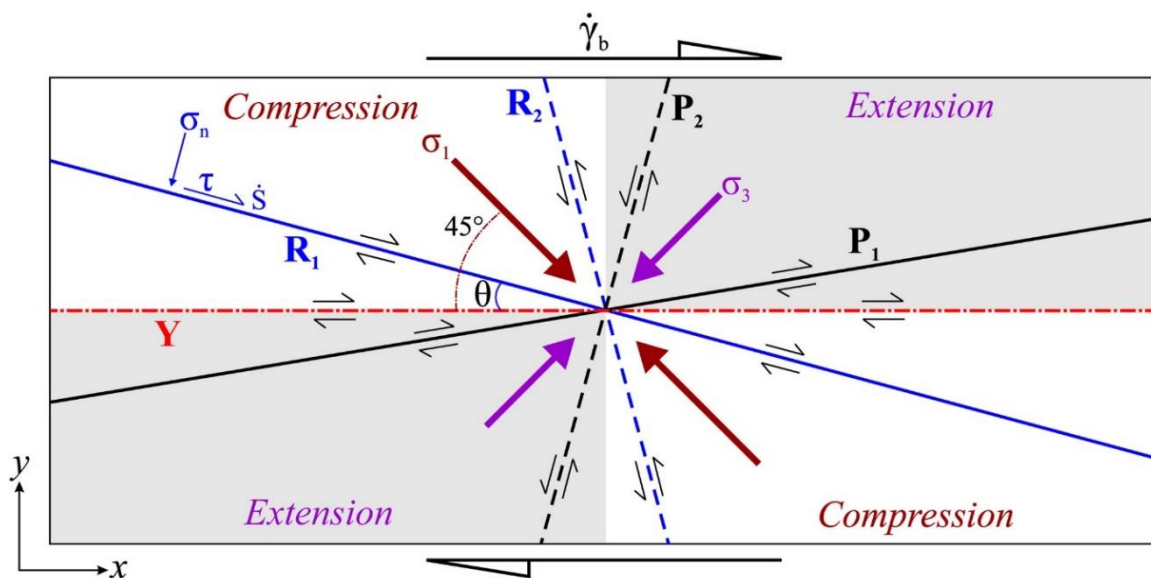
Figure 7.2: Multiple sets of secondary shear bands: R (Riedel), Y and P and their geometrical relationship with the bulk sense (dextral) of shear in a typical brittle shear zone. R and P shear form in conjugate sets, subscripted as 1 and 2, with antithetic and sympathetic vergence to the bulk shear direction, respectively; R_1 and P_1: synthetic shear at low angles and, R_2 and P_2: antithetic shear at high angles to the bulk shear direction. Y is the unique shear band with constant orientation parallel to the shear zone boundary.

It follows from the above discussion that strain localization represents a critical state of failure in ductile materials, its mechanical understanding paves the way to predict failure-driven phenomena, like slab detachment subduction zones. Consequently, shear bands have remained a focus of research in materials sciences (Hill (1962), Nadai (1950), Mandel (1962), Prager (1954), Rice (1977), Thomas (1961)) and geodynamics. Compression test experiments show mechanically

isotropic, homogeneous solids undergo shear failure to produce a conjugate set of shear bands symmetrically oriented to the applied compression direction (Anand & Spitzig, 1980; Bowden & Raha, 1970; Hutchinson & Tvergaard, 1981; Tvergaard et al., 1981). Employing various yield criteria, many workers have provided theoretical solutions to predict the band orientation (angle to the compression direction: θ) as a function of material parameters, such as coefficient of internal friction, dilatancy factor, and strain hardening and softening properties (Anand & Spitzig, 1980, 1982; Du Bernard et al., 2002; Hobbs et al., 1990; Roscoe, 1970; Rudnicki & Rice, 1975; Vardoulakis et al., 1978; Vermeer, 1990). A parallel line of study investigates the failure process in brittle and ductile materials under shear deformation, which is found to be more complex than in compressional deformations (Anand et al., 1987; H. Horii & S. Nemat-Nasser, 1986; Harris & Cobbold, 1985; N. S. Mancktelow, 2006; Meyer et al., 2017; Renshaw & Schulson, 2001; Rice, 1985). It has been demonstrated from shear experiments on brittle materials that the shear failure gives rise to multiple sets of shear bands at varied angles (Logan, 1979; Logan et al., 1992) to the applied shear stress direction, which are described as R-, Y-, and P-bands (Fig. 7.2). R-bands generally occur in conjugate sets (R_1 and R_2) at low and high angle to the shear direction. Ductile shear zones also often produce multiple sets of shear bands, such as low- and high-angle shear bands, comparable to R_1 and R_2 bands. Similar to Y-shear, deformation bands formed parallel to the bulk shear direction, called *C-bands* are a characteristic structure of natural ductile shear zones on micro- (Berthé et al., 1979; Lister & Snoke, 1984; Platt, 1984; Platt & Vissers, 1980) to crustal-scale tectonics (Chester & Logan, 1987; Lin, 2001). According to the classical yield theory (e.g., Coulomb-Navier criterion), shear bands should localize along the planes of maximum effective shear stress (i.e., the resultant of driving and resistive shear stresses), which

207

are experimentally as well as theoretically found to be oriented at angles less than 45° to the principal compression axis (σ_1). It means that the shear bands must form at an angle to the direction of applied shear stress, as the σ_1-axis is oriented at 45° to the shear direction in simple shear deformation (Coulomb, 1773; Roscoe, 1970). This discussion triggers an imminent question: what are the mechanical conditions in which shear bands develop parallel to the bulk shear direction? This study ventures into this question and addresses the problem of C-band formation, which one frequently encounters in ductile shear zones and large-scale strike slip tectonic regimes.

Ductile shear zones in naturally deformed rocks generally show localization of exceptionally large finite strains. They occur on a wide range of scales, and are effectively invariant along their length (Casey, 1980; Cobbold, 1977a, 1977b; Ramsay, 1980; Ramsay & Graham, 1970). According to Rutter (1986), the term "ductility" is used independent to any mechanistic connotation, but it merely signifies continuous deformation in shear zones, without developing any macroscopic fractures. However, many workers have reported brittle deformation bands, such as Riedel also from ductile shear zones (M. Finch et al., 2014; Fossen & Cavalcante, 2017; Fusseis et al., 2006; Fusseis & Handy, 2008; Mukherjee & Koyi, 2010; Paterson & Wong, 2005). Mancktelow & Pennacchioni, (2005) explicitly showed the occurrence of R bands in ductile shear zones under amphibolitic facies condition in the Eastern Alps area. Similarly, Guermani & Pennacchioni, (1998) reported from Western Alps the spatial and temporal association of brittle and plastic structures in sheared granite. Some workers (Coelho et al., 2006) have demonstrated the evolution of low- and high-angle Riedel bands (R_1 and R_2) in natural as well as experimental ductile shear zones. The

two sets of bands are oriented at an angle of about $\phi/2$ and (90°- $\phi/2$) respectively to the bulk shear direction, where ϕ is the angle of internal friction. Considering nonlinear viscous rheology, Katz et al., (2006) showed the growth of similar low- and high-angle shear bands in a ductile regime as a function of the stress exponent ($n = 1$ to 6). Their theoretical model predicts nonlinear viscous rheology ($n > 1$) as the most critical factor in controlling the shear band orientation. However, Mancktelow, 2006 argued that strain localization in ductile shear zones cannot be appropriately modelled using power-law viscous rheology. He invoked a pressure dependent plastic yield criterion in his mechanical model to explain their characteristic phenomena, e.g. fluid influx into shear zones.

A robust line of shear zone studies involves rock deformation experiments under high pressure and temperature conditions, mainly to investigate the mechanism of shear localization in ductile creep regimes. Shear experiments on quartz aggregates at a temperature of 1025 °C and confining pressure of 350 MPa produced shear bands in two sets, oriented at low and high angles to the applied shear direction (Schmocker et al., 2003). Similarly, Misra, Burlini, et al., 2009 demonstrated the formation of low-angle Riedel shear bands (10° – 28°) in metapelites in a ductile deformation regime under low shear-strain conditions at 750° C and 300 MPa. They concluded that localization of brittle shear bands facilitated the permeability and porosity of rocks during ductile shear deformation. Holtzman et al., (2003) demonstrated the formation of low-angle shear bands, oriented at 15°- 20° to the shear plane in partially molten mantle rocks. These bands act as a preferential conduit of melt flow within the deep-seated molten mantle rocks. Analogue model experiments suggest that the degree of mechanical anisotropy can significantly

influence the preferential growth of low-angle shear bands in brittle-ductile shear zones (Misra et al., 2009). These experiments produced a single set of low-angle shear bands when the degree of mechanical anisotropy was extremely high.

Most of the earlier studies discussed above dealt with the origin of low- and high-angle shear bands. Surprisingly, natural ductile shear zones rarely show these bands. They are rather frequented by spatially abundant shear- parallel C bands, often imparting a major fabric in the sheared rocks (Lister & Snoke, 1984; Platt, 1984; Platt & Vissers, 1980). This disagrees with most of the earlier experiments (Byerlee et al., 1978; Misra et al., 2009; Power & Tullis, 1989; Rutter et al., 1986), which produced dominantly low-angle shear bands, virtually without any traces of C-shear bands. Such contrasting observations in nature and experiments motivates the present thesis work to address an obvious question: what controls the mechanism of C-shear band growth in natural shear zones? This knowledge gap forms the primary theme of this study.

7.3. INTERNAL STRUCTURES OF NATURAL SHEAR ZONES: FIELD STUDIES
7.3.1. GEOLOGICAL DESCRIPTION OF THE STUDY AREA

The development of secondary shear bands in ductile shear zones was studied in two tectonic regimes of the Precambrian craton in Eastern India (Fig. 7.3): 1) Singhbhum Shear Zone (SSZ) and 2) Chotanagpur Granite Gneiss Complex (CGGC). The SSZ is a spectacular arcuate, about 200 km long and 2 km wide shear zone (thrust) that delineates the interface between the Archean nucleus on south and the North Singhbhum Mobile belt. A part of the field study was carried out in the southeastern
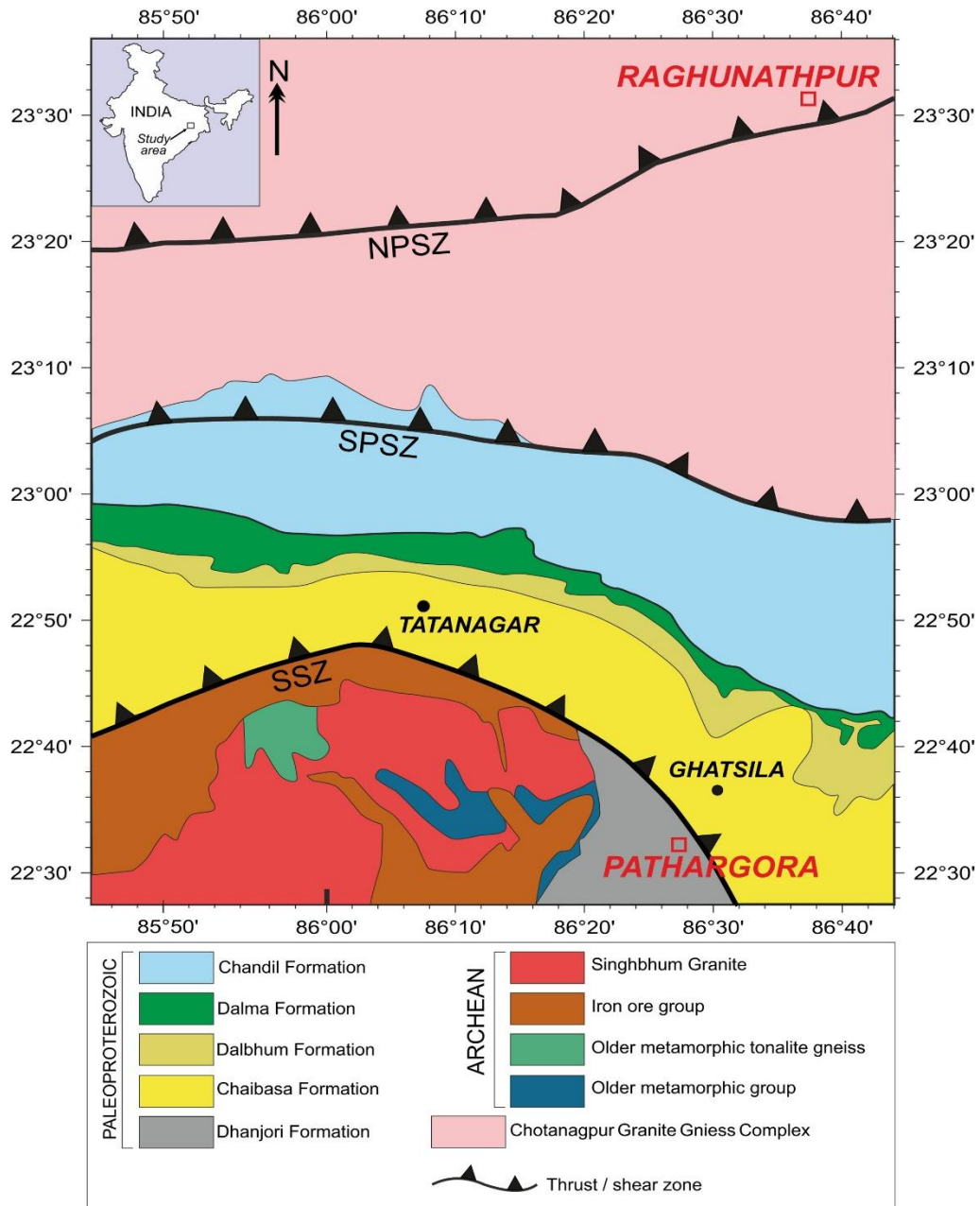
Figure 7.3: A simplified geological map of the East Indian Precambrian craton, showing the locations of the Singhbhum Shear Zone (SSZ), the South Purulia Shear Zone (SPSZ) and the North Purulia Shear Zone (NPSZ) [modified after Mazumder et al., 2012; Saha, 1994; Sengupta et al., 2000]. Field areas and sample locations are marked by red square box in the map.

flank of this shear zone in a place called Patheragora near the old Surda copper mines.

Patherogora is a small village in Purbi Singhbhum district, Jharkhand (22°32′37.911″N, 86°26′31.223″E, altitude: 146 m, accuracy: ±3 m). Here massive alkali granite has been transformed into mylonites to different grades, varying weakly sheared protomylonite to extremely sheared phyllonites. The shear zone displays a

dominant macroscopic north-dipping (40° to 60°) foliation, containing a strong down-dipping lineation. Structural evidences, such C-S angular relations, asymmetric fold vergence and rotated porphyroclasts suggest thrust kinematics. ZX thin sections of the mylonites are used to study microscale shear bands within the framework of well-constrained bulk shear sense.

The CGGC lies north of NSMB, covered mostly a variety of granite gneisses, dotted with minor lithologies, e.g., mafic and ultramafic intrusives (Mahadevan, 1992). Another part of the field investigation was taken up in the northern part of Purulia District (23°33′N 86°40′E, altitude: 155 m, accuracy: ±3 m), where excellent outcrop scale ductile shear zones are exposed in granite gneisses. These shear zones ranged from a few centimeters to tens of meters long, with their thickness varying from a fraction of centimeters to several centimeters, and they display shear-associated internal structures on a wide spectrum. The shear zones are mostly vertical showing strike-slip motion, manifested in sharp deflections of the steeply dipping across foliations in the host rocks. From foliation drag structures, earlier studies suggested their kinematics dominated by simple shear strain with kinematical vorticity number (W_k) = 0.8 -1 (ref.--).

7.3.2. PRINCIPAL TYPES OF BANDS IN SHEAR ZONES

On the eastern flank of the Singhbhum shear zone near Patheragora (details are given in supplementary section S1), the sheared alkali granite contains a strong microscale planar fabric imparted by closely spaced C-bands. These bands contain substantial biotite concentrations (Fig. 7.4a) with offset veins indicating a synthetic shear sense on them. Unlike an anastomosing network (Carreras et al., 2010; Fusseis et al., 2006), the bands occur in parallel sets, with their spacing varying from 500 to

1500 µm. Low-angle shear bands (LSB) occur as a minor band at angles of 14º- 22º to the principal C-bands (Fig. 7.4b, c). Their spatial density ($\lambda^* = 1/\lambda$, where λ is the spacing normalized to W_c) is much lower than that of C-bands. In places, the C-bands abruptly deflect their trajectories due to local interactions with R-bands (Fig. 7.4c). To summarize, C-band formation is found to be the principal mechanism to accommodate the bulk shear in this shear zone.
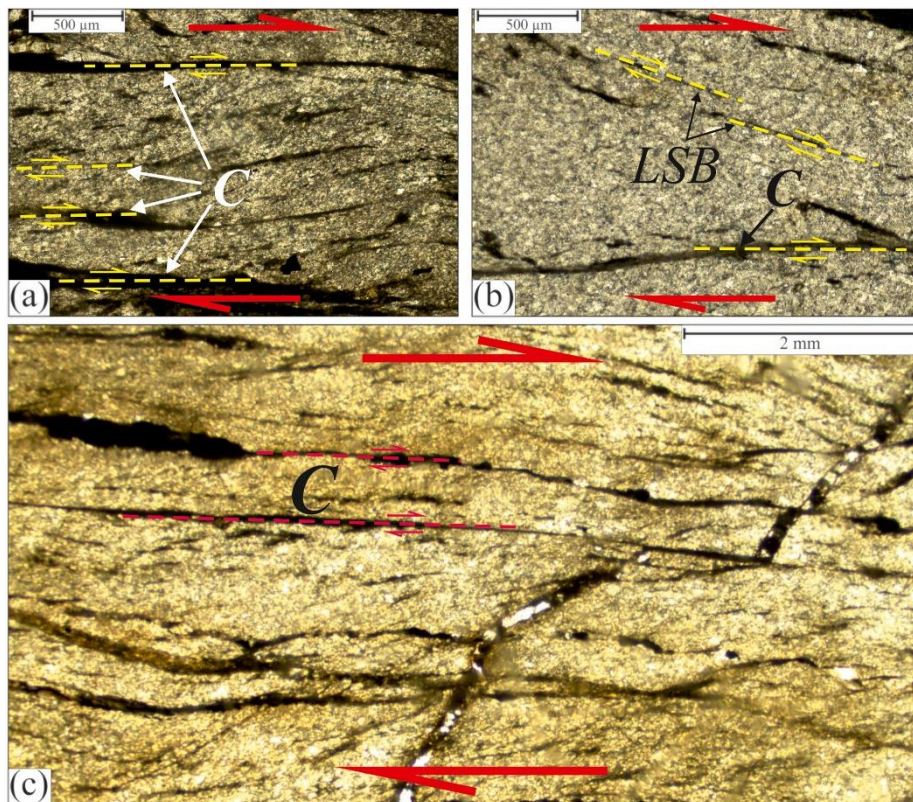
Figure 7.4: Photomicrographs of shear bands in sheared rocks collected from the Singhbhum Shear Zone area. Two principal types of shear bands are observed: i) shear bands parallel- or sub- parallel to the shear zone boundary (C) and ii) shear bands that form at low angles (15°) to the shear zone boundary. (a) Closely spaced C-bands. (b) C-bands associated with minor low-angle shear bands (dextral sense). (c) Occurrence of C-bands parallel to the shear direction (dextral shear marked by offsetting of quartz veins on right side).

Outcrop scale ductile shear zones in the CGGC typically consist of a core zone of strongly sheared rocks, flanked by foliation drag zones that represent a transition between the core and un-sheared wall rocks. For a systematic description of the band structures, the shear zones are categorized according to their host rock types.

Narrow (length: 20 to 100 cm and thickness: 5 mm to 5 cm) shear zones in banded gneisses show excellent shear bands, marked by deflections of the gneissic foliations in the host rock (Fig. 7.5). Some of them, however, display sharp boundaries with the walls, implying a sharp transition in the shear strain from the core to wall
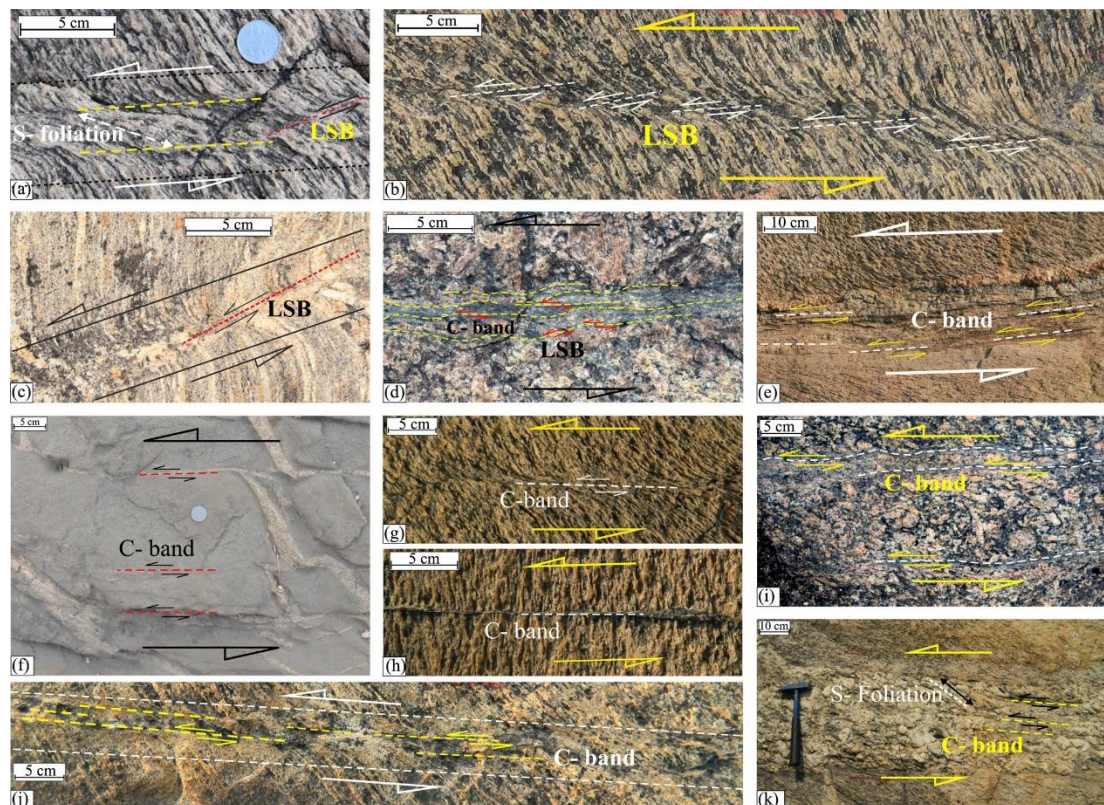
Figure 7.5: Field photographs of ductile shear zones in the Chotanagpur Granite Gneiss Complex. i) Narrow shear zones in banded gneiss (a, b, c, f, g, h, and j), ii) relatively wide shear zones in augen gneiss host (d, e, and i), and iii) narrow to wide shear zones with pegmatitic cores and K-feldspar crystals (k). Notice two principal types of shear bands: low-angle shear bands (15°) and C (0°) in them (see text for their detailed descriptions).

(Fig. 7.5g, j). This type of narrow shear zone (W_c = 2 –5 mm) is dominated by macroscopic C-bands, forming a parallel set with a spacing of 1 - 2 mm. They are generally devoid of macroscopic low-angle shear bands (LSB). LSB were observed in relatively thick shear zones (W_c = 10 to 25 cm) with diffuse foliation drag zones. The bands were oriented at angles of 13° to 25° to the shear zone boundary. They occurred systematically in an en-echelon array or sporadically in shear zones (Fig. 7.5a,b,c). High-angle shear bands (HSB) were remarkably absent in the study area.

A shear zone, about ~100m long and 40 to 50 cm thick, within the augen gneiss host in a small hillock near Raghunathpur displays prominent shear band structures. The shear zone consists of a uniformly thick core (W_c = 25 - 30 cm), flanked by very wide drag zones, and comprises alternate thick (5 to 10 cm) C-bands of dark colored fine-grained mylonites, spotted with feldspar porphyroclasts (Fig. 7.5e, l). These bands are laterally persistent, covering strike lengths from tens of centimeters to a few meters depending upon their thickness. Their spatial density (λ^*) is ~ 5.5 - 7.7. The shear zone is devoid of any LSB and HSB, at least on macroscopic scales.

A group of shear zones often show pegmatitic cores, flanked by drag zones at their interfaces with the gneissic wall rocks, indicating a spectacular variation in finite shear across them (Fig. 7.5k, m). Assuming a simple shear strain, the inclination of S-foliation was used to constrain a minimum finite shear (~1.2) in the shear zones after the pegmatitic emplacement. The bulk shear in the shear zone core is partitioned along a number of macroscopically visible wide-spaced (λ^*= ~2.9 - 4) parallel C-bands, traceable lengthwise for 30 - 40 cm. To conclude the field findings, the LSB are extremely rare, both on micro- and macro-scales in the shear zones present in the study areas. The field findings thus described above suggest that the two types of shear band (LSB and C bands) are mainly present in the ductile shear zones studied in the CGGC area. The close association of diverse types of shear zone localization thus demands experimental verifications to explore the exact mechanisms in which such bands develop so that the geometrical, kinematic and rheological parameters controlling the different modes of shear band formation can be identified.

7.4. NUMERICAL MODELLING OF SHEAR ZONES

7.4.1. BASIC THEORY

Natural ductile shear zone is modelled as a narrow zone of viscous-plastic material, undergoing Stokes flow, as applicable for incompressible slow viscous fluids without any inertial forces. The material is assumed to yield at a threshold stress and produce shear bands. To describe the condition of plastic yielding (details of the representative mechanical model shown in Fig. 7.6a), the two invariants are considered: I_1 and I_2 of the stress tensor (σ_{ij}), the expressions of which follow:

$$I_1 = \sigma_{jj} ; \tag{7.1}$$

$$I_2 = \frac{\sigma_{ii}\sigma_{jj} - \sigma_{ij}\sigma_{ij}}{2} \tag{7.2}$$

The index notation in Eq. (7.2) applies repetition of the tensor indices to represent the summation of their components, i.e., their traces. Decomposing σ_{ij} into the isotropic ($\sigma^o{}_{ij}$) and the deviatoric stress ($\sigma^s{}_{ij}$) tensors, results in

$$\sigma^o{}_{ij} = \tfrac{1}{3}\sigma_{kk}\delta_{ij} \text{ and } \sigma^s{}_{ij} = \sigma_{ij} - \sigma^o{}_{ij} \tag{7.3}$$

where δ_{ij} is Kronecker delta. From Eq. (7.2) & (7.3), the second stress invariant, I_2 is expressed as;

$$I_2 = 3\sigma^o{}_{jj}{}^2 - \tfrac{1}{2}\sigma_{ij}\sigma_{ij} \tag{7.4}$$

Assuming an incompressible visco-plastic rheology, I_2 is treated as the key dynamic quantity to determine the plastic creep at the yield point. The deviatoric stress tensor ($\sigma^s{}_{ij}$) is then equated with the strain rate tensor ($\dot{\varepsilon}_{ij}$) as,

$$\sigma^s{}_{ij} = 2\eta_{eff}\dot{\varepsilon}_{ij} \tag{7.5}$$

where $\dot{\varepsilon}_{ij} = \frac{1}{2}\left(\frac{\partial v_i}{\partial x_j} + \frac{\partial v_j}{\partial x_i}\right)$ and η_{eff} is the effective viscosity, which includes viscosities η_v (viscous creep) and η_p (plastic creep) in their reciprocal form as,

$$\frac{1}{\eta_{eff}} = \frac{1}{\eta_v} + \frac{1}{\eta_p} \tag{7.6}$$

Similarly, the strain rate tensor $(\dot{\varepsilon}_{ij})$ at an instant is split into viscous ($\dot{\varepsilon}_v$) and plastic $(\dot{\varepsilon}_p)$ strain rate tensors,

$$\dot{\varepsilon}_{ij} = \dot{\varepsilon}^v_{ij} + \dot{\varepsilon}^p_{ij} + \dot{\varepsilon}^e_{ij} \tag{7.7}$$

where

$$\dot{\varepsilon}_v = \frac{1}{2}\frac{\sigma^s{}_{ij}}{\eta_v}, \tag{7.8}$$

$$\dot{\varepsilon}_p = \begin{cases} 0, & I_2 < \sigma_e \\ \chi\left(\frac{1}{2}\frac{\sigma^s{}_{ij}}{I_2}\right), & I_2 \geq \sigma_e \end{cases} \tag{7.9}$$

$$\dot{\varepsilon}^e_{ij} = \frac{1}{2G}\frac{D\sigma^s{}_{ij}}{Dt} \tag{7.10}$$

In the above equations, σ_e denotes the yield strength of the material, and χ is a plastic multiplier, satisfying the yield condition, $I_2 = \sigma_e$. In the present models, the shear modulus (G) is set at large values to keep the elastic strain component negligibly small ($\sim\dot{\varepsilon}_e \rightarrow 0$), as compared to the viscous and plastic strain components in (7.7)

It is noteworthy that the steady-state long- term permanent deformation is of the prime concern in the simulation of ductile shear zones, and the effects of elastic deformation are therefore neglected. Equating the flow stress with the yield stress at the moment of yielding gives

$$\eta_{eff} = \frac{\sigma^s{}_{ij}}{2|\dot{\varepsilon}|},$$

(7.11)

satisfying the flow rules in Eq. (7.8) & (7.9). $|\dot{\varepsilon}|$ represents the second invariant of $\dot{\varepsilon}_{ij}$. η_{eff} represents the reduced viscosity, once the yield limit is reached. It is to note that the non-linearity introduced by the plastic rheology is solved from Eq. 10 iteratively. This equation provides the necessary conditions required to self-lubricate shear zones with parametrically imposed strain rate weakening laws, as implemented in many earlier viscoplastic models (Bercovici, 1993; Govers & Wortel, 1995; Huismans & Beaumont, 2002). A non-linearly decreasing effective viscosity with increasing finite strain is demonstrated in Fig. 7.6b.

In the shear-band modelling a pressure dependent plasticity criterion (Drucker-Prager) is employed, as considered for ductile shear zone modelling by earlier workers (e.g., Mancktelow, 2006). Based on this criterion, a yield function, $\mathcal{F}$ can be defined in the following form (Drucker & Prager, 1952).

$$\mathcal{F} = \sigma_e - \sqrt{3}\,\sin\emptyset\,P - \sqrt{3}\,C(\gamma_{pl})\cos\emptyset$$

(7.12)

where $P = -\frac{1}{3}I_1$ (first stress invariant, Eq. (7.1)), C is the material cohesion, expressed as a function of plastic strain γ_{pl}, and $\emptyset$ is the angle of internal friction. For each particle in the model, the actual viscosity is calculated locally by first computing
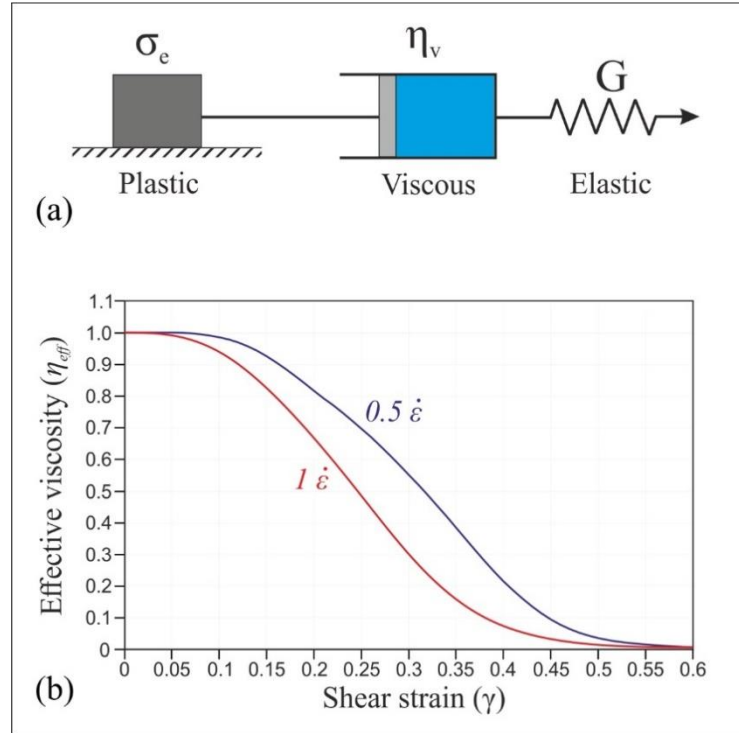
Figure 7.6: (a) One-dimensional rheological representation of the model material used for numerical simulations of ductile shear zones. This decomposition can be interpreted as Maxwell viscoelastoplastic rheology, where plastic, viscous and elastic networks are connected in series. σ_e, η_v, and G represent the plastic yield stress, material viscosity and shear modulus of the material, respectively (b) viscous weakening of the material, introduced by plastic yielding where the modified viscosity decreases nonlinearly with increasing strain. This implies a strain softening rheology for the shear zone models.

the viscous stress. If the parameter obtained thereby leads to $\mathcal{F} > 0$, the behaviour of the material is treated as viscous, with its effective viscosity equal to the initial value. On the other hand, if the failure criterion satisfies the condition, $\mathcal{F} \leq 0$, the material behaviour is plastic and the effective viscosity (η_{eff}) must be adjusted to ensure that the stress state lies on the yield surface $\mathcal{F} = 0$.

The cohesive strength of the material is assumed to decrease with increasing accumulation of plastic strain as (Lemiale et al., 2008):

$$C = C_i + \left(C_f - C_i\right) min(1, \tfrac{\gamma_{pl}}{\gamma_o}), \tag{7.13}$$

where C_i is the initial cohesion and C_f is the final cohesion of the material. Also, $\gamma_{pl} = \int_0^t \dot{\varepsilon}_p \, dt$, indicates plastic strain in regions where the yield stress is reached and $\gamma_o =$

0.1 is taken as the reference strain. All types of healing effects on the cohesion are excluded in the models.

7.4.2. MODEL DESIGN

Based on the mathematical formulation described in the preceding section, 2D shear zone models are developed using the open-source finite element code of Underworld 2 (http://www.underworldcode.org/). The code follows a continuum mechanics approximation, used to describe a variety of geological and geophysical processes (Mansour et al., 2020). As previously shown (Lemiale et al., 2008; Moresi
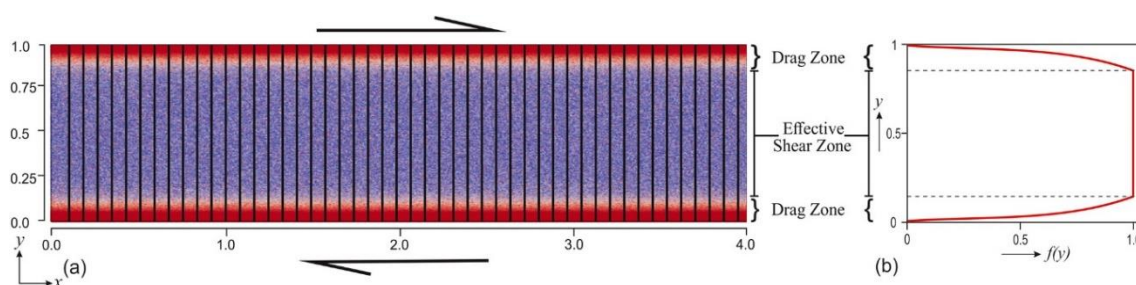

Figure 7.7: (a) Two-layer (core + drag zones) configuration of the viscoplastic shear zone model chosen for numerical experiments. Equally spaced bold vertical lines were used as passive markers to track the shear strain patterns in the shear zone. Different boundary conditions employed in the model are explained in the text. (b) Graphical presentation of the hyperbolic tangent function employed to design the composite structure of a ductile shear zone.

et al., 2007), the code divides the geometrical domain into a standard Eulerian finite element mesh, and is coupled with the particle-in-cell approach (Evans et al., 1957). So, the code successfully discretizes the material domain into sets of Lagrangian material points. These material points carry material properties that are history dependent (in this case, the plastic history of material), and can be tracked over the entire simulation run. The mass, momentum, and energy conservation equations are solved under incompressible conditions to find the pressure and velocity conditions within the shear zone domain. Physical properties of the shear zone materials, such

as density and viscosity are mapped using these equations through particle indexing. Here, the effects of temperature diffusion and inertia in the system are neglected.

The shear zone models are developed in a *L* by 4*L* rectangular domain, where
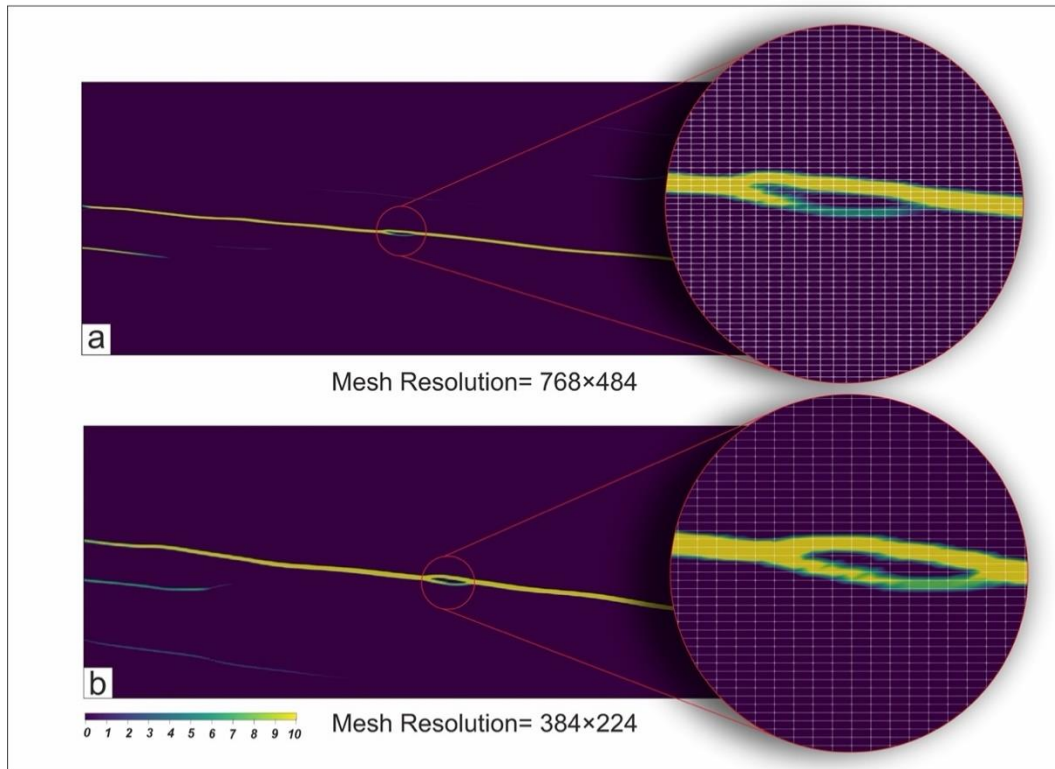
Figure 7.8: Two numerical simulations run under the same conditions, but with different mesh resolution: a) 768x484 b) 384x224.

L represents the reference length scale of simulations. The long model walls were subjected to shear motion, keeping the sidewalls under a periodic boundary condition (Fig. 7.7). The model domain, occupied by incompressible visco-plastic materials, is discretized into quadrilateral mesh elements comprising of 384 x 224 elements. Mesh refinement tests were performed to assess the mesh resolution effects on simulation results (Fig. 7.8).

A three-layer model architecture is considered to simulate ductile shear zones structurally similar to those observed in the field (an intensely sheared core with drag

zones on its either side, hosted in unsheared rocks). A modified version of the shear zone model, developed by Lemiale et al. (2008) is adopted to model the strain variation in the core-wall transition with a hyperbolic tangent function, expressed as

$$\mathcal{F}(y) \ = \ [tanh\left((S_w - y)H_F\right) + \ tanh\left(H_F(y)\right) - \ tanh\left(H_F\right)]^{2p} \qquad (7.14)$$

where y stands for the normal distance of a given point from the shear zone boundary, S_w is the distance between the shear zone boundaries, H_F is a non-dimensional constant, and p stands as an exponent factor. The parameter, H_F and p, are manipulated to simulate a sharp or a diffuse drag zone between the core and the wall. Low values of H_F and p give rise to sharp drag structures. On the contrary, their large values result in diffused drag zones. In the numerical model, the function is multiplied with the plastic strain value at every point of the shear zone in every iteration. The value of the function is 0 at the model boundary and 1 at the shear zone core. Therefore, the plastic strain value, inside the shear zone core remains unaltered in every step. Also, the plastic strain value at the model boundary remains 0 at each numerical step. Inside the drag zone, the plastic strain is dampened considerably which hinders the plastic strain accumulations and subsequent failure. Consider the following conditions in the model.

Plastic strain = p,

In each numerical step, modified plastic strain = $p*F(y)$,

Inside shear zone core: modified plastic Strain = $p*F(y) = p*1 = p$,

At Model Boundary: Modified plastic Strain = $p*F(y) = p*0 = 0$.

The above hyperbolic tangent function is chosen as it satisfies a two- fold objective. The function not only prevents the localized strain to reach the shear zone boundary

but also helps in defining the property (diffused or sharp) and thickness of the drag zone relative to the total shear zone thickness. Fig. 7.9 shows the change in shape of the function when the constants are varied. Low H_F values simulates diffused drag zones, which become sharp at higher values of H_F.

The model simulations presented in the following sections mainly focus upon the three major parameters: 1) normalized effective shear zone thickness (δ), 2) bulk viscosity (η_v) and 3) bulk shear rates ($\dot{\gamma}_b$), which characterize the geometry, rheology and kinematics of a shear zone, respectively. δ is set in the range 0.25 to 0.85, as applicable to the field studies. η_v is varied between $1\eta_0$ and $20\eta_0$, and similarly, $\dot{\gamma}_b$ between $1\dot{\gamma}_o$ and $20\dot{\gamma}_o$, where η_0 and $\dot{\gamma}_o$ are the reference viscosity and shear rate,
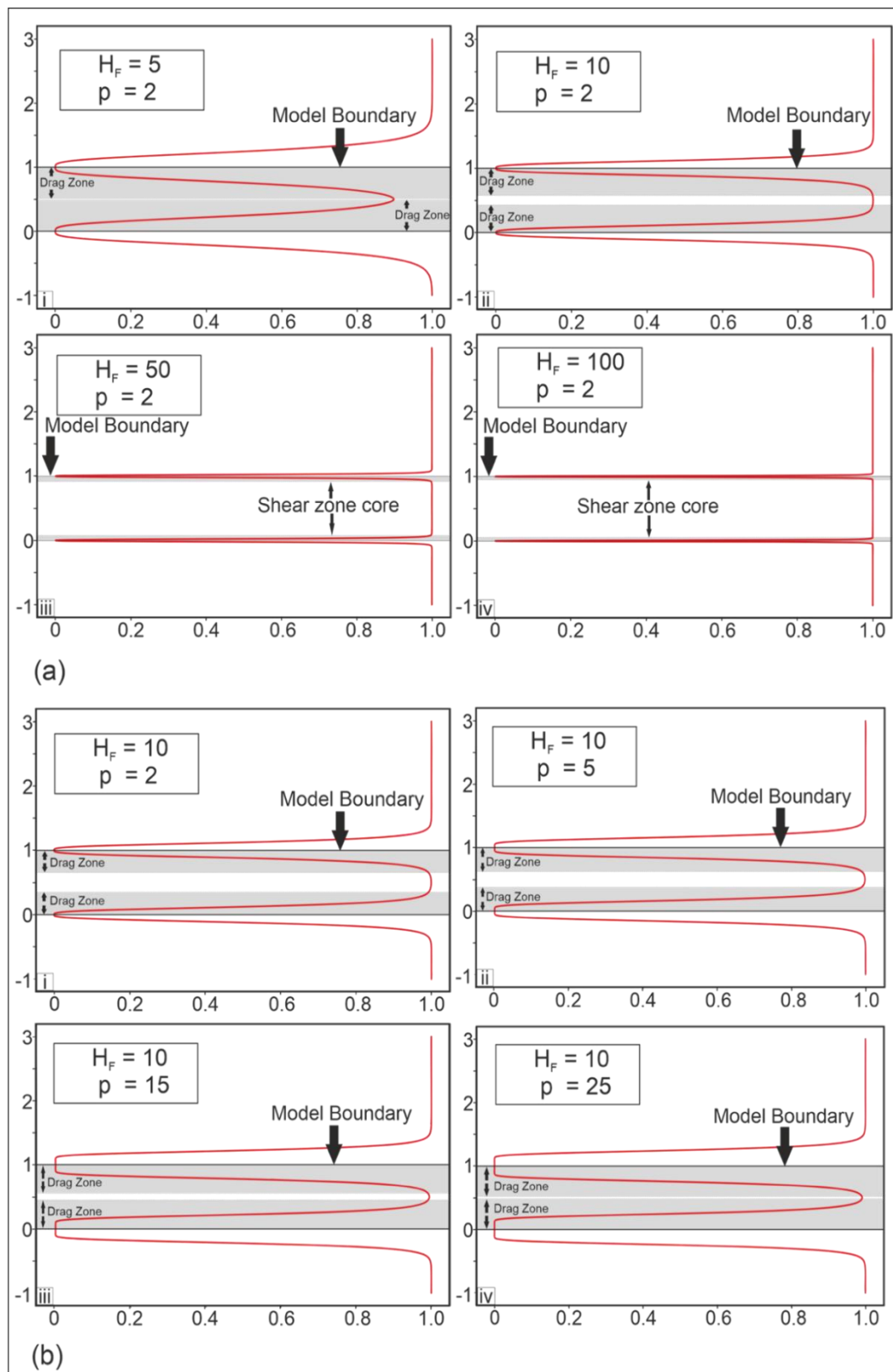
Figure 7.9: Graphical presentation of the hyperbolic tangent function for varying a) the parameter HF b) the exponent factor p. The function is applicable in the range 0 < y < 1 for the present shear zone models. (i.e. Sw = 1 for all cases)

respectively (M. A. Finch et al., 2020; Kaus, 2010; Lemiale et al., 2008). All model

material parameters have been summarized in Table 7.1.

7.4.3. MODEL RESULTS

Reference model simulations: In this section the characteristics and progressive evolution of three shear zone simulations are presented that were chosen as reference models (RM), based on the distinct modes of shear band development, which satisfy a range of geological observations. The first reference model (RM1) simulation, run with δ = 0.7, η_v= $1\eta_0$ and $\dot{\gamma}_b$= $1\dot{\gamma}$, produced LSB but without any discernible HSB for a bulk shear (γ_b) of 0.18 (Fig. 7.10a). With increasing γ_b, LSB grew in large concentrations with a persistent orientation ($\sim$15°), forming a penetrative fabric ($\lambda^*\sim$142.8) to accommodate a bulk homogeneous strain in the shear zone. A sharp transition occurred from homogeneous to heterogeneous strain field, following shear partitioning selectively along widely spaced ($\lambda^*\sim$ 4) LSB. They defined a distinct set of parallel band structures with θ= $\sim$13°. However, individual bands did not grow equally, and some of them became progressively inactive. Such an unequal growth reduced the number of active LSB in the population, and the partitioning of bulk shear became strongly heterogeneous in an advanced stage (γ_b= 0.35) of the shear zone. The band evolution further reduced the shear band density, leaving a few widely spaced ($\lambda^*\sim$3.3) LSB with θ= $\sim$14° at γ_b= 0.37. The model estimates showed an exponential decrease of the LSB frequency with increasing bulk shear [Fig. 7.10a (i - iv)]. The RM1 simulation did not show C-band growth at any stage of the shear zone evolution, barring sporadic shear parallel surfaces as links between the two low-angle shear bands.

The second reference model (RM2) simulation was run at higher bulk shear rates ($\dot{\gamma}_b$= $2.5\dot{\gamma}$), and larger viscosity (η_v= $4\eta_0$), keeping δ = 0.7. For γ_b= 0.07, the

simulation developed finely spaced LSB and HSB in conjugate sets with a dihedral angle of ~72º, where LSB dominated over HSB, imparting a distinct low-angle fabric (θ = ~13°) in the shear zone (Fig.7.10b). The low-angle shear surfaces were more active in shear partitioning to grow faster than the HSB and attained long band geometry with progressive bulk shear (γ_b = 0.15). Their preferential growth continued with progressive shear, leaving HSB as a relic structural element in the evolved band structure for γ_b = 0.2. The HSB eventually occurred as isolated short
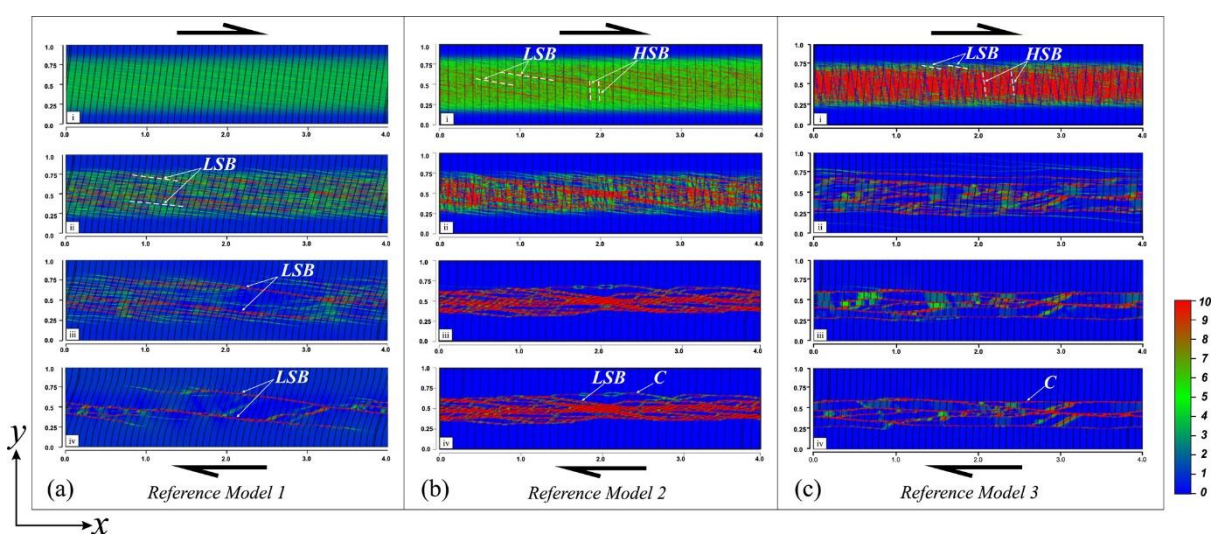

Figure 7.10: Progressive development of shear bands in three reference models (RM) under dextral shear. (a) Reference model 1: δ = 0.7, η_v = 1η_0 & $\dot{\gamma}_b$ = 1$\dot{\gamma}_0$. (b) Reference model 2: δ = 0.7, η_v = 4η_0 & $\dot{\gamma}_b$ = 2.5$\dot{\gamma}_0$. (c) Reference model 3: δ = 0.53, η_v = 5η_0 and $\dot{\gamma}_b$ = 7$\dot{\gamma}_0$, where η_0 and $\dot{\gamma}_0$ represent the reference values of the bulk viscosity and the bulk shear rate, respectively. The color bar represents the magnitude of strain rate invariant. Notice a transition of LSB to C band formation from RM 1 to 3. RM2 and RM3 produce high-angle shear bands in the initial stage of shear deformation (γ_b < 2, and the bands die out with progressive shear.

bands with relatively large spacing (λ^* ~5.5), whereas the LSB appeared as closely spaced (λ^* ~125) long bands. RM1 and RM2 show a marked difference in oblique band orientations, where the latter formed two distinct populations, oriented at ~13° and ~85° to the shear direction (Fig.7.10b-ii). Further increase in γ_b resulted in a dramatic transformation of the band structure, forming shear-parallel C bands. This newly formed C- and earlier LSB in combination controlled the dynamics of shear band growth, keeping HSB as a minor element (Fig.7.10b-iv). The RM2 simulations

showed that the spatial density of C was similar to that of LSB. With increasing γ_b, the C-band population continued to increase their spatial density ($\lambda^* \sim 33.3$) with the accretion of shear parallel bands, which were locally connected by the remnant low-angle bands.

The third reference model (RM3) simulation, run with $\eta_v = 3.5\,\eta_0$, $\dot{\gamma}_b = 7\dot{\gamma}_o$, and $\delta = 0.53$, showed the band growth pattern markedly different from RM1 and RM2 (Fig. 7.10c).Two prominent sets of shear bands: LSB and HSB localized in conjugate orientations with a dihedral angle of $\sim 70°$, but with contrasting geometry; LSB were narrow, long and very closely spaced ($\lambda^* \sim 166.67$), whereas HSB were thick, short and relatively wide spaced ($\lambda^* \sim 5.2$). The conjugate bands showed extremely transient behaviour, and underwent a complete transformation with the appearance of a set of C bands for $\gamma_b > 0.4$. The band structure ultimately consisted of a set of subparallel wide-spaced ($\lambda^* \sim 3.8$) C-shear surfaces, showing virtually no trace of LSB and HSB (Fig. 7.10c-iv).

Parametric analysis: The three reference model simulations presented in the preceding section suggest that C- and LSB structures represent two end-member modes of shear localization in shear zones, as also revealed from the field investigations. To analyze the LSB versus C band growth, the following parameters were varied: effective shear zone thickness (geometrical), bulk shear rate (kinematic) and bulk viscosity (rheological), keeping the failure parameters: yield strength (σ_e) and angle of internal friction (∅) constant. Numerical simulations were performed in which each of the parameters was varied, keeping the others constant.

➢ *Geometrical factors:* The effective shear zone thickness (W_c) is varied from $0.25W_o$ to $0.85W_o$ in the model (Fig. 7.11a), where W_o is the reference effective shear zone thickness. For $W_c = 0.25W_o$, a train of LSB localized at $\gamma_b = 0.2$, but they coalesced with one another to form a well-defined C-band. This band shared 58% of bulk shear displacement, where the ratio of localized to bulk shear rate was 0.8. Increase in W_c to $0.5W_o$ led to a transition in the mode of shear localization, forming few widely spaced LSB at $\theta \sim 15°$. The ratio of homogeneous viscous strain to bulk shear is characteristically large ($\gamma_r = \gamma_v/\gamma_p = 68\%$). Further increase in W_c (> $0.85\ W_o$) multiplied LSB, and resulted in their higher spatial density ($\lambda^* \sim 5.5$).
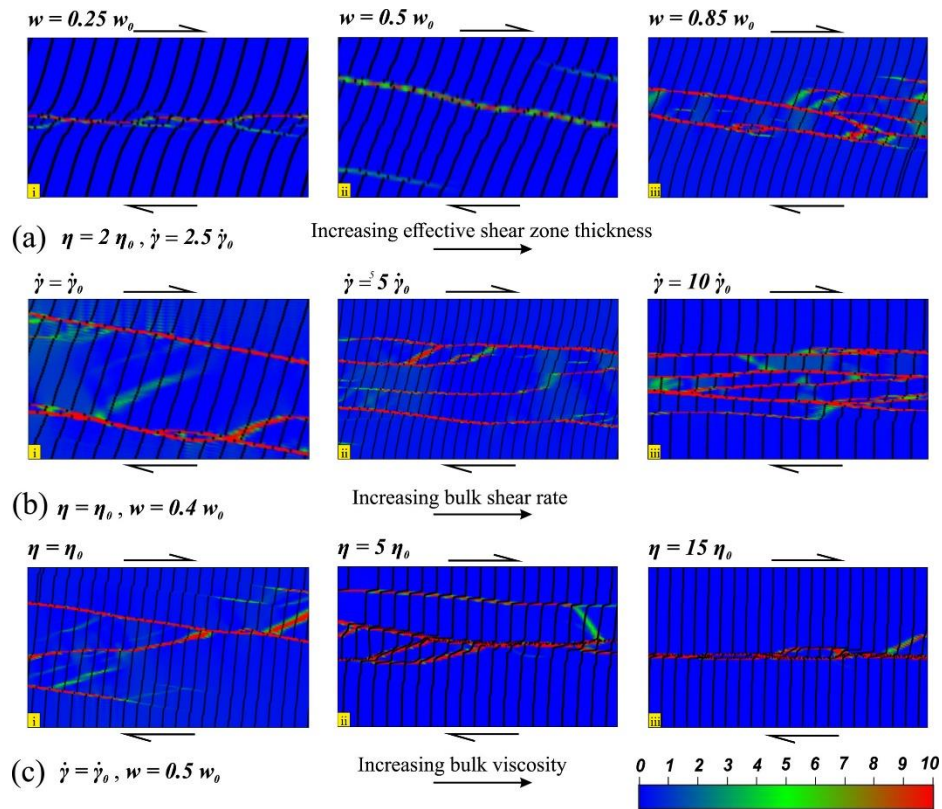
Figure 7.11: Controls of a) the geometrical factor, W_c (effective shear zone thickness) b) the kinematic factor, $\dot{\gamma}_b$ (bulk shear rate) and c) the rheological factor, η_v (bulk viscosity) on the development of shear band in dextral shear zones. The color bar represents the magnitude of strain rate invariant. The failure parameters: yield strength (σ_e) and angle of internal friction (μ) constant are held constant. W_0, $\dot{\gamma}_0$ and η_0 represents the reference effective shear zone width, bulk shear rate and bulk viscosity respectively.

➢ *Bulk shear rate*: Low bulk shear rates ($\dot{\gamma}_b = 1\dot{\gamma}_o$) produced dominantly LSB, with extremely weak HSB growth at low finite bulk shear (Fig. 7.11b). With increase in γ_b, the HSB died out, leaving a single set of widely spaced ($0.5W_o$ ~3.57), parallel LSB, oriented at θ= ~13°. The shear partitioning along LSB was low, sharing 38% of the total shear displacement. According to the model estimate, the maximum ratio of LSB-accommodated shear and bulk viscous shear rates was 0.35. This suggests that shear zones under slow shear rates accommodate the bulk shear mostly by distributed homogeneous viscous strain. Secondly, they do not form C bands. A moderate shear rate ($\dot{\gamma}_b = 5\dot{\gamma}_o$) produced LSB and HSB nearly at equal rates. Both the sets amplified due to preferential shear localization, but they died out after a threshold γ_b = 0.25, and there occurred a transition from LSB to C mode. For γ_b = 0.35, the shear zone was dominated by C-bands, which shared a major part of the bulk shear (62%). The LSB remained active to interact with the evolving C-bands, forming a set of wavy shear surfaces grossly parallel to the shear zone. Under high shear rates ($\dot{\gamma}_b = 10\dot{\gamma}_o$) the shear zone initially localized LSB, conjugated by HSB. With progressive shear, they were completely replaced by a multiple set of C bands. The bulk shear was strongly partitioned along the C surfaces (78% of the total shear displacement). The ratio of localized shear to distributed viscous shear rates in the shear zone was found to be extremely large (> 2).

➢ *Bulk viscosity of shear zone:* Simulations with η_v= $1\eta_0$, produced a pair of parallel low-angle bands at θ~13°. An increase in η_v transformed the mode of shear localization to C-band formation. For η_v = $5\eta_0$, the band structure evolved through C/LSB interactions, ultimately giving rise to wavy shear surfaces,

grossly parallel to the shear zone. The LSB then phased out, while the C-band formation became the principal mechanism of shear localization when $\eta_v = 15\eta_0$. The model estimate showed that the degree of shear partitioning multiplied (from 0.58 to 2.2) with the increase of η_v from $1\eta_0$ to $15\eta_0$ (Fig. 7.11c).

Shear band pattern classification: Reference model (RM) experiments are presented in this section to demonstrate how the process of shear surface networking is mediated principally by the interactions of R-(LSB), C- and P- shears in an evolving shear zone. The networking progressively produces band patterns, which satisfy a range of geological observations, including those presented in the preceding section. The RM simulation was run at a constant bulk shear rate ($\dot{\gamma}_b = 5\dot{\gamma}_o$), and an initial bulk viscosity ($\eta_v = 8\eta_0$), keeping $\delta = 0.7$. For $\gamma_b = 0.07$, the simulation initially develops finely spaced R_1- and R_2-bands in conjugate sets with a dihedral angle of ~72°, where R_1 dominates over R_2 to form a distinct low-angle shear fabric in the shear zone. R_1 and R_2 constitute two distinct populations of bands with orientations, $\theta = $ ~13° and ~85° to the shear direction. The low-angle shear surfaces become more active in shear partitioning and grow faster than R_2 to attain typically a band-like structure with progressive bulk shear ($\gamma_b = 0.15$). The preferential growth of R_1 continued to take place with increasing shear, leaving R_2 as a relic structural element in the evolved band structure at $\gamma_b = 0.2$. R_1-shears eventually occur as closely spaced ($\lambda^* \sim 12$) long bands. Further increase in γ_b leads to the reduction in the number of R_1-shear bands, which interact with the P-bands to produce a typical rhombic structure commonly observed in the field. Strain localization is at its most dominant with few shear-parallel C-bands forming as a minor element.
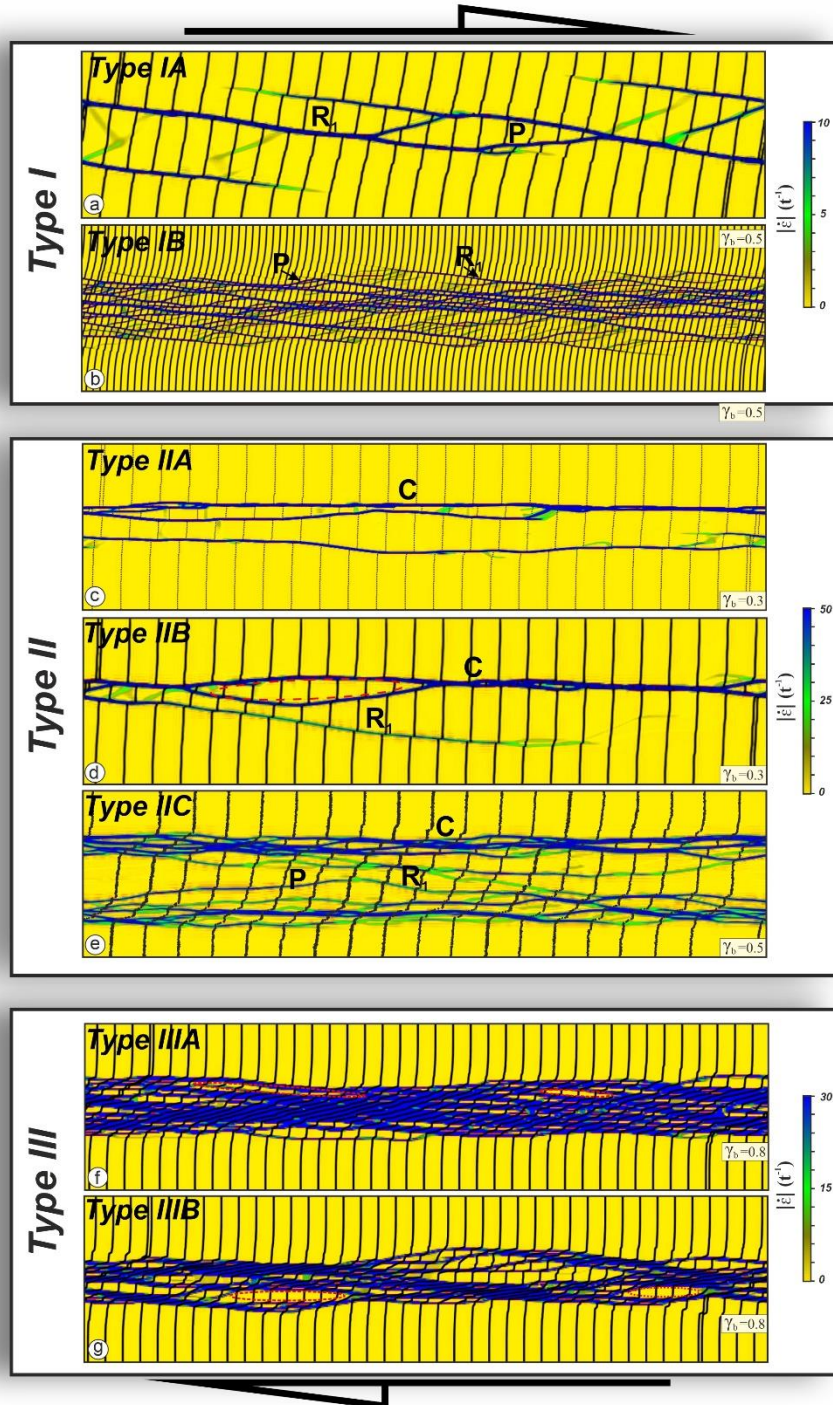
Figure 7.12: Type I, II and III network structures produced in numerical simulations with varying model parameters. a) Type IA: multiple widely spaced R1, but without any development of C-shear bands. $\eta_v=1\eta_0$, $\dot{\gamma}_b = 1\dot{\gamma}_0$ and $\delta = 0.7$. b) Type IB: Formation of closely spaced R1 bands, showing weak interactions with P bands. $\eta_v=1\eta_0$, $\dot{\gamma}_b = 10\dot{\gamma}_0$ and $\delta = 0.8$. c) Type IIA: sub-parallel C-shear bands. $\eta_v=10\eta_0$, $\dot{\gamma}_b = 6\dot{\gamma}_0$ and $\delta = 0.58$. d) Type IIB: a single C-shear surfaces, with relict R1 bands, leading to a shear band network. $\eta_v=15\eta_0$, $\dot{\gamma}_b = 2.5\dot{\gamma}_0$ and $\delta = 0.38$. e) Type IIC: Development of a less deformed zone, sandwiched between two domains of closely spaced parallel to sub-parallel C-shear bands. $\eta_v=15\eta_0$, $\dot{\gamma}_b = 10\dot{\gamma}_0$ and $\delta = 0.62$. (f) Type IIIA: Development of finely spaced C bands, forming homogeneously sheared domains, containing isolated, low-angle unsheared lenses produced by networking of C and R1 bands. $\eta_v=4\eta_0$, $\dot{\gamma}_b = 10\dot{\gamma}_0$ and $\delta = 0.78$. g) Type IIIB: homogeneously distributed shear domains containing shear parallel undeformed lenses, formed by networking of C, R1 and P bands. $\eta_v=4\eta_0$, $\dot{\gamma}_b = 5\dot{\gamma}_0$ and $\delta = 0.67$. γ_b represents the total finite shear.

Parametric analysis of band network patterns: A large number of simulations were run by varying the three model parameters: 1) bulk viscosity (η_v), 2) bulk shear rate ($\dot{\gamma}_b$), and 3) normalized effective shear zone thickness (δ), with an aim to constrain specific rheological, kinematic and geometrical conditions for the evolution of Type I, II and III network structures classified from the field studies.

> *Type 1A*: This band network evolves in simulations run with δ = 0.75, η_v = $1\eta_0$ and $\dot{\gamma}_b$ = $1\dot{\gamma}_o$, forming closely spaced R_1 bands, but without any discernible R_2 at a bulk shear (γ_b) of 0.18. With increasing γ_b, R_1 bands multiply in number to increase their spatial density with a preferred orientation ($\sim$15°) and impart a penetrative fabric (λ^* $\sim$142.8). Under this set of model conditions R_1-shear localization acts as the principal mechanism to accommodate the bulk homogeneous shear in the shear zone. However, a set of widely spaced ($\lambda^* \sim$ 4) R_1 bands at θ = $\sim$15° become selectively more active to accommodate the bulk shear, resulting in a sharp transition from homogeneous to heterogeneous shear distribution in the shear zone. This transition reduces the number of active Riedel shear bands in the population and facilitates strongly heterogeneous strain in the shear zone at an advanced stage (γ_b = 0.35). The band density reduced further, leaving a few widely spaced R_1 bands (λ^* $\sim$3.3) with θ = $\sim$14° at γ_b = 0.37 (Fig. 7.12a). The model estimates show an exponential decrease of the R_1 frequency with increasing bulk shear.

> *Type IB*: This type of band networking is observed in simulations run with δ = 0.8, η_v = $1\eta_0$ and $\dot{\gamma}_b$ = $10\dot{\gamma}_o$. The model produces multiple R_1 bands, but in association with a few R_2 bands at γ_b = 0.2. With increase in γ_b, R_1 grows in large concentrations with a persistent orientation ($\sim$15°), forming a penetrative fabric similar to Type IA, which accommodates bulk homogeneous shear in the

shear zone. In contrast, R$_2$ bands weaken their activity with reducing numbers. Unlike the previous model, this model shows a transition from homogeneous to heterogeneous shear partitioning along a set of closely spaced ($\lambda^* \sim 15$) parallel R$_1$ bands an angle of θ = $\sim 15°$. The individual bands grew equally to form a large number of active R$_1$ bands in the population at γ_b = 0.35. The shear zone evolution did not reduce the shear band density, resulting in a typical pattern of closely spaced R$_1$ bands with θ= $\sim 14°$ at γ_b = 0.37 (Fig. 7.12b). With further increase in bulk shear a set of minor P bands evolve in the shear zone and interacts with the low-angle R$_1$ bands to form an asymmetric network, consistently verging in the bulk shear direction. The R-P network eventually gives rise to rhombic domains of little or no shear with actual angles pointing to the shear direction.

➢ *Type IIA*: Simulations run with η_v = $10\eta_0$, $\dot{\gamma}_b$= $6\dot{\gamma}_o$, and δ = 0.58, produce Type IIA network of the secondary shear bands. Two prominent sets of Riedel bands localize in conjugate orientations with a dihedral angle of $\sim 70°$, but with contrasting geometry; R$_1$ bands are narrow, long, and very closely spaced ($\lambda^* \sim 166.6$), whereas R$_2$ bands are thick, short, and widely spaced ($\lambda^* \sim 5.2$). The conjugate bands show extremely transient behaviour, undergoing a drastic transformation with the appearance of a set of C-bands at γ_b > 0.4. The band structure ultimately consists of a group of sub-parallel, wide-spaced ($\lambda^* \sim 3.8$) C-shear surfaces, forming a weak network, although locally with the earlier R$_1$-bands (Fig. 7.12c). P-bands localize sporadically, but showing no strong tendency to network with the C-bands.

> *Type IIB*: A condition with $\eta_v = 15\eta_0$, $\dot{\gamma}_b = 2.5\dot{\gamma}_o$, and $\delta = 0.38$ yields this type of band networking. In the initial stage of the simulation run $\gamma_b < 0.15$) Riedel bands localize along a single set of low-angle narrow, long, and widely spaced ($\lambda^* \sim 2$) bands (R1) to accommodate the bulk shear. With increase in γ_b, R1 bands give way to the formation of a single shear- parallel C band which accommodates the majority of the bulk shear deformation. At $\gamma_b > 0.3$ the C bands ultimately dominates in the network, and there are a few relict R1 bands that locally interact with the C band (Fig. 7.12d). The C-band formation accommodates a significant amount of plastic strain, as revealed from the deformed passive markers in the model.

> Type IIC: Simulations run with $\eta_v = 15\eta_0$, $\dot{\gamma}_b = 10\dot{\gamma}_o$, and $\delta = 0.62$, develop Type IIC band structures. The band structures initially evolve in two. prominent sets: R1 and R2, which is progressively dominated by a set of widely spaced R1, as in the previous model. The band evolution subsequently takes a different course, forming densely packed C-bands preferentially along two distinct domains on either side of the shear zone core. These C-bands occur in a low density in the shear zone core, where they network with both R1 and P bands, giving rise to symmetrical anastomosing geometry oriented in the bulk shear direction (Fig. 7.12e). Interestingly, the model reproduces typical paired shear zones reported from naturally deformed rocks [41].

> *Type IIIA*: This type of band structures is produced in a condition of high bulk shear rates ($\dot{\gamma}_b = 10\dot{\gamma}_o$) and moderate viscosity ($\eta_v = 4\eta_0$), keeping $\delta = 0.78$. For $\gamma_b = 0.07$ (Supplementary Video S6). The model develops finely spaced R bands in conjugate sets with a dihedral angle of $\sim72^\circ$. As R1 grows much faster than

R$_2$, the structure transforms into a distinct low-angle shear fabric (θ= ~15°). Their preferential growth eventually gives rise to a single set of bands, leaving R$_2$ as isolated incipient bands that ultimately die out in course of progressive bulk shear (γ_b =0.15). The Riedel shearing event is followed by localization of C-bands, which rapidly grow and multiply in number with progressive shear, and later start to network with the earlier R$_1$ bands. With increasing γ_b their population density becomes remarkably high due to continuous accretion of new shear parallel bands. Low-angle R$_1$ bands are locally preserved in the form of an anastomosing patterns, which give rise to isolated less deformed, elongated lenses with their long axes oriented at angle of ~13° to the shear direction (Fig. 7.12f). A histogram plot of their aspect ratios shows a roughly symmetrical distribution with a major frequency peak of 21 to 26 within a range of 10 to 40.

➢ Type IIIB: This type of shear band pattern is obtained in a simulation run at moderate bulk shear rates ($\dot{\gamma}_b$ = 5$\dot{\gamma}_o$), and viscosity (η_v = 4η_0), keeping δ = 0.67. This model condition yields a similar course of band evolution with increasing bulk shear, as in Type IIIA. However, P bands appear as an additional element, which interact with the dominant C bands and earlier R$_1$ bands to form symmetrical anatomizing pattern along the shear direction. This networking of C bands with R$_1$- and P-bands produces symmetrical undeformed lenses, which are hosted in homogeneously sheared domains (Fig. 7.12g). These lenses are much more rounded than those in Type IIIA, and their long axes are oriented nearly parallel to the bulk shear direction. A histogram plot of their aspect ratios characteristically displays an asymmetric distribution with a frequency peak value of 10 to 15 within a range of 6 to 21.

Parameters	Symbol	Natural Values	Numerical Input Values	Range of Input Values
Model length	L	40 km	4	
Model width	W	10 km	1	0.25 – 0.9
Model reference strain rate	$\dot{\gamma}_o$	1.00e^{-15}	1	0.5 - 20
Model reference density	ρ	2700 kg m^{-3}	1	
Model reference viscosity	η_0	1e^{20} Pas	1	1 - 20
Initial Cohesion	C_i	65 Mpa	0.25	
Angle of friction	ϕ	25° - 30°	25° - 30°	
Maximum Yield stress	σ_{max}	1000 Mpa	0.04	
Minimum Yield stress	σ_{min}	10 Mpa	3.7	

Table 7.1: Model parameters and their values

7.5. FIELD DIAGRAM: SHEAR PARALLEL VS LOW-ANGLE SHEAR BANDS

A compilation of the simulation runs reveals that the two competing shear localization mechanisms: C and LSB are mediated by two non-dimensional parameters: $\Omega = \frac{\eta_v \dot{\gamma}_b}{C_i}$ and $\delta = \frac{W_C}{W}$, where C_i is the initial cohesion of shear zone materials, and W is the total shear zone thickness. Two distinct fields for LSB and C band localization are obtained, separated by a hybrid field (C + LSB) in the Ω- δ space (Fig. 7.13a). The field diagram indicates that a shear zone can localize C bands only when Ω attains a threshold value, which can be achieved by increasing either viscosity (η_v), shear rate ($\dot{\gamma}_b$) (Fig. 7.13a) or by lowering the cohesive strength (C_i). Similarly, under a fixed dynamic condition (i.e., constant Ω), shear zones can produce C-bands if their effective thickness lies below a threshold value. The field diagram also suggests that the possibility of LSB formation becomes limited as the effective shear zone thickness becomes low (Fig. 7.13a). Such narrow shear zones would localize C-bands, as widely observed in fields. Figure 7.13b presents a graphical plot of the three
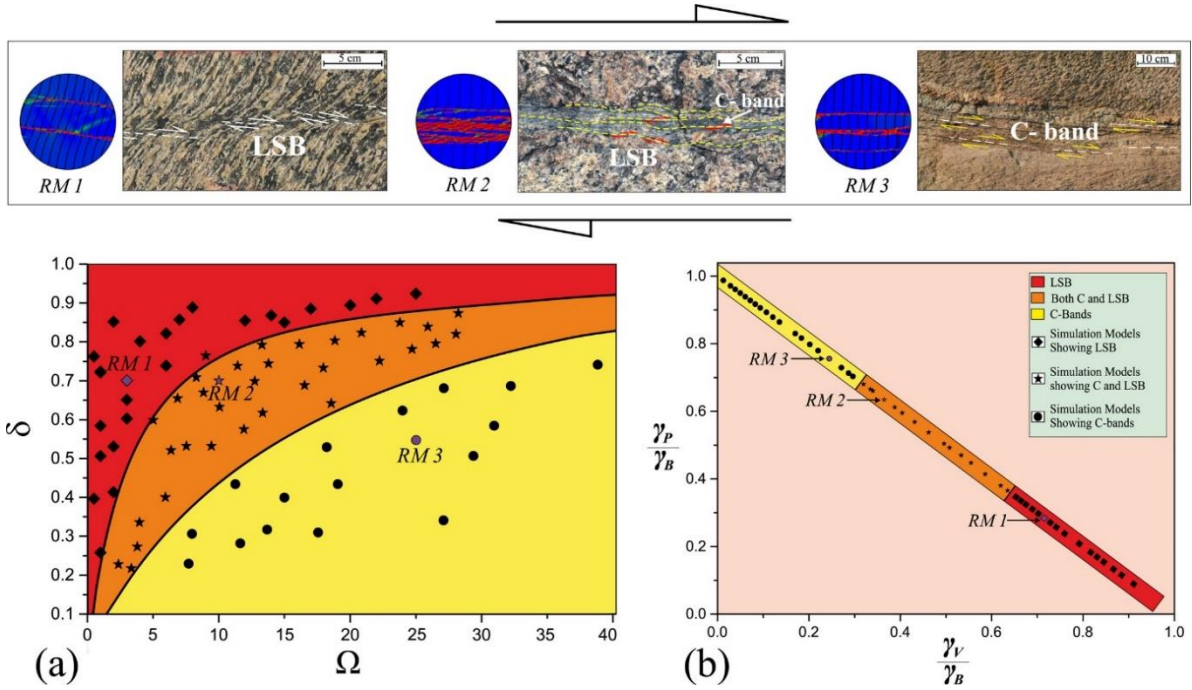
Figure 7.13: (a) Fields of the three competing modes of secondary shear band formation: pure low-angle shear band (LSB), hybrid (LSB+C) and pure C in the Ω-δ space, where $\Omega = \frac{\eta_v \times \dot{\gamma}_b}{c_i}$ and $\delta = \frac{W_c}{W}$ (b) Model calculated plots showing contrasting viscous versus plastic shear strain partitioning in shear zones for the three modes: LSB, C and C+LSB; γ_v, γ_p and γ_b represent viscous, plastic and bulk shear respectively.

types of shear localization: LSB, C and C-LSB in γ_v-γ_p space, where γ_v and γ_p represents the normalized viscous and plastic strains, respectively. According to this plot, the C band formation involves the lowest viscous strain partitioning, which linearly increases with the transition from C to LSB field.

The simulation results for the band network patterns were compiled to find a functional relation of Type I, II and III band network patterns with the effective thickness (W_c), bulk shear rate ($\dot{\gamma}_b$) and bulk viscosity (η_v) of shear zones. The plot shows their distinct fields in δ - $\dot{\gamma}_{b_n}$ spaces for given η_v (δ and $\dot{\gamma}_{b_n}$: normalized W_c and $\dot{\gamma}_b$ values) (Fig. 7.14). The field diagram indicates that large δ values facilitate Type 1 band networking, which is replaced by Type II with reducing δ. On the other hand, increasing bulk shear rates results in a transition from Type 1 to Type III and ultimately, to Type II. Comparing the field diagrams for low ($\eta_v < 4\eta_0$), moderate ($8\eta_0 < \eta_v < 8\eta_0$) and high ($\eta_v > 8\eta_0$) values of η_v, it is found that low-viscosity shear

zones of larger effective thickness ($\delta > 0.6$) appear to network their bands dominantly in Type III, particularly at high shear rates ($\dot{\gamma}_{b_n} > 5$).
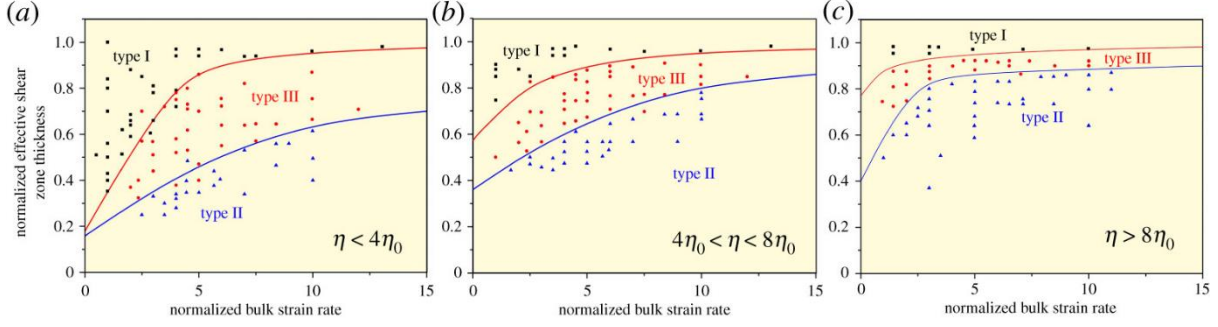

Figure 7.14: Fields of type I, type II and type III band networking in a space defined by normalized bulk strain rate $\dot{\gamma}_{b_n}$ and normalized effective shear zone thickness (δ). (a) Type I networking to dominate in shear zones with relatively low bulk viscosity ($\eta_v < 4\eta_0$), (b) narrowing of type I and type III fields with increasing η_v and (c) dominant growth of type III shear band network with parallel C-shear bands when η_v is extremely large ($>8\eta_0$).

7.6. THEORETICAL INTERPRETATIONS

A theoretical analysis is developed to explain the LSB/C transition observed in the numerical simulations. Consider a low-angle shear band at an angle θ with the shear direction in a shear zone of total thickness W. At the moment of shear failure, the driving shear stress along the band must satisfy the following dynamic condition,

$$|\tau| = C_0 - \mu\sigma - \tau_v \tag{7.15}$$

where C_o is the cohesive strength at the moment of failure, μ is the coefficient of internal friction. The shear band at an angle θ with the shear direction and undergoing slip at a rate $\dot{S}$. This slip creates an overall strain in y- direction at a rate,

$$\dot{\epsilon}_{yy} = \frac{\dot{S} \sin\theta}{d} \tag{7.16}$$

This can be accommodated by viscous deformation perpendicular to the shear zone, given as

$$\sigma_{yy} = 2\,\eta_v\,\dot{\epsilon}_{yy} = \frac{2\,\eta_v\,\dot{S}\,\sin\theta}{d} \tag{7.17}$$

This stress will create a resistance to the slip, which can be derived in the following way,

$$\tau_v = -\frac{\sigma_{yy} - \sigma_{xx}}{2} \sin\left\{2\left(\frac{\pi}{2} - \theta\right)\right\} \tag{7.18}$$

$$\tau_v = -\frac{\sigma_{yy}}{2} \sin 2\theta \quad [\sigma_{xx} = 0] \tag{7.19}$$

$$\tau_v = -\frac{\eta_v \dot{S} \sin\theta \sin 2\theta}{d} \tag{7.20}$$

Thus τ_v is an additional term that represents the viscous resistance, given by

$$\tau_v = -\frac{\eta_v \dot{S} \sin\theta \sin 2\theta}{d} \tag{7.21}$$

where $\dot{S}$ is the slip rate in the band and $d = \frac{w_c}{2}$. Eqs. (7.15) & (7.21) lead to

$$|\tau| = C_o - \mu\sigma + \frac{\eta_v \dot{S} \sin\theta \sin 2\theta}{d} \tag{7.22}$$

It is known that;

$$\sigma = \sigma_e \sin 2\theta \tag{7.23}$$

$$\tau = -\sigma_e \cos 2\theta. \tag{7.24}$$

$\sigma_e = 2\eta_{eff} \dot{\gamma}_b$ is the yield strength of material in the shear zone at the moment of failure, where $\eta_{eff}, \dot{\gamma}_b$ are bulk viscosity and bulk shear rate respectively. Substituting σ and τ in Eq. (7.22), it follows

$$\sigma_e \cos 2\theta = C_o - \mu \sigma_e \sin 2\theta + \frac{\eta_v \dot{S} \sin\theta \sin 2\theta}{d} \tag{7.25}$$

Differentiating Eq. (7.25) with respect to θ and implementing some algebraic manipulation,

$$-2\eta_{eff}\,\dot{\gamma}_b \sin 2\theta \; + \; 2\,\mu\,\eta_{eff}\,\dot{\gamma}_b \cos 2\theta \; - \; \frac{\eta_v\,\dot{S}}{d}(2\sin\theta\cos 2\theta + \tag{7.26}$$

$$\sin 2\theta \cos\theta\,) = 0$$

$$\frac{(\mu \cos 2\theta - \sin 2\theta\,)}{(2\sin\theta\cos 2\theta + \sin 2\theta\cos\theta)} = \frac{\eta_v\,\dot{S}}{d\sigma_e} \tag{7.27}$$

For constant $\dot{S}$, when the effective shear zone thickness becomes extremely large (i.e., $d \to \infty$), Eq. (7.27) takes the following form,

$$\mu \cos 2\theta - \sin 2\theta = 0 \tag{7.28}$$

$\theta = \frac{\emptyset}{2}$, where $\mu = tan\emptyset$, $\emptyset$ is the angle of internal friction. The result indicates that LSB formation is the mechanically favored mechanism of shear localization in thick shear zones, which agrees well with the observations in numerical simulations (Fig. 7.10).

Eq (7.27) can be re-written as,

$$\frac{(\mu \cos 2\theta - \sin 2\theta\,)}{(2\sin\theta\cos 2\theta + \sin 2\theta\cos\theta)} = \frac{2A\eta_v\,\dot{\gamma}_b}{\delta\sigma_e} \tag{7.29}$$

For simplification, in deriving Eq. (7.29), it has been assumed that the slip rate $\dot{S}$ is linearly proportional to the rate of displacement $(W\dot{\gamma}_b)$ at the shear zone boundary, where A is the proportionality constant. From Eq. (7.29), extremely large shear viscosity $(\eta_v \to \infty)$, high shear rates $(\dot{\gamma}_b \to \infty)$ and low shear zone thickness $(\delta \to 0)$ lead to

$$2\sin\theta\cos 2\theta + \sin 2\theta\cos\theta = 0 \tag{7.30}$$

One of the solutions of this equation is: $\theta = 0$, implying that the shear zone will

localize parallel to the shear direction to produce C bands. Eq. (22) similarly predicts
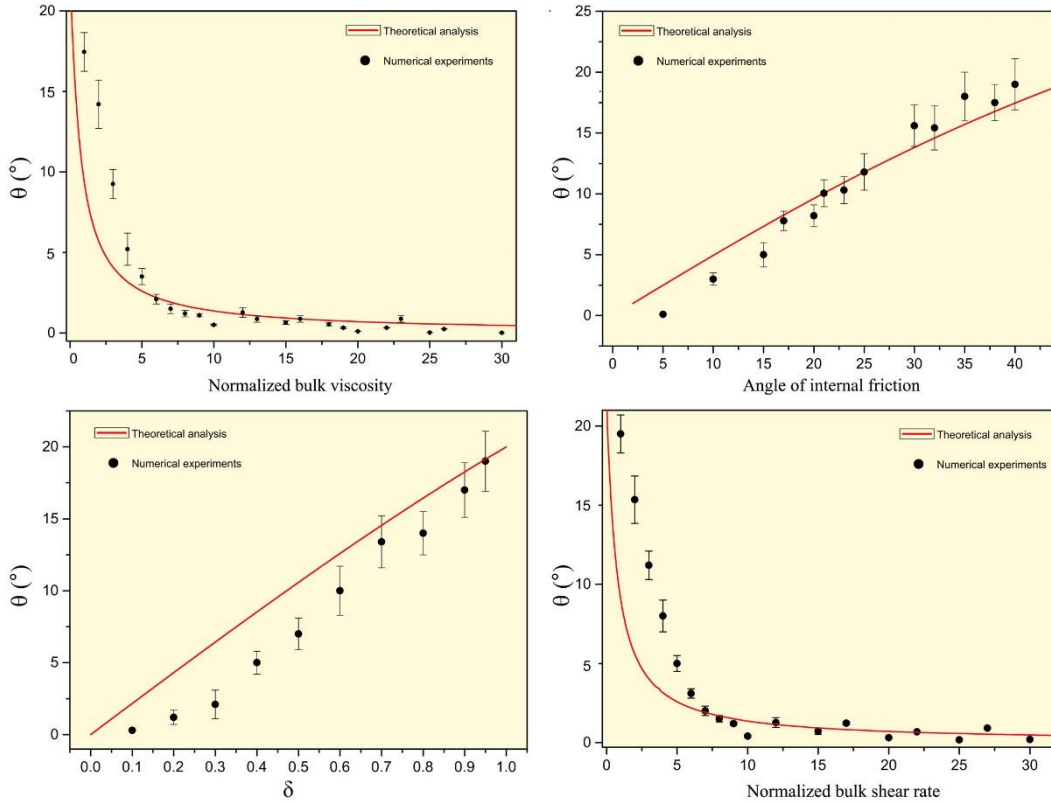

Figure 7.15: Comparison of the shear band angles (θ), obtained from numerical simulations for varying (a) normalized bulk viscosity (η_v), (b) angle of internal friction (ϕ), (c) normalized effective shear zone thickness (δ), and (d) normalized bulk shear rate ($\dot{\gamma}_b$), with the theoretical solutions (solid red lines).

that a decrease in yield strength (i.e., $\sigma_e \to 0$) will result in transition of LSB to C band

localization. Another solution of Eq. (7.30), gives $\theta \sim 55°$. Earlier theoretical studies

also predicted two potential orientations for shear band formation in shear

deformation (Katz et al., 2006, Misra et al., 2009). However, the high-angle bands fail

to compete with the growth rate of the low-angle ones as they undergo advection by

simple shear to attain an unfavourable orientation for their growth (Katz et al., 2006).

The shear zone is eventually dominated by shear parallel bands, as observed in the

field (Fig. 7.5) as well as numerical simulations (Fig. 7.10).

The theoretically predicted shear-band angles as a function of the kinematic

($\dot{\gamma}_b$), rheological (η_v, ϕ) and geometric parameters (δ) are compared with the results

obtained from numerical simulations (Fig. 7.15). The data in turn confirms that the

shear-band angles can be explained with the theoretical model presented here.

7.7 REFERENCES

Altunkaynak, Ş., & Genç, Ş. C. (2008). Petrogenesis and time-progressive evolution of the Cenozoic continental volcanism in the Biga Peninsula, NW Anatolia (Turkey). *Lithos*, *102*(1–2), 316–340. https://doi.org/10.1016/J.LITHOS.2007.06.003

Anand, L., & Spitzig, W. A. (1980). Initiation of localized shear bands in plane strain. *Journal of the Mechanics and Physics of Solids*. https://doi.org/10.1016/0022-5096(80)90017-4

Anand, L., & Spitzig, W. A. (1982). Shear-band orientations in plane strain. *Acta Metallurgica*. https://doi.org/10.1016/0001-6160(82)90236-X

Anand, L., Kim, K. H., & Shawki, T. G. (1987). Onset of shear localization in viscoplastic solids. *Journal of the Mechanics and Physics of Solids*. https://doi.org/10.1016/0022-5096(87)90045-7

Andersen, T. B., Jamtveit, B., Dewey, J. F., & Swensson, E. (1991). Subduction and eduction of continental crust: major mechanisms during continent-continent collision and orogenic extensional collapse, a model based on the south Norwegian Caledonides. *Terra Nova*, *3*(3), 303–310. https://doi.org/10.1111/J.1365-3121.1991.TB00148.X

Andrews, E. R., & Billen, M. I. (2009). Rheologic controls on the dynamics of slab detachment. *Tectonophysics*, *464*(1–4), 60–69. https://doi.org/10.1016/J.TECTO.2007.09.004

Austermann, J., Ben-Avraham, Z., Bird, P., Heidbach, O., Schubert, G., & Stock, J. M. (2011). Quantifying the forces needed for the rapid change of Pacific plate motion at 6 Ma. *Earth and Planetary Science Letters*, *307*(3–4), 289–297. https://doi.org/10.1016/J.EPSL.2011.04.043

Babist, J., Handy, M. R., Konrad-Schmolke, M., & Hammerschmidt, K. (2006). Precollisional, multistage exhumation of subducted continental crust: The Sesia Zone, western Alps. *Tectonics*, *25*(6), 6008. https://doi.org/10.1029/2005TC001927

Bercovici, D. (1993). A simple model of plate generation from mantle flow. *Geophysical Journal International*, *114*(3), 635–650. https://doi.org/10.1111/j.1365-246X.1993.tb06993.x

Du Bernard, X., Eichhubl, P., & Aydin, A. (2002). Dilation bands: A new form of localized failure in granular media. *Geophysical Research Letters*. https://doi.org/10.1029/2002GL015966

Berthé, D., Choukroune, P., & Jegouzo, P. (1979). Orthogneiss, mylonite and non coaxial deformation of granites: the example of the South Armorican Shear

Zone. *Journal of Structural Geology*. https://doi.org/10.1016/0191-8141(79)90019-1

Bowden, P. B., & Raha, S. (1970). The formation of micro shear bands in polystyrene and polymethylmethacrylate. *Philosophical Magazine*. https://doi.org/10.1080/14786437008225837

Buiter, S. J. H., Govers, R., & Wortel, M. J. R. (2002). Two-dimensional simulations of surface deformation caused by slab detachment. *Tectonophysics*, *354*(3–4), 195–210. https://doi.org/10.1016/S0040-1951(02)00336-0

Burkett, E. R., & Billen, M. I. (2010). Three-dimensionality of slab detachment due to ridge-trench collision: Laterally simultaneous boudinage versus tear propagation. *Geochemistry, Geophysics, Geosystems*, *11*(11). https://doi.org/10.1029/2010GC003286

Byerlee, J., Mjachkin, V., Summers, R., & Voevoda, O. (1978). Structures developed in fault gouge during stable sliding and stick-slip. *Tectonophysics*. https://doi.org/10.1016/0040-1951(78)90068-9

Carreras, J., Czeck, D. M., Druguet, E., & Hudleston, P. J. (2010). Structure and development of an anastomosing network of ductile shear zones. *Journal of Structural Geology*. https://doi.org/10.1016/j.jsg.2010.03.013

Casey, M. (1980). Mechanics of shear zones in isotropic dilatant materials. *Journal of Structural Geology*, *2*(1–2), 143–147. https://doi.org/10.1016/0191-8141(80)90044-9

Chester, F. M., & Logan, J. M. (1987). Composite planar fabric of gouge from the Punchbowl Fault, California. *Journal of Structural Geology*. https://doi.org/10.1016/0191-8141(87)90147-7

Cobbold, P. R. (1977a). DESCRIPTION AND ORIGIN OF BANDED DEFORMATION STRUCTURES - 1. REGIONAL STRAIN, LOCAL PERTURBATIONS, AND DEFORMATION BANDS. *Can J Earth Sci*, *14*(8), 1721–1731. https://doi.org/10.1139/e77-147

Cobbold, P. R. (1977b). DESCRIPTION AND ORIGIN OF BANDED DEFORMATION STRUCTURES - 2. RHEOLOGY AND THE GROWTH OF BANDED PERTURBATIONS. *Can J Earth Sci*, *14*(11), 2510–2523. https://doi.org/10.1139/e77-217

Coelho, S., Passchier, C., & Marques, F. (2006). Riedel-shear control on the development of pennant veins: Field example and analogue modelling. https://doi.org/10.1016/j.jsg.2006.05.009

Coulomb, C. A. (2007). Essai sur une application des regles de maximis et minimis quelques problemes de statique, relatits a l'architecture. *Memoires de*

Mathematique de l'Academie Royale de Science 7, Paris.
https://doi.org/10.1016/j.msea.2007.01.047

Drucker, D. C., & Prager, W. (1952). Soil mechanics and plastic analysis or limit design. *Quarterly of Applied Mathematics.*
https://doi.org/10.1090/qam/48291

Duretz, T., & Gerya, T. V. (2013). Slab detachment during continental collision: Influence of crustal rheology and interaction with lithospheric delamination. *Tectonophysics*, *602*, 124–140. https://doi.org/10.1016/J.TECTO.2012.12.024

Duretz, Thibault, Gerya, T. V., & May, D. A. (2011). Numerical modelling of spontaneous slab breakoff and subsequent topographic response. *Tectonophysics*, *502*(1–2), 244–256.
https://doi.org/10.1016/J.TECTO.2010.05.024

Evans, M., Harlow, F., & Bromberg, E. (1957). *The Particle-In-Cell Method for Hydrodynamic Calculations.* Retrieved from
https://apps.dtic.mil/sti/citations/ADA384618

Ferrari, L. (2004). Slab detachment control on mafic volcanic pulse and mantle heterogeneity in central Mexico. *Geology*, *32*(1), 77–80.
https://doi.org/10.1130/G19887.1

Finch, M., Hasalová, P., Weinberg, R. F., & Fanning, C. M. (2014). Switch from thrusting to normal shearing in the Zanskar shear zone, NW Himalaya: Implications for channel flow. *Bulletin of the Geological Society of America*, *126*(7–8), 892–924. https://doi.org/10.1130/B30817.1

Finch, M. A., Bons, P. D., Steinbach, F., Griera, A., Llorens, M. G., Gomez-Rivas, E., et al. (2020). The ephemeral development of C′ shear bands: A numerical modelling approach. *Journal of Structural Geology.*
https://doi.org/10.1016/j.jsg.2020.104091

Fossen, H., & Cavalcante, G. C. G. (2017, August 1). Shear zones – A review. *Earth-Science Reviews.* Elsevier B.V. https://doi.org/10.1016/j.earscirev.2017.05.002

Fusseis, F., & Handy, M. R. (2008). Micromechanisms of shear zone propagation at the brittle-viscous transition. *Journal of Structural Geology*, *30*(10), 1242–1253.
https://doi.org/10.1016/j.jsg.2008.06.005

Fusseis, F., Handy, M. R., & Schrank, C. (2006). Networking of shear zones at the brittle-to-viscous transition (Cap de Creus, NE Spain). *Journal of Structural Geology.* https://doi.org/10.1016/j.jsg.2006.03.022

Gerya, T. V., Yuen, D. A., & Maresch, W. V. (2004). Thermomechanical modelling of slab detachment. *Earth and Planetary Science Letters*, *226*(1–2), 101–116.
https://doi.org/10.1016/J.EPSL.2004.07.022

Govers, R., & Wortel, M. J. R. (1995). Extension of stable continental lithosphere and the initiation of lithospheric scale faults. *Tectonics*, *14*(4), 1041–1055. https://doi.org/10.1029/95TC00500

Guermani, A., & Pennacchioni, G. (1998). Brittle precursors of plastic deformation in a granite: An example from the Mont Blanc massif (Helvetic, western Alps). *Journal of Structural Geology*, *20*(2–3), 135–148. https://doi.org/10.1016/S0191-8141(97)00080-1

Harris, L. B., & Cobbold, P. R. (1985). Development of conjugate shear bands during bulk simple shearing. *Journal of Structural Geology*, *7*(1), 37–44. https://doi.org/10.1016/0191-8141(85)90113-0

H. Horii, & S. Nemat-Nasser. (1986). Brittle failure in compression: splitting faulting and brittle-ductile transition. *Philosophical Transactions of the Royal Society of London. Series A, Mathematical and Physical Sciences*. https://doi.org/10.1098/rsta.1986.0101

Hildebrand, R. S., & Bowring, S. A. (1999). Crustal recycling by slab failure. *Geology*, *27*(1), 11–14. Retrieved from https://watermark.silverchair.com/i0091-7613-27-1-11.

Hobbs, B. E., Mühlhaus, H. B., & Ord, A. (1990). Instability, softening and localization of deformation. *Geological Society Special Publication*. https://doi.org/10.1144/GSL.SP.1990.054.01.15

Holtzman, B. K., Kohlstedt, D. L., Zimmerman, M. E., Heidelbach, F., Hiraga, T., & Hustoft, J. (2003). Melt segregation and strain partitioning: Implications for seismic anisotropy and mantle flow. *Science*. https://doi.org/10.1126/science.1087132

Huismans, R. S., & Beaumont, C. (2002). Asymmetric lithospheric extension: The role of frictional plastic strain softening inferred from numerical experiments. *Geology*, *30*(3), 211–214. https://doi.org/10.1130/0091-7613(2002)030<0211:ALETRO>2.0.CO;2

van Hunen, J., & Allen, M. B. (2011). Continental collision and slab break-off: A comparison of 3-D numerical models with observations. *Earth and Planetary Science Letters*, *302*(1–2), 27–37. https://doi.org/10.1016/j.epsl.2010.11.035

Hutchinson, J. W., & Tvergaard, V. (1981). Shear band formation in plane strain. *International Journal of Solids and Structures*. https://doi.org/10.1016/0020-7683(81)90053-6

Huw Davies, J., & von Blanckenburg, F. (1995). Slab breakoff: A model of lithosphere detachment and its test in the magmatism and deformation of collisional orogens. *Earth and Planetary Science Letters*, *129*(1–4), 85–102. https://doi.org/10.1016/0012-821X(94)00237-S

Katz, R. F., Spiegelman, M., & Holtzman, B. (2006). The dynamics of melt and shear localization in partially molten aggregates. *Nature*. https://doi.org/10.1038/nature05039

Kaus, B. J. P. (2010). Factors that control the angle of shear bands in geodynamic numerical models of brittle deformation. *Tectonophysics*. https://doi.org/10.1016/j.tecto.2009.08.042

Lemiale, V., Mühlhaus, H. B., Moresi, L., & Stafford, J. (2008). Shear banding analysis of plastic models formulated for incompressible viscous flows. *Physics of the Earth and Planetary Interiors*, *171*(1–4), 177–186. https://doi.org/10.1016/j.pepi.2008.07.038

Lin, A. (2001). S-C fabrics developed in cataclastic rocks from the Nojima fault zone, Japan and their implications for tectonic history. *Journal of Structural Geology*. https://doi.org/10.1016/S0191-8141(00)00171-1

Lister, G. S., & Snoke, A. W. (1984). S-C Mylonites. *Journal of Structural Geology*. https://doi.org/10.1016/0191-8141(84)90001-4

Logan, J. M. (1979). Experimental studies of simulated gouge and their application to studies of natural fault zones. *In Proceedings of Conference VIII-Analysis of Actual Fault Zones in Bedrock*, (pp. 305-343).

Logan, J. M., Dengo, C. A., Higgs, N. G., & Wang, Z. Z. (1992). Fabrics of Experimental Fault Zones: Their Development and Relationship to Mechanical Behavior. *International Geophysics*. https://doi.org/10.1016/S0074-6142(08)62814-4

Mancktelow, N. S. (2006). How ductile are ductile shear zones? *Geology*. https://doi.org/10.1130/G22260.1

Mancktelow, N. S., & Pennacchioni, G. (2005). The control of precursor brittle fracture and fluid-rock interaction on the development of single and paired ductile shear zones. *Journal of Structural Geology*, *27*(4), 645–661. https://doi.org/10.1016/j.jsg.2004.12.001

Mansour, J., Giordani, J., Moresi, L., Beucher, R., Kaluza, O., Velic, M., et al. (2020). Underworld2: Python Geodynamics Modelling for Desktop, HPC and Cloud. *Journal of Open Source Software*, *5*(47), 1797. https://doi.org/10.21105/joss.01797

Mazumder, R., Van Loon, A. J., Mallik, L., Reddy, S. M., Arima, M., Altermann, W., et al. (2012). Mesoarchaean-Palaeoproterozoic stratigraphic record of the Singhbhum crustal province, Eastern India: A synthesis. *Geological Society Special Publication*. https://doi.org/10.1144/SP365.3

REFERENCE

Meyer, S. E., Kaus, B. J. P., & Passchier, C. (2017). Development of branching brittle and ductile shear zones: A numerical study. *Geochemistry, Geophysics, Geosystems*. https://doi.org/10.1002/2016GC006793

Misra, S., Mandal, N., & Chakraborty, C. (2009). Formation of Riedel shear fractures in granular materials: Findings from analogue shear experiments and theoretical analyses. *Tectonophysics*. https://doi.org/10.1016/j.tecto.2009.02.017

Misra, S., Burlini, L., & Burg, J. P. (2009). Strain localization and melt segregation in deforming metapelites. *Physics of the Earth and Planetary Interiors*, *177*(3–4), 173–179. https://doi.org/10.1016/j.pepi.2009.08.011

Moresi, L., Quenette, S., Lemiale, V., Mériaux, C., Appelbe, B., & Mühlhaus, H. B. (2007). Computational approaches to studying non-linear dynamics of the crust and mantle. *Physics of the Earth and Planetary Interiors*. https://doi.org/10.1016/j.pepi.2007.06.009

Morley, C. K., & Back, S. (2008). Estimating hinterland exhumation from late orogenic basin volume, NW Borneo. *Journal of the Geological Society*, *165*(1), 353–366. https://doi.org/10.1144/0016-76492007-067/ASSET/FD379CE3-17DA-4C6F-8E99-CE757BA40A49/ASSETS/GRAPHIC/07067-8.JPEG

Mugnier, J. L., & Huyghe, P. (2006). Ganges basin geometry records a pre-15 Ma isostatic rebound of Himalaya. *Geology*, *34*(6), 445–448. https://doi.org/10.1130/G22089.1

Mukherjee, S., & Koyi, H. A. (2010). Higher Himalayan Shear Zone, Zanskar Indian Himalaya: Microstructural studies and extrusion mechanism by a combination of simple shear and channel flow. *International Journal of Earth Sciences*, *99*(5), 1083–1110. https://doi.org/10.1007/s00531-009-0447-z

Paterson, M. S., & Wong, T. F. (2005). *Experimental rock deformation - The brittle field*. *Experimental Rock Deformation - The Brittle Field* (Vol. 13). https://doi.org/10.1007/b137431

Pennacchioni, G., & Mancktelow, N. S. (2007). Nucleation and initial growth of a shear zone network within compositionally and structurally heterogeneous granitoids under amphibolite facies conditions. *Journal of Structural Geology*, *29*(11), 1757–1780. https://doi.org/10.1016/j.jsg.2007.06.002

Platt, J. P. (1984). Secondary cleavages in ductile shear zones. *Journal of Structural Geology*. https://doi.org/10.1016/0191-8141(84)90045-2

Platt, J. P., & Vissers, R. L. M. (1980). Extensional structures in anisotropic rocks. *Journal of Structural Geology*. https://doi.org/10.1016/0191-8141(80)90002-4

Power, W. L., & Tullis, T. E. (1989). The relationship between slickenside surfaces in fine-grained quartz and the seismic cycle. *Journal of Structural Geology*. https://doi.org/10.1016/0191-8141(89)90105-3

Ramsay, J. G. (1980). Shear zone geometry: A review. *Journal of Structural Geology*. https://doi.org/10.1016/0191-8141(80)90038-3

Ramsay, J. G., & Graham, R. H. (1970). Strain variation in shear belts. *Canadian Journal of Earth Sciences*, *7*(3), 786–813. https://doi.org/10.1139/e70-078

Regard, V., Bellier, O., Thomas, J. C., Bourlès, D., Bonnet, S., Abbassi, M. R., et al. (2005). Cumulative right-lateral fault slip rate across the Zagros-Makran transfer zone: Role of the Minab-Zendan fault system in accommodating Arabia-Eurasia convergence in southeast Iran. *Geophysical Journal International*, *162*(1), 177–203. https://doi.org/10.1111/J.1365-246X.2005.02558.X/2/M_162-1-177-EQ013.JPEG

Regard, Vincent, Faccenna, C., Bellier, O., & Martinod, J. (2008). Laboratory experiments of slab break-off and slab dip reversal: insight into the Alpine Oligocene reorganization. *Terra Nova*, *20*(4), 267–273. https://doi.org/10.1111/J.1365-3121.2008.00815.X

Renshaw, C. E., & Schulson, E. M. (2001). Universal behaviour in compressive failure of brittle materials [5]. *Nature*. https://doi.org/10.1038/35091045

Rice, J. R. (1985). Fracture mechanics. *Applied Mechanics Reviews*. https://doi.org/10.1115/1.3143689

Rogers, R. D., Ká, H., & Van Der Hilst, R. D. (2002). Epeirogenic uplift above a detached slab in northern Central America. *Geology*, *30*(11), 1031–1034. Retrieved from http://pubs.geoscienceworld.org/gsa/geology/article-pdf/30/11/1031/3523209/i0091-7613-30-11-1031.pdf

Roscoe, K. H. (1970). The Influence of Strains in Soil Mechanics, 10th Rankine Lecture. *Géotechnique*. https://doi.org/10.1680/geot.1970.20.2.129

Rudnicki, J. W., & Rice, J. R. (1975). Conditions for the localization of deformation in pressure-sensitive dilatant materials. *Journal of the Mechanics and Physics of Solids*. https://doi.org/10.1016/0022-5096(75)90001-0

Rutter, E. H. (1986). On the nomenclature of mode of failure transitions in rocks. *Tectonophysics*, *122*(3–4), 381–387. https://doi.org/10.1016/0040-1951(86)90153-8

Rutter, E. H., Maddock, R. H., Hall, S. H., & White, S. H. (1986). Comparative microstructures of natural and experimentally produced clay-bearing fault gouges. *Pure and Applied Geophysics PAGEOPH*. https://doi.org/10.1007/BF00875717

Saha, A. K. (1994). Crustal evolution of Singhbhum - north Orissa, eastern India. *Crustal Evolution of Singhbhum - North Orissa, Eastern India*. https://doi.org/10.1016/0301-9268(95)00058-5

Schmocker, M., Bystricky, M., Kunze, K., Burlini, L., Stünitz, H., & Burg, J.-P. (2003). Granular flow and Riedel band formation in water-rich quartz aggregates experimentally deformed in torsion. *Journal of Geophysical Research: Solid Earth*. https://doi.org/10.1029/2002jb001958

Sengupta, S., Sarkar, G., Ghosh Roy, A. K., Bhaduri, S. K., Gupta, S. N., & Mandal, A. (2000). Geochemistry and Rb-Sr geochronology of acid tuffs from the Northern Fringe of the singhbhum craton and their significance in the precambrian evolution. *Indian Minerals*.

Ton, S. Y. M. W. A., & Wortel, M. J. R. (1997). Slab detachment in continental collision zones: An analysis of controlling parameters. *Geophysical Research Letters*, *24*(16), 2095–2098. https://doi.org/10.1029/97GL01939

Tvergaard, V., Needleman, A., & Lo, K. K. (1981). Flow localization in the plane strain tensile test. *Journal of the Mechanics and Physics of Solids*. https://doi.org/10.1016/0022-5096(81)90019-3

Vardoulakis, I., Goldscheider, M., & Gudehus, G. (1978). Formation of shear bands in sand bodies as a bifurcation problem. *International Journal for Numerical and Analytical Methods in Geomechanics*. https://doi.org/10.1002/nag.1610020203

Vermeer, P. A. (1990). The orientation of shear bands in biaxial tests. *Geotechnique*. https://doi.org/10.1680/geot.1990.40.2.223

Yoshioka, S., & Wortel, M. J. R. (1995). Three-dimensional numerical modeling of detachment of subducted lithosphere. *Journal of Geophysical Research: Solid Earth*, *100*(B10), 20223–20244. https://doi.org/10.1029/94JB01258

Zeck, H. P. (1996). Betic-Rif orogeny: subduction of Mesozoic Tethys lithosphere under eastward drifting Iberia, slab detachment shortly before 22 Ma, and subsequent uplift and extensional tectonics. *Tectonophysics*, *254*(1–2), 1–16. https://doi.org/10.1016/0040-1951(95)00206-5

van de Zedde, D. M. A., & Wortel, M. J. R. (2001). Shallow slab detachment as a transient source of heat at midlithospheric depths. *Tectonics*, *20*(6), 868–882. https://doi.org/10.1029/2001TC900018

Zlotnik, S., Fernández, M., Díez, P., & Vergés, J. (2008). Modelling Gravitational Instabilities: Slab Break-off and Rayleigh-Taylor Diapirism. *Earth Sciences and Mathematics*, 1491–1510. https://doi.org/10.1007/978-3-7643-9964-1_3

Chapter 8.

CONCLUSIONS

8.1. GENERAL REMARKS

Understanding the mechanics of instability phenomena that trigger geological and geophysical processes is a key step to the endeavour in geodynamics research. Several instability-driven processes play a critical role in the Earth's evolution throughout the entire geological time spectrum. With this background, the present thesis takes a fluid mechanics approach to address the mechanical and thermo-mechanical problems of geodynamic phenomena in the light of the theory of instabilities on different scales. The main concerns of the thesis are itemized below.

➢ Effects of global horizontal flows on the growth of deep-source thermal plumes in Earth's mantle.

➢ Dynamic evolution of same-dip double-subduction systems and its impact on global plate tectonics.

➢ Consequence of retarding convergence motion in India-Asia collision tectonics.

➢ Factors determining the mechanisms of shear band formation in ductile rocks.

Each of these issues has been studied through analytical, numerical, or laboratory experiments or a combination of these techniques. A major part of these investigations implements Computational Fluid Dynamics (CFD) simulations utilizing the particle-in-cell finite element code UNDERWORLD2, which is one of the most widely used codes in geodynamic modelling. Additionally, the physical experiments presented in this thesis have been conducted using analogue laboratory models appropriately scaled to represent the natural settings. The following visualisation

251

techniques: particle image velocimetry (PIV), and photogrammetry (MICMAC), have been used to accurately capture the model results. The principle outcomes from this thesis work are concluded below.

8.2. *PLUME GROWTH IN GLOBALLY FLOWING EARTH'S MANTLE*

Chapters 3 and 4 of this thesis deals with the mechanics of RT instability initiation under the influence of horizontal global flows, with an aim to address the problem of plume formation from the thermal boundary layer (TBL) at the core-mantle boundary (CMB). Combining CFD simulation results with a linear stability analysis, the thesis leads to the following main conclusions.

1. Horizontal global flows in the mantle always dampen the growth of RT instabilities, where the degree of dampening can vary depending on the initial physical setting, e.g., viscosity ratio of a two-layer system. Under a given initial condition, the system will completely impede the instability growth, entirely suppressing the system to form a characteristic plume structure when the global flow velocity attains a threshold magnitude.

2. The linear stability analysis also predicts dampening effects of the global flow on the instability growth, suggesting that the layer-parallel flow velocity magnitudes >30 times the initial plume ascent velocity dampen short as well as long-wave instabilities. In addition, the analysis reveals that the dominant instability wavelengths, normalized to the initial layer thickness, tend to increase (10 to 40) with increasing normalized ambient velocity (10 to 30).

3. The theory also predicts the growth rate of an instability in an RTI system as a function of the following additional factors: density ratio, source-layer viscosity

and layer thickness. All the three physical parameters act as a driving role in facilitating the instability growth rate.

4. The dampening effects of global flows established in this study explain the mechanics of plume generation in various geodynamic settings, such as subduction zones and the 660 km transition zone. Finally, the thesis provides a new insight into the origin of spatially distant primary mantle plumes, manifested a few hotspots on earth's surface.

8.3. THE EVOLUTION OF DOUBLE SUBDUCTION SYSTEMS

In Chapter 5, this thesis examines the formation and spatio-temporal dynamics of double subduction systems that initiate spontaneously. The present study introduces novel dynamic models that demonstrate the thermo-mechanical evolution of double subduction systems, emphasizing upon the initiation of same-dip double subduction systems by pre-existing weaknesses in the initial plate configurations. The geodynamic models consider the interactions between the two subducting slabs, which although spatially separated, play a crucial role in influencing their complex evolution. To investigate the conditions in which a system can sustain itself as a double subduction system, the thesis utilizes time-dependent and self-consistently evolving particle-in-cell finite element numerical model techniques. Furthermore, the study explores the spatio-temporal variations of the temperatures at the slab-Moho (the boundary between the crust and the mantle within the subducting slab) and the top of the slab within a double subduction tectonic setting. The primary findings of this Chapter are concluded along the following points.

1. Double subduction systems can form spontaneously in presence of lithospheric-scale mechanical weaknesses, e.g., faults, without any aid of kinematic

253

perturbations, as suggested in earlier studies. Throughout the temporal progression of a double subduction system, the slab subducting first influences the kinematics of the counter subducting slab and the flow patterns in the mantle wedge.

2. Double subduction systems can remain active for a large period of time (>25 Ma) if they form in an oceanic setting, i.e., formation of simultaneous subduction between two large oceanic plate. In such cases, the system develops exceptionally high convergence velocities, lying in the range of 16-17 cm/year during an extended period of time.

3. The presence of a continental fragment or plate in the initial tectonic configuration greatly influence the mode of double-subduction evolution. Continental microplates can assist in the termination of subduction in one slab, resulting in tectonic transformation of a double to a typically single subduction system.

4. During the initiation of a double subduction, both the slab temperatures at the slab Moho (the boundary between the crust and the mantle within the subducting slab) and the slab top decrease rapidly at a specific depth. Following this, the temperatures at the slab Moho experience an additional cooling phase, which occurs during the rapid convergence of the slab as it freely sinks. Once the slab collides with the strong lower mantle, the convergence rate decreases, and significant cooling ceases.

5. The double-subduction models presented in this Chapter explain the complete geodynamical evolutionary history of three specific paleo double subduction systems, namely the Trans-Tethyan intra-oceanic system, India-Andaman-Burma subduction system, and Amirante-India-Eurasia subduction. Their

petrological, geophysical and geochemical evidences match fairly well with those derived from the models.

8.4. EXTENSIONAL TECTONICS IN THE HIMALAYA- TIBET MOUNTAIN SYSTEM

The study presented in Chapter 6, substantiates the topography induced gravitational collapse theory for the Tibetan plateau to explain the extensional crustal deformations in the Himalaya-Tibet system. Field and geophysical evidences suggest the need of coupled dynamics to explain the extension across and along the orogen, i.e. N-S and E-W, respectively. The scaled analogue experiments lead to the following conclusions:

1. Steady-state kinematics of India-Asia collision at either high or low convergence rates would not produce the present-day crustal flow and deformation patterns in the Tibetan plateau, as predicted from GPS observations.

2. The onset of eastward crustal flow and related ESE-WNW extension in Tibet is interpreted as a consequence of decelerating Indian indentation velocity (I_{DEC}), from ~5.5 cm/year at ~50 Ma to ~3.5 cm/year at 19±3 Ma in the India-Asia collision history. The rigid Tarim block, located in the northern boundary of Tibet has played a critical role in developing an eastward first-order topographic gradient by 19±3 Ma. This topographic gradient later dictated the crustal material to flow in the east direction, resulting in a transition of NNE-SSW contraction to ESE-WNW extensional tectonics and formation of widespread nearly N-S trending grabens in southern and central Tibet when I_{DEC} decreased to ~3.5 cm/year at 19±3 Ma.

3. The present model also suggests that the eastward crustal flow eventually encountered the rigid Sichuan basin in eastern Tibet, which forced the flow to

take a turn (clockwise rotation) in the southern direction. The orogen-parallel velocity component in model Tibet follows approximately a parabolic variation from its southern to northern boundary, which broadly agrees with the GPS velocity profile. Poiseuille-type kinematics, is thus proposed for the orogen-parallel flow component, driven by a pressure difference due to the west to east topographic gradient. This Poiseuille-type flow explains the localization of sinistral and dextral strike-slip faults preferentially in the northern and the southern parts of Tibet. Finally, the laboratory model estimates of extensional and contractional strain rates: 0.8 to 2.2 ×10^{-8} yr^{-1} and 3.2 to 4.2 ×10^{-8} yr^{-1} agree with the GPS-based strain rates in central Tibet and its eastern flank, respectively.

4. It is the drop in dynamic pressure in the Himalayan wedge that dictated the N-S extension in southern Tibet (Maiti et al., 2021), whereas the topography-driven gravity current developed due to the eastward topographic gradient set in the E-W extension in central Tibet. However, the two tectonic events did not occur exactly in the same time frame; the N-S extension (22 – 11 Ma) ceased to operate as the dynamic pressure regained its initial state with ongoing topographic collapse, but the E-W extension (18-4 Ma) continued to take place in response to the eastward topographic slope under the present-day convergence kinematics. Therefore, it is suggested that reducing Indian plate's indentation velocity actually controlled the coupled extensional dynamics. Far-field tectonic stresses or convective instability might have provided additional influences on extensional tectonics (Schellart et al., 2019). But, a complete synthesis of the model results point to that a combined effect of the crustal heterogeneity and

the reducing Indian indentation velocity is necessary and sufficient to explain the E-W extension.

8.5. MECHANISMS OF SHEAR FAILURE IN LITHOSPHRE

Chapter 7 combines field observations with numerical experiments to show shear parallel (C) and low-angle shear band (LSB) formation as two competing mechanisms of shear localization in ductile shear zones. The principal conclusions of this study are as follows.

1. The effective shear zone thickness (W_c), bulk viscosity (η_v) and the bulk shear rates ($\dot{\gamma}_b$) are the key factors to mediate the LSB versus C growth under a given yield strength of the shear zone materials. Increasing η_v and $\dot{\gamma}_b$ or decreasing W_c switches a transition from LSB to C. These three parameters also critically determine the type of band networking observed in ductile shear zones.

2. A specific combination of these three factors gives rise to localization of a single C band along the central line of the shear zone, as frequently observed in the field.

3. Two non-dimensional factors: dynamic (Ω) and geometric (δ) define two distinct fields for LSB- and C-shear bands, separated by a region of the hybrid [C + LSB] type. The LSB-field becomes remarkably narrow for $\Omega > 10$. Under this dynamic condition LSB can occur only when $\delta > 0.75$. On the other end, the C-field largely widens with increasing Ω, and the C-band formation becomes the dominant mechanism for shear localization in shear zones with $\delta < 0.75$).

4. The bulk finite shear in a shear zone is partitioned into distributed viscous shear (γ_v) and slip-associated localized shear (γ_p). The LSB versus C mechanism

determines the shear partitioning ratio (γ_v/ γ_p). The LSB localization facilitates the distributed viscous shear partitioning, whereas the C-mechanism facilitates the localized shear. Viscoplastic rheology with a pressure dependent plasticity is found to be an ideal rheological model to constrain the LSB versus C-band growth in ductile shear zones.

5. The network structure is a consequence of the three competing mechanisms of secondary shear band formation in a shear zone: i) R (LSB), ii) C- (shear-parallel) and iii) P (shear with sympathetic vergence). These competing mechanisms give rise to three type of band network: Type I (networking of R with P), Type II (network of localized C with R or P). Type III (network defined by penetrative C-bands with R). Numerical model results indicate strain softening rheology and pressure dependent plasticity as prerequisite rheology for the three types of networking under simple shear kinematics. This finding revokes the postulate of transpressional kinematics as a necessary condition for anastomosing band structures in ductile shear zones.

JOURNAL PUBLICATIONS

- **Roy, A**., Roy, N., Saha, P., & Mandal, N. (2021). Factors determining shear-parallel versus low-angle shear band localization in shear deformations: Laboratory experiments and numerical simulations. Journal of Geophysical Research: Solid Earth, 126, e2021JB022578. https://doi.org/10.1029/2021JB022578

- **Roy, A.,** Ghosh, D., and Mandal, N. (2023). Dampening effect of global flows on Rayleigh-Taylor instabilities: Implications for deep-mantle plumes vis-`a-vis hotspot distributions. (In Revision) In Geophysical Journal International (Manuscript ID: GJI- S-23-0401). [DOI: 10.31223/X5HD3B]

- **Roy, A.,** Mandal, N., J.V., Hunen. Competing dynamic evolution of same-dip double-subduction systems: Insights from thermo-mechanical modelling. (In prep for Earth and Planetary Science Letters)

- Maiti, G., **Roy, A.,** Sen, J., & Mandal, N. (2021). Impact of decelerating India-Asia convergence on the crustal flow kinematics in Tibet: An insight from scaled laboratory modeling. Geochemistry, Geophysics, Geosystems, 22, e2021GC009967. https://doi.org/10.1029/2021GC009967

- Roy, N., **Roy, A.,** Saha, P., Mandal, N. (2022). On the origin of shear-band network patterns in ductile shear zones. Proceedings of the Royal Society A, 478(2264), 20220146.

- Mukhopadhyay, M., Roy, A., & Mandal, N. (2023). Mechanisms of shear band formation in heterogeneous materials under compression: The role of pre-existing mechanical flaws. Journal of Geophysical Research: Solid Earth, 128, e2022JB026169. https://doi.org/10.1029/2022JB026169

- Maiti, G., **Roy, A.,** Mandal, N. (2022) N-S versus E-W extension in the Tibetan plateau: Are they driven by the same dynamics? (In Revision) In Geophysical Journal International (Manuscript ID: GJI-S-22-0915L)

CONFERENCE ABSTRACTS

- **Roy, A.,** Ghosh, D., and Mandal, N. (2023). Evolution of Large Igneous Provinces modulated by the competing dynamics of Rayleigh-Taylor instability and global horizontal flows in Earth's mantle. Submitted in AGU General Assembly 2023.

- **Roy, A.,** Saha, P., and Mandal, N. (2022). Viscoplastic Rheological Modelling- A Realistic Approach to Natural Ductile Shear Zones, EGU General Assembly 2022, Vienna, Austria, 23–27 May 2022, EGU22-162. https://doi.org/10.5194/egusphere-egu22-162, 2022

- **Roy, A.**, Saha, P., and Mandal, N. (2022). Structural complexity in natural ductile shear zones. In: Rock Deformation and Structure Conference (RDS-VII), 2022, Banaras Hindu University, India.

- **Roy, A.,** Saha, P., and Mandal, N. (2021). What controls shear-parallel C-band localization in ductile shear zones? In: Rock Deformation and Structure Conference (RDS-VI), 2021, Central University Kerala, India.

- **Roy, A.,** Maiti, G., Sen, J., & Mandal, N. (2020). Tectonic transitions in the Tibetan plateau during India-Asia collision: Findings from scaled laboratory models. Earth and Space Science Open Archive ESSOAr. In AGU General Assembly 2020.

- **Roy, A.,** Roy, N., Saha, P., & Mandal, N. (2020, May). Development of C-shear bands in brittle-ductile shear zones: Insights from analogue and numerical models. In EGU General Assembly Conference Abstracts (p. 960).

- **Roy, A.,** Maiti, G., Sen, J., and Mandal, N. (2018). Crustal flow patterns in the Himalaya-Tibet collision zone: insight from analogue and numerical simulation. In: Rock Deformation and Structure Conference (RDS-V), 2018, Delhi University, India.